Contract Report EL-93-2
June 1993

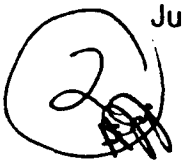

US Army Corps of Engineers
Waterways Experiment Station

Chesapeake Bay Sediment Flux Model

by Dominic M. Di Toro, James J. Fitzpatrick
HydroQual, Inc.

Prepared for U.S. Environmental Protection Agency
and U.S. Army Engineer District, Baltimore

Contract Report EL-93-2
June 1993

Chesapeake Bay Sediment Flux Model

by *Dominic M. Di Toro, James J. Fitzpatrick*
HydroQual, Inc.

One Lethbridge Plaza
Mahwah, NJ 07430

Final report

Approved for public release; distribution is unlimited

Prepared for Chesapeake Bay Program Office
U.S. Environmental Protection Agency
Annapolis, MD 21403

and U.S. Army Engineer District, Baltimore
P. O. Box 1715
Baltimore, MD 21203-1715

Under Contract DACW39-88-D0035

Monitored by Environmental Laboratory
U.S. Army Engineer Waterways Experiment Station
3909 Halls Ferry Road, Vicksburg, MS 39180-6199

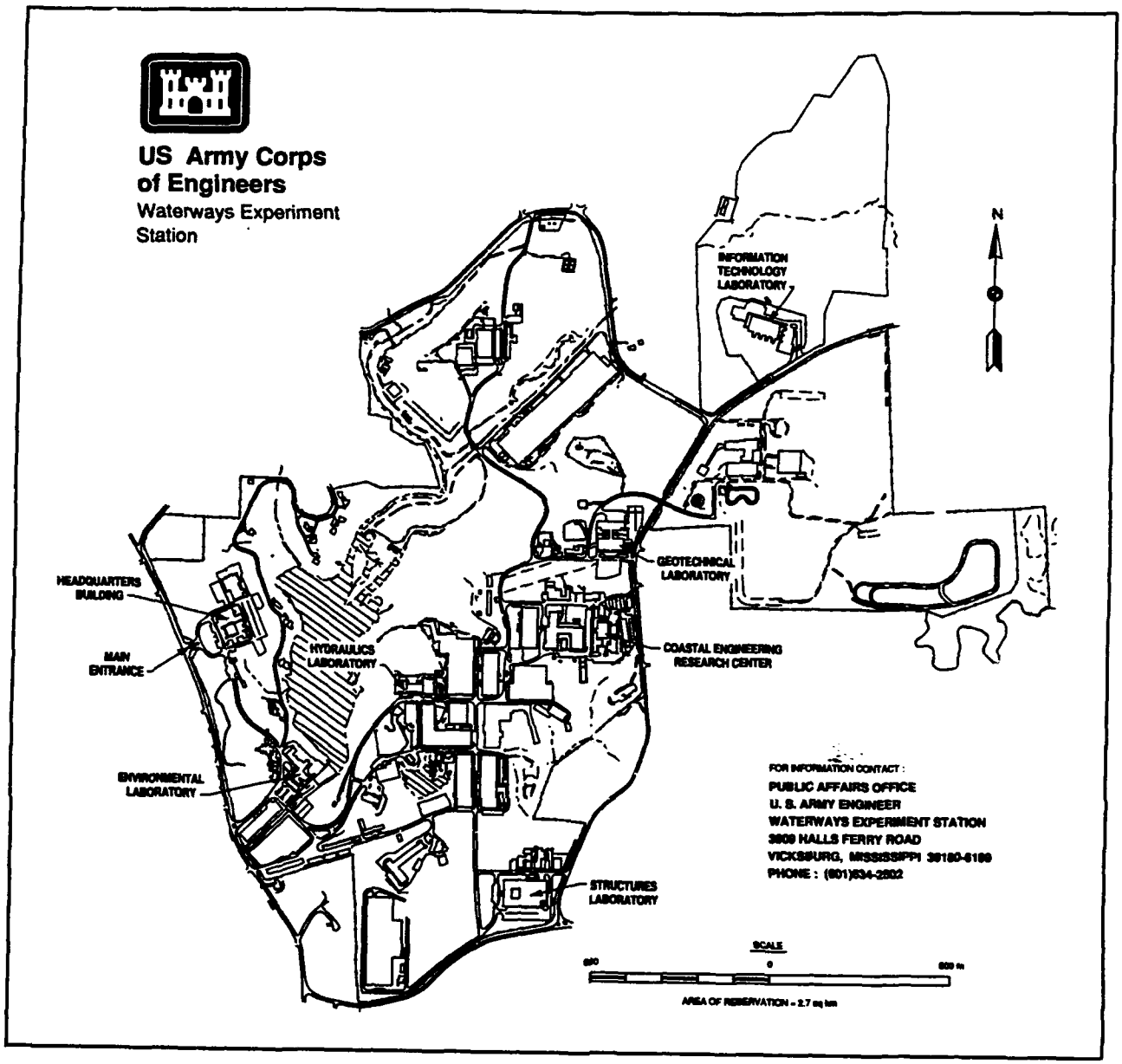

Waterways Experiment Station Cataloging-in-Publication Data

Di Toro, Dominic M.

Chesapeake Bay sediment flux model / by Dominic M. Di Toro, James J. Fitzpatrick ; prepared for Chesapeake Bay Program Office, U.S. Environmental Protection Agency and U.S. Army Engineer District, Baltimore ; monitored by Environmental Laboratory, U.S. Army Engineer Waterways Experiment Station.

316 p. : ill. ; 28 cm. — (Contract report ; EL-93-2)

Includes bibliographical references.

1. Sedimentation and deposition — Chesapeake Bay (Md. and Va.) — Mathematical models. 2. Marine sediments — Chesapeake Bay (Md. and Va.) — Gas content. 3. Sediment compaction — Mathematical models. I. Fitzpatrick James J. II. United States. Environmental Protection Agency. Chesapeake Bay Program. III. United States. Army. Corps of Engineers. Baltimore District. IV. U.S. Army Engineer Waterways Experiment Station. V. Title. VI. Series: Contract report (U.S. Army Engineer Waterways Experiment Station) ; EL-93-2.

TA7 W34c no.EL-93-2

PREFACE

The study reported herein was conducted as part of the Chesapeake Bay Three-Dimensional Model Study. It was sponsored by the Chesapeake Bay Program Office (CBPO), U.S. Environmental Protection Agency, and the U.S. Army Engineer District, Baltimore. Investigations were completed under Contract DACW39-88-D0035. Project monitors were Mr. Lewis Linker, CBPO, and Mr. Larry Lower of the Baltimore District.

This report was prepared by Dr. Dominic Di Toro and Mr. James Fitzpatrick of HyroQual, Inc., Mahwah, NJ. Project management was provided by Mr. Donald L. Robey, Chief, Environmental Processes and Effects Division, Environmental Laboratory (EL), U.S. Army Engineer Waterways Experiment Station (WES), Vicksburg, MS. It was conducted under the general supervision of Dr. John Harrison, Director, EL. Technical review was provided by Drs. Carl F. Cerco and Barry Bunch, Water Quality and Contaminant Modeling Branch, EL, WES.

At the time of publication of this report, Director of WES was Dr. Robert W. Whalin. Commander was COL Leonard G. Hassell, EN.

This report should be cited as follows:

DiToro, D. M., and Fitzpatrick, J. J. "Chesapeake Bay sediment flux model," Contract Report EL-93-2, U.S. Army Engineer Waterways Experiment Station, Vicksburg, MS.

Table of Contents

Table of Tables

I. INTRODUCTION

The Chesapeake Bay Model development project has as it goal the development of a comprehensive model of eutrophication in the estuary. It is a mass balance model that relates the inputs of nutrients to the growth and death of phytoplankton and the resulting extent and duration of the hypoxia and anoxia. The aim is to identify and quantify the causal chain that begins with nutrient inputs and ends with the dissolved oxygen distributions in space and time. The modeling framework is based on a mass balance of the carbon, nitrogen, phosphorus, silica, and dissolved oxygen in the bay. It requires a detailed specification of the transport that affects all these components and the kinetics that describe the growth and death of phytoplankton biomass, the nutrient cycling, and the resulting dissolved oxygen distribution in the bay and estuaries. A critical component of the model is the role of sediments in recycling nutrients and consuming oxygen. This report presents the formulation and calibration of a sediment model which quantifies these processes within the context of mass balances in the sediment compartment.

The development of the sediment model starts with a model for ammonia flux. The reason is that by comparison with the other fluxes of concern the factors which control its magnitude are better understood and can be formulated more directly. The analysis is followed by the model for nitrate flux. For the remaining fluxes it is convenient to analyze the general case and apply it to the fluxes of sulfide, phosphate and silica. The flux of oxygen to the sediment follows as a consequence of the oxidation of sulfide and ammonia.

Steady state solutions are analyzed to provide a basis for understanding the more complex time variable results that follow. The inadequacies of the steady state approximation are instructive and point to the critical non steady state phenomena. The remaining chapters present the non steady state formulation and the results of the calibration of the model to the data set.

A. Background

The development of sediment flux models has been based primarily on models of concentration profiles in sediment interstitial water. These were originally developed by Berner (1971, 1980) and his colleagues. Once the concentration profile is modeled, the flux can be obtained from the slope of the profile at the sediment - water interface.

Vanderborght et al. (1977a, 1977b) proposed a two layer model of this type that considers the production of ammonia, nitrification of ammonia to nitrate, the consumption of sulfate, and the production of silica. Oxygen is consumed at a zero order rate in the upper layer and at a first order rate in the lower layer. Eleven model parameters are required. Four are determined from the silica profile. The ratio of ammonia production to sulfate consumption is estimated from the reaction stoichiometry. The remaining six parameters are obtained from fitting the model to the ammonia, nitrate, and sulfate profiles. Similar models with zero order (Jahnke et al., 1982) and first order (Goloway and Bender, 1982) oxygen consumption rates have been proposed as part of more comprehensive nitrate reduction models for marine sediments.

For simple kinetics and non-interacting species the differential equations can be solved analytically. Extending these solutions to include more realistic kinetic formulations, to explicitly consider soluble and particulate species, and to distinguish the aerobic and anaerobic zones, rapidly leads to intractable equations. An alternate formulation results from representing the sediment as a series of homogeneous layers (e.g. Klapwijk and Snodgrass, 1986). For the model developed in this report, the sediment is represented using two well mixed layers which represent the aerobic and active anaerobic layers of the sediment. This choice has a number of advantages. Analytical solutions to the steady state equations are available for reasonably realistic formulations. They provide useful results that clarify which parameter groups determine the fluxes. Although numerical integrations are still required for time variable solutions to obtain the

annual cycle of fluxes, the structure of the model is clarified by the steady state results. Further, a comparison of the two layer solution and the continuous analytical solution for the ammonia flux model indicates that little is lost by using the two layer discretization.

B. Model Framework

The modeling framework for the sediment model is diagramed in Fig. 1.1. Three separate processes are considered. (1) Particulate organic matter (POM) from the overlying water is deposited into the aerobic and anaerobic layers of the sediment. This is referred to as the depositional flux. (2) The particulate organic matter is mineralized in the sediment. This reaction, which is termed diagenesis, converts POM into soluble intermediates. (3) Reactions can convert a portion of the soluble species into particulate species. These species are transported by diffusion and particle mixing into the aerobic layer, from which they are either transferred to the overlying water, further react and possibly consume oxygen, or are re-mixed into the anaerobic layer. Finally, particulate and dissolved chemicals are buried via sedimentation. This general framework is employed for each of the chemical species considered below.

C. Data Set

The calibration of a comprehensive and interactive nutrient and oxygen flux model requires, above all, a high quality and comprehensive data set. This data set is the result of the efforts of the scientists who developed the methods for reliably measuring sediment fluxes and applied these techniques in a systematic investigation of the Chesapeake Bay. Their efforts are specifically acknowledged and appreciated.

Upper Chesapeake Bay

W. Boynton, J. Cornwell, J. Garber, W.M. Kemp, P. Sampou.

University of Maryland System

Lower Chesapeake Bay

D. Burdige.

Old Dominion University, Norfolk, VA

Hunting Creek, Gunston Cove

C. Cerco.

Corp of Engineers, Vicksburg, MS.

Pore water Data

O. Bricker.

U.S. Geological Survey, Reston VA.

1. Description of data set

The SONE data set (Boynton et al., 1985, 1986, 1988; Garber et al., 1988) used in this analysis consists of nutrient and oxygen fluxes measured four times a year from 1985 through 1988 in Chesapeake Bay. Four main bay stations, two stations in the Potomac estuary, two in the Patuxent estuary, and two in the Choptank are monitored. Fig. 1.2 presents the station locations. Fluxes of NH_4, NO_3, O_2, PO_4, and Si are measured in triplicate from sub-cores taken from a large box core obtained from each station. In addition, solid phase data: POC, PON, POP, and chlorophyll are determined.

The BEST data set (Boynton et al., 1989; Burdige, 1989) is an expanded set of measurements taken in 1988 that extended the sampling stations into the southern bay and the lower tributaries. The same sampling techniques were employed and some additional parameters were measured

The interstitial water data set (Bricker et al, 1977) was developed during the years 1971 to 1976. Stations throughout the main bay were sampled for pH, Eh, pS, and interstitial water concentrations of SO_4, CO_3, Fe, Mn, PO_4, NH_4, and SiO_2. The data has been reported and

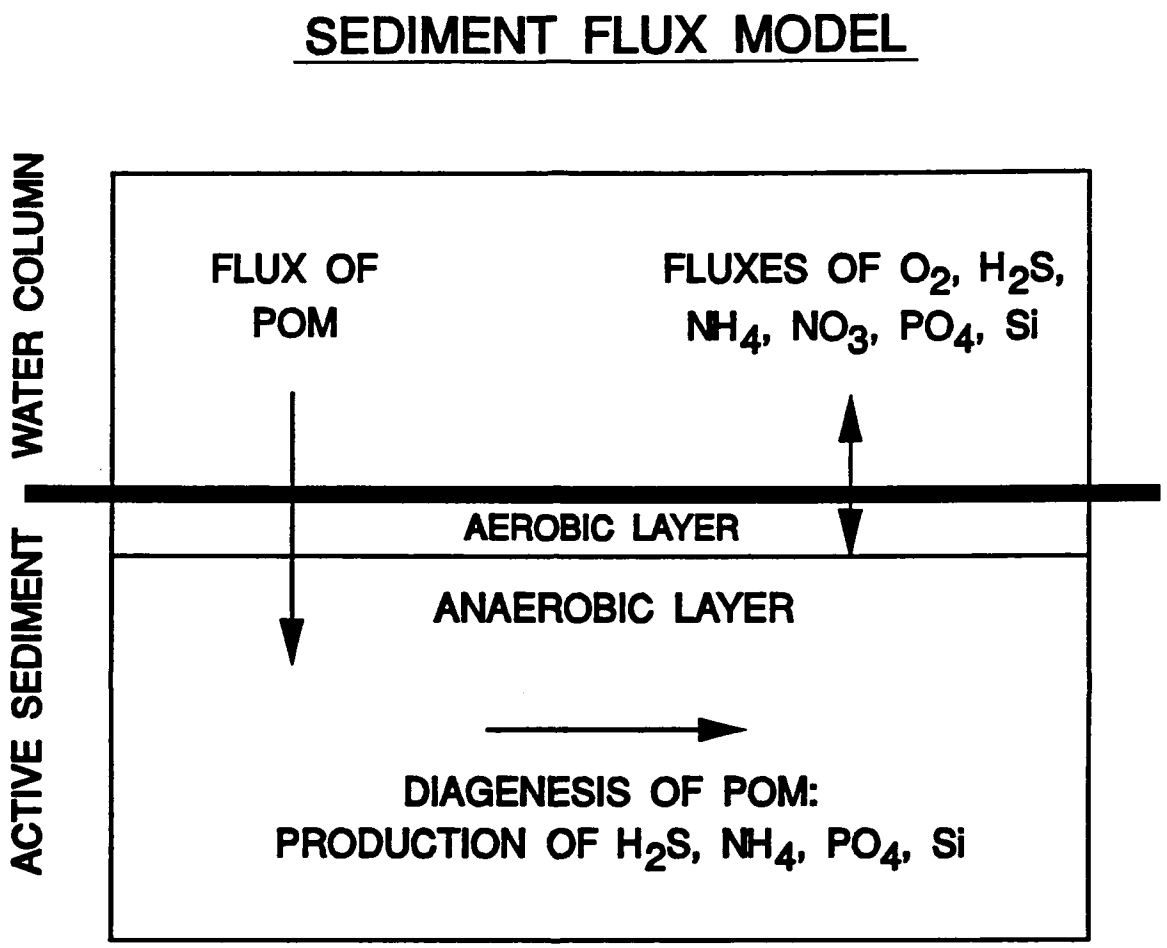
SEDIMENT FLUX MODEL
WATER COLUMN
ACTIVE SEDIMENT
FLUX OF POM
FLUXES OF O_2, H_2S, NH_4, NO_3, PO_4, Si
AEROBIC LAYER
ANAEROBIC LAYER
DIAGENESIS OF POM:
PRODUCTION OF H_2S, NH_4, PO_4, Si

Figure 1.1

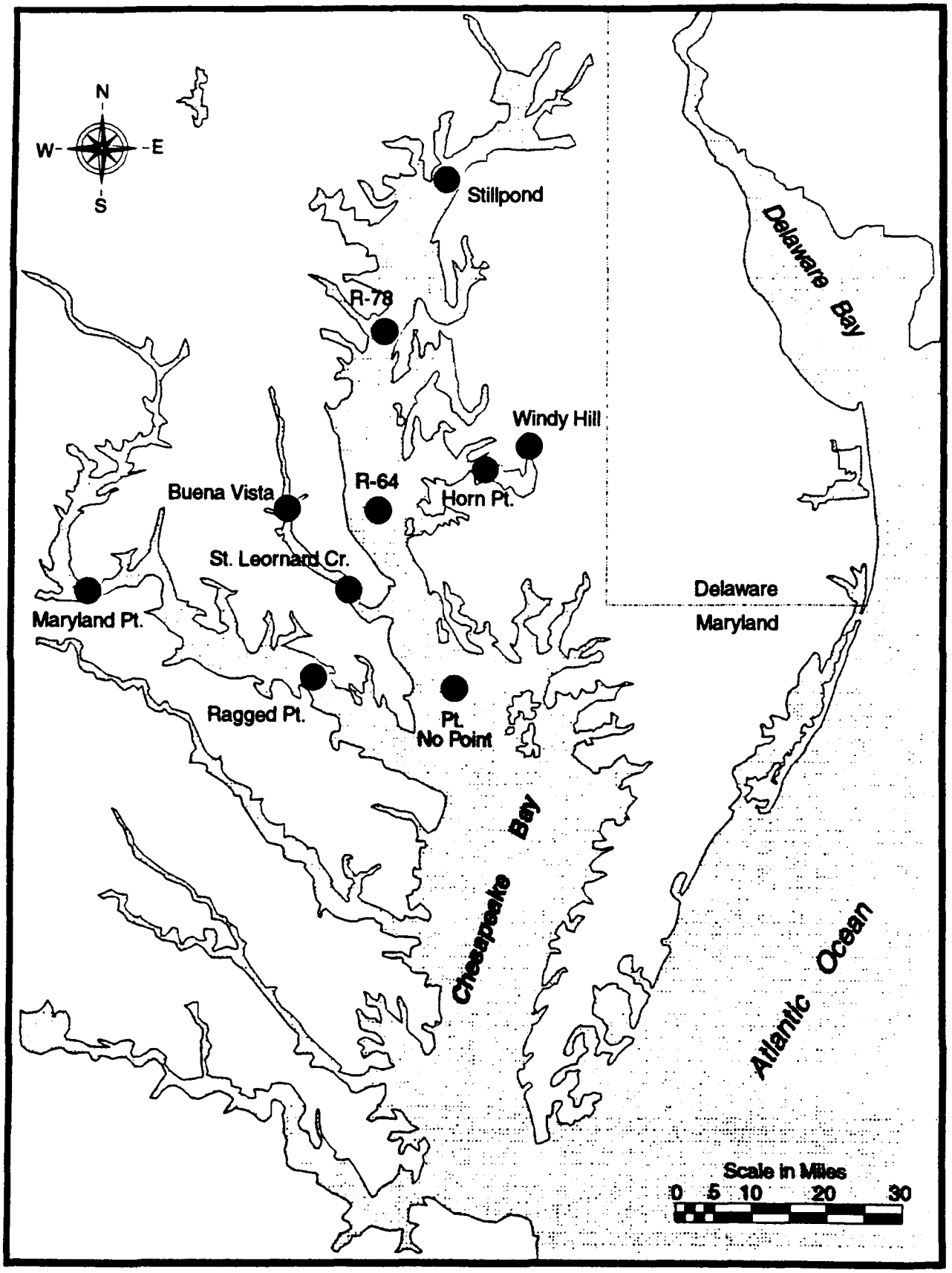
N
W
E
S
Stillpond
R-78
Windy Hill
R-64
Horn Pt.
Buena Vista
St. Leornard Cr.
Maryland Pt.
Ragged Pt.
Pt.
No Point
Delaware Bay
Delaware
Maryland
Chesapeake Bay
Atlantic Ocean
Scale in Miles
0 5 10 20 30

Figure 1.2

analyzed in a number of dissertations and papers (Bray, 1973; Bray et al., 1973; Bricker and Troup, 1975; Holdren, 1977; Holdren et al., 1975; Matisoff, 1977; Matisoff et al., 1975; Troup, 1974; Troup et al., 1974; Troup and Bricker, 1975).

D. Structure of the Report

This report is structured as follows. Ammonia and nitrate flux models are considered in Chapters II and III. A general steady state model is formulated and analyzed in Chapter IV. The sulfide, oxygen, phosphate and silica flux models are considered in Chapter V to VII. In each case the steady state solutions are analyzed and a calibration to flux data is presented. Chapter VIII presents the diagenesis model. Chapter IX presents the structure of the time variable version of the model. Chapter X presents the calibration of the model. Finally, Chapter XI examines the model's transient response.

E. Acknowledgement

The authors are pleased to acknowledge the contributions of our colleagues at HydroQual, particularly Kai-Yuan Yang; at the Corps of Engineers: Carl Cerco, Mark Dortch, and Don Robey; and the members of the technical review committee: Robert Thomann, Manhattan College; Donald Harleman; MIT; Jay Taft, Harvard University; and the members of the Modeling Subcommittee. Also the contributions of colleagues at the Horn Point and Solomons laboratories of the University of Maryland: Walter Boynton, Jeffery Cornwell, Jonathan Garber, Michael Kemp, and Peter Sampou; Dave Burdige, Old Dominion University; and Grace Brush, Johns Hopkins University, are gratefully acknowledged. The work was performed under contract to the U.S. Army Corps of Engineers, Contract No. DACW39-88-D0035.

F. References

Berner, R.A. (1971): Principles of Chemical Sedimentology. McGraw-Hill, N.Y.

Berner, R.A. (1980): Early Diagenesis. A Theoretical Approach. Princeton Univ. Press, Princeton, N.J.

Boynton, W.R., W.M, Kemp, L. Lubbers, K.V. Wood and C.W. Keefe, 1985. Ecosystem Processes Component, Pilot Study. Maryland Office of Envir. Programs. UMCEES[CBL]85-3.

Boynton, W.R., W.M. Kemp, L. Lubbers, K.V. Wood and C.W. Keefe, 1985. Ecosystems Processes Component. Date Rept. No. 1 [UMCEES]CBL Ref. No. 84-109.

Boynton, W.R., W.M. Kemp and J.M. Barnes, 1985. Ecosystem Processes Component. Data Rept. No. 2. [UMCEES]CBL No. 85-121.

Boynton, W.R., W.M. Kemp, L. Lubbers, K.V. Wood, C.W. Keefe and J.M. Barnes, 1985. Ecosystems Process Component. Study Plan. [UMCEES] CBL Ref. No. 85-16.

Boynton, W.R., W.M. Kemp, J.M. Barnes and J.H. Garber, 1986. Ecosystem Processes Component Level I Interim Rept. [UMCEES] CBL Ref No. 86-56a.

Boynton, W.R., W.M. Kemp, J.H. Garber and J.M. Barnes, 1986. Ecosystem Processes Component Level I Data Interim Rept. [UMCEES]CBL Ref No. 86-56.

Boynton, W.R., W.M. Kemp, J.H. Garber, J.M. Barnes, L.L. Robertson, and J.L.Watts, 1988. Ecosystem Process Component. Maryland Chesapeake Bay Water Quality Monitoring Program. Maryland Department of the Environment. Level I. Rept. No. 4. [UMCEES] CBL Ref. 88-06.

Boynton, W.R., W.M. Kemp, J.H. Garber, J.M. Barnes, L.L. Robertson, and J.L. Watts, 1988. Ecosystem Process Component. Maryland Chesapeake Bay Water Quality Monitoring Program. Maryland Department of the Environment. Level I. Rept. No. 5 [UMCEES] CBL Ref. 88-69.

Boynton, W.R., W.M. Kemp, J.H. Garber, J.M. Barnes, L.L. Robertson, and J.L. Watts, 1988. Ecosystem Process Component. Maryland Chesapeake Bay Water Quality Monitoring Program. Maryland Department of the Environment. Level I. Rept. No. 6 [UMCEES] CBL Ref. No. 88-126.

Bray, J.T., 1973, The behavior of phosphate in the interstitial waters of Chesapeake Bay sediments: Ph.D. dissertation, The Johns Hopkins University, Baltimore, Maryland, 136 p.

Bray, J.T., Bricker, O.P., and Troup, B.N., 1973, Phosphate in interstitial waters of anoxic sediments: Oxidation effects during sampling procedure: Sci., v. 180, p. 1362-1364.

Bricker, O.P., and Troup, B.N., 1975, Sediment-water exchange in Chesapeake Bay: in Estuarine research, L.E. Cronin, ed., Academic Press, New York, p. 3-27.

Bricker, O.P., Matisoff, G. and Holdren Jr, G.R. (1977): Interstitial Water Chemistry of Chesapeake Bay Sediments Basic Data Report No.9. Maryland Geological Survey.

Burdige, D.J. (1989): 1988 Sediment Monitoring Program in the Southern Chesapeake Bay. Old Dominion Univ. Norfolk VA, Dept. of Oceanogr.

Garber, J.H., W.R. Boynton, and others, 1988. Ecosystem Processes Component and Benthic Exchange and Sediment Transformations. Combined Rept. No. 1. Maryland Department of the Environment. [UMCEES] CBL Ref. No. 88-90.

Garber, J.H., W.R. Boynton, and others, 1988. Ecosystem Processes Component and Benthic Exchange and Sediment Transformations. Combined Rept. No. 2. Maryland Department of the Environment. [UMCEES] CBL Ref. No. 88-152.

Goloway, F. and Bender, M. (1982): Diagenetic models of interstitial nitrate profiles in deep sea suboxic sediments. Limnol. Oceanogr. 27(4): pp. 624-638.

Holdren, Jr., G.R., 1977, Distribution and behavior of manganese in the interstitial waters of Chesapeake Bay sediments during early diagenesis: Ph.D. Dissertation, The Johns Hopkins University, Baltimore, Maryland, 191 p.

Holdren, Jr., G.R., Bricker, O.P., and Matisoff, G., 1975, A model for the control of dissolved manganese in the interstitial waters of Chesapeake Bay: in Marine chemistry in the coastal environment, T.M. Church, ed., ACS Symposium ser. 18, Am. Chem. Soc., Washington, D.C., p. 364-381.

Jahnke, R.A., Emerson, S.R. and Murray, J.W. (1982): A Model of Oxygen Reduction, Denitrification, and Organic Matter Mineralization in Marine Sediments. Limnol. Oceanogr. 27(4): pp. 610-623.

Klapwijk, A. and Snodgrass, W.J. (1986): Biofilm Model for Nitrification, Denitrification, and Sediment Oxygen Demand in Hamilton Harbor. In: Sediment Oxygen Demand. Processes, Modeling and Measurement, pp. 75-97. Editor: K.J. Hatcher. Inst. of Nat. Res., Univ. of Georgia, Athens, Ga. 30602.

Matisoff, G., 1977, Early diagenesis of Chesapeake Bay sediments: A time series study of temperature, chloride and silica: Ph.D. dissertation submitted to The Johns Hopkins University, Baltimore, Maryland.

Matisoff, G., Bricker, O.P., Holdren, Jr., G.R., Kaerk, P., 1975, Spatial and temporal variations in the interstitial water chemistry of Chesapeake Bay sediments: in Marine chemistry in the coastal environment: T.M. Church, ed., ACS Symposium ser. 18, Am. Chem. Soc., Washington, D.C., p. 343-363

Troup, B.N., 1974, The interaction of iron with phosphate, carbonate and sulfide in Chesapeake Bay interstitial waters: A thermodynamic interpretation: Ph.D. dissertation, The Johns Hopkins University, Baltimore, Maryland, 114 p.

Troup, B.N., Bricker, O.P., and Bray, J.T., 1974, Oxidation effect on the analysis of iron in the interstitial water of recent anoxic sediments: Nature. v. 249, no. 5454, p. 237-239.

Troup, B.N., and Bricker, O.P., 1975, Processes affecting the transport of materials from continents to oceans: in Marine chemistry in the coastal environment, T.M. Church, ed., ACS Symposium ser. 18, Am. Chem. Soc., Washington, D.C., p. 133-149.

Vanderborght, J.P., Wollast, R. and Billen, G. (1977a): Kinetic models of diagenesis in disturbed sediments. Part I. Mass transfer properties and silica diagenesis. Limnol. Oceanogr. 22(5): pp. 787-793.

Vanderborght, J.P., Wollast, R. and Billen, G. (1977b): Kinetic models of diagenesis in disturbed sediments. Part 2. Nitrogen diagenesis. Limnol. Oceanogr. 22(5): pp. 794-803.

II. AMMONIA

A. Introduction

Models for the concentration distribution of ammonia in pore water and for the flux of ammonia from sediments have been proposed by various workers (Berner, 1971, 1980; Vanderborght et al., 1977a,b; Billen, 1978; Billen, 1982; Klapwijk and Snodgrass, 1986; Billen and Lancelot, 1988; Billen et al., 1989; Klump and Martens, 1989; Di Toro et al., 1990). The original models focused on the mechanisms that generated the pore water profile: the mineralization of organic nitrogen and the mixing and adsorption processes. Subsequent models focused on the processes that occur in the aerobic layer of the sediment: primarily the nitrification reaction, and the ammonia flux that results. The model presented below is an extension of these formulations.

B. Model Components

The model schematization for ammonia is presented in Fig. 2.1. Ammonia is produced by diagenesis in the aerobic and anaerobic layers. The production in the aerobic layer is small relative to the anaerobic layer because of the relative depths of the layers. Nevertheless, it is included in this initial formulation for the sake of completeness. Diffusion transports ammonia from the anaerobic to the aerobic layer and to the overlying water.

If ammonia were a conservative substance, then the ammonia flux would be equal to the diagenetically produced ammonia. However, ammonia can be nitrified to nitrate in the presence of oxygen. Nitrification is initially formulated as a first order reaction with respect to ammonia. Since the reaction can only occur where oxygen is present it is restricted to the aerobic layer. This model has been analyzed previously in its continuous form (Di Toro et al., 1990). Refinements to the nitrification kinetics: the use of Monod kinetics and the inclusion of the oxygen dependency of the nitrification rate, are subsequently included.

C. Mass Balance Equations

The model is based on mass balance equations for the aerobic and anaerobic layer. Fig. 2.1 presents the schematization. The mass balance equations for the two layers are:

$$H_1 \frac{d[NH_4(1)]}{dt} = -K_{NH4,1}[NH_4(1)]H_1 - K_{L01}([NH_4(1)]-[NH_4(0)]) + K_{L12}([NH_4(2)]-[NH_4(1)]) + J_{N1} \quad (1)$$

$$H_2 \frac{d[NH_4(2)]}{dt} = -K_{L12}([NH_4(2)]-[NH_4(1)]) + J_{N2} \quad (2)$$

where H_1 and H_2 are the depths of the aerobic (1) and anaerobic (2) layers; $[NH_4(0)]$, $[NH_4(1)]$ and $[NH_4(2)]$ are the ammonia concentrations in the overlying water (0) and layers (1) and (2); $K_{NH4,1}$ is the nitrification rate constant in the aerobic layer; K_{L01} is the mass transfer coefficient between the overlying water and the aerobic layer, which will be referred to as the surface mass transfer coefficient; and K_{L12} is the mass transfer coefficient between the aerobic and anaerobic layers. Finally J_{N1} and J_{N2} are the sources of ammonia in the two layers which result from the diagenesis of particulate organic nitrogen, PON.

This two layer formulation employs mass transfer coefficients to parameterize the rate at which mass is transferred between the overlying water and the aerobic layer:

$$K_{L01}([NH_4(1)]-[NH_4(0)]) \quad (3)$$

and between the aerobic and anaerobic layers:

$$K_{L12}([NH_4(2)]-[NH_4(1)]) \quad (4)$$

The dimensions of K_{L01} and K_{L12} are length per unit time. Mass transfer coefficients are typically used in situations where mass is being transferred between layers whose thicknesses are

AMMONIA FLUX MODEL

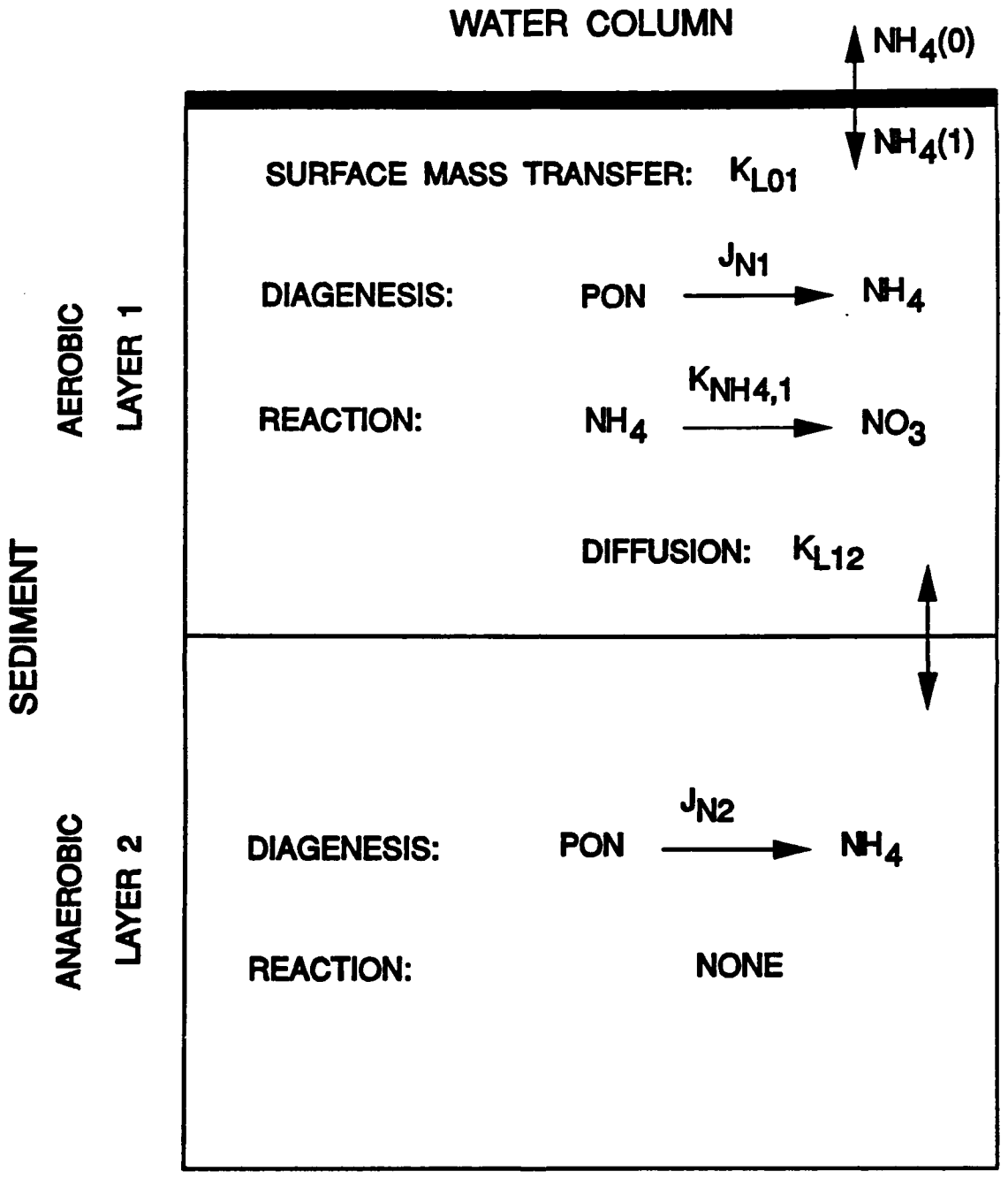

Figure 2.1

uncertain. For a well understood problem such as mass transport via molecular diffusion, the mass transfer coefficient is the ratio of the diffusion coefficient and the thickness of the layer. Thus for layer (1):

$$K_{L01} = \frac{D_1}{H_1} \tag{5}$$

where D_1 is the diffusion coefficient in layer (1). This result will be used subsequently.

1. Solution

The solution of the mass balance equations is elementary for the steady state case where the derivatives are zero. Adding the steady state equations yields:

$$0 = -K_{NH4,1}[NH_4(1)]H_1 - K_{L01}([NH_4(1)]-[NH_4(0)]) + J_{N1} + J_{N2} \tag{6}$$

which can be solved for the aerobic layer ammonia concentration:

$$[NH_4(1)] = \frac{J_N + K_{L01}[NH_4(0)]}{K_{L01} + K_{NH4,1}H_1} \tag{7}$$

where $J_N = J_{N1} + J_{N2}$, the total ammonia diagenesis flux. The anaerobic layer concentration follows from eq.(2):

$$[NH_4(2)] = \frac{J_{N2}}{K_{L12}} + [NH_4(1)] \tag{8}$$

The flux of ammonia from the sediment to the overlying water is:

$$J[NH_4] = K_{L01}([NH_4(1)]-[NH_4(0)]) \tag{9}$$

Using eq.(7) for $[NH_4(1)]$ yields:

$$J[NH_4] = K_{LOI}\frac{J_N - K_{NH4,1}H_1[NH_4(0)]}{K_{LOI} + K_{NH4,1}H_1} \qquad (10)$$

This solution can be written in two parts that separate the sources of ammonia:

$$J[NH_4] = J_N\frac{K_{LOI}}{K_{LOI} + K_{NH4,1}H_1} - [NH_4(0)]\left(\frac{1}{K_{LOI}} + \frac{1}{K_{NH4,1}H_1}\right)^{-1} \qquad (11)$$

The first term quantifies the fraction of diagenetically produced ammonia, J_N, that escapes as an ammonia flux. If the surface mass transfer coefficient, K_{LOI}, is large relative to the nitrification rate - aerobic depth product, $K_{NH4,1}H_1$, then all the ammonia produced escapes to the overlying water. Conversely, a large $K_{NH4,1}H_1$ reduces the ammonia flux since ammonia in the aerobic layer is being nitrified to nitrate faster than it can be transported to the overlying water.

The second term determines the extent to which overlying ammonia, $[NH_4(0)]$, is nitrified in the sediment. The form of the coefficient multiplying $[NH_4(0)]$: a reciprocal of the reciprocal sum of parameters, is analogous to electrical resistors in parallel(1) . The smaller of the two parameters determines the extent of nitrification. The reason is that the reciprocal of the smaller number is the larger number and it dominates the value of the sum. For example, if the surface mass transfer coefficient, K_{LOI}, is the larger parameter, than the nitrification rate - aerobic depth product, $K_{NH4,1}H_1$, controls the extent of nitrification. Intuitively this is a reasonable result. The extent to which overlying water ammonia is nitrified is controlled by which of the two necessary processes is slower: either the mass transfer from the overlying water to the aerobic layer, or the rate of nitrification. The faster process does not limit the rate of the overall reaction.

---

(1) This analogy is often incorrectly referred to as resistors in series. The resistance of resistors in series is the sum of the individual resistances. It is resistors in parallel for which the formula is: $1/R_T = 1/R_1 + 1/R_2 + \ldots + 1/R_N$. The reason for the miss-statement is that for mass transfer problems it is *mass transfer* resistances in series that give rise to the sum of reciprocal formula.

Two parameters: $K_{NH4,1}H_1$ and K_{LO1} are required to quantify the ammonia flux. A method for estimating the latter parameter is discussed next.

2. Surface Mass Transfer Coefficient

The critical observation is that the surface water mass transfer coefficient, K_{LO1}, can be related to the sediment oxygen demand, SOD (Di Toro et al., 1990). The SOD is the mass flux of dissolved oxygen into the sediment. Thus, it can be calculated from the mass transfer equation:

$$SOD = D_1 \frac{d[O_2(z)]}{dz}\Big|_{z=0} \tag{12}$$

where $[O_2(z)]$ is the concentration profile of dissolved oxygen as a function of depth, z, and D_1 is the diffusion coefficient in the aerobic layer. To a very good approximation the oxygen profile ir the aerobic layer can be represented by a straight line connecting the overlying water oxygen concentration, $[O_2(0)]$ and $[O_2(H_1)] = 0$ at the bottom of the aerobic layer (Revsbech et al., 1980; Jorgensen and Revsbech, 1985; Di Toro et al., 1990). Hence, the derivative can be replaced by the difference of the two concentration:

$$D_1 \frac{d[O_2(z)]}{dz}\Big|_{z=0} \approx D_1 \frac{[O_2(0)]-[O_2(H_1)]}{H_1} = \frac{D_1}{H_1}[O_2(0)] \tag{13}$$

Therefore, using eq.(5), the surface mass transfer coefficient can be expressed as:

$$K_{LO1} = \frac{D_1}{H_1} = \frac{SOD}{[O_2(0)]} = s \tag{14}$$

which is the ratio of SOD and overlying water oxygen concentration. For notational simplicity this ratio is termed $s = SOD/[O_2(0)]$, as shown in eq.(14).

This result, $K_{L01} = s$, is important because if an ammonia flux measurement is accompanied by an oxygen flux measurement and the overlying water oxygen concentration, then the surface mass transfer coefficient has been measured directly. Knowing this parameter, it is possible to estimate the other model parameter.

3. Depth of the Aerobic Zone and Reaction Velocities

The remaining term in the equation for ammonia flux, eq.(11), is the product of the reaction rate and the depth of the aerobic zone $K_{NH4,1} H_1$. The depth of the aerobic zone, H_1, can be estimated from eq.(14):

$$H_1 = D_1 \frac{[O_2(0)]}{SOD} = \frac{D_1}{s} \tag{15}$$

Using this result in the reaction rate - depth product yields:

$$K_{NH4,1} H_1 = \frac{D_1 K_{NH4,1}}{s} \tag{16}$$

The product $D_1 K_{NH4,1}$ is made up of two coefficients, neither of which is well known. The diffusion coefficient in a millimeter layer of sediment at the sediment - water interface may be much larger than the diffusion coefficient in the bulk of the sediment due to the effects of overlying water shear. It is, therefore, convenient to define the parameter:

$$\kappa_{NH4,1} = \sqrt{D_1 K_{NH4,1}} \tag{17}$$

which can be termed a "reaction velocity" since its dimensions are length/time. The square root is used to conform to the analogous expression in the continuous form of the solution (Di Toro et al., 1990).

4. Final Solution

The surface mass transfer coefficient and the reaction velocity can be substituted into eq.(7) to obtain the ammonia concentrations in the aerobic layer:

$$[NH_4(1)] = \frac{s(J_N + s[NH_4(0)])}{s^2 + \kappa^2_{NH4,1}} \tag{18}$$

and into eq.(11) for the ammonia flux:

$$J[NH_4] = J_N \frac{s^2}{s^2 + \kappa^2_{NH4,1}} - [NH_4(0)]\left(\frac{1}{s} + \frac{s}{\kappa^2_{NH4,1}}\right)^{-1} \tag{19}$$

This solution can be compared to the analogous result from a continuous two layer model. For the case where $[NH_4(0)] = 0$ the continuous solution is (Di Toro et al., 1990):

$$J[NH_4] = J_N[1 - sech(\kappa_{NH4,1} s)] \tag{20}$$

where sech(x) = 1/cosh(x) = 2/[exp(x)+exp(-x)]. A comparison is shown in Fig. 2.2A. A slight modification is required to produce the closer comparison: $1.2\kappa_{NH4,1}$ is used in the continuous solution, whereas $\kappa_{NH4,1}$ is used in the two layer model. With this modification the two layer model produces essentially the same result as the continuous model, Fig. 2.2B.

5. Monod Kinetics

The nitrification reaction is known to follow Monod kinetics with respect to the ammonia concentration (Painter, 1983). Although the first order approximation is reasonable for small ammonia concentrations, the interstitial water ammonia concentrations can exceed the half saturation constant for ammonia oxidation, $K_{M,NH4} \approx 1.0$ mg N/L. Therefore, it is necessary to use Monod kinetics to extend the applicable range. In addition, the nitrification reaction rate decreases with decreasing oxygen concentrations. This can also be included using a Michaelis Menton expression with $K_{O2,NH4}$ as the half saturation constant for oxygen. Table 2.1 presents a

summary of the information available for these parameters and their temperature coefficients. The nitrification rate constants are not included in the table since the more modern formulations include bacterial biomass as part of the rate expression whereas a first order rate constant is employed above. However, the temperature coefficient is still applicable. It is applied to the square of the reaction velocity since the square of the defining equation (17) is linear in the reaction rate constant, $K_{NH4,1}$:

$$\kappa^2_{NH4} = D_1 K_{NH4,1} \theta^{(T-20)}_{NH4} \tag{21}$$

Hence, the aerobic layer mass balance equation (1) becomes:

$$H_1 \frac{d[NH_4(1)]}{dt} = -\left(\frac{K_{M,NH4}\theta^{(T-20)}_{K_{M,NH4}}}{K_{M,NH4}\theta^{(T-20)}_{K_{M,NH4}} + [NH_4(1)]}\right)\left(\frac{[O_2(1)]}{K_{O2,NH4} + [O_2(1)]}\right)$$
$$\cdot \frac{\kappa^2_{NH4,1}\theta^{(T-20)}_{NH4}}{s}[NH_4(1)]$$
$$- s([NH_4(1)] - [NH_4(0)])$$
$$+ K_{L12}([NH_4(2)] - [NH_4(1)]) + J_{N1} \tag{22}$$

where the oxygen dependency is expressed in terms of the aerobic layer oxygen concentration, $[O_2(1)]$. Since the oxygen profile is assumed to be linear in the aerobic layer, starting at $[O_2(0)]$ at the sediment-water interface, and ending at zero at the aerobic-anaerobic boundary, H_1, the average aerobic layer oxygen concentration is:

$$[O_2(1)] = \frac{[O_2(0)] + [O_2(H_1)]}{2} = \frac{[O_2(0)]}{2} \tag{23}$$

This substitution can be used in the Michaelis Menton expression:

$$\frac{[O_2(1)]}{[O_2(1)] + K_{O2,NH4}} = \frac{\frac{1}{2}[O_2(0)]}{\frac{1}{2}[O_2(0)] + K_{O2,NH4}} = \frac{[O_2(0)]}{[O_2(0)] + 2K_{O2,NH4}} \tag{24}$$

Comparison of Continuous and Two Layer Solutions

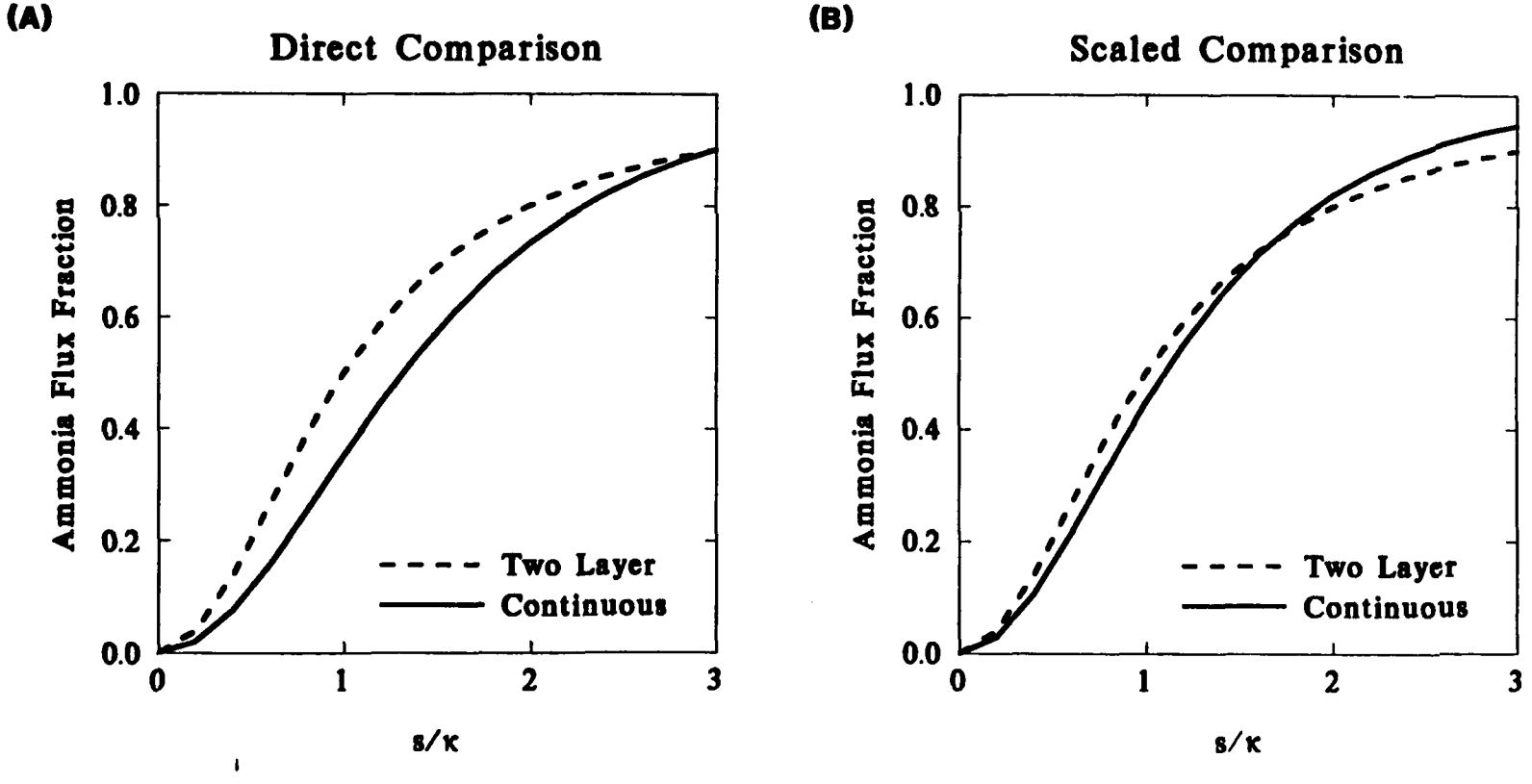

CHES2LY2

Figure 2.2

The ammonia concentration dependency has been formulated so that the reaction velocity, $\kappa_{NH4,1}$, has the same meaning as in eq.(17). That is, for $[NH_4(1)] \ll K_{M,NH4}$ and $[O_2(0)] \gg 2K_{O2,NH4}$ this equation reduces to eq.(1).

The solution is obtained by assuming steady state and adding this equation to the layer 2 mass balance equation (2):

$$0 = -\left(\frac{K_{M,NH4}\theta_{K_{M,NH4}}^{(T-20)}}{K_{M,NH4}\theta_{K_{M,NH4}}^{(T-20)} + [NH_4(1)]}\right)\left(\frac{[O_2(0)]}{2K_{O2,NH4} + [O_2(0)]}\right)$$
$$\cdot \frac{\kappa_{NH4,1}^2 \theta_{NH4}^{(T-20)}}{s}[NH_4(1)] - s([NH_4(1)] - [NH_4(0)]) + J_N \qquad (25)$$

which is a quadratic equation in $[NH_4(1)]$ and can easily be solved, as shown below.

The predicted ammonia fluxes and aerobic layer ammonia concentrations for the first order and Monod kinetics models are compared in Fig. 2.3. The pairs of curves represent increasing ammonia diagenesis (J_N = 100, 1000, 10,000 mg N/m^2-d). When the diagenesis flux is small, there is no difference between the two solutions because the aerobic layer ammonia concentrations are well below the half saturation constant, $K_{M,NH4}$ (Fig. 2.3B). However, for large diagenesis fluxes, the difference increases because the aerobic layer ammonia concentration starts to exceed the half saturation constant. This causes the rate of nitrification to decrease relative to the first order kinetic formulation. As a consequence, less ammonia is nitrified and more escapes to the overlying water.

D. Data Analysis

Two approaches are employed to estimate the remaining parameters in the ammonia flux model. The first is a graphical analysis that provides an average estimate of the reaction velocity. The second is based on regression analysis which provides more detailed results.

1. Graphical Analysis

The ammonia flux, eq.(19), is determined by the two sources of ammonia: diagenesis, J_N, and overlying water ammonia, $s[NH_4(0)]$. If the latter is a small contribution, then only the diagenesis term is significant and:

$$J[NH_4] = J_N \frac{s^2}{s^2 + \kappa_{NH4,1}^2} \tag{26}$$

The model predicts that $J[NH_4]$ should vary as s^2 for small s. For large s, the ammonia flux equals the ammonia diagenesis flux, J_N. Fig. 2.4 is a plot of ammonia flux versus $s = SOD/[O_2(0)]$ for all stations and times in the SONE and BEST data sets. The triplicates are plotted separately. The line is a least squares fit of eq.(26) to the data.

The data appear to roughly conform to the expected relationship: smaller ammonia fluxes are associated with smaller s. However there is substantial scatter about the fitted line. This is not unexpected since this comparison assumes that J_N is the same for every station at every sampling time. Since this is clearly not the case, one would expect considerable scatter in a pointwise comparison using data from different locations in the bay and from different seasons of the year.

In order to compensate for this variation, some data averaging is appropriate. The following has been found to be useful. The data are averaged within intervals of the independent variable, in this case, s. Fig. 2.5 compares the model calculation to the data that have been grouped into 0.1 $\log_{10}$ intervals of s. The average and the standard error of the mean for $J[NH_4]$ are shown for intervals with more than five data points. The fit is quite remarkable. The estimated parameter values are listed in Table 2.2 The relationship to s^2 is clear as is the flattening out of the profile at larger s.

Comparison of First Order and Michaelis Menton Kinetics

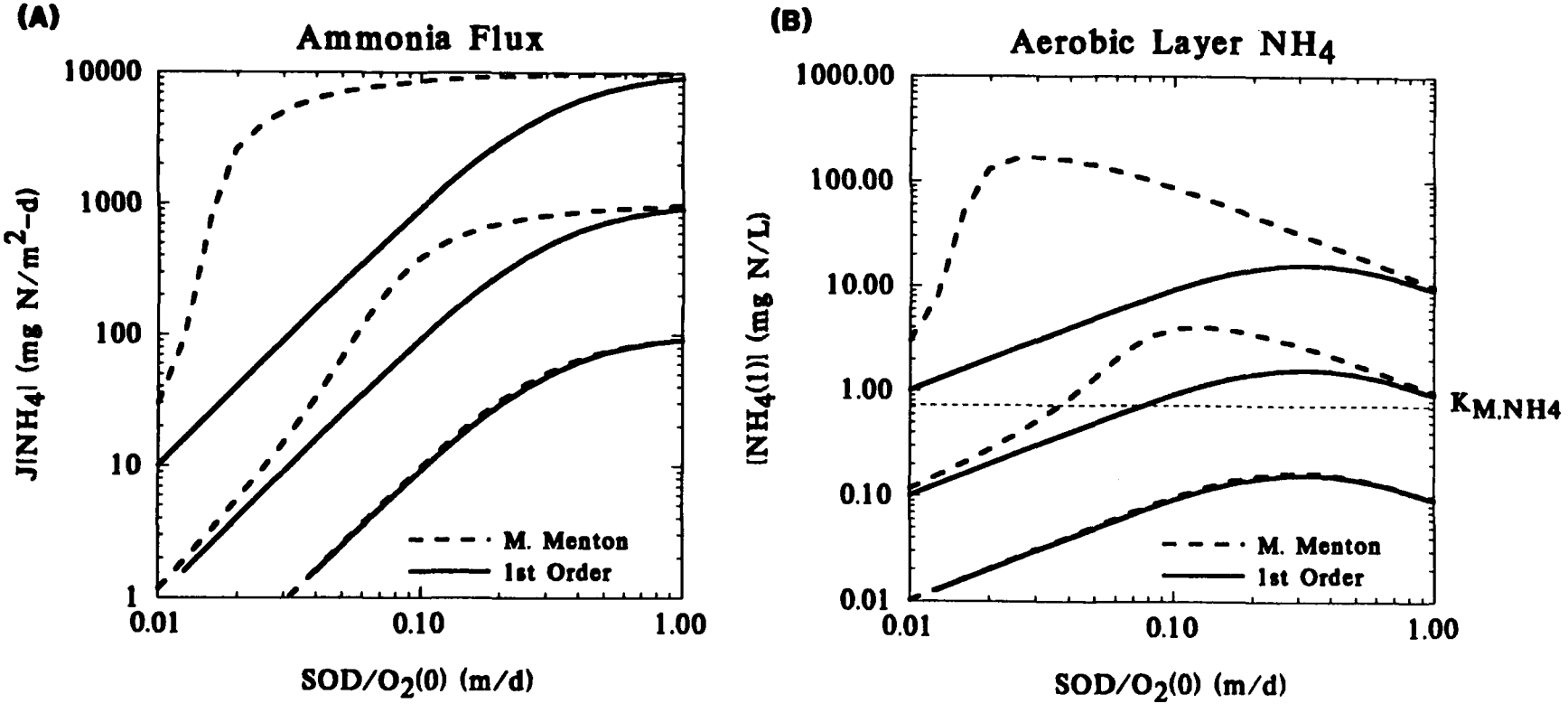

NH4MM5

Figure 2.3

Ammonia Flux vs Surface Mass Transfer Coefficient

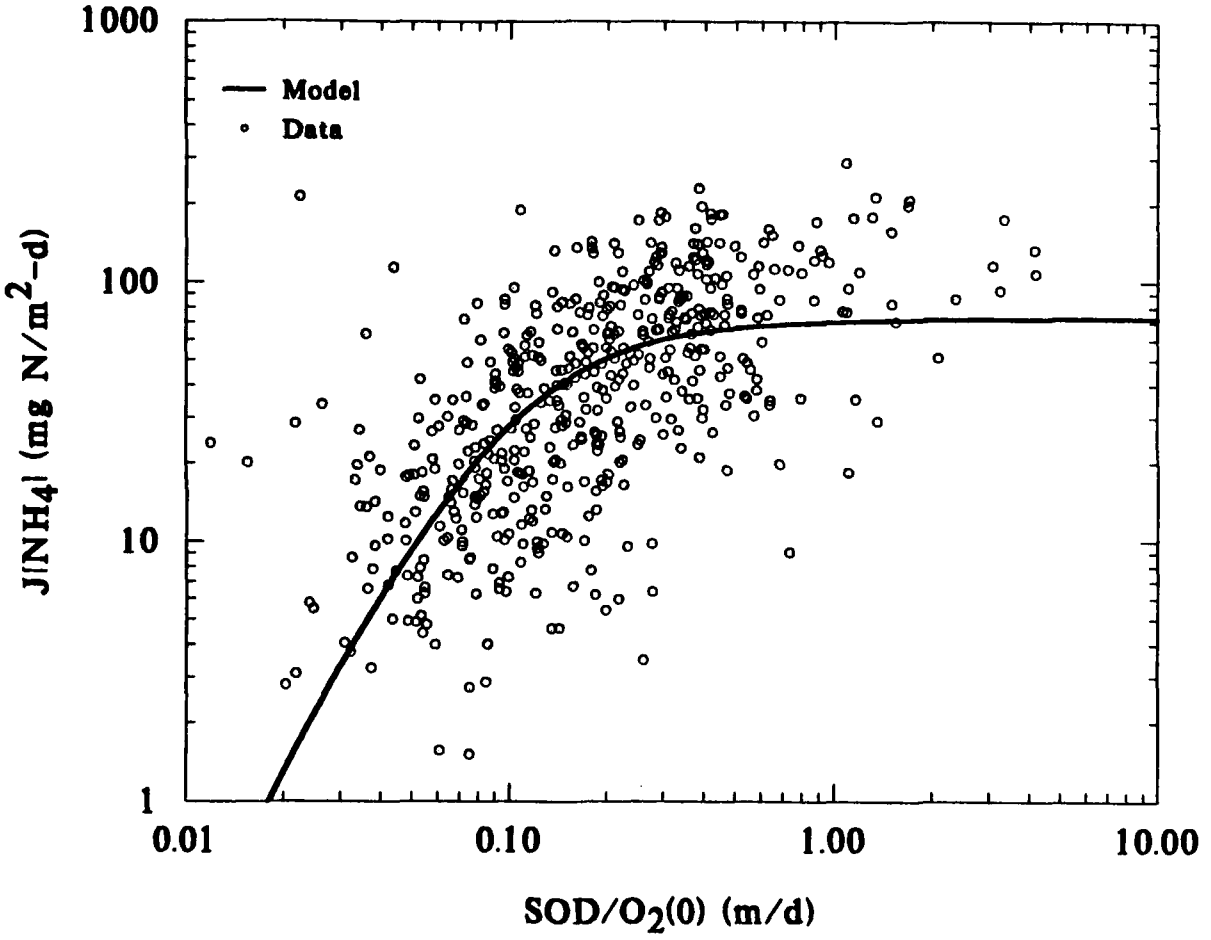

FFLXP7A

Figure 2.4

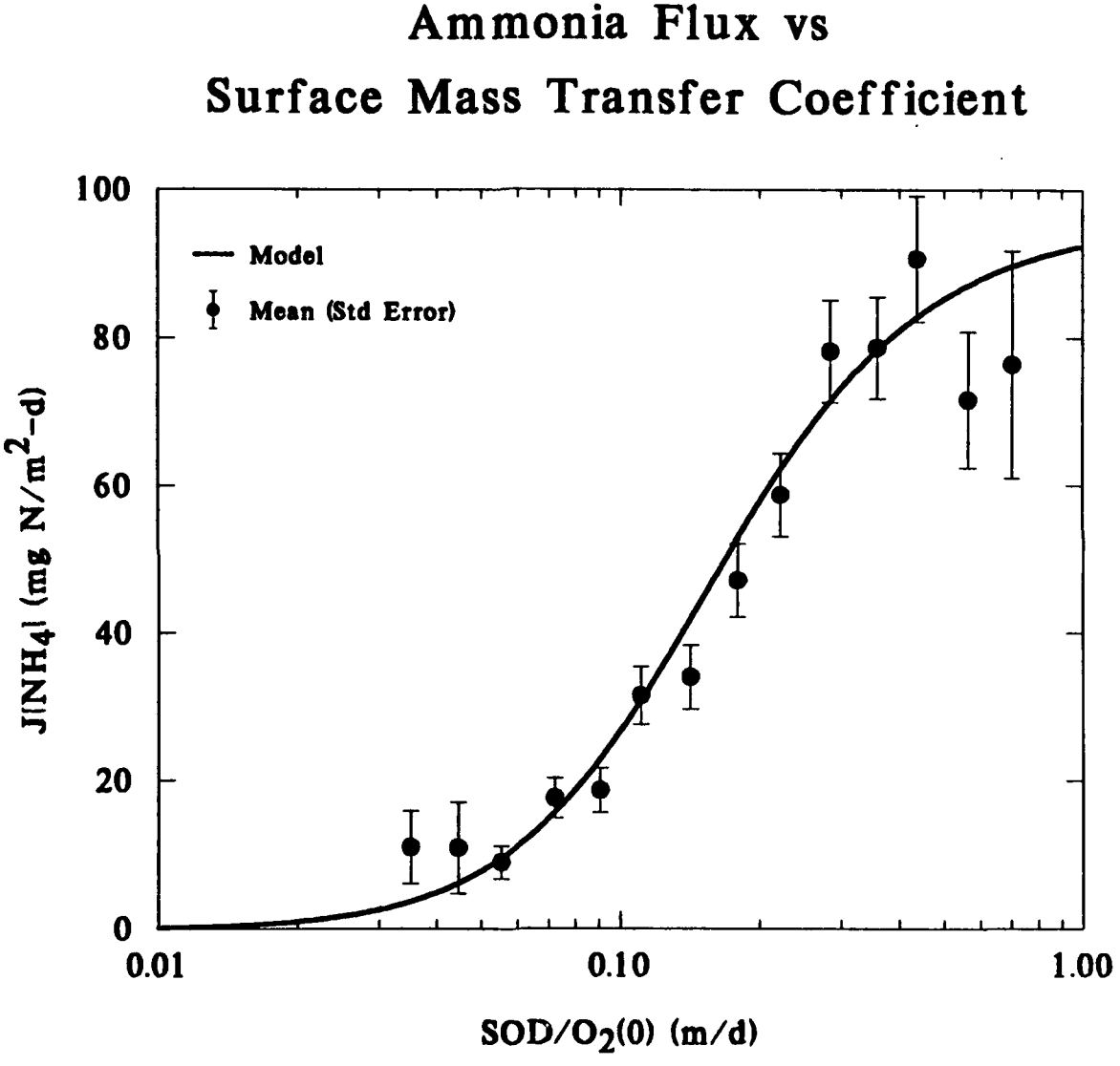

FFLXP7E

Figure 2.5

This graphical analysis should be viewed as only a first step. A more rigorous approach is to use regression methods to estimate the parameters of the model.

2. Nonlinear Regression

The graphical analysis presented above assumes that the ammonia diagenesis flux, J_N, is a constant in time and space. This assumption can be removed by letting J_N be a function of space and time. The spatial variation can be accommodated by defining station specific diagenesis fluxes, $J_N(i)$. The temporal variation can be included by relating ammonia diagenesis to the temperature, $T_{i,j}$, at location i and time t_j via the exponential approximation to the Arrhenius relationship. The result is that the diagenesis flux, $J_N(i,t_j)$, is parameterized as:

$$J_N(i,t_j) = J_N(i)\theta_N^{(T_{i,j}-20)} \tag{27}$$

The unknown parameters are the station specific diagenesis fluxes: $J_N(i)$, the temperature coefficient for diagenesis, θ_N, and the nitrification reaction velocity, $\kappa_{NH4,1}$. The median of the reported values in Table 2.1 is used for the nitrification temperature coefficient. The equation for ammonia flux that would be used in the regression analysis if linear nitrification kinetics are employed is:

$$J[NH_4(i,t_j)] = J_N(i)\theta_N^{(T_{i,j}-20)} \frac{s_{i,j}^2}{s_{i,j}^2 + \kappa_{NH4,1}^2 \theta_{NH4}^{(T_{i,j}-20)}} - [NH_4(0)]_{i,j}\left(\frac{1}{s_{i,j}} + \frac{s_{i,j}}{\kappa_{NH4,1}^2 \theta_{NH4}^{(T_{i,j}-20)}}\right)^{-1} \tag{28}$$

where the subscripts i,j indicate that the temperature, $T_{i,j}$, the surface mass transfer coefficient, $s_{i,j} = SOD_{i,j}/[O_2(0)]_{i,j}$, and the overlying water ammonia concentrations, $[NH_4(0)]_{i,j}$, are for station i at time t_j.

The regression equation using Monod kinetics is computed as follows. The aerobic layer mass balance equation (22) for temporal steady state is:

$$0 = -\left(\frac{K_{M,NH4}\theta_{K_{M,NH4}}^{(T_{i,j}-20)}}{K_{M,NH4}\theta_{K_{M,NH4}}^{(T_{i,j}-20)} + [NH_4(1)]_{i,j}}\right)\left(\frac{[O_2(0)]_{i,j}}{2K_{O2,NH4} + [O_2(0)]_{i,j}}\right)$$
$$\cdot \frac{\kappa_{NH4,1}^2 \theta_{NH4}^{(T_{i,j}-20)}}{s}[NH_4(1)]_{i,j}$$
$$- s([NH_4(1)]_{i,j} - [NH_4(0)]_{i,j}) + J_N(i)\theta_N^{(T_{i,j}-20)} \qquad (29)$$

which is a quadratic equation in the unknown $[NH_4(1)]_{i,j}$. The solution is:

$$[NH_4(1)]_{i,j} = -\frac{b}{2a}\left(1 \pm \sqrt{1 - \frac{4ac}{b^2}}\right) \qquad (30)$$

where:

$$a = -s_{i,j}^2 \qquad (31)$$

$$b = s_{i,j}J_N(i)\theta_N^{(T_{i,j}-20)} - s_{i,j}^2\left(K_{M,NH4}\theta_{K_{M,NH4}}^{(T_{i,j}-20)} - [NH_4(0)]_{i,j}\right)$$
$$- \kappa_{NH4,1}^2 \theta_{NH4}^{(T_{i,j}-20)} K_{M,NH4}\theta_{K_{M,NH4}}^{(T_{i,j}-20)} \frac{[O_2(0)]_{i,j}}{2K_{O2,NH4} + [O_2(0)]_{i,j}} \qquad (32)$$

$$c = s_{i,j}K_{M,NH4}\theta_{K_{M,NH4}}^{(T_{i,j}-20)}\left(J_N(i)\theta_N^{(T_{i,j}-20)} + s_{i,j} + [NH_4(0)]_{i,j}\right) \qquad (33)$$

The sign of the root in eq.(30) is chosen so that $[NH_4(1)]_{i,j}$ is positive. The ammonia flux is computed using:

$$J[NH_4(i,t_j)] = s_{i,j}([NH_4(1)]_{i,j} - [NH_4(0)]_{i,j}) \qquad (34)$$

The data used in the regression analysis is restricted to the ten SONE stations for the years 1985 through 1988. The regression is performed using Monod kinetics, eqs (30-34). Table 2.1 lists the reported values for nitrification kinetic coefficients. The median values are used in the regression. The data are analyzed in two ways: replicate flux measurements are treated as individual measurements, and the average of the replicates are used.

The initial regression results indicated that it is not possible to estimate both $J_N(i)$ and $\kappa_{NH4,1}$ simultaneously. The results are too unstable to be reliable. The cause of the problem can be understood using the simplest version of the ammonia flux model, eq.(26). Consider what occurs when the surface mass transfer coefficient is much less than the nitrification reaction velocity, $s^2 \ll \kappa^2_{NH4,1}$. In this case:

$$J[NH_4] = J_N \frac{s^2}{s^2 + \kappa^2_{NH4,1}} \approx \frac{J_N}{\kappa^2_{NH4,1}} s^2 \qquad (35)$$

and the two parameters to be estimated: J_N, and $\kappa_{NH4,1}$, are indistinguishable in the quotient. A larger J_N can be compensated for with a larger $\kappa_{NH4,1}$. Therefore, the ability to make independent estimates depends on the existence of a significant fraction of data for which $s^2 \gg \kappa^2_{NH4,1}$ so that J_N can be estimated independently. Since the regression is unstable additional data must be added.

3. Estimates of J_N

The diagenesis of organic matter releases both organic carbon and ammonia to the sediment interstitial water. As shown below in Chapter V, the organic carbon is oxidized using sulfate as the electron acceptor. The sulfide that results is either buried, oxidized using oxygen as the electron acceptor, or escapes as a sulfide flux. If all the sulfide were oxidized, then the oxygen flux to the sediment would be related to the carbon diagenesis at that time. This information could be used to make as estimate of ammonia diagenesis. This could be used to provide the necessary

additional information to the regression analysis.

However, there are a number of intermediate steps between carbon diagenesis and eventual oxidation. Therefore, it is not true that the oxygen flux to the sediment (SOD) at any instant in time is equal to the carbon diagenesis flux (in oxygen equivalents) at that time. Nevertheless, if most of the carbon diagenesis is eventually oxidized, then the long term average SOD could be used to make a reasonable estimate of the long term average ammonia diagenesis using suitable stoichiometric relationships. The relationship between the long term average J_N and SOD is:

$$\overline{J_N(i)}^{est} = \frac{\overline{SOD(i)}^{obs}}{a_{C,N} a_{O2,C}} \tag{36}$$

where $\overline{J_N(i)}^{est}$ is the estimate of the long term average ammonia diagenesis flux for station i, and $\overline{SOD(i)}^{obs}$ is the long term average SOD at station i. The Redfield stoichiometry is: $a_{O2,C}$ = 2.67 g O_2/g C and $a_{C,N}$ = 5.68 g C/g N. As shown in Chapter VIII, these ratios are consistent with the stoichiometry of decaying sediment organic matter in Chesapeake Bay.

The relationship between SOD and ammonia diagenesis, eq.(36), only applies for stations where no significant sulfide flux occurs. These are stations where the overlying water DO concentration does not approach zero. For the remaining stations with significant periods of anoxia , a significant fraction of the oxygen equivalents escapes as a sulfide flux, so that using the long term average SOD underestimates the diagenesis flux. Hence, this relationship is used only for those stations for which the minimum DO is always greater than 1 mg/L.

The idea is to use these estimates of $J_N(i)$ as part of the regression criteria used to fit the ammonia flux. This can be done as follows. The criteria to be minimized in ordinary least squares is:

$$\min_{J_N(i),\theta_N,\kappa_{NH4,1}} \frac{1}{N_{obs}} \sum_{i,j}^{N_{obs}} \left(J[NH_4]_{i,j}^{obs} - J[NH_4]_{i,j}^{model} \right)^2 \tag{37}$$

A mixed criteria, which includes requiring that $J_N(i)$ be close to the estimate, $\overline{J_N(i)}^{est}$, requires that fitting criteria be properly augmented and each part of the criteria be properly weighted. The augmented criteria without weighting has the form:

$$\min_{J_N(i),\theta_N,\alpha_{NH4,1}} \{\frac{1}{N_{obs}} \sum_{i,j}^{N_{obs}} \left(J[NH_4]_{i,j}^{obs} - J[NH_4]_{i,j}^{model}\right)^2 + \frac{1}{N_{sta}} \sum_{i}^{N_{sta}} \left(\overline{J_N(i)}^{est} - J_N(i)\right)^2\} \quad (38)$$

The natural choice for weights are the standard deviations of the ammonia fluxes, $\sigma_{J[NH_4(i)]}$, which can be computed from the replicates, and the standard deviation of the estimates of the diagenesis fluxes. However, it is not clear how to compute the latter standard deviations. Instead, the average itself is used as the weight for each station. This amounts to assuming that $\sigma_{\overline{J_N(i)}^{est}} = \overline{J_N(i)}^{est}$, i.e. that the coefficient of variation for $\overline{J_N(i)}^{est}$ is one. The criteria that results is:

$$\min_{J_N(i),\theta_N,\alpha_{NH4,1}} \{\frac{1}{N_{obs}} \sum_{i,j}^{N_{obs}} \left(\frac{J[NH_4]_{i,j}^{obs} - J[NH_4]_{i,j}^{model}}{\sigma_{J[NH_4(i)]}}\right)^2 + \frac{1}{N_{sta}} \sum_{i}^{N_{sta}} \left(\frac{\overline{J_N(i)}^{est} - J_N(i)}{\overline{J_N(i)}^{est}}\right)^2\} \quad (39)$$

where the sum over N_{sta} includes only the oxic stations. The magnitudes of $\sigma_{J[NH_4(i)]}$ and $\overline{J_N(i)}^{est}$ are approximately equal to the magnitudes of the numerator terms. Thus each term measures the deviation of the numerator relative to an approximately equal magnitude in the denominator. This weights each term approximately equally.

A numerical procedure is used to minimize the criteria, eq.(39). A second criteria, using absolute values instead of squares as the measure of the deviations, i.e.:

$$\min_{J_N(i),\theta_N,\kappa_{NH4,1}} \{ \frac{1}{N_{obs}} \sum_{i,j}^{N_{obs}} | \frac{J[NH_4]^{obs}_{i,j} - J[NH_4]^{model}_{i,j}}{\sigma_{J[NH_4(i)]}} |$$

$$+ \frac{1}{N_{sta}} \sum_{i}^{N_{sta}} | \frac{\overline{J_N(i)}^{est} - J_N(i)}{\overline{J_N(i)}^{est}} | \} \qquad (40)$$

is also employed. The individual ammonia fluxes are log transformed if the fluxes are positive, or are used as is if the flux is negative. The appropriate logarithmic or arithmetic standard deviations are used in the sum.

The results of the regressions are listed in Table 2.2. The nitrification reaction velocity is estimated to be in the range of $\kappa_{NH4,1}$ = 0.073 to 0.151 (m/day) depending on whether the individual or averaged data set is used and whether the absolute value or the squared criteria is used. This is reasonably stable behavior. The estimates of ammonia diagenesis for each station are reasonably close to the estimates derived from the average SODs for those stations without significant anoxia, if least squares is used, or are essentially equal to them, if the absolute value criteria is used. Note that if ammonia diagenesis is estimated to be smaller than the SOD derived estimates (case b), then the reaction velocity is also estimated to be smaller, consistent with eq.(35). The results for the least squares criteria (case c) are illustrated in Fig. 2.6. Both the individual fluxes (average of the replicates), $J[NH_4]^{obs}_{i,j}$, and the station averages, $\overline{J_N(i)}^{est}$, are compared to the model estimates: $J[NH_4]^{model}_{i,j}$ and $J_N(i)$. There is a significant scatter if the individual fluxes are compared. However, the model can reproduce the station average diagenesis fluxes reasonably well. This is not too surprising since these are part of the regression parameters. Nevertheless, their estimates are constrained by the long term average SOD estimates for the oxic stations.

The final parameter values to be used subsequently are those estimated using the least squares criteria and the averaged data set (case c). This criteria corresponds to the maximum

Regression Analysis of Ammonia Flux

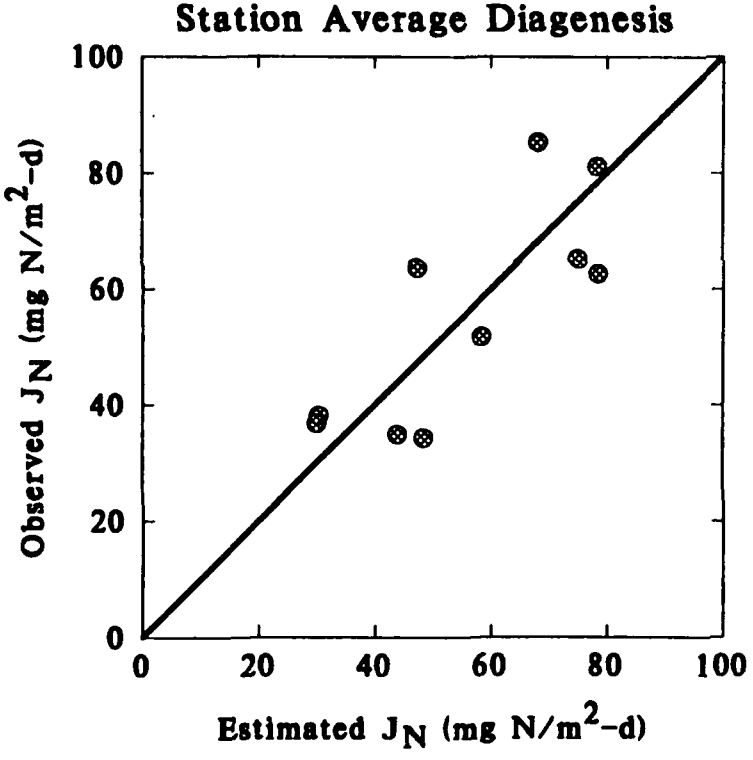

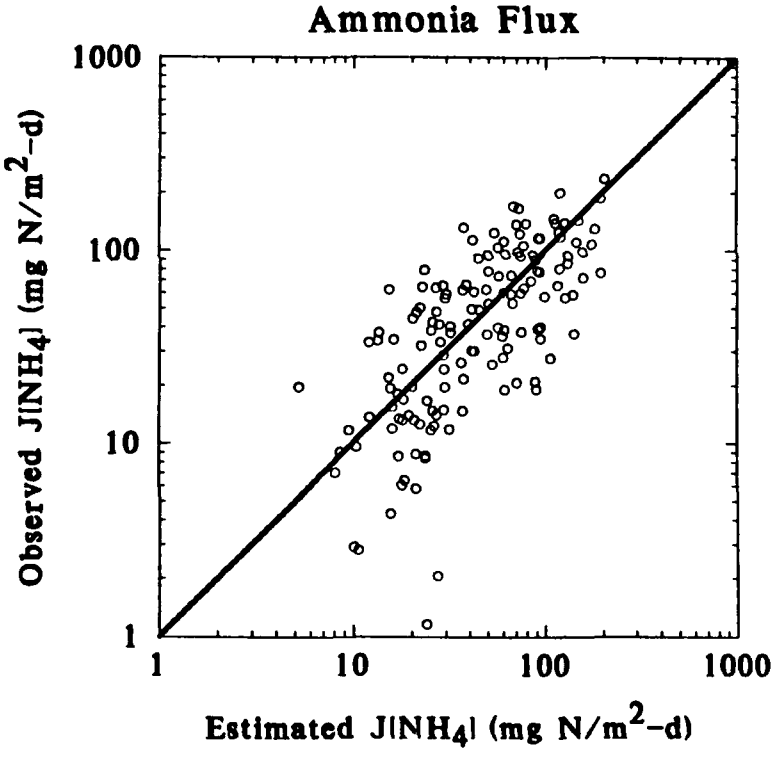

NH4REGR5

Figure 2.6

likelihood estimate for a lognormal distribution of the errors, and the replicate averages stabilizes the estimate of $s_{i,j}$ which are used in the regression. This appears to be the optimal estimation procedure.

E. Extent of Nitrification

The model behavior is examined in Fig. 2.7 which presents estimates of average ammonia diagenesis, J_N, ammonia flux, $J[NH_4]$, and by difference, the source of nitrate to the aerobic layer, $S[NO_3]$. The extent of nitrification varies from almost none at station R-64 to almost 50% for Still Pond. This is controlled by the magnitude of the surface mass transfer coefficient and the depth of the aerobic zone, both of which are quantified using s.

The nitrate produced in the aerobic layer can either be transferred to the overlying water or be denitrified. This is examined in the next chapter.

F. Observations of Chesapeake Bay Nitrification

Direct measurements of the rate of nitrification in Chesapeake Bay sediments have been made during 1988 (Sampou et al., 1989; Kemp et al., 1990). These are compared to model predictions in two ways. For the stations where measurements over a season have been made (Still Pond and R-64), the station average nitrification flux is calculated and compared to the observations. The procedure is to use the model, eq.(30), to compute the aerobic layer ammonia concentration, $[NH_4(1)]_{i,j}$, using the observed surface mass transfer coefficient, $s_{i,j}$, and temperatures, $T_{i,j}$. The model parameters are the medians in Table 2.1 and the case (c) estimates in Table 2.2. The nitrification flux, denoted by $S[NO_3]$, is computed by evaluating the nitrification kinetic expression in the mass balance equation (29):

$$S[NO_3] = \left(\frac{K_{M,NH4}\theta_{K_{M,NH4}}^{(T_{i,j}-20)}}{K_{M,NH4}\theta_{K_{M,NH4}}^{(T_{i,j}-20)} + [NH_4(1)]_{i,j}} \right) \left(\frac{[O_2(0)]_{i,j}}{2K_{O2,NH4} + [O_2(0)]_{i,j}} \right)$$

$$\cdot \frac{\kappa_{NH4,1}^2 \theta_{NH4}^{(T_{i,j}-20)}}{s} [NH_4(1)]_{i,j} \qquad (41)$$

The station averages are computed from the individual estimates. The comparison is made in Fig. 2.8. The results are in reasonable agreement considering the difficulty in measuring nitrification fluxes (Kemp et al., 1990; Rudolph et al., 1991).

An alternate method of computing the nitrification flux is to estimate the aerobic layer ammonia concentration using the observed ammonia flux, surface mass transfer coefficient, and overlying water ammonia concentration. This obviates the need for an estimate of the ammonia diagenesis flux which is required if the ammonia flux model is used. Instead, the estimate is made from the flux equation:

$$J[NH_4] = s([NH_4(1)] - [NH_4(0)]) \qquad (42)$$

so that:

$$[NH_4(1)] = \frac{J[NH_4]}{s} + [NH_4(0)] \qquad (43)$$

With $[NH_4(1)]$ determined, the kinetic expression, eq.(41) is used to compute the nitrification flux. Note that all the model nitrification parameters are used to compute $S[NO_3]$ so that this is still a test of the model formulation. The results are compared to the observations in Fig. 2.9. There is considerable scatter in the model estimates since they are based on observed ammonia fluxes. Nevertheless, the comparison to the observations is reasonable. In particular, the temporal variation in nitrification appears to be reproduced.

Extent of Nitrification

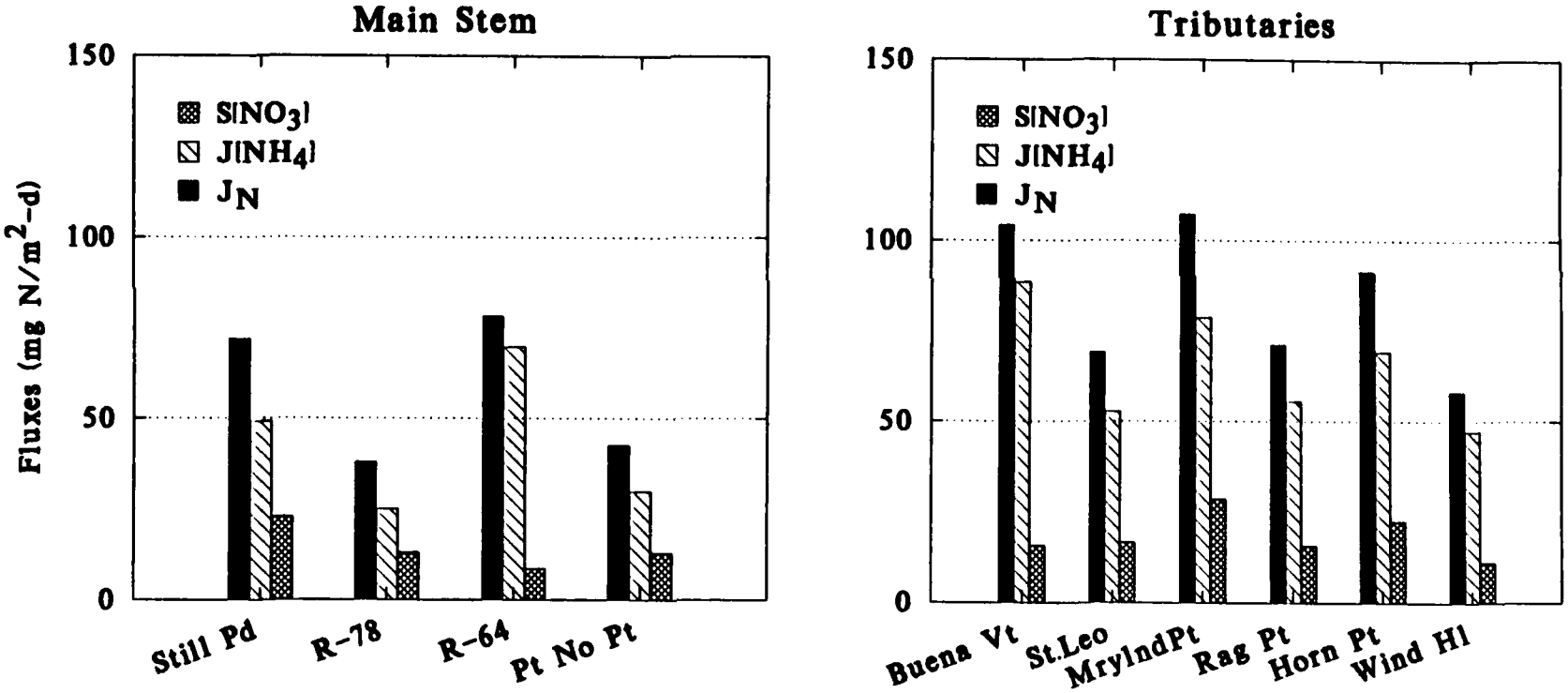

FDENITP2

Figure 2.7

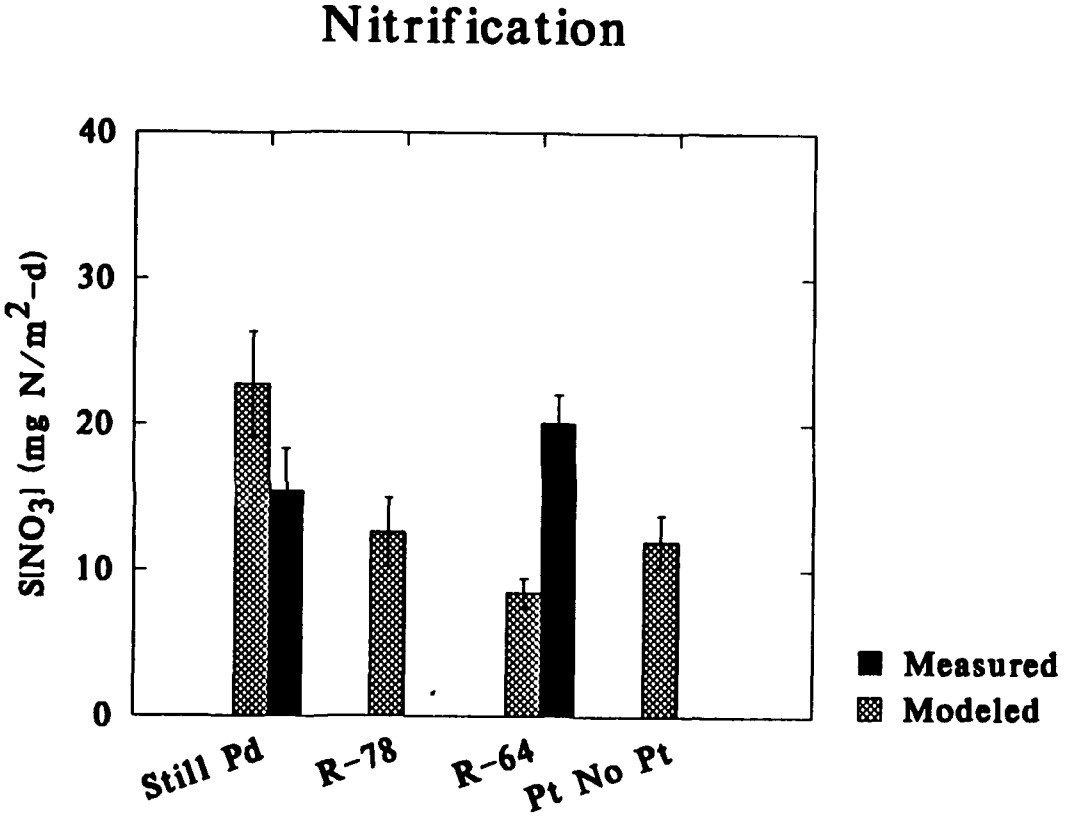

FDENIT7C

Figure 2.8

Nitrification

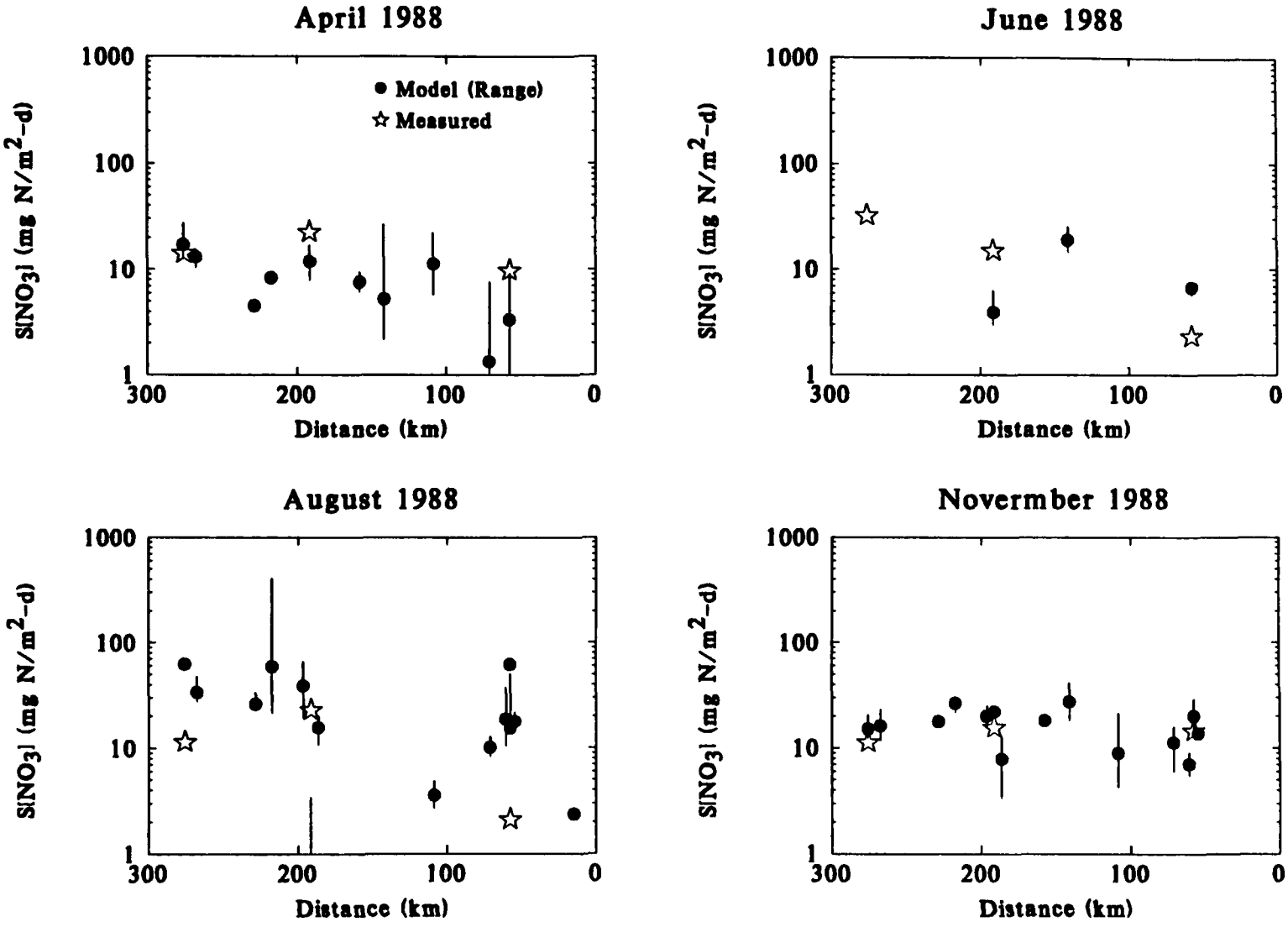

FDENIT6B

Figure 2.9

G. Non Steady State Features

It has been pointed out (Boynton et al., 1990) that ammonia fluxes in Chesapeake Bay are not a single function of temperature, but rather display a hysteresis behavior. The average monthly fluxes for the main stem stations and the model fluxes are plotted versus temperature in Fig. 2.10. Note the circular paths that are traversed by the data. The ammonia fluxes are generally higher in the spring months than in the fall months at the same temperature. This effect is not reproduced very well by the steady state ammonia flux model. As can be seen from the dashed lines representing the model computations, there is some hysteresis, but not as large as at most of the stations. A similar analysis using the time variable model, Chapter X, indicate that ammonia flux hysteresis is a time variable effect that can be reproduced by the time variable model.

H. Conclusions

The steady state ammonia flux model can reproduce major features of the observed ammonia flux data. The variation with surface mass transfer coefficient, s, determines the extent to which nitrification takes place. A regression analysis is used to estimate the nitrification reaction velocity and the station specific ammonia diagenesis fluxes. These are of critical importance for the analysis of the other fluxes, as will be clear in the subsequent chapters. A comparison to independently measured nitrification fluxes indicates that the model is consistent with these observations as well. However, the steady state model is not able to reproduce the hysteresis that is observed during the seasonal progression of ammonia fluxes. This limitation is directly related to the steady state assumption employed in this chapter.

Table 2.1
Ammonia Nitrification Parameters

Nitrification temperature coefficient	Ammonia half saturation constant	Temperature coefficient	Oxygen half saturation constant	Reference
θ_{NH4}	$K_{M,NH4}$ (mg N/L)	$\theta_{K_{M,NH4}}$	$K_{O2,NH4}$ (mg O_2/L)	
1.123	-	-	-	Antonion (1990)
1.125	0.728	-	-	Argaman (1979)
-	0.630	-	-	Cooke (1988)
-	0.700	-	-	Gee (1990)
-	1.0	-	0.32	Hauaki (1990)
1.076	-	-	-	Painter (1983)
-	0.329	-	-	Shuh (1979)
-	-		0.3, 0.25, 0.8, 0.42, 2.0	Stenstrom (1980)
1.127	0.730	1.125	-	Stevens (1989)
1.081	-	-	-	Warwick (1986)
1.123	0.728	1.125	-	Young (1979)
1.123	**0.728**	**1.125**	**0.370**	**Median**

Ammonia Flux vs Temperature

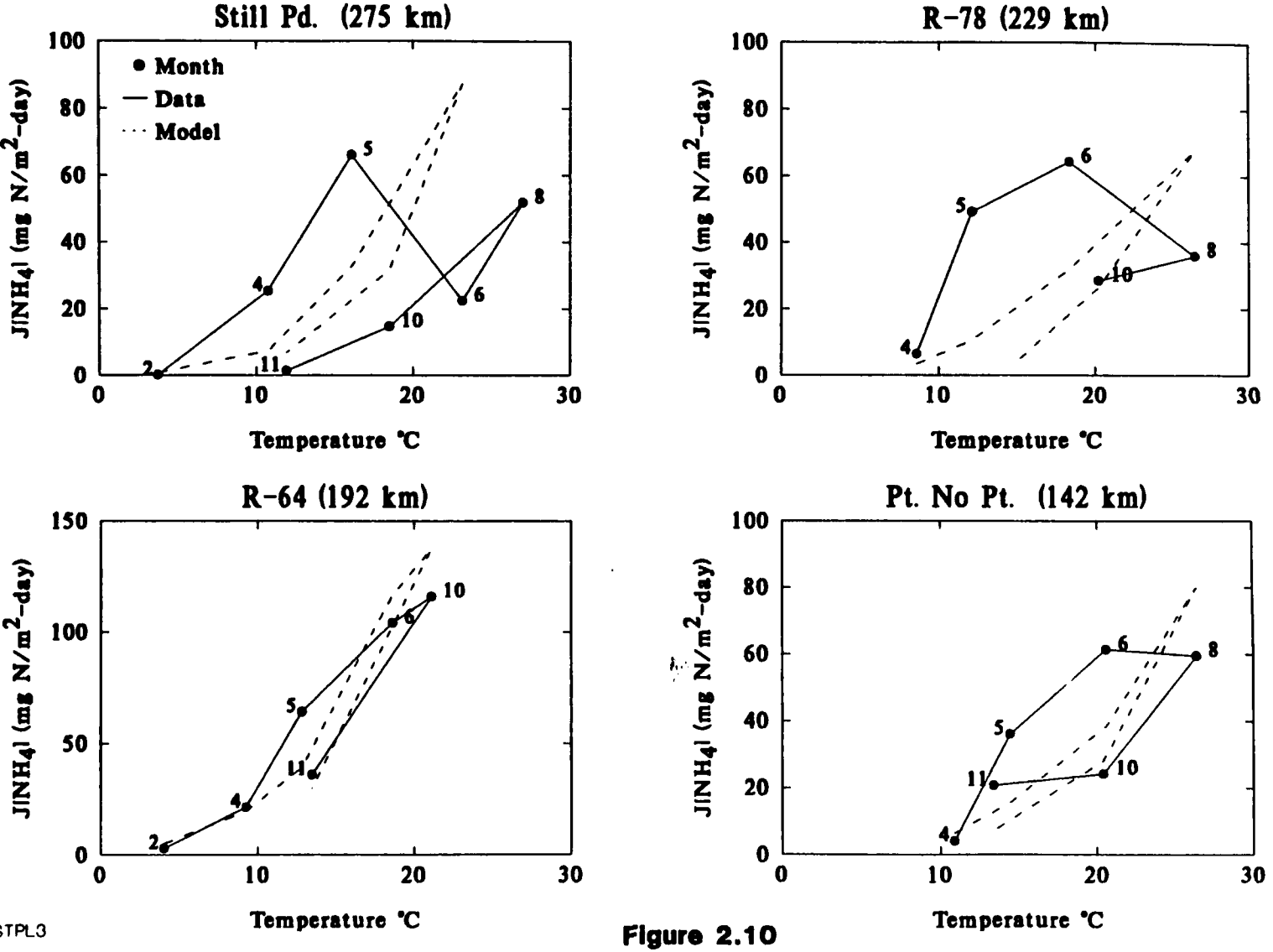

HYSTPL3

Figure 2.10

Table 2.2
Ammonia Model Parameters

Parameter	Symbol	Estimation Method (a)	(b)	(c)	(d)	(e)
Nitrification reaction velocity	$\kappa_{NH4,1}$ (m/d)	0.166	0.0722	0.116	0.151	0.148
Average Ammonia diagenesis	J_N (mg N/m^2-d)	92.2	-	-	-	-
Temperature coefficient	θ_N	-	1.112	1.142	1.141	1.153

Ammonia Diagenesis: $J_N(20)$ (mg N/m^2-d)	$\overline{J_N(20)}^{est}$ (*)	(a)	(b)	(c)	(d)	(e)
Point No Pt.#	56.9	-	39.3	43.1	62.6	54.6
R-64#	44.5	-	79.2	90.6	95.8	93.8
R-78#	40.8	-	41.6	38.5	50.7	49.6
Still Pond	72.4	-	53.0	63.7	76.6	72.4
St. Leo	92.7	-	49.6	60.3	93.4	92.7
Buena Vista	101.6	-	67.5	73.6	105.6	101.6
Horn Pt.	88.3	-	62.5	71.1	90.1	88.3
Windy Hill#	118.4	-	39.6	44.0	56.1	56.5
Ragged Pt.#	72.7	-	109.6	98.7	109.4	100.0
Maryland Pt.	73.8	-	66.0	78.8	71.6	73.9
Mean				66.2		

*Four year average computed from arithmetic average SOD and Redfield stoichiometry. The average temperatures for the data are very nearly 20 °C.

#Stations with significant anoxic periods. These are not used not used in the regression.

(a)Nonlinear regression analysis, Fig. 2. 5. (b)Individual replicates, least squares

(c)Averaged replicates, least squares (d)Individual replicates, least absolute value

(e)Averaged replicates, least absolute value

I. References

Berner, R.A. (1971): Principles of Chemical Sedimentology. McGraw-Hill, N.Y.

Berner, R.A. (1980): Early Diagenesis. A Theoretical Approach. Princeton Univ. Press, Princeton, N.J.

Billen, G. (1978): A budget of nitrogen recycling in North Sea sediments off the Belgian coast. Est. Coast. Mar. Sci. 7: pp. 127- 146.

Billen, G. (1982): An idealized model of nitrogen recycling in marine sediments. Am. J. Sci. 282: pp. 512-541.

Billen, G. (1988): Modelling benthic nitrogen cycling in temperate coastal ecosystems. In: Nitrogen Cycling in Coastal Marine Environments, pp. 341-378. Editors: T.H. Blackburn and J. Sorensen. J. Wiley & Sons. Ltd., New York.

Billen, G., Dessery, S., Lancelot, C. and Maybeck, M. (1989): Seasonal and inter-annual variations of nitrogen diagenesis in the sediments of a recently impounded basin. Biogeochemistry 8: pp. 73-100.

Boynton, W.R., Kemp, W.M., Barnes, J.M., Cowan, J.L.W., Stammerjohn, S.E., Matteson, L.L., Rohland, F.M. and Garber, J.H. (1990): Long-term characteristics and trends of benthic oxygen and Nutrient Fluxes in the Maryland portion of Chesapeake Bay. In: New Perspectives in the Chesapeake System: A research and management partnership., pp. 339-354. Editor:. Chesapeake Res. Consortium #137, Baltimore, MD.

Di Toro, D.M., Paquin, P.R., Subburamu, K. and Gruber, D.A. (1990): Sediment Oxygen Demand Model: Methane and Ammonia Oxidation. J. Environ. Engineering ASCE 116(5): pp. 945-986.

Goloway, F. and Bender, M. (1982): Diagenetic models of interstitial nitrate profiles in deep sea suboxic sediments. Limnol. Oceanogr. 27(4): pp. 624-638.

Jahnke, R.A., Emerson, S.R. and Murray, J.W. (1982): A Model of Oxygen Reduction, Denitrification, and Organic Matter Mineralization in Marine Sediments. Limnol. Oceanogr. 27(4): pp. 610-623.

Jorgensen, B.B. and Revsbech, N.P. (1985): Diffusive boundary layers and the oxygen uptake of sediments and detritus. Limnol. Oceanogr. 30(1): pp. 111-122.

Klapwijk, A. and Snodgrass, W.J. (1986): Biofilm Model for Nitrification, Denitrification, and Sediment Oxygen Demand in Hamilton Harbor. In: Sediment Oxygen Demand. Processes, Modeling and Measurement, pp. 75-97. Editor: K.J. Hatcher. Inst. of Nat. Res., Univ. of Georgia, Athens, Ga. 30602.

Kemp, W.M., Sampou, P., Caffrey, J., Mayer, M., Henriksen, K. and Boynton, W.R. (1990): Ammonium recycling versus denitrification in Chesapeake Bay sediments. Limnol. Oceanogr. 35(7): pp. 1545-1563.

Klump, J.V. and Martens, C.S. (1989): The seasonality of nutrient regeneration in an organic-rich sediment: Kinetic modeling of changing pore-water nutrient and sulfate distributions. Limnol. Oceanogr. 34(3): pp. 559-577.

Revsbech, N.P., Sorensen, J. and Blackburn, T.H. (1980): Distribution of oxygen in marine sediment measured with microelectrodes. Limnol. Oceanogr. 25(3): pp. 403-411.

Rudolph, J., Frenzel, P. and Pfennig, N. (1991): Acetylene inhibition technique underestimates in situ denitrification rates in intact cores of freshwater sediment. FEMS Microbiology Ecology 85: pp. 101-106.

Sampou, P., Kemp, W.M., Cornwell, J., Rosman, L. and Owens, M. (1989): Chesapeake Bay sediment data collection program 1988/1989: Nitrogen cycling and anaerobic processes. CEES, Univ. of Maryland, Cambridge, MD.

Vanderborght, J.P., Wollast, R. and Billen, G. (1977a): Kinetic models of diagenesis in disturbed sediments. Part I. Mass transfer properties and silica diagenesis. Limnol. Oceanogr. 22(5): pp. 787-793.

Vanderborght, J.P., Wollast, R. and Billen, G. (1977b): Kinetic models of diagenesis in disturbed sediments. Part 2. Nitrogen diagenesis. Limnol. Oceanogr. 22(5): pp. 794-803.

III. NITRATE

A. Introduction

The model presented in the previous chapter quantifies the fraction of ammonia - either produced by diagenesis of organic matter or transferred to the sediment from the overlying water - that is oxidized in the aerobic zone. The result is a source of nitrate. This may either escape as a flux to the overlying water, or may be denitrified to nitrogen gas. In addition, the flux of nitrate from the overlying water to the sediment adds to the nitrate that is available for denitrification. This chapter presents a model for the sediment nitrate flux.

B. Model Formulation and Solution

The model schematic is shown in Fig. 3.1. Denitrification can occur in the both the aerobic and anaerobic layers. The conventional formulation is to have denitrification occur only in a layer below the aerobic layer (Vanderborght et al. 1977a, 1977b; Billen, 1978; Jahnke et al., 1982; Goloway and Bender, 1982; Billen, 1982; Klapwijk and Snodgrass, 1986; Billen and Lancelot, 1988; Billen et al., 1989; Blackburn, 1990). For the model formulated in this chapter, denitrification can take place in the aerobic zone as well as the anaerobic zone. Three sources of evidence are offered to support the existence of aerobic layer denitrification

The first is the experimental results of Jenkins and Kemp, (1984). An ammonia tracer, $^{15}NH_4$, was added to the water overlying sediment cores taken from two stations in the Patuxent River estuary. After 48 hours of incubation the distribution of ^{15}N among the nitrogen species was determined for the interstitial and overlying water. Approximately 10 to 20% remained as $^{15}NH_4$, the rest appeared either as $^{15}N_2$ or ^{15}PON. No appreciable $^{15}NO_3$ was observed (see Fig.3 in Jenkins and Kemp, 1984). Their interpretation is that nitrification and denitrification occur in close spatial proximity. Brezonik (1977) and Jorgensen (1977) suggest the existence of

NITRATE FLUX MODEL

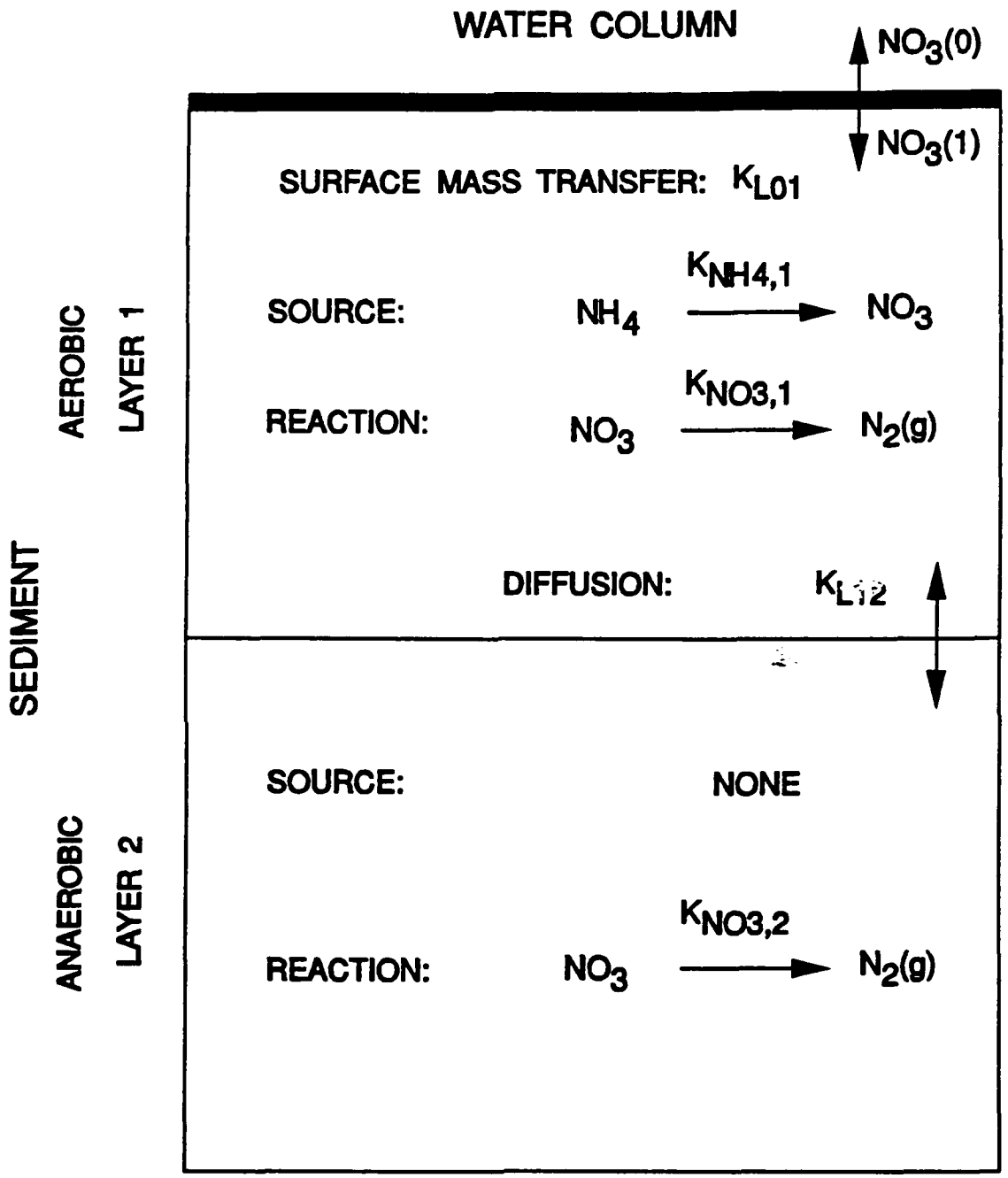

CHAP31

Figure 3.1

"anoxic microsites." For example, the interior of aggregate organic particles may be anaerobic even if the exterior is aerobic. Thus both nitrification and denitrification can coexist in the same location.

The second source of evidence is the consequence of assuming that no denitrification occurs in the aerobic layer. The result is that one half of the nitrate formed by the nitrification of diagenetically produced ammonia escapes as a nitrate flux to the overlying water (Di Toro et al., 1990). As will be seen below, large nitrate fluxes from sediments are not observed.

The third source of evidence is the analysis of the measured gas flux data from the Milwaukee River (Di Toro et al., 1990). These data suggest that most if not all the nitrate produced by sediment nitrification must be denitrified to nitrogen gas. Otherwise the magnitude of nitrogen gas flux measured from the sediments cannot be explained.

It is assumed, therefore, that the nitrate produced in the aerobic zone of the sediment can be denitrified to nitrogen gas with a first order rate constant $K_{NO3,1}$. In addition, nitrate that is transported to the anaerobic layer can be denitrified as well with a first order rate constant $K_{NO3,2}$. The remainder of the formulation parallels the ammonia flux model (Chapter II).

The mass balance equations for the two layers are:

$$H_1\frac{d[NO_3(1)]}{dt} = -K_{NO3,1}[NO_3(1)]H_1 - K_{L01}([NO_3(1)]-[NO_3(0)]) + K_{L12}([NO_3(2)]-[NO_3(1)]) + S[NO_3] \quad (1)$$

$$H_2\frac{d[NO_3(2)]}{dt} = -K_{NO3,2}[NO_3(2)]H_2 - K_{L12}([NO_3(2)]-[NO_3(1)]) \quad (2)$$

where $S[NO_3]$ is the source of nitrate from ammonia nitrification in the aerobic layer. The solutions to these mass balance equations are slightly more complex than in the case of ammonia

oxidation for which there is only an aerobic layer reaction rate. Steady state is assumed and eqs. (1-2) are solved simultaneously for $[NO_3(1)]$ and $[NO_3(2)]$. The resulting nitrate concentration in the aerobic and anaerobic layers are:

$$[NO_3(1)] = \frac{S[NO_3] + K_{LO1}[NO_3(0)]}{K_{NO3,1}H_1 + K_{LO1} + \left(\frac{1}{K_{NO3,2}H_2} + \frac{1}{K_{LI2}}\right)^{-1}} \tag{3}$$

$$[NO_3(2)] = [NO_3(1)]\frac{K_{LI2}}{K_{NO3,2}H_2 + K_{LI2}} \tag{4}$$

The equality $s = K_{LO1}$, (eq.II-14), is used for the surface mass transfer coefficient where $s = SOD/O_2(0)$. The aerobic denitrification reaction velocity is defined as:

$$\kappa_{NO3,1} = \sqrt{D_1 K_{NO3,1}} \tag{5}$$

The rationale for using reaction velocities is presented in Chapter II. The anaerobic denitrification parameter group, $K_{NO3,2}H_2$, has units of length/time and therefore formally qualifies as a reaction velocity.

$$\kappa_{NO3,2} = K_{NO3,2}H_2 \tag{6}$$

This parameter is defined for convenience of nomenclature only. It is not equivalent to the aerobic layer reaction velocities which include a diffusion coefficient as well as a reaction rate constant.

The reciprocal of the sum of the reciprocals of $\kappa_{NO3,2}$ and K_{LI2} in eq.(3) can be replaced by an overall layer 2 denitrification reaction velocity:

$$\kappa^{\bullet}_{NO3,2} = \left(\frac{1}{\kappa_{NO3,2}} + \frac{1}{K_{LI2}}\right)^{-1} \tag{7}$$

Using this notation, eqs.(3) and (4) become:

$$[NO_3(1)] = \frac{S[NO_3] + s[NO_3(0)]}{\frac{\kappa^2_{NO3,1}}{s} + s + \kappa^*_{NO3,2}} \tag{8}$$

$$[NO_3(2)] = [NO_3(1)] \frac{K_{L12}}{\kappa_{NO3,2} + K_{L12}} \tag{9}$$

The source of nitrate to the aerobic layer, $S[NO_3]$, which is the result of ammonia oxidation, can be quantified in a number of ways. For example, the rate of nitrification can be evaluated directly using eq.(II-7):

$$S[NO_3] = K_{NH4,1} H_1 [NH_4(1)] = \frac{D_1 K_{NH4,1}}{s} [NH_4(1)] = \frac{\kappa^2_{NH4,1}}{s} [NH_4(1)] \tag{10}$$

However, a simple mass balance argument is more instructive. Since all the sources balance all the sinks, the nitrification sink can be found by difference. The sources of ammonia are ammonia diagenesis, J_N, and ammonia transferred from the overlying water, $s[NH_4(0)]$. The sinks of ammonia are the flux to the overlying water, $s[NH_4(1)]$, and loss via nitrification, $S[NO_3]$. Hence, the nitrate source from nitrification can be found as the difference between the sum of the ammonia sources and the ammonia loss to the overlying water:

$$\begin{aligned} S[NO_3] &= J_N + s[NH_4(0)] - s[NH_4(1)] \\ &= J_N - s([NH_4(1)] - [NH_4(0)]) \\ &= J_N - J[NH_4] \end{aligned} \tag{11}$$

where the third equality follows from the mass transfer equation for ammonia flux, eq.(II-9):

$$J[NH_4] = s([NH_4(1)] - [NH_4(0)]) \tag{12}$$

The nitrate flux, with the convention that positive fluxes are from the sediment, is:

$$J[NO_3] = s([NO_3(1)] - [NO_3(0)]) \tag{13}$$

Substituting eqs. (8-9) into eq.(13) and using this in eq.(12) yields the final expression for the nitrate flux:

$$J[NO_3] = s\left(\frac{s[NO_3(0)] + J_N - J[NH_4]}{\frac{\kappa^2_{NO3,1}}{s} + s + \kappa^*_{NO3,2}} - [NO_3(0)]\right) \qquad (14)$$

It is important to note that the nitrate flux is a linear function of the overlying water nitrate concentration, $[NO_3(0)]$. This can be seen by re-arranging eq.(14):

$$J[NO_3] = \left(\frac{s^2}{\frac{\kappa^2_{NO3,1}}{s} + s + \kappa^*_{NO3,2}} - s\right)[NO_3(0)] + \left(\frac{s(J_N - J[NH_4])}{\frac{\kappa^2_{NO3,1}}{s} + s + \kappa^*_{NO3,2}}\right) \qquad (15)$$

The model's behavior can be examined from this point of view. The intercept quantifies the extent to which nitrate produced by nitrification in the sediment appears as a nitrate flux from the sediment to the overlying water. The slope quantifies the extent to which overlying water nitrate is denitrified in the sediment.

C. Nitrate Source from the Overlying Water

If the internal production of nitrate, $J_N - J[NH_4]$, is small relative to the nitrate delivered from the overlying water, $s[NO_3(0)]$, then the constant term in eq.(15) is small and the slope term dominates:

$$J[NO_3] = \left(\frac{s^2}{\frac{\kappa^2_{NO3,1}}{s} + s + \kappa^*_{NO3,2}} - s\right)[NO_3(0)]$$

$$= -s\left(1 - \frac{s}{\frac{\kappa^2_{NO3,1}}{s} + s + \kappa^*_{NO3,2}}\right)[NO_3(0)] \qquad (16)$$

This equation suggests if the nitrate flux is normalized using the overlying water nitrate concentration, then a one-to-one relationship exists between the normalized nitrate flux to the sediment and the surface mass transfer coefficient, s:

$$\frac{J[NO_3]}{[NO_3(0)]} = -s\left(1 - \frac{s}{\frac{\kappa^2_{NO3,1}}{s} + s + \kappa^*_{NO3,2}}\right) \tag{17}$$

This result is used below in the data analysis of nitrate fluxes.

Two limiting forms of this equation exist which depend on the magnitude of s. These can be found by examining eq.(17) in the following form:

$$\frac{J[NO_3]}{[NO_3(0)]} = -s\left(\frac{\frac{\kappa^2_{NO3,1}}{s} + \kappa^*_{NO3,2}}{\frac{\kappa^2_{NO3,1}}{s} + s + \kappa^*_{NO3,2}}\right) \tag{18}$$

For small s the bracketed term approaches one and eq.(18) becomes:

$$\frac{J[NO_3]}{[NO_3(0)]} = -s \qquad s \to 0 \tag{19}$$

This result can be understood as follows. The surface mass transfer coefficient, s, is the ratio of SOD to $O_2(0)$, i.e. the ratio of the oxygen flux into the sediment, $J[O_2]$, and the overlying water oxygen concentration. The left hand side of eq.(19) is the ratio of the flux of nitrate to the sediment to the overlying water nitrate concentration. Hence eq.(19) is:

$$\frac{J[NO_3]}{[NO_3(0)]} = -s = \frac{(-SOD)}{[O_2(0)]} = \frac{J[O_2]}{[O_2(0)]} \tag{20}$$

The reason for the symmetry between the equations for nitrate and oxygen fluxes is illustrated in Fig. 3.2. For small s the depth of the aerobic layer, H_1, is large enough and the residence time

is long enough so that all of the nitrate is denitrified either in the aerobic layer or in the anaerobic layer. Note that the bracketed term in eq.(18) approaches one even if there were no aerobic layer denitrification and $\kappa_{NO3,1} = 0$. Hence the nitrate concentration at the aerobic - anaerobic layer boundary is zero. By definition the concentration of oxygen at the aerobic - anaerobic layer boundary is also zero. Hence, both profiles connect the overlying water concentration to a zero concentration. Thus the normalized fluxes are equal.

The other limiting case is for large s. The limiting form can be found from eq.(18), but it is instructive to derive it directly. For large s the aerobic zone is quite small and there is no significant denitrification or mass transfer resistance in this layer. Hence $[NO_3(1)] \approx [NO_3(0)]$ and the layer 2 nitrate mass balance equation can be written as:

$$0 = H_2 \frac{d[NO_3(2)]}{dt} = -\kappa_{NO3,2}[NO_3(2)] - K_{L12}([NO_3(2)] - [NO_3(0)]) \quad (21)$$

which can be solved for $[NO_3(2)]$:

$$[NO_3(2)] = \frac{K_{L12}}{\kappa_{NO3,2} + K_{L12}}[NO_3(0)] \quad (22)$$

The nitrate flux is:

$$J[NO_3] = K_{L12}([NO_3(2)] - [NO_3(0)]) \quad (23)$$

where the mass transfer coefficient that governs is now K_{L12} since the aerobic layer mass transfer resistance is negligibly small. The solution follows from substituting eq.(22) into eq.(23):

$$\frac{J[NO_3]}{[NO_3(0)]} = -\kappa^*_{NO3,2} = -\left(\frac{1}{\kappa_{NO3,2}} + \frac{1}{K_{L12}}\right)^{-1} \quad (24)]$$

Vertical Profiles of Oxygen and Nitrate

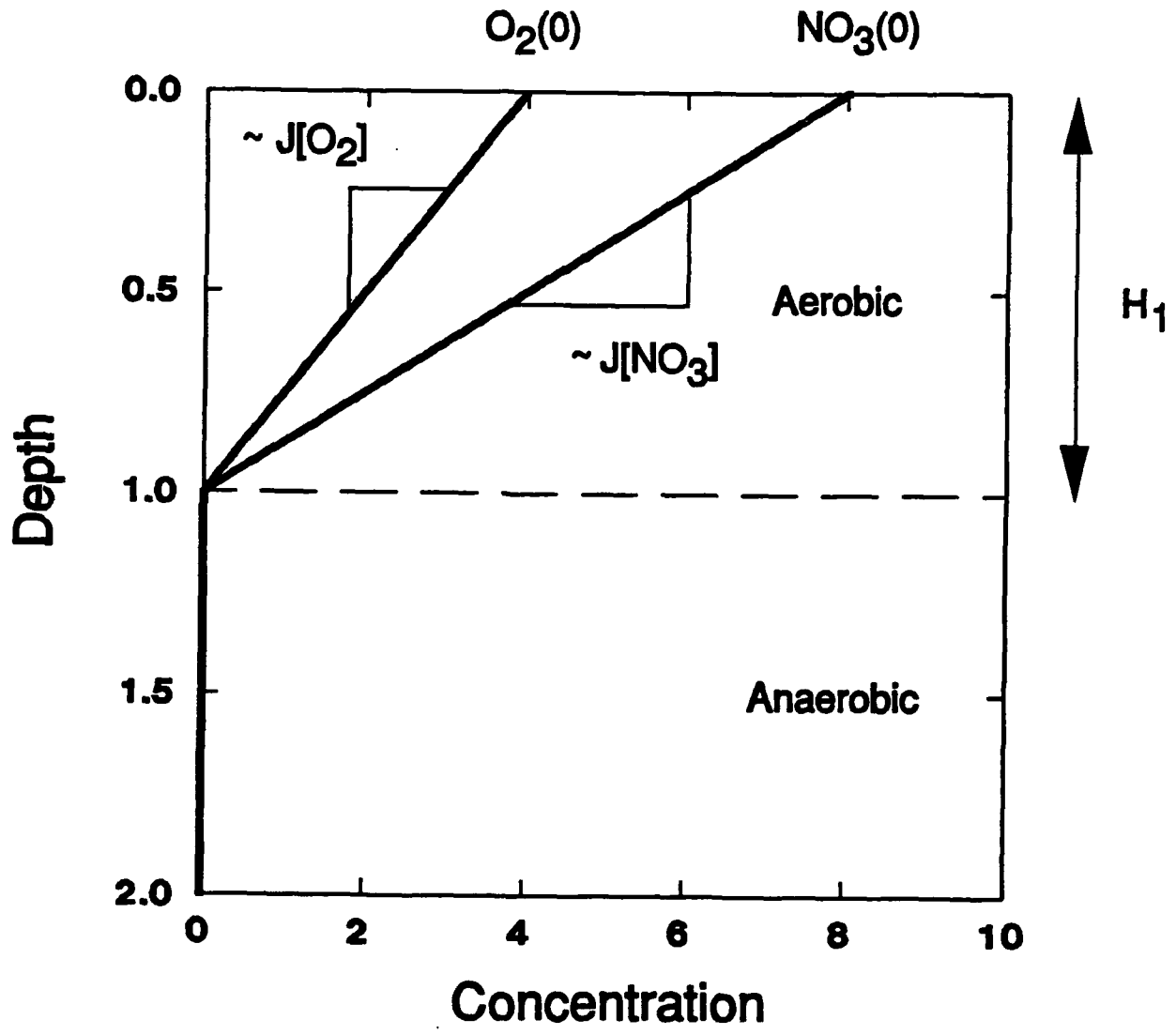

NJNO38L

Figure 3.2

The result is a constant normalized flux. The nitrate flux is determined by the reciprocal of the reciprocal sum of the two parameters that determine the extent of denitrification: the denitrification reaction velocity and the aerobic - anaerobic layer mass transfer coefficient. The magnitude of the smaller parameter determines the extent of denitrification. This is similar to that portion of the ammonia flux expression associated with the overlying water ammonia concentration, eq.(II-11) where the analogy to electrical resistors in parallel is explained.

To summarize the results, if the internal production of nitrate is small relative to the flux of nitrate from the overlying water, then the normalized nitrate flux to the sediment is linear in s for small s and constant for large s:

$$\frac{J[NO_3]}{[NO_3(0)]} = -s \qquad s \to 0 \qquad (25)$$

$$\frac{J[NO_3]}{[NO_3(0)]} = -\kappa^{*}_{NO3,2} = -\left(\frac{1}{\kappa_{NO3,2}} + \frac{1}{K_{L12}}\right)^{-1} \qquad s \to \infty \qquad (26)$$

1. Application to Hunting Creek

The relationship between nitrate flux and the surface mass transfer coefficient can be investigated using a data set collected for Hunting Creek sediments (Cerco, 1988). As part of an investigation of the variation of SOD as a function of overlying water DO, the denitrification flux was measured as well. Because the overlying water nitrate concentrations used in the experiments were large, it is reasonable to ignore the internal production of nitrate. Hence eq.(17) applies and an analysis of $J[NO_3]/[NO_3(0)]$ versus s is appropriate.

The nitrate flux data are presented in Fig. 3.3 as a function of overlying water nitrate concentration (Fig. 3.3A), oxygen concentration (Fig. 3.3B), and SOD (Fig. 3.3C). The unfilled circles represent experiments with more rapid mixing of the overlying water. The nitrate flux exhibits a decreasing dependency to overlying water DO, (Fig. 3.3B), a weaker relationship to SOD, (Fig. 3.3C), and almost no relationship to overlying water nitrate concentration, (Fig. 3.3A).

The analysis presented above suggests that the proper analysis is to examine the relationship between normalized nitrate flux, $J[NO_3]/[NO_3(0)]$, and the surface mass transfer coefficient, s . The result is presented in Fig. 3.3D, together with a model fit to the data. The dotted straight line is $J[NO_3]/[NO_3(0)] = s$, the small s limit. The parameter values are listed in Table 3.1

D. Nitrate Source from Nitrification

The intercept of the nitrate flux versus overlying water nitrate concentration is controlled by the quantity of ammonia that is nitrified but not denitrified. This is clear from the form of the constant term in eq.(15):

$$J[NO_3] = (J_N - J[NH_4]) \frac{s}{\frac{\kappa^2_{NO3.1}}{s} + s + \kappa^*_{NO3.2}} \qquad (27)$$

If the source of ammonia from the overlying water is small relative to the that produced by diagenesis, then eq.(II-26) can be substituted for $J[NH_4]$ and eq.(27) becomes:

$$J[NO_3] = J_N \left(\frac{\kappa^2_{NH4.1}}{\kappa^2_{NH4.1} + s^2} \right) \left(\frac{s}{\frac{\kappa^2_{NO3.1}}{s} + s + \kappa^*_{NO3.2}} \right) \qquad (28)$$

which delineates the various contributory factors. The flux is linear in ammonia diagenesis since this is the only source that is assumed to be significant. The next term is the fraction of ammonia that is nitrified to nitrate. The last term is the ratio of the rate of mass transfer to the overlying water to the sum of the rates - in mass transfer terms - of the three sinks of nitrate. It is the fraction of nitrate that escapes denitrification in either the aerobic or anaerobic layers and, therefore, escapes to the overlying water.

Hunting Creek

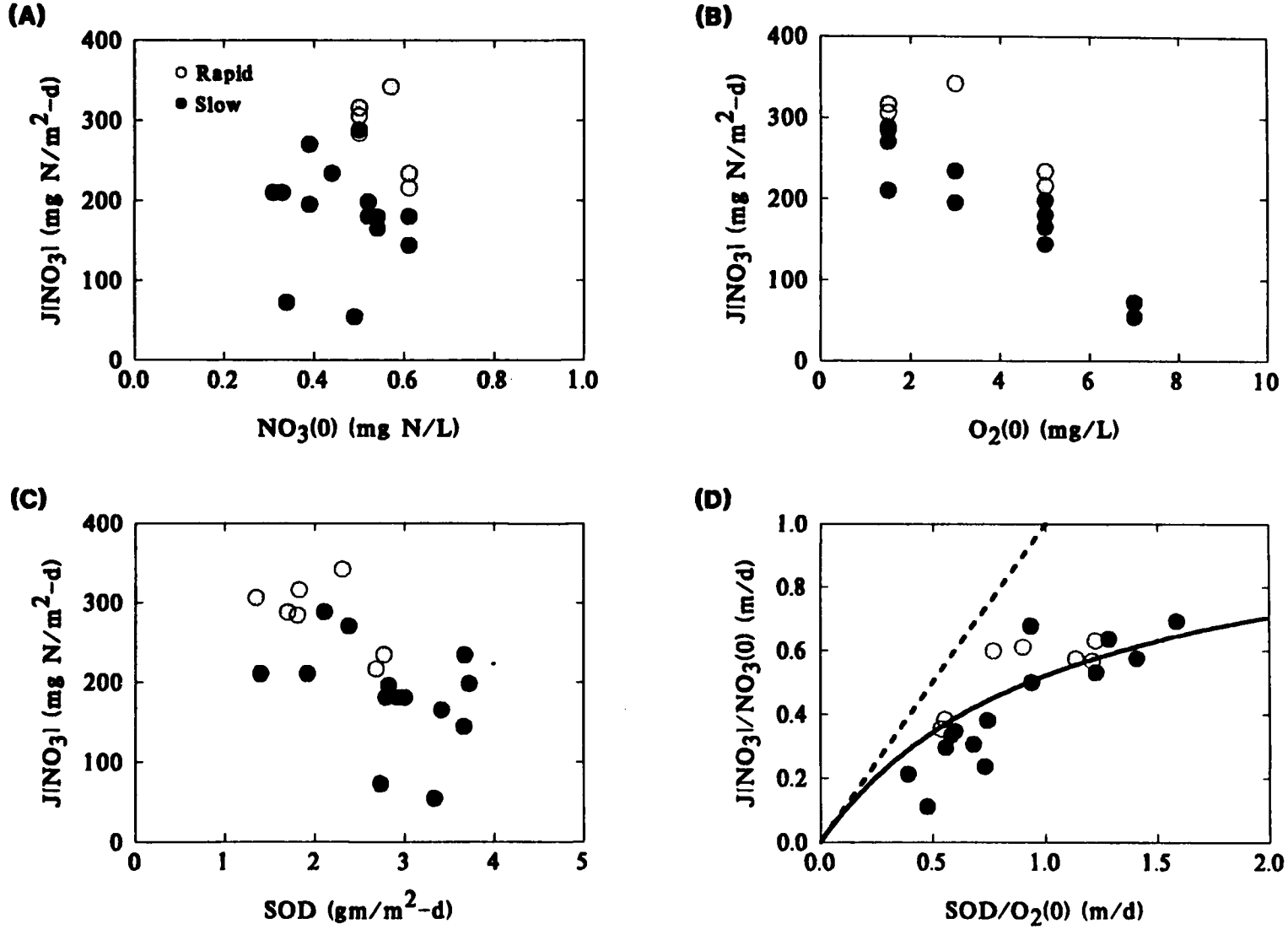

HUNTF1

Figure 3.3

E. Model Applications

1. Sensitivity

The behavior of the nitrate flux model, eq.(14), with respect to the controlling variables is illustrated in Fig. 3.4. The reaction velocities used in the computations which are obtained from a calibration to Chesapeake Bay data discussed below, are listed in Table 3.1. Equation (II-26) is used for $J[NH_4]$ as discussed above in Section D.

Table 3.1
Nitrate Model Parameters for
Sensitivity Analysis

Parameter	Value
$\kappa_{NH4,1}$	0.131 (m/d)
$\kappa_{NO3,1}$	0.05 (m/d)
$\kappa^{\bullet}_{NO3,2}$	0.10 (m/d)

For a fixed s, the effect of increasing J_N is to increase the nitrate flux uniformly, that is, to increase the intercept of the linear relationship (Fig. 3.4A). This additional nitrate flux is that portion of the nitrate produced by the nitrification of ammonia that is not denitrified. The slope of the relationship, which is determined by s and the κ's, is unaffected.

For a fixed J_N, varying s affects both the slope and intercept (Fig. 3.4B). For small s = 0.01 (m/d), the nitrate flux is essentially zero, independent of overlying water nitrate concentration. The reason is that the amount of overlying water nitrate that is transferred to the aerobic zone, $s[NO_3(0)]$, is small enough, and the aerobic zone is deep enough so that denitrification is essentially complete. For the nitrate produced by nitrification, the same

reasoning applies, namely, that the residence time in the sediment is sufficient so that denitrification is essentially complete. The result is that the nitrate produced by both sources is completely denitrified.

As s increases to 0.1 (m/d), the slope of the nitrate flux - nitrate concentration relationship increases. Surface mass transfer is increasing and aerobic layer depth is decreasing so that more nitrate is transferred to the sediment where it denitrifies. The intercept starts to increase as well, reflecting the increasing nitrate flux due to nitrate produced by ammonia nitrification. However, as s continues to increases to 1.0 (m/d), the intercept starts to decrease. The aerobic layer depth is now getting so small that less ammonia is nitrified producing less nitrate that is available for transfer to the overlying water.

2. Application to Chesapeake Bay

The straight line relationship between nitrate flux and overlying water nitrate concentration can be used to examine data in a straightforward fashion. The aggregated Chesapeake Bay SONE data set is shown in Fig. 3.5. The data has been divided into two classes with respect to concentration of overlying water dissolved oxygen. The observed surface mass transfer coefficient and nitrate flux are averaged in bins of width 0.2 $\log_{10}$ $[NO_3(0)]$. The number of observations in each bin is shown by the histogram. Since there appears to be no trend in the relationship between s and $[NO_3(0)]$ a constant is used in the calculation as indicated in Fig. 3.5A,B. The reaction velocities are obtained from an analysis described below in Section F. The computed nitrate fluxes are compared to the observations are shown in Fig. 3.5C,D. For aerobic conditions, $[O_2(0)]>2$, the data suggest a positive nitrate flux for small $[NO_3(0)]$ and exhibit the expected linear behavior as overlying water nitrate concentration increases. For hypoxic conditions, $[O_2(0)]<2$, and an almost constant relationship is predicted. Note that the abscissa scale has been changed in Fig. 3.5D. The data appear to support the absence of positive nitrate fluxes for small $[NO_3(0)]$. As $[NO_3(0)]$ increases, the model predicts that the flux should remain constant whereas the data suggest a decrease although the number of data points are small.

Sensitivity Analysis

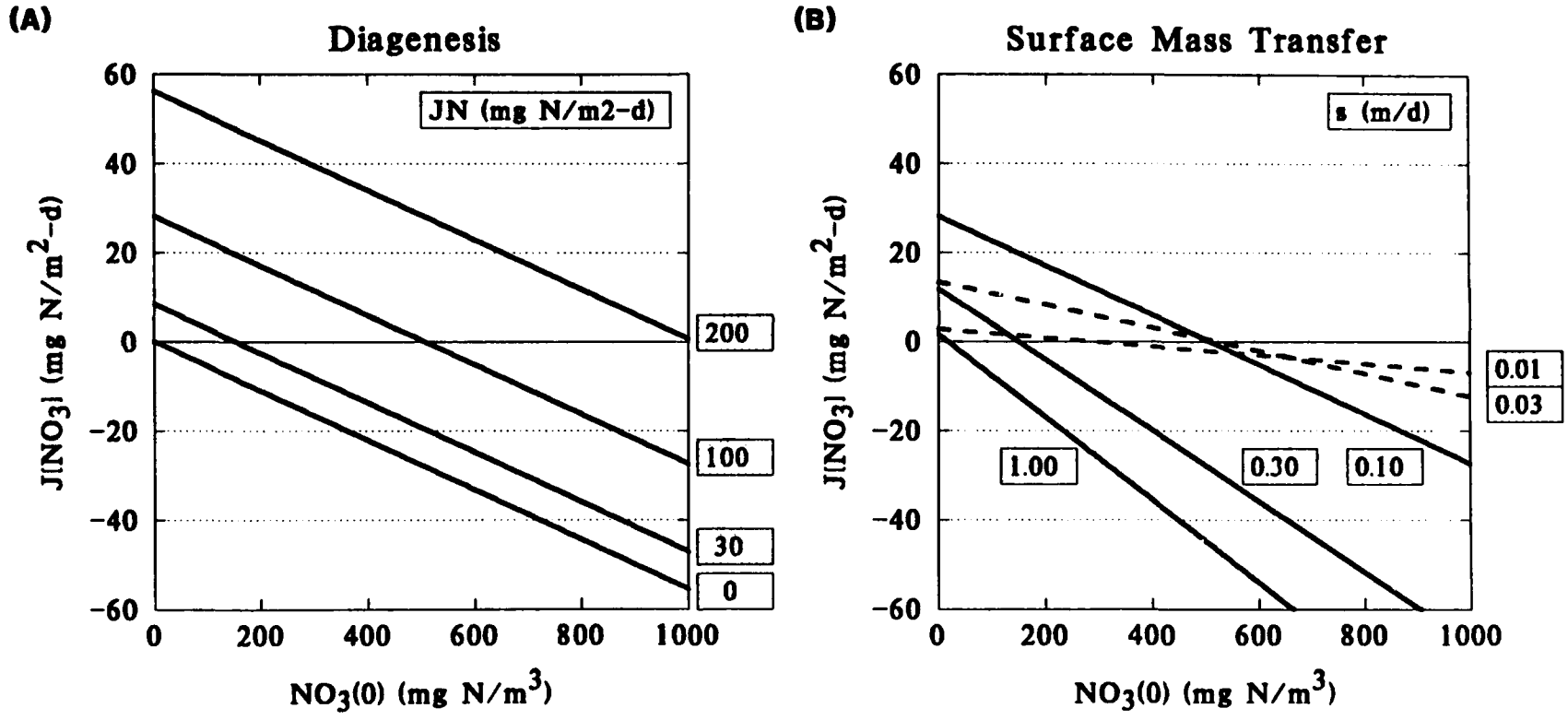

NJNO3F2

Figure 3.4

Chesapeake Bay

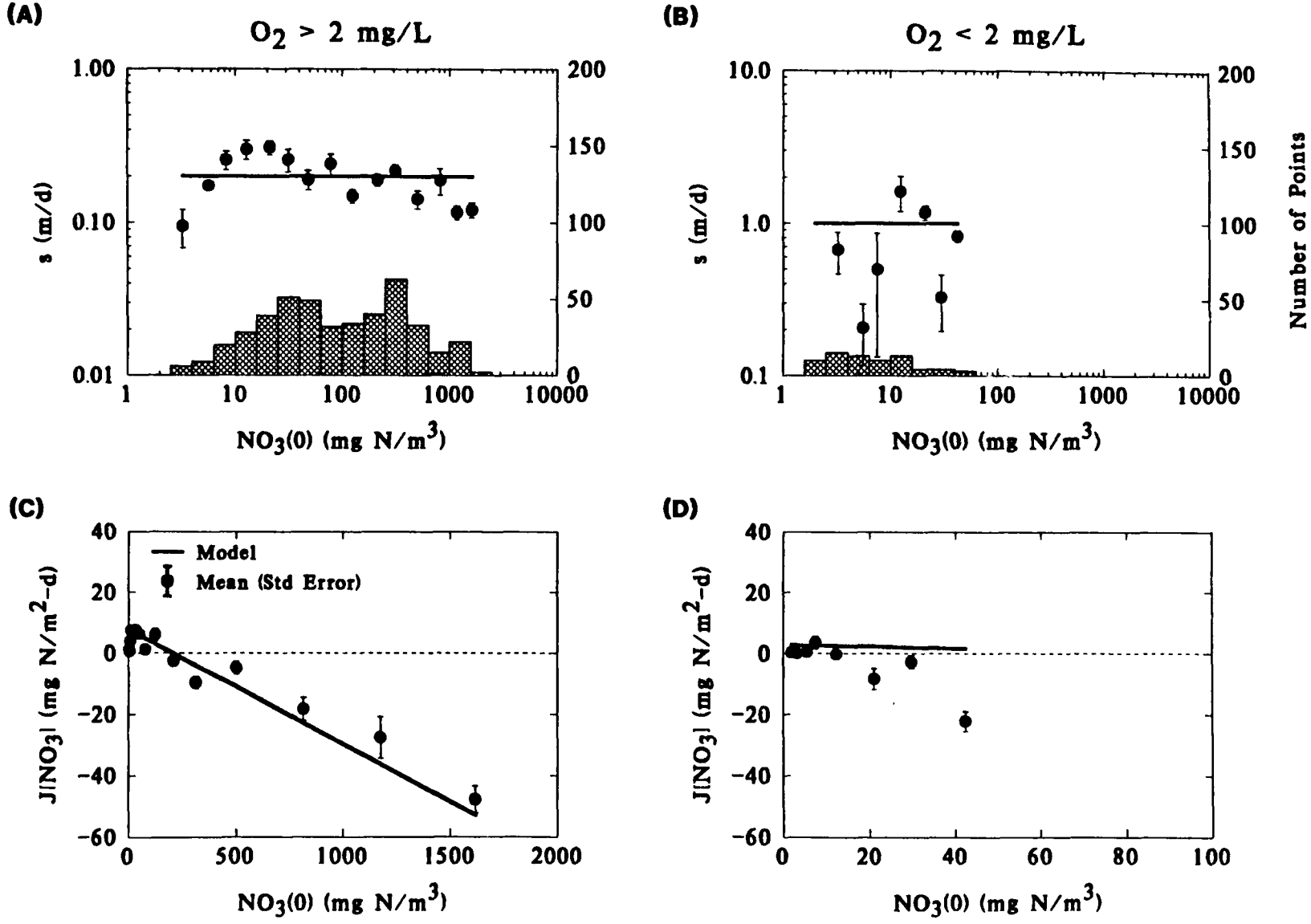

NJNO3S4

Figure 3.5

3. Application to Gunston Cove

A set of nutrient and oxygen flux measurements have been made by Cerco (1985, 1988) in Gunston Cove, a small tidal freshwater embayment of the Potomac river. Both in situ and laboratory measurements are reported. The temperature, overlying water DO, and nitrate concentrations span a reasonably wide range so that their effects can be seen. In order to analyze these data within the framework of the model presented above it is necessary to specify the variables: s and J_N.

The surface mass transfer coefficient is available from measurements of SOD and $O_2(0)$, Fig. 3.6B. The observations versus temperature and a comparison to the expression:

$$s = s_{20}\theta_s^{T-20)} \tag{29}$$

is shown where the parameters, s_{20} and θ_s are estimated by regression. This formula is used strictly as a convenient interpolation for s versus temperature.

Ammonia diagenesis can be inferred from the measured ammonia fluxes using the model presented in the previous chapter, eq.(II-26):

$$J[NH_4] = J_N \frac{S^2}{S^2 + K^2_{NH4.1}} \tag{30}$$

Ammonia diagenesis is assumed to be given by an exponential function of temperature:

$$J_N(T) = J_N(20)\theta_N^{(T-20)} \tag{31}$$

The two parameters, $J_N(20)$ and θ_N are found by fitting the ammonia flux model, eq.(30), to the observations. The result is shown in Fig. 3.6A, and the parameters are listed in Table 3.1.

With these parameters established as a function of temperature, the nitrate flux can be predicted as a function of overlying water nitrate concentration. The reaction velocities for denitrification are found from a nonlinear least squares fit of the model, eq.(14), to the data using eqs. (29 and 31) for s and J_N at the temperature of the observation. Table 3.1 present the results. Fig. 3.7 (bottom right) compares observations and predictions.

A more informative presentation can be made if the data are grouped into temperature classes. Ammonia diagenesis and surface mass transfer are calculated for the temperature indicated in each panel in Fig. 3.7. The model prediction is a straight line relationship between nitrate flux and overlying water nitrate concentration. The slopes progressively increase as s increases with temperature. The intercept also increases as diagenesis increases with temperature. In general, the model appears to conform to the major features of these data: the linear relationship between nitrate flux and nitrate concentration, and the relationships of the slope and intercept to the surface mass transfer coefficient and the endogenous production of nitrate. However, there is considerable scatter when individual fluxes are compared to model predictions, Fig. 3.7F. As we shall see, this scatter is not unique to nitrate fluxes.

F. Flux Normalization and Parameter Estimation

A comprehensive method for the analysis of the nitrate flux data employs a normalization of the nitrate fluxes suggested by the structure of the model. Eq.(14) for nitrate flux can be written in the form:

$$\frac{J[NO_3]}{s} = \frac{s[NO_3(0)] + J_N - J[NH_4]}{\frac{\kappa^2_{NO3,1}}{s} + s + \kappa^*_{NO3,2}} - [NO_3(0)] \qquad (32)$$

Note that the unknown reaction velocities are in the denominator of the first term. Solving for this term yields:

Gunston Cove – Forcing Functions

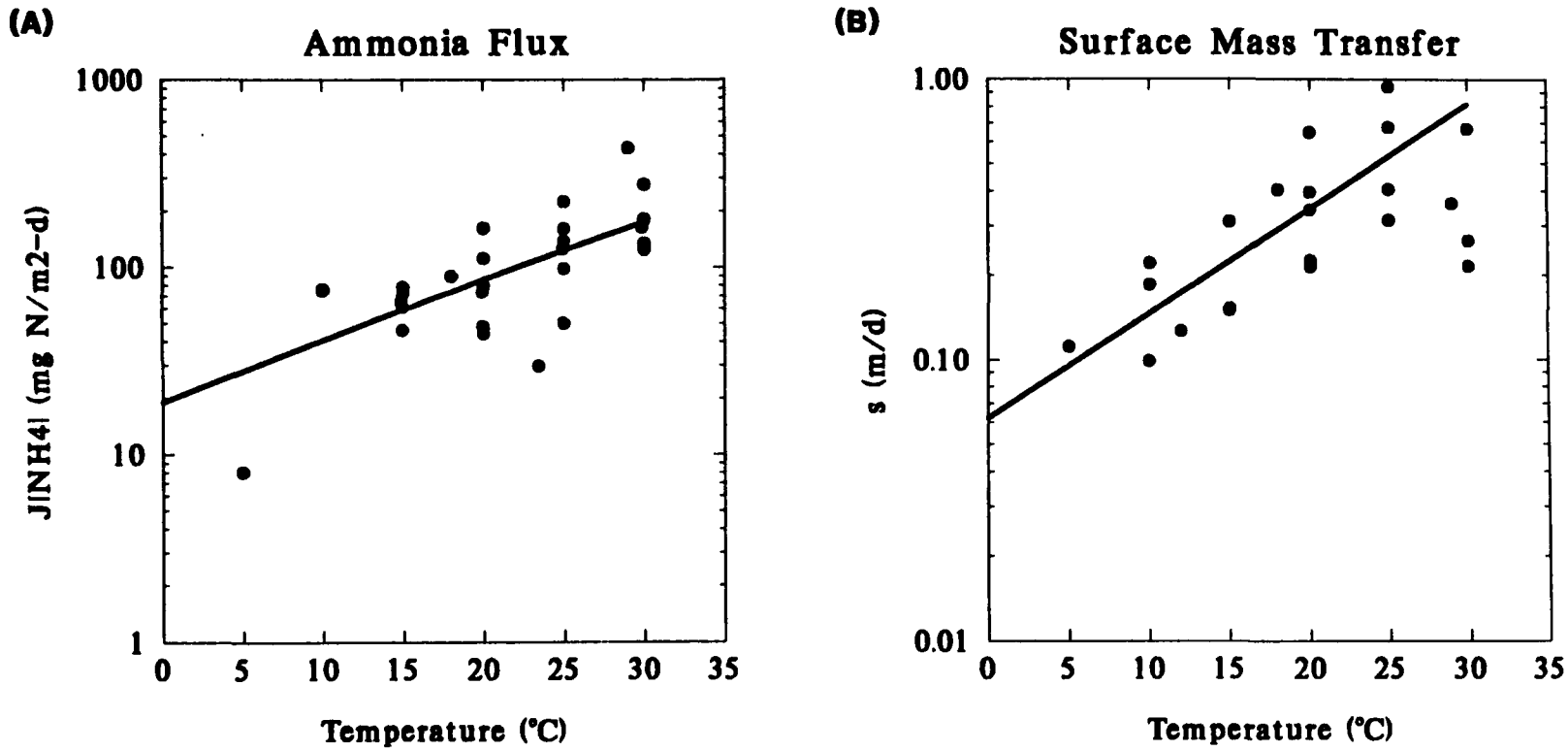

GUNFF

Figure 3.6

Gunston Cove

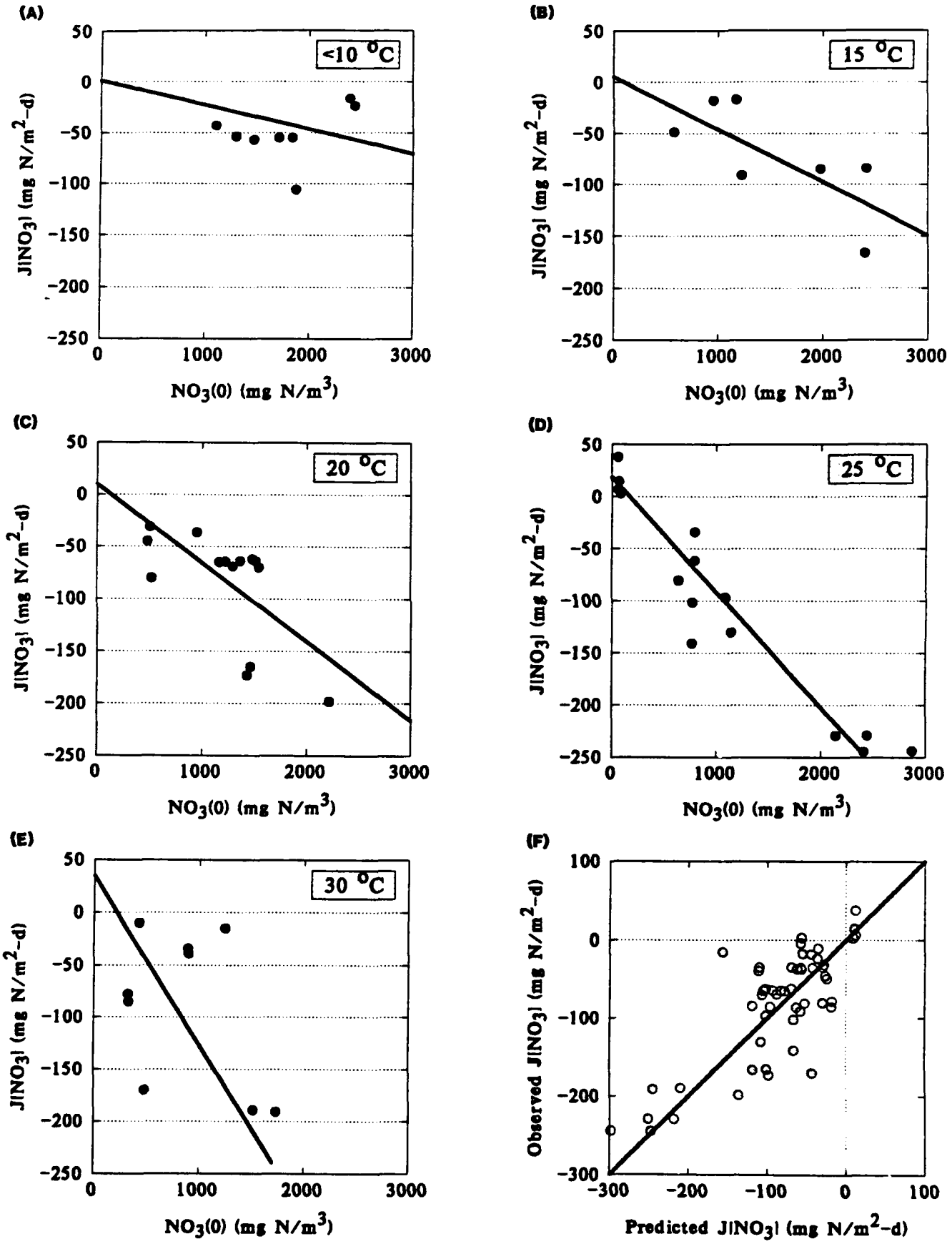

GUNJNO3

Figure 3.7

$$\frac{\kappa^2_{NO3,1}}{s} + s + \kappa^*_{NO3,2} = \frac{s[NO_3(0)] + J_N - J[NH_4]}{\frac{J[NO_3]}{s} + [NO_3(0)]} \tag{33}$$

The numerator of the right hand side of this equation is the total source of nitrate in the aerobic layer from both the overlying water and aerobic layer nitrification. The denominator is the aerobic layer nitrate concentration, $[NO_3(1)]$. This can be seen if the nitrate mass transfer equation (13) is expressed as:

$$[NO_3(1)] = \frac{J[NO_3]}{s} + [NO_3(0)] \tag{34}$$

Hence eq.(33) becomes:

$$\frac{\kappa^2_{NO3,1}}{s} + s + \kappa^*_{NO3,2} = \frac{S[NO_3]_T}{[NO_3(1)]} \tag{35}$$

where $S[NO_3]_T = S[NO_3] + s[NO_3(0)]$, the total nitrate source to the aerobic layer.

1. Mechanisms

The left hand side of this equation (35) is made up of three terms that represent the mechanisms by which nitrate is lost from the aerobic layer: (1) aerobic layer denitrification, (2) mass transfer to the overlying water, and (3) diffusion and denitrification in the anaerobic layer. For small s, so that the aerobic layer depth is large, aerobic layer denitrification predominates. For intermediate s, diffusive transport to the anaerobic layer followed by denitrification dominates. Finally, for large s, surface mass transfer dominates.

The presence of the aerobic and anaerobic denitrification terms in this equation is expected. However, the presence of the mass transfer term, s, requires clarification. The question is: under what circumstances does:

$$\frac{S[NO_3]_T}{[NO_3(1)]} \rightarrow s \tag{36}$$

This can be seen by examining the normalized flux expression, eq.(33):

$$\frac{S[NO_3]_T}{[NO_3(1)]} = \frac{s[NO_3(0)] + J_N - J[NH_4]}{\frac{J[NO_3]}{s} + [NO_3(0)]} \tag{37}$$

Two cases produce the limiting behavior. The first corresponds to the case where both the nitrate source due to nitrification, $J_N - J[NH_4]$, and the nitrate flux to or from the sediment, $J[NO_3]$, are small relative to the mass transfer flux to the sediment, $s[NO_3(0)]$. This occurs for large s and/or large $[NO_3(0)]$. It is the usual situation.

The second case occurs if nitrate is behaving conservatively in the sediment and no denitrification is occurring. For this case nitrate flux is equal to the production of nitrate:

$$J[NO_3] = J_N - J[NH_4] \tag{38}$$

Thus eq.(37) becomes:

$$\frac{S[NO_3]_T}{[NO_3(1)]} = \frac{s[NO_3(1)]}{[NO_3(1)]} = s \tag{39}$$

because $s[NO_{(0)}] + J_N - J[NH_4] = s[NO_3(1)] + J[NO_3] = s[NO_3(1)]$. This situation corresponds to the low temperature periods when $\kappa_{NO3,1}$ and $\kappa_{NO3,2}$ are small and nitrate is behaving conservatively.

2. Sensitivity Analysis

A sensitivity analysis for the normalized flux equation is presented in Fig. 3.8. The straight line corresponds to both $\kappa_{NO3,1}$, and $\kappa^*_{NO3,2}$ equaling zero. As the κ's increase, the normalized flux increases as s becomes smaller. What distinguishes aerobic and anaerobic layer

Sensitivity to Reaction Velocity

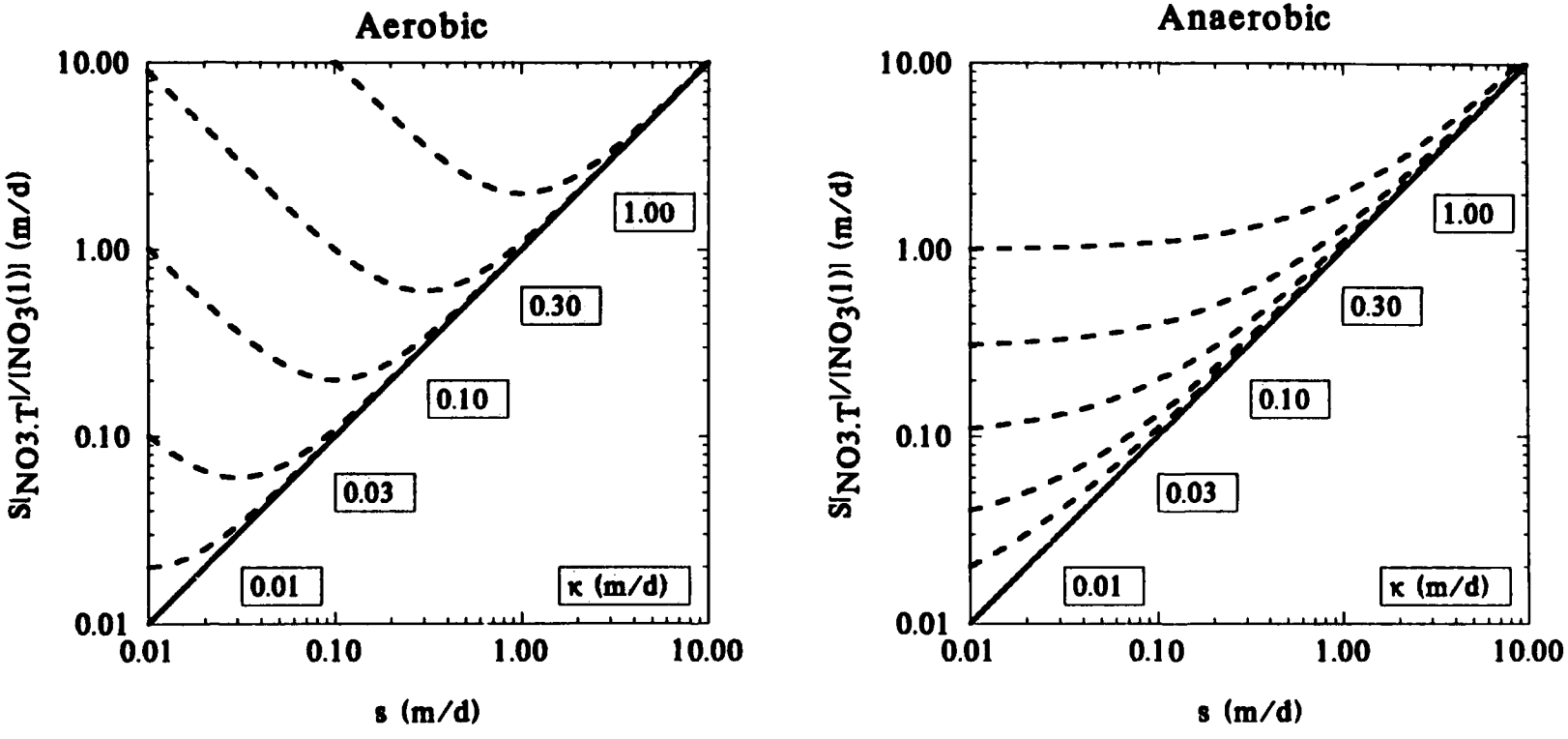

NJNO3F 1

Figure 3.8

denitrification is that aerobic layer denitrification increases sharply at small s's whereas anaerobic layer denitrification reaches a plateau. Unless the normalized data has a distinctive upward curvature at small s's, it would be difficult to identify whether the denitrification was occurring in the aerobic or anaerobic layer.

3. Diffusive Mass Transfer Coefficient

There is an additional constraint that limits the extent of anaerobic layer denitrification. It can be limited by the rate at which nitrate is transported from the aerobic to the anaerobic layer. This is controlled by the diffusive mass transfer coefficient between the two layers K_{L12}. An independent estimate of this parameter is necessary to evaluate the extent of anaerobic layer denitrification.

A direct estimate of K_{L12} is available using a result from the ammonia flux model. The anaerobic layer ammonia concentration is given by eq.(II-8):

$$[NH_4(2)] = \frac{J_N}{K_{L12}} + [NH_4(1)] \tag{40}$$

The aerobic layer ammonia concentration can be estimated from the flux equation (II-9):

$$[NH_4(1)] = \frac{J[NH_4]}{s} + [NH_4(0)] \tag{41}$$

Therefore:

$$\frac{J_N}{K_{L12}} = [NH_4(2)] - [NH_4(1)]$$

$$= [NH_4(2)] - \frac{J[NH_4]}{s} - [NH_4(0)] \tag{42}$$

Therefore K_{L12} can be estimated using an estimate of J_N, and measurements of ammonia flux, overlying ammonia concentration, observed $[NH_4(2)]$ concentration, and s. This result is applied in the next section.

G. Application to Chesapeake Bay

The anaerobic layer ammonia concentration data from the Bricker data set is summarized in Fig. 3.9A. The box symbols represent the median (the horizontal line), the 25th and 75th percentiles (the lower and upper limits of the box), and the ranges, excluding outliers. The data include all the stations analyzed from 1971 to 1974. The histograms specify the number of data points in each box. An ammonia concentration of $[NH_4(2)] = 10.0$ mg N/L is representative.

The aerobic layer ammonia concentration, $[NH_4(1)]$, is estimated from the SONE data set using eq.(41). Concentrations are less than 1.0 mg N/L, Fig. 3.9B, so that $[NH_4(1)] \ll [NH_4(2)]$. Thus, from eq.(42):

$$K_{L12} \approx \frac{J_N}{[NH_4(2)]} \tag{43}$$

For an average ammonia diagenesis of $J_N = 100$ mg N/m^2-d and $[NH_4(2)] = 10.0$ mg N/L, the diffusive exchange mass transfer coefficient is: $K_{L12} = 0.01$ (m/d).

This result can be compared to the diffusion coefficient using the relationship:

$$K_{L12} = \frac{D_2}{H_2} \tag{44}$$

which follows from eq.(II-5). Using the depth of the anaerobic layer $H_2 = 0.1$ m, the diffusion coefficient is estimated to be $D_2 = 0.001$ m^2/d = 10 cm^2/d. This is approximately ten fold higher

Porewater Ammonia Concentration

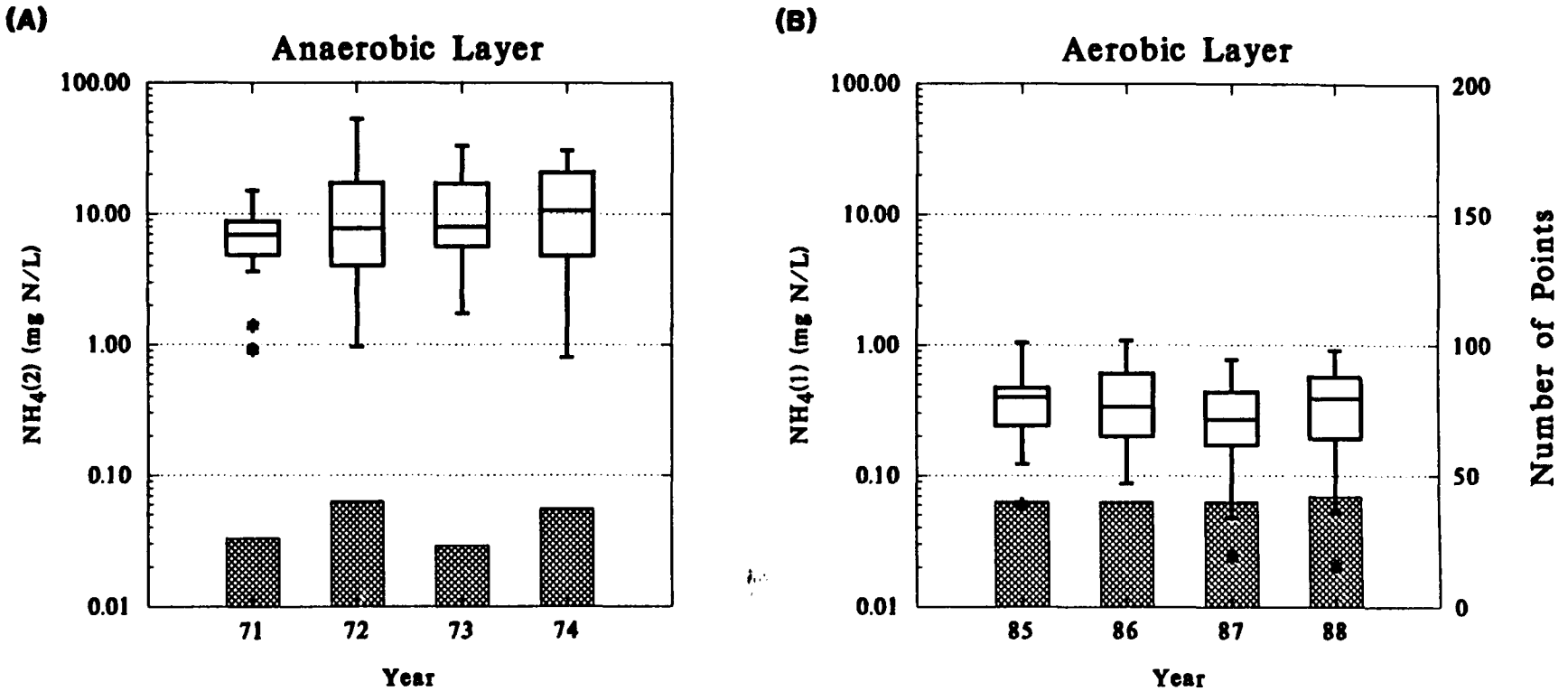

BRICP2G

Figure 3.9

than the molecular diffusivity of ammonia. This results suggests that additional mixing is present, probably due to the activities of benthic organisms (bio-irrigation). This phenomena is examined in further detail is Chapter IX.

H. Estimate of the Denitrification Reaction Velocities

The flux normalization equation (33) has all measured or estimated quantities on the right hand side, and the three term expression involving the unknown parameters on the left hand side as a function of s. Therefore a plot of $S[NO_3]_T/[NO_3(1)]$, eq.(37), versus s can be used to estimate $\kappa_{NO3,1}$ and $\kappa^*_{NO3,2}$. There is a problem, however, because temperature affects the reaction velocities. Therefore, eq.(33) becomes:

$$\frac{\kappa^2_{NO3,1}\theta^{(T-20)}_{NO3}}{s} + s + \kappa^*_{NO3,2}\theta^{(T-20)}_{NO3} = \frac{S[NO_3]_T}{[NO_3(1)]} \qquad (45)$$

where θ_{NO3} is the temperature coefficient for the denitrification reaction and θ_{NO3} is the temperature coefficient for either $\kappa^2_{NO3,1}$ or $\kappa^*_{NO3,2}$. Table 3.3 lists the reported values. The terms involving the κ's are most important for small s. It happens that the temperatures are low for these observations. It is for these temperatures that the temperature correction is important. For larger s the temperatures are closer to 20 °C and the correction is not significant. This suggests it may be a reasonable approximation to move the temperature correction to the right hand side of the equation:

$$\frac{\kappa^2_{NO3,1}}{s} + s + \kappa^*_{NO3,2} \approx \frac{S[NO_3]_T}{[NO_3(1)]\theta^{(T-20)}_{NO3}} = \frac{s[NO_3(0)] + J_N - J[NH_4]}{[NO_3(1)]\theta^{(T-20)}_{NO3}} \qquad (46)$$

We have found that this approximation is preferable to ignoring the temperature dependence.

The equations used for evaluating eq.(46) are as follows. The aerobic layer nitrate concentration, $[NO_3(1)]$, is estimated using eq.(34). The numerator terms are s and $[NO_3(0)]$ which are measured, and the nitrate produced by nitrification, $J_N - J[NH_4]$. This can be estimated by evaluating the kinetic expression:

$$S[NO_3] = J_N - J[NH_4] = \left(\frac{K_{M,NH4}\theta_{K_{M,NH4}}^{(T-20)}}{K_{M,NH4}\theta_{K_{M,NH4}}^{(T-20)} + [NH_4(1)]} \right) \left(\frac{[O_2(0)]}{2K_{O2,NH4} + [O_2(0)]} \right) \cdot \frac{\kappa_{NH4,1}^2 \theta_{NH4}^{(T-20)}}{s} [NH_4(1)] \quad (47)$$

where the aerobic layer ammonia concentration is estimated using:

$$[NH_4](1) = \frac{J[NH_4]}{s} + [NH_4(0)] \quad (48)$$

Since all these estimates involve measured quantities the individual estimates are quite variable. Thus an averaging procedure is employed to reduce the variability. The result is shown in Fig. 3.10. The normalized flux in binned into 0.1 $\log_{10}$ units of s. The mean and standard error of the mean is shown. The histogram indicates the number of data points in each bin. The straight line is $S[NO_3]_T/[NO_3(1)] = s$. The fitted line corresponds to anaerobic layer denitrification limited by the aerobic - anaerobic layer diffusive mixing: $\kappa_{NO3,2}^{\bullet} \approx K_{L12} = 0.01$ (m/d), and $\kappa_{NO3,1} = 0.1$ (m/d). Note that the normalized flux data exhibits an increased flux for intermediate s and an upward curvature that indicates aerobic layer denitrification. The model is able to reproduce the aerobic layer denitrification at the lower s, but there is some deviation from the data at intermediate s (0.1 to 0.3 m/d). This could be remedied by increased anaerobic layer denitrification (see Fig. 3.8B). However, the constraint is due to the analysis of the anaerobic layer pore water ammonia concentration which limits the diffusive exchange to 0.01 (m/d). As shown in Fig. 3.8, this limits the possible contribution of anaerobic layer denitrification to only a small part of the overall denitrification that is taking place.

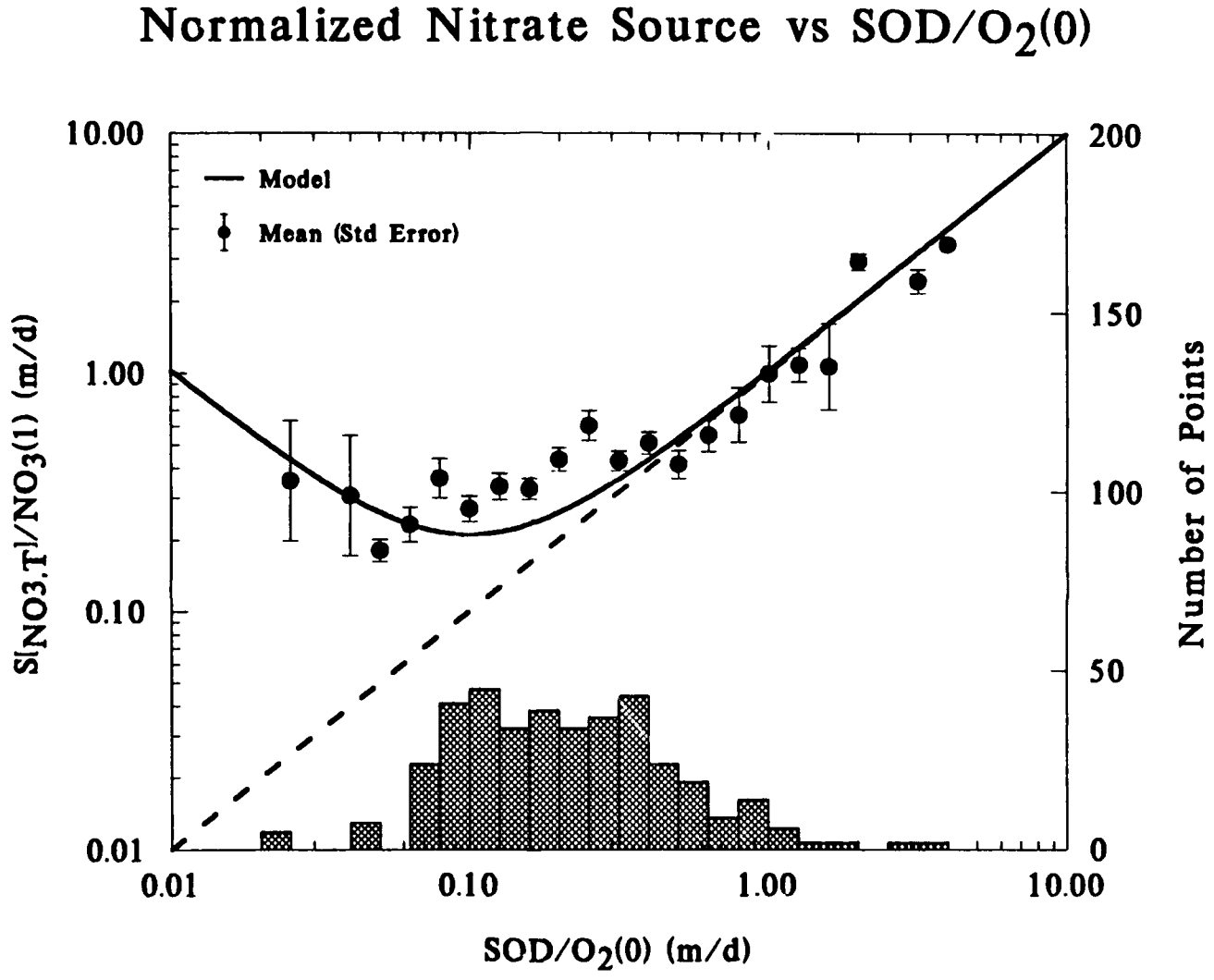

FSNO3P2A

Figure 3.10

I. Observations of Chesapeake Bay Denitrification

Direct measurements of the rate of denitrification in Chesapeake Bay sediments have been made during 1988 (Sampou et al., 1989; Kemp et al., 1990). These are compared to model predictions in two ways. The difference is in how the model prediction is computed. For the main stem stations, where flux measurements over a season have been made, the ammonia flux model has been applied (Fig. 2.8) and estimates of the nitrification source of nitrate, $S[NO_3]_{i,j}$, are available. Thus the aerobic layer nitrate concentration can be computed using the model, eq.(8),

$$[NO_3(1)]_{i,j} = \frac{S[NO_3]_{i,j} + s_{i,j}[NO_3(0)]_{i,j}}{\frac{\kappa^2_{NO3,1}\theta^{(T_{i,j}-20)}_{NO3}}{s_{i,j}} + s_{i,j} + K_{L12}\theta^{(T_{i,j}-20)}_{K_{L12}}} \tag{49}$$

with the observed surface mass transfer coefficient, $s_{i,j}$, and the temperature, $T_{i,j}$.

The anaerobic layer nitrate concentration follows from eq.(9):

$$[NO_3(2)]_{i,j} = [NO_3(1)]_{i,j} \frac{K_{L12}\theta^{(T_{i,j}-20)}_{K_{L12}}}{\kappa_{NO3,2}\theta^{(T_{i,j}-20)}_{NO3} + K_{L12}\theta^{(T_{i,j}-20)}_{K_{L12}}} \tag{50}$$

With the layer concentrations determined, the kinetic expression, eq.(41) is used to compute the denitrification flux:

$$\begin{aligned} J[N_2(g)]_{i,j} &= K_{NO3,1}H_1[NO_3(1)]_{i,j} + K_{NO3,2}H_2[NO_3(2)]_{i,j} \\ &= \frac{\kappa^2_{NO3,1}\theta^{(T_{i,j}-20)}_{NO3}}{s_{i,j}}[NO_3(1)]_{i,j} + \kappa_{NO3,2}\theta^{(T_{i,j}-20)}_{NO3}[NO_3(2)]_{i,j} \end{aligned} \tag{51}$$

which is the flux of nitrogen gas to the overlying water. The model parameters that are used are the medians in Table 3.3 and the case (d) estimates in Table 3.1.

The comparison is made in Fig. 3.11. The station averages for the main stem stations are computed from the individual estimates. The results are in reasonable agreement considering the difficulty in measuring denitrification fluxes (Kemp et al., 1990).

An alternate method of computing the denitrification flux is to use the observed nitrate flux, surface mass transfer coefficient, and overlying water nitrate concentration, to estimate the aerobic layer nitrate concentration. The estimate is made from the flux equation (13) so that:

$$[NO_3(1)] = \frac{J[NO_3]}{s} + [NO_3(0)] \qquad (52)$$

The anaerobic layer concentration is estimated using eq.(50) and the estimate of $J[N_2 g)]$ then follows from eq.(51) as before. The results are compared to the observations in Fig. 3.12. There is considerable scatter in the model estimates since they are based on observed ammonia and nitrate fluxes. Nevertheless, the comparison to the observations is not unreasonable.

J. Extent of Denitrification and the Nitrogen Balance

The objective of the ammonia and nitrate flux models is to compute the extent of nitrification and denitrification. The results from the model applied to the four years of data are summarized in this section for main stem and tributary SONE stations. The extent of denitrification is examined in Fig. 3.13. The source of nitrate from nitrification, $S[NO_3]$, is shown and compared to the flux of nitrate to (+) or from (-) the sediment, and the flux of nitrogen gas. For most stations, the nitrification source produces a small nitrate flux to the overlying water and a larger nitrogen gas flux. Where the nitrate flux is to the sediment (-), the nitrogen gas flux is considerably larger since overlying water nitrate is being transported to the sediment and denitrified. These stations are characterized by high overlying water nitrate concentrations.

The nitrogen balance for the SONE stations are given in Fig. 3.14. The quantity of ammonia nitrogen produced by diagenesis, J_N, is shown. A fraction is released to the overlying water as an ammonia flux, $J[NH_4]$. The remainder becomes nitrate. A portion either escapes to the

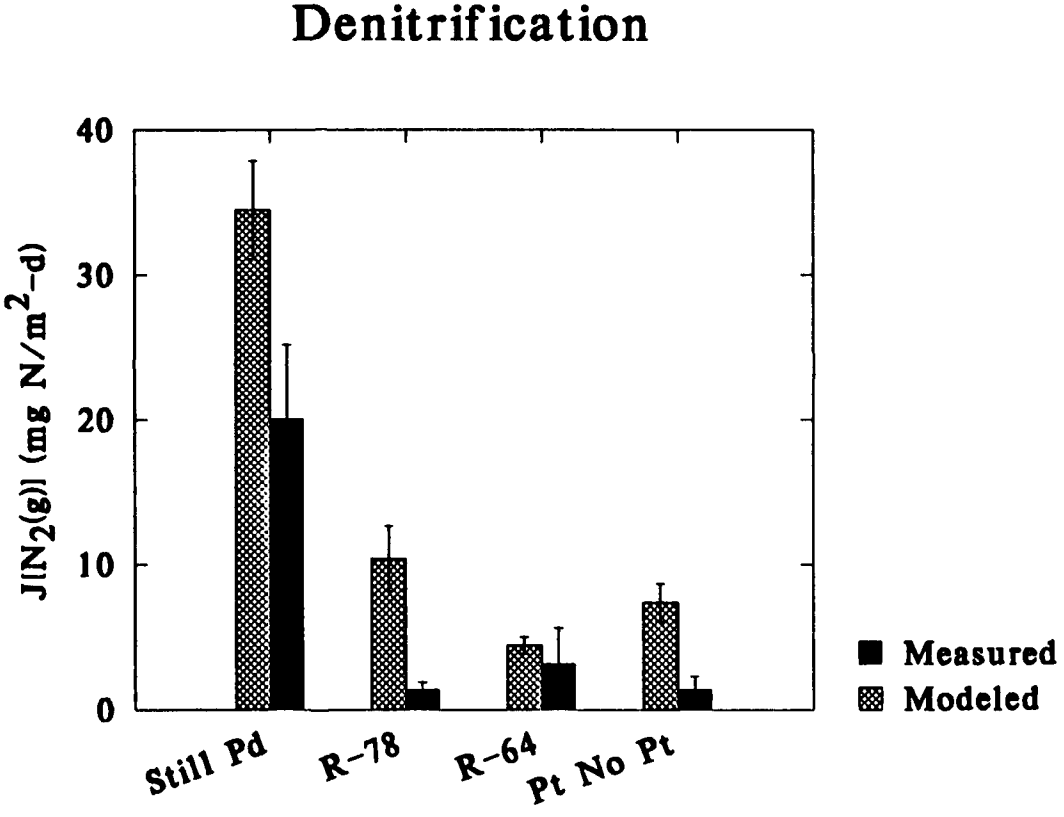

FDENIT7D

Figure 3.11

Denitrification

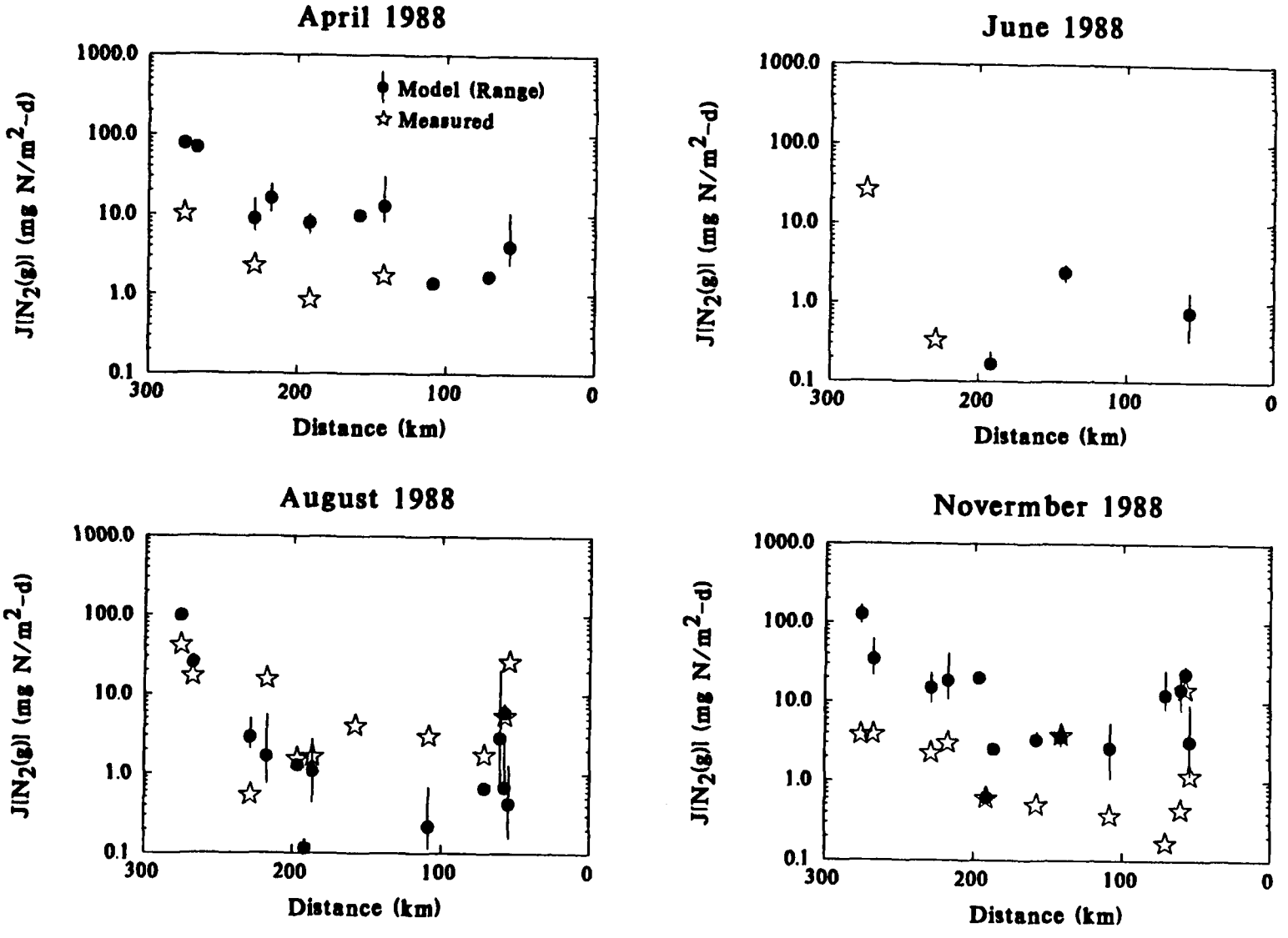

FDENIT6A

Figure 3.12

Extent of Denitrification

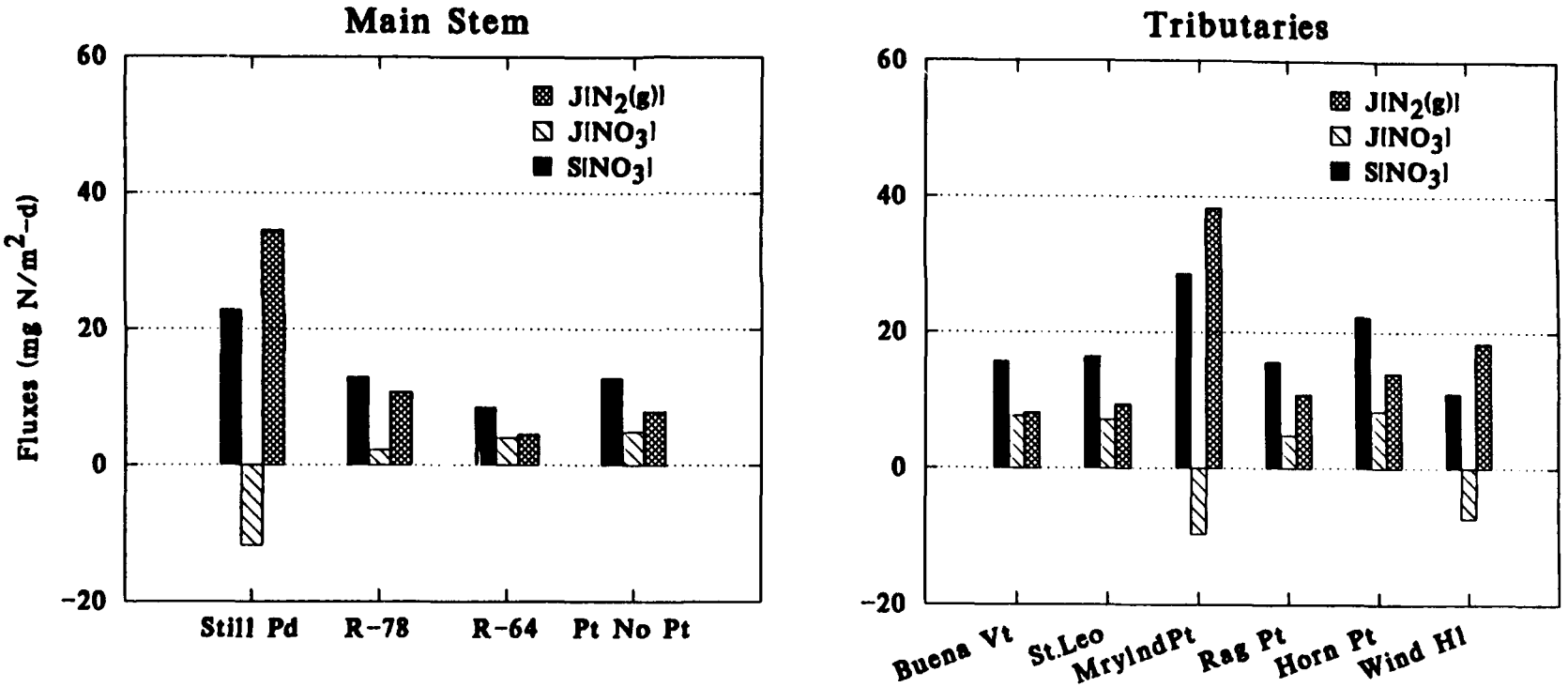

FDENITP1

Figure 3.13

Nitrogen Balance

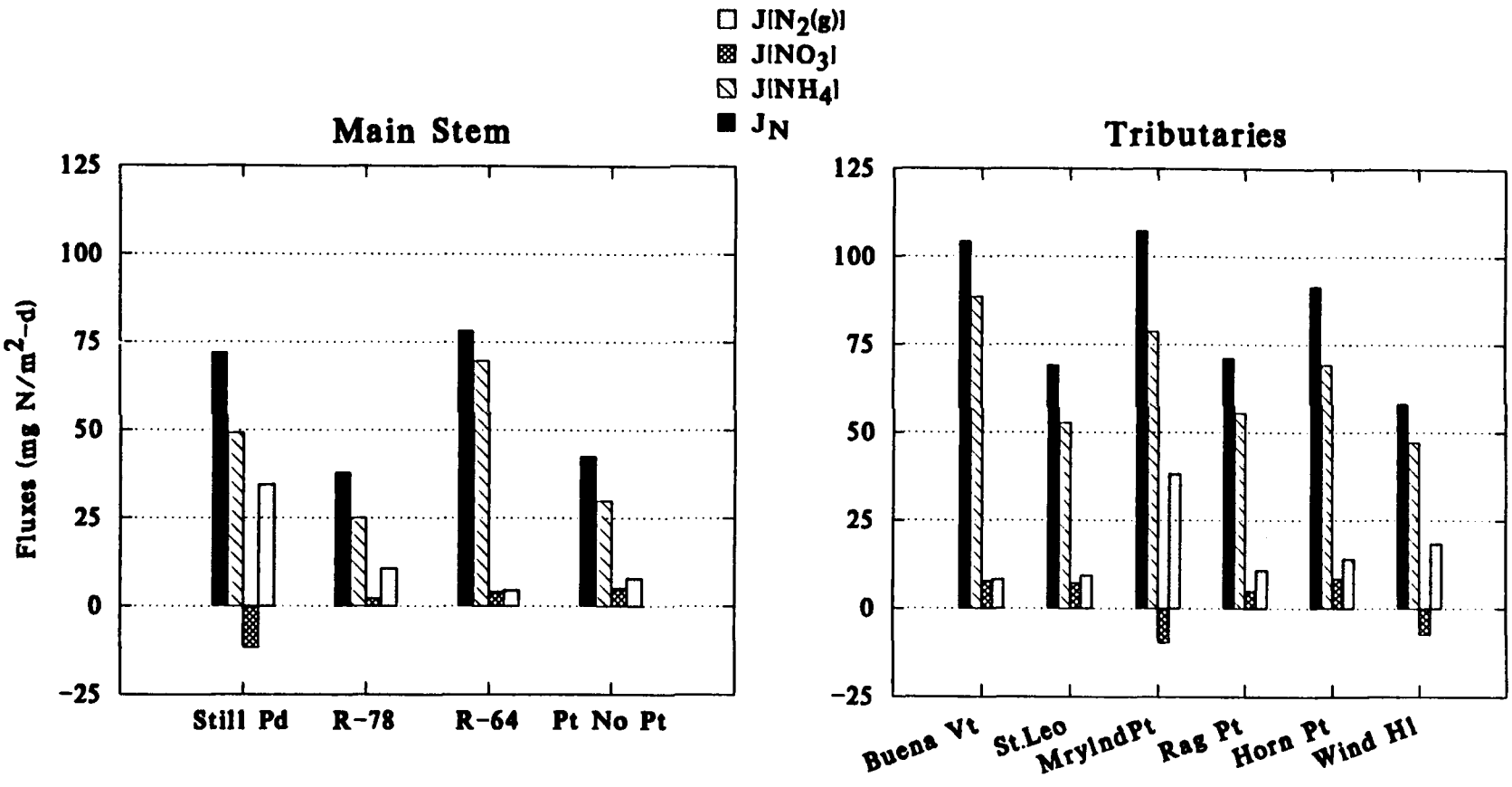

FDENITP3

Figure 3.14

overlying water, or additional nitrate is transported to the sediment, $J[NO_3]$. The quantity that remains is denitrified and a flux of nitrogen gas, $J[N_2(g)]$ results. These are all shown in Fig. 3.14.

K. Conclusions

The nitrate flux model reproduces the major features that relate the flux to the overlying water nitrate concentration, and to the surface mass transfer coefficient. This latter relationship combines the effects of mass transport and the thickness of the aerobic layer, as it does in the ammonia flux model. The surprising result is that the primary site of denitrification is in the *aerobic* layer. Mass transfer of nitrate to the anaerobic layer is insufficient for significant denitrification to occur in that layer. It is possible that this result is an artifact of the two layer segmentation. Recent measurements of vertical profiles of oxygen and nitrate in sediment pore waters indicate that the zone of nitrate reduction is below the oxic zone (Sorensen and Revsbech, 1990). However, it is difficult to reconcile this result with the results of an analysis (Di Toro et al., 1990) that without aerobic layer denitrification, substantial fluxes of nitrate to the overlying water would result.

The magnitude of the denitrification flux predicted by the model is roughly comparable to independent measurements, although as with any pointwise comparison, there is considerable scatter. For the main stem and tributary stations, 76% of ammonia diagenesis is returned as ammonia flux. The rest is either denitrified or returned as a nitrate flux. The nitrogen gas flux is 22% of the ammonia diagenesis flux, but this includes the denitrification of overlying water nitrate as well.

Table 3.2

Nitrate Model Parameters

Parameter	Symbol	(a)	(b)	(c)	(d)
Aerobic denitrification velocity	$\kappa_{NO3,1}$ (m/d)	0.0*	0.10	0.05	0.10
Anaerobic denitrification coefficient	$\kappa^{*}_{NO3,2}$ (m/d)	1.09	0.0096	0.075	0.0096
Anaerobic denitrification velocity	$\kappa_{NO3,2}$ (m/d)	-	0.25	-	0.25
Mass transfer coefficient	K_{LI2} (m/d)	-	0.01	-	0.01
Surface mass transfer coefficient (20 ℃)	s_{20} (m/d)	-	-	0.323	(e)
Surface mass transfer temperature coefficient	θ_s	-	-	1.120	(e)
Ammonia diagenesis (20 ℃)	$J_N(20)$ (mg N/m^2-d)	0.0*	66.2	77.2	(f)
Ammonia diagenesis temperature coefficient	θ_N	-	1.142	1.100	(f)

*Assigned

(a)Hunting Creek

(b)Chesapeake Bay Linear Analysis

(c)Gunston Cove

(d)Chesapeake Bay Normalized Analysis

(e) Observations are used

(f) From Table 2.2, case (c)

Table 3.3

Denitrification Parameters

Temperature coefficient	Nitrate half saturation constant	Temperature coefficient	Oxygen half saturation constant	Reference
θ_{NO3}	$K_{M,NO3}$ (mg N/L)	$\theta_{K_{M,NO3}}$	$K_{O2,NH4}$ (mg O_2/L)	
1.200	0.1	-	-	Argaman (1979)
1.070	-	-	-	Lewandoswki (1982)
1.100	3.06	-	-	Messer (1984)
1.056, 1.098, 1.074	0.98	-	0.080	Nakajima (1984)
1.086	**0.98**		**0.080**	**Median**

L. References

Argaman, Y. and Miller, E. (1979): Modeling recycled systems for biological nitrification and denitrification. J. Water Pollut. Cont. Fed. 51(4): pp. 749-758.

Billen, G. (1978): A budget of nitrogen recycling in North Sea sediments off the Belgian coast. Est. Coast. Mar. Sci. 7: pp. 127- 146.

Billen, G. (1982): An idealized model of nitrogen recycling in marine sediments. Am. J. Sci. 282: pp. 512-541.

Billen, G. (1988): Modelling benthic nitrogen cycling in temperate coastal ecosystems. In: Nitrogen Cycling in Coastal Marine Environments, pp. 341-378. Editors: T.H. Blackburn and J. Sorensen. J. Wiley & Sons. Ltd., New York.

Billen, G., Dessery, S., Lancelot, C. and Maybeck, M. (1989): Seasonal and inter-annual variations of nitrogen diagenesis in the sediments of a recently impounded basin. Biogeochemistry 8: pp. 73-100.

Blackburn, T.H. (1990): Denitrification model for marine sediment. In: Denitrification in Soil and Sediment, pp. 323-337. Editors: N.P. Revsbech and J. Sorensen. Plenum Press, New York.

Brezonik, P.L. (1977): Denitrification in natural waters. Prog. Water Technol 8: pp. 373-392.

Cerco, C.F. (1985): Effect of Temperature and Dissolved Oxygen on Sediment-Water Nutrient Flux. Virginia Inst. of Marine Science, Virginia 23062.

Cerco, C.F. (1986): Sediment Oxygen Demand in Hunting Creek. Virginia Inst. of Marine Science, Virginia, 23062.

Cerco, C.F. (1987): Effect of Mixing and Dissolved Oxygen Concentration on Sediment Oxygen Demand. Virginia Inst. of Marine Science, Virginia, 23062.

Cerco, C.F. (1988): Sediment nutrient fluxes in a tidal freshwater embayment. Water Resources Bulletin 24(3): pp. 255-260.

Di Toro, D.M., Paquin, P.R., Subburamu, K. and Gruber, D.A. (1990): Sediment Oxygen Demand Model: Methane and Ammonia Oxidation. J. Environ. Engineering ASCE 116(5): pp. 945-986.

Goloway, F. and Bender, M. (1982): Diagenetic models of interstitial nitrate profiles in deep sea suboxic sediments. Limnol. Oceanogr. 27(4): pp. 624-638.

Jahnke, R.A., Emerson, S.R. and Murray, J.W. (1982): A Model of Oxygen Reduction, Denitrification, and Organic Matter Mineralization in Marine Sediments. Limnol. Oceanogr. 27(4): pp. 610-623.

Jenkins, M.C. and Kemp, W.M. (1984): The coupling of nitrification and denitrification in two estuarine sediments. Limnol. Oceanogr. 29(3): pp. 609-610.

Jorgensen, B.B. (1977): Bacterial sulfate reduction within reduced microniches of oxidized marine sediments. Mar. Biol. 41: pp. 7- 17.

Kemp, W.M., Sampou, P., Caffrey, J., Mayer, M., Henriksen, K. and Boynton, W.R. (1990): Ammonium recycling versus denitrification in Chesapeake Bay sediments. Limnol. Oceanogr. 35(7): pp. 1545-1563.

Klapwijk, A. and Snodgrass, W.J. (1986): Biofilm Model for Nitrification, Denitrification, and Sediment Oxygen Demand in Hamilton Harbor. In: Sediment Oxygen Demand. Processes, Modeling and Measurement, pp. 75-97. Editor: K.J. Hatcher. Inst. of Nat. Res., Univ. of Georgia, Athens, Ga. 30602.

Lewandoswki, Z. (1982): Temperature dependency of biological denitrification with organic materials addition. Wat. Res. 16: pp. 19- 22.

Messer, J. and Brezonik, P. (1984): Laboratory evaluation of kinetic parameters for lake sediment denitrification models. Ecological Modeling 21: pp. 277-286.

Nakajima, M., Hayamizu, T. and Nishimura, H. (1984): Effect of oxygen concentration on the rates of denitratification and denitritification in the sediments of an eutrophic lake. Water Res. 18(3): pp. 335-338.

Sampou, P., Kemp, W.M., Cornwell, J., Rosman, L. and Owens, M. (1989): Chesapeake Bay sediment data collection program 1988/1989: Nitrogen cycling and anaerobic processes. CEES, Univ. of Maryland, Cambridge, MD.

Sorensen, J. and Revsbech, N.P. (1990): Denitrification in stream biofilm and sediment: in situ variation and control factors. In: Denitrification in Soil and Sediment, pp. 277-289. Editors: N.P. Revsbech and J. Sorensen. Plenum Press, New York.

Vanderborght, J.P., Wollast, R. and Billen, G. (1977a): Kinetic models of diagenesis in disturbed sediments. Part I. Mass transfer properties and silica diagenesis. Limnol. Oceanogr. 22(5): pp. 787-793.

Vanderborght, J.P., Wollast, R. and Billen, G. (1977b): Kinetic models of diagenesis in disturbed sediments. Part 2. Nitrogen diagenesis. Limnol. Oceanogr. 22(5): pp. 794-803.

IV. STEADY STATE MODEL

A. Introduction

This chapter presents the formulation for the general sediment flux model which will be applied in the succeeding chapters to model the fluxes of sulfide, oxygen, phosphorus, and silica. The model is structured to include both dissolved and particulate species since both are important in determining the fluxes of these chemicals. A model with similar mathematical structure, which describes water column - sediment interactions, has been formulated and analyzed (Di Toro et al., 1982). It provides the basis for the analysis presented below. Analytical solutions are obtained for steady state conditions which provide valuable insights into the behavior of the model.

1. Dissolved and Particulate Phases

An important feature of the chemicals produced by mineralization of organic matter in sediments is the extent to which they become particulate species. This distribution directly effects the magnitude of the chemical that is returned to the overlying water. Therefore, any model of sediment fluxes must include this mechanism in its formulation.

For the model developed below, the distribution of a chemical between the particulate and dissolved phases in a sediment is parameterized using a linear partitioning coefficient. The choice is made for a number of reasons. First, the resulting equations can be solved analytically which is an important aid to understanding the model's behavior. Second, linear partitioning can sometimes be a realistic description of the relationship between dissolved and particulate chemical. Finally, the general problem of computing the chemical composition of pore water would involve using a numerical chemical equilibrium model. Mass balance equations are required for the various chemicals that affect the pore water chemistry - for example hydrogen ion, carbon dioxide, and so on (e.g. Di Toro, 1976). Thermodynamic data are required for the relevant

aqueous complexes, stable and meta-stable mineral phases, some of which are uncertain. Finally, sorption as well as precipitation reactions need to be considered. All this is necessary to compute the fraction of a chemical that is either dissolved or particulate.

The equivalent partitioning model employs only a partition coefficient, the ratio of particulate to dissolved chemical concentration. If necessary, it can be varied as a function of other physical and chemical parameters in order to produce more realistic behavior. The practical question is: does the added difficulty of including equilibrium chemistry into the model structure result in added realism? Whatever the answer, it is prudent to begin the modeling using linear partitioning and examine the utility of the results.

2. Particle Mixing

The inclusion of particulate as well as dissolved species requires that the transport of particulate species be considered. The rate of mixing in the sediment is formulated using a particle mixing velocity. This is equivalent to representing particle mixing using a diffusion model. More elaborate models have been proposed (Robbins, 1986; Boudreau, 1986) which mimic more directly the mixing activity of benthic organisms. However, as with the choice a model for chemical partitioning, simple diffusion appears to be a reasonable first step.

B. Modeling Framework

The diagram in Fig. 4.1 presents the framework and defines the variables used in the model. The total concentrations (the sum of the dissolved and particulate species) in layer 1 and 2 are C_{T1} and C_{T2} respectively. The sources of chemical are denoted by J_{T1} and J_{T2}, the areal production rate in the aerobic and anaerobic layers, respectively. The fractions of the total concentration that is dissolved, f_d, and particulate, f_p, in layer 1 and 2 are specified by f_{d1}, f_{d2}, and, f_{p1}, f_{p2}, respectively. These fractions depend on the solids concentration and partition coefficients, as shown below.

The removal reactions in layer 1 and 2 are first order with rate constants: K_1 and K_2. The mass transport of dissolved chemical between layer 1 and 2 is via diffusion which is parameterized by a mass transfer coefficient, K_{L12}, as before. The mixing of particles between layers 1 and 2 due to physical and biological mechanisms is parameterized by a mixing velocity, w_{12}, which has the same units as the mass transfer coefficient. Burial from layer 1 to layer 2 and out of layer 2 occurs at the sedimentation velocity, w_2. Finally, the magnitude of the flux of dissolved chemical into or out of the sediment from the overlying water is determined by the surface mass transfer coefficient, K_{L01}.

C. Mass Balance Equations

The mass balance equations for this model are formulated on the basis of the total chemical concentration. For the transport coefficients that affect only the dissolved or particulate chemical, the total concentration is multiplied by the fractions dissolved or particulate. Equations written in this form assume local equilibrium for the partitioning reaction.

The mass balance equations for layer 1 and 2 are:

$$H_1\frac{dC_{T1}}{dt} = -K_1H_1C_{T1} + K_{L01}(f_{d0}C_{T0} - f_{d1}C_{T1}) + w_{12}(f_{p2}C_{T2} - f_{p1}C_{T1}) + K_{L12}(f_{d2}C_{T2} - f_{d1}C_{T1}) - w_2C_{T1} + J_{T1} \quad (1)$$

$$H_2\frac{dC_{T2}}{dt} = -K_2H_2C_{T2} - w_{12}(f_{p2}C_{T2} - f_{p1}C_{T1}) - K_{L12}(f_{d2}C_{T2} - f_{d1}C_{T1}) + w_2(C_{T1} - C_{T2}) + J_{T2} \quad (2)$$

The terms in eq.(1) represent, respectively, the removal of chemical by reaction, the exchange of dissolved chemical between layer 1 and the overlying water (layer 0), the exchange of particulate

chemical between layers 1 and 2 via particle mixing, the exchange of dissolved chemical between layers 1 and 2 via diffusive transport, the loss of both dissolved and particulate chemical by burial into layer 2, and the source of chemical to layer 1.

The terms in eq.(2) represent, respectively, the removal of chemical by reaction, the exchange of particulate and dissolved chemical between layers 1 and 2, the gain of chemical from layer 1 and the loss of chemical from layer 2 by burial, and the source of chemical to layer 2. Note that the dissolved and particulate exchange terms have the opposite signs in layers 1 and 2. The reason is that the transport of chemical from layer 1 is a sink in that layer and a source to layer 2, and vise-versa.

The dissolved, f_d, and particulate, f_p, fractions are computed from the partitioning equations:

$$f_{d1} = \frac{1}{1 + m_1 \pi_1} \qquad f_{p1} = 1 - f_{d1} \tag{3}$$

$$f_{d2} = \frac{1}{1 + m_2 \pi_2} \qquad f_{p2} = 1 - f_{d2} \tag{4}$$

where the solids concentrations are m_1, and m_2, and the partition coefficients are π_1 and π_2 respectively. Note that it is the solids concentration - partition coefficient products: $m_1 \pi_1$ and $m_2 \pi_2$ that determine the extent of partitioning. The concentrations of dissolved and particulate chemical are obtained as products of these fractions and the total concentrations, C_{T1} and C_{T2}.

D. Solution - Anaerobic Layer Source

The analytical solutions for these equations are presented in two parts. First, the solution is found for only a source in the anaerobic layer. Then, only the sources to the aerobic layer are considered. Since these equations are linear, the complete solution is the sum of the solutions for the individual sources. This procedure simplifies the derivation and the form of the solutions.

The mass balance equation for layer 1 without the source terms is:

$$H_1 \frac{dC_{T1}}{dt} = -K_1 H_1 C_{T1} - K_{L01} f_{d1} C_{T1} + w_{12}(f_{p2} C_{T2} - f_{p1} C_{T1}) + K_{L12}(f_{d2} C_{T2} - f_{d1} C_{T1}) - w_2 C_{T1} \quad (5)$$

The steady state solutions to eq.(2) and (5) are found by setting the time derivatives to zero and adding the equations:

$$0 = -K_{T1} H_1 C_{T1} - (K_2 H_2 + w_2) C_{T2} + J_{T2} \quad (6)$$

where K_{T1} is defined as the total first order removal rate constant in layer 1:

$$K_{T1} H_1 = K_1 H_1 + K_{L01} f_{d1} \quad (7)$$

The overall mass balance equation (6) contains fewer terms because the internal mass transport terms cancel out. Only the source and removal terms remain - the terms that represent sources to or removal from the entire active sediment layer. Eq.(6) can be solved for C_{T2} to yield:

$$C_{T2} = \frac{J_{T2}}{K_2 H_2 + w_2 + K_{T1} H_1 \frac{C_{T1}}{C_{T2}}} \quad (8)$$

The ratio: C_{T1}/C_{T2} which is denoted by r_{12}, can be found by solving eq.(5) at steady state:

$$r_{12} = \frac{C_{T1}}{C_{T2}} = \frac{w_{12} f_{p2} + K_{L12} f_{d2}}{w_2 + w_{12} f_{p1} + K_{L12} f_{d1} + K_{T1} H_1} \quad (9)$$

This definition of r_{12} is slightly different from that used in the previous analysis of this model, (Di Toro et al., 1982), but the idea is the same. Note that r_{12} is a function only of the reaction and transport parameters of the model. Hence, from an algebraic point of view, it is a known quantity. Thus, the anaerobic layer concentration , eq.(8), can be rewritten using this quantity:

$$C_{T2} = \frac{J_{T2}}{K_2 H_2 + w_2 + K_{T1} H_1 r_{12}} \tag{10}$$

Finally eq.(6) can be solved for the aerobic layer concentration:

$$C_{T1} = \frac{J_{T2}}{K_{T1} H_1 + (K_2 H_2 + w_2) r_{21}} \tag{11}$$

where:

$$r_{21} = r_{12}^{-1} \tag{12}$$

The simplicity of this solution, which is due to the lack of source terms in the aerobic layer equation - compare eq.(1) to eq.(5) - is the motivation for considering these source terms separately.

1. Concentration Ratio

The role of r_{12} and r_{21} in these solutions can be explained as follows. In eq.(10) for C_{T2}, the layer 2 sinks, $K_2 H_2$ and w_2, are applied directly to the denominator of the solution. The layer 1 sinks, $K_{T1} H_1$, are modified by $r_{12} = C_{T1}/C_{T2}$ so that they are applied to the equivalent layer 1 concentration. Since r_{12} is determined only by the parameters of the model, it can be viewed as a known quantity rather than the ratio of the two unknown concentrations. The inverse of this ratio, r_{21}, plays the same role in the solution for C_{T1} in eq.(11).

These ratios are the only place where the layer 1 - 2 mixing and partitioning parameters appear. An interesting special case occurs if the partitioning parameters are equal in both layers: $f_{p1} = f_{p2}$ which implies that $f_{d1} = f_{d2}$. In addition, if the layer mixing parameters are large relative to the reaction and burial terms: $w_{12} f_{p2} + K_{L12} f_{d2} \gg w_2 + K_{T1} H_1$, then:

$$r_{12} = \frac{C_{T1}}{C_{T2}} = \frac{w_{12} f_{p2} + K_{L12} f_{d2}}{w_2 + w_{12} f_{p1} + K_{L12} f_{d1} + K_{T1} H_1} \rightarrow 1 \qquad (13)$$

That is, the mixing - either particle mixing or dissolved phase mixing - equalizes the concentrations in the two layers.

2. Final Form

For the sake of completeness the method for evaluating the aerobic layer reaction rate - depth product: $K_{T1} H_1$, discussed in Chapter II and III, is repeated here. The surface mass transfer coefficient, K_{L01}, and the depth of the aerobic zone, H_1, are evaluated using the ratio of the sediment oxygen demand and the overlying water oxygen concentration:

$$K_{L01} = \frac{SOD}{[O_2(0)]} = s \qquad (14)$$

$$H_1 = D_1 \frac{[O_2(0)]}{SOD} = \frac{D_1}{s} \qquad (15)$$

The definitions of the reaction velocities follows the convention established for ammonia and nitrate reactions:

$$\kappa_1 = \sqrt{D_1 K_1} \qquad (16)$$

$$\kappa_2 = K_2 H_2 \qquad (17)$$

Hence, the term $K_{T1} H_1$, eq.(7), becomes:

$$K_{T1} H_1 = \frac{\kappa_1^2}{s} + s f_{d1} \qquad (18)$$

The total concentrations in layers 1 and 2 become:

$$C_{T1} = \frac{J_{T2}}{\frac{\kappa_1^2}{s} + s f_{d1} + (\kappa_2 + w_2) r_{21}} \tag{19}$$

$$C_{T2} = \frac{J_{T2}}{\left(\frac{\kappa_1^2}{s} + s f_{d1}\right) r_{12} + \kappa_2 + w_2} \tag{20}$$

The flux of chemical to the overlying water - not the net flux which would also include the flux from the overlying water to the sediment - is:

$$J_{aq} = s f_{d1} C_{T1} = J_{T2} \frac{s f_{d1}}{\frac{\kappa_1^2}{s} + s f_{d1} + (\kappa_2 + w_2) r_{21}} \tag{21}$$

It is convenient to define the flux reacted in layer 2, $J_{re,2} = \kappa_2 C_{T2}$, and the burial flux, $J_{br} = w_2 C_{T2}$. These can be calculated using eq.(20) for the concentration C_{T2}:

$$J_{re,2} = \kappa_2 C_{T2} = \kappa_2 r_{21} C_{T1}$$

$$= J_{T2} \frac{\kappa_2 r_{21}}{\frac{\kappa_1^2}{s} + s f_{d1} + (\kappa_2 + w_2) r_{21}} \tag{22}$$

$$J_{br} = w_2 C_{T2} = w_2 r_{21} C_{T1}$$

$$= J_{T2} \frac{w_2 r_{21}}{\frac{\kappa_1^2}{s} + s f_{d1} + (\kappa_2 + w_2) r_{21}} \tag{23}$$

The terms in these equations suggest the definition of the following mass transfers and equivalent reaction velocity expressions:

$$f r_{re,1} = \frac{\kappa_1^2}{s} \tag{24}$$

$$fr_{aq} = s f_{d1} \tag{25}$$

$$fr_{re,2} = \kappa_2 r_{21} \tag{26}$$

and:

$$fr_{br} = w_2 r_{21} \tag{27}$$

These mass transfer and reaction velocities correspond to the reaction in layer 1, diffusion to the overlying water, reaction in layer 2, and burial, respectively. When compared one to another, they can be thought of as the fraction of total diagenesis that is routed to each of the pathways. Using these definitions, eqs. (21-23) can be expressed as:

$$J_{aq} = J_{T2} \frac{fr_{aq}}{fr_{re,1} + fr_{aq} + fr_{re,2} + fr_{br}} \tag{28}$$

$$J_{re,2} = J_{T2} \frac{fr_{re,2}}{fr_{re,1} + fr_{aq} + fr_{re,2} + fr_{br}} \tag{29}$$

and:

$$J_{br} = J_{T2} \frac{fr_{br}}{fr_{re,1} + fr_{aq} + fr_{re,2} + fr_{br}} \tag{30}$$

The final flux, which is the chemical that is reacted in layer 1, follows as the difference between the diagenesis flux and the loss via diffusion to the overlying water, layer 2 reaction, and burial:

$$J_{re,1} = J_{T2} - J_{aq} - J_{re,2} - J_{br} \tag{31}$$

so that:

$$J_{re.1} = J_{T2}\frac{fr_{re.1}}{fr_{re.1} + fr_{aq} + fr_{re.2} + fr_{br}} \qquad (32)$$

3. Properties

The general behavior of the steady state version of the model can be deduced from the form of these equations. The diagenesis flux is apportioned between the four removal processes: reaction in layers 1 and 2; flux to the overlying water, and burial from layer 2. The relative magnitudes of the mass transfer and reaction velocity parameters, eqs.(24-27), determine the magnitude of each of these terminal sinks. It is important to realize that, since the model is based on a mass balance, there is no other possible behavior. The chemical produced by diagenesis must exit to one of these sinks.

The parameters in the model are the reaction velocities in layer 1 and 2: κ_1 and κ_2; the mass transfer coefficients for layer 1 - layer 2 dissolved and particulate mixing: K_{L12} and ω_{12}; the partition coefficients in the two layers, π_1 and π_2; and the sedimentation velocity, ω_2. Estimates of the parameters and the behavior of the model are examined in the next chapters where it is applied to sulfide, phosphorus, and silica.

E. Aerobic Layer Source

The sources to the aerobic layer: the diffusive exchange source from the overlying water to the sediment, $K_{L01} f_{d0} C_{T0}$, and the diagenesis source, J_{T1}, are combined into a single source term:

$$J_{Tot.1} = J_{T1} + K_{L01} f_{d0} C_{T0} \qquad (33)$$

The steady state solution is found as before by setting the time derivatives to zero and adding the aerobic and anaerobic layer equations (1) and (2), with $J_{T2} = 0$:

$$0 = -K_{T1} H_1 C_{T1} - (K_2 H_2 + \omega_2) C_{T2} + J_{Tot.1} \qquad (34)$$

This equation can be solved for C_{T1} to yield:

$$C_{T1} = \frac{J_{Tot,1}}{K_{T1}H_1 + (K_2H_2 + w_2)\frac{C_{T2}}{C_{T1}}} \tag{35}$$

The ratio: C_{T2}/C_{T1} which will be denoted by r^*_{21}, to distinguish it from r_{21}, eq.(12), can be found by solving eq.(2) with $J_{T2} = 0$ at steady state:

$$r^*_{21} = \frac{C_{T2}}{C_{T1}} = \frac{w_{12}f_{p1} + K_{L12}f_{d1} + w_2}{w_{12}f_{p2} + K_{L12}f_{d2} + w_2 + K_2H_2} \tag{36}$$

Thus the aerobic layer concentration is:

$$C_{T1} = \frac{J_{Tot,1}}{K_{T1}H_1 + (K_2H_2 + w_2)r^*_{21}} \tag{37}$$

Eq.(34) can be solved for the anaerobic layer concentration:

$$C_{T2} = \frac{J_{Tot,1}}{(K_{T1}H_1)r^*_{12} + K_2H_2 + w_2} \tag{38}$$

where:

$$r^*_{12} = (r^*_{21})^{-1} \tag{39}$$

1. Comparisons

The solutions for the source in the aerobic and anaerobic layer are quite similar. In fact, it might be suspected that the solutions for the source in layer 1 can be derived from the layer 2 source solutions by an interchange of the corresponding terms in layers 1 and 2. This can be checked by comparing the solutions in the layer receiving the source term: eq.(37) to eq.(10).

$$C_{T1} = \frac{J_{Tot.1}}{K_{T1}H_1 + (K_2H_2 + w_2)r^*_{21}} \tag{40}$$

$$C_{T2} = \frac{J_{T2}}{K_2H_2 + w_2 + K_{T1}H_1 r_{12}} \tag{41}$$

The solutions would be identical with the replacement: $K_2H_2 + w_2 \leftrightarrow K_{T1}H_1$. However, it is also necessary that $r^*_{21} = r_{12}$ with $1 \leftrightarrow 2$. That this is not the case can be seen by inspection:

$$r^*_{21} = \frac{w_{12}f_{p1} + K_{L12}f_{d1} + w_2}{w_{12}f_{p2} + K_{L12}f_{d2} + w_2 + K_2H_2} \tag{42}$$

$$r_{12} = \frac{w_{12}f_{p2} + K_{L12}f_{d2}}{w_{12}f_{p1} + K_{L12}f_{d1} + w_2 + K_{T1}H_1} \tag{43}$$

The internal mixing is completely symmetric - the loss to the overlying water in layer 1 is equivalent to loss from layer 2 by burial. However, the burial flux between layers 1 and 2 is not symmetric. It is a unidirectional advective flux from layer 1 to layer 2. The consequence is reflected in the difference between r^*_{21} and r_{12}: the appearance of w_2 in the numerator of r^*_{21}.

A more practical question is: does the location of the source term have any significant effect on the concentrations? This can be examined by comparing the layer 1 solutions for both cases:

$$C_{T1} = \frac{J_{Tot.1}}{K_{T1}H_1 + (K_2H_2 + w_2)r^*_{21}} \tag{44}$$

$$C_{T1} = \frac{J_{T2}}{K_{T1}H_1 + (K_2H_2 + w_2)r_{21}} \tag{45}$$

The concentration ratios are:

$$r_{21}^{*} = \frac{w_{12} f_{p1} + K_{L12} f_{d1} + w_2}{w_{12} f_{p2} + K_{L12} f_{d2} + w_2 + K_2 H_2} \tag{46}$$

$$r_{21} = \frac{w_{12} f_{p1} + K_{L12} f_{d1} + w_2 + K_{T1} H_1}{w_{12} f_{p2} + K_{L12} f_{d2}} \tag{45}$$

which are not the same. However, for the case when the mixing terms are large relative to the reaction rate terms and the sedimentation velocity, $r_{21}^{*} \approx r_{21} \approx 1$, and the solutions are identical. Therefore, for this special case, sources into either layer can be treated as though they were sources into the other layer. This simplification will be used subsequently in the application of the model to phosphorus and silica.

F. References

Boudreau, B.P. (1986): Mathematics of tracer mixing in sediments: II. Nonlocal mixing and biological conveyor-belt phenomena. Am. J. Sci. 286: pp. 199-238.

Di Toro, D.M. (1976): Combining chemical equilibrium and phytoplankton models - a general methodology. In: Modeling Biochemical Processes in Aquatic Ecosystems, pp. 233-256. Editor: R. Canale. Ann Arbor Science Press, Ann Arbor, Mich.

Di Toro, D.M., O'Connor, D.J., Thomann, R.V. and St. John, J.P. (1982): Simplified model of the fate of partitioning chemicals in lakes and streams. In: Modeling the Fate of Chemicals in the Environment, pp. 165-190. Editors: K.L. Dickson, A.W. Maki and J. Cairns Jr. Ann Arbor Science Publications, Ann Arbor, MI.

Robbins, J.A. (1986): A model for particle-selective transport of tracers in sediments with conveyor belt deposit feeders. J. Geophysical Res. 91(c7): pp. 8542-8558.

V. SULFIDE AND OXYGEN

A. Introduction

This chapter presents a model of sulfide production and oxygen consumption. The equations for the general model developed in the previous chapter are applied to the sulfide distribution is sediments. Previous models of sediment oxygen demand have been reviewed (Di Toro et al., 1990). This model focuses on the formation and oxidation of sulfide as the principle end product of carbon diagenesis.

B. Sulfide Production

The sediment oxygen demand in marine waters is directly coupled to the production of sulfide as the end product of sulfate reduction (Jorgensen, 1977; Jorgensen, 1982; Howarth and Jorgensen, 1984; Jorgensen et al., 1983; Jorgensen and Revsbech, 1990). The electrons liberated by carbon diagenesis are primarily accepted by sulfate which is reduced to sulfide. The reaction is(2) :

$$2CH_2O + H_2SO_4 \rightarrow 2CO_2 + H_2S + 2H_2O \qquad (1)$$

The dissolved sulfide that is produced reacts with the iron in the sediment to form particulate iron sulfide (Morse et al., 1987). Therefore, the model must distinguish between the solid and dissolved sulfide phases. The situation is illustrated in Fig. 5.1. Sulfide is produced in the anaerobic zone where a portion of it precipitates as iron monosulfide, FeS(s). The remaining dissolved sulfide diffuses into the aerobic zone where it is oxidized to sulfate, consuming oxygen in the process. If the overlying water DO is low, then the dissolved sulfide is not completely oxidized

---

(2) The redox reaction is written in terms of uncharged species in order to properly balance the electron stoichiometry. A more realistic reaction, which applies at the pH of pore water is :
$2CH_2O + SO_4^{=} \rightarrow 2HCO_3^{-} + HS^{-} + H^{+} + 2H_2O$

and sulfide can diffuse into the overlying water. The particulate sulfide is also mixed into the aerobic zone where it can be oxidized to ferric oxyhydroxide, $Fe_2O_3(s)$, consuming oxygen. Finally FeS(s) can be buried by sedimentation.

These are the only pathways for the reduced end products of carbon diagenesis considered in this model. Therefore, the model apportions the end products of carbon diagenesis to the oxidation of sulfide, diffusion of sulfide to the overlying water, and burial. The possibility of the formation of methane gas and its escape is not included. Actually, only the escape of methane has been excluded from consideration. Carbon diagenesis can produce methane in the deeper part of the sediment. However, if it does not escape as methane bubbles, it diffuses into the zone of sulfate reduction. Since no appreciable concentrations of dissolved methane are found in this zone (Barnes and Goldberg, 1976; Martens and Berner, 1977; Reeburgh and Heggie, 1974), the methane must be oxidized and sulfate, as the terminal electron acceptor, is reduced to sulfide. Therefore, the end result of carbon diagenesis is the production sulfide as indicated in eq.(1).

C. Sulfide Oxidation

Both dissolved and particulate sulfide are oxidized in the aerobic layer. Therefore, dissolved and particulate sulfide reaction velocities are required. The reaction rates are linear in sulfide and are either a linear or a fractional power of the oxygen concentration (Almegren, 1974; Millero, 1991; Millero et al., 1987; Morse et al., 1987; Nelson, 1978; O'Brien, 1977; Wilmot, 1988; Zhang, 1991). A linear dependency is adopted (Cline and Richards, 1969; Millero, 1986; Boudreau, 1991). A constant, $K_{M.H2S.O2}$, is used to scale the overlying water oxygen concentration. It is included for convenience only. At $[O_2(0)] = K_{M.H2S.O2}$ the sulfide oxidation reaction velocity is at its nominal value. Hence the aerobic reaction rate depth product is:

$$K_1 H_1 = (k_{H2S.dl} f_{dl} + k_{H2S.pl} f_{pl}) \theta_{H2S}^{(T-20)} \frac{[O_2(1)]}{K_{M.H2S.O2}} H_1 \qquad (2)$$

SULFIDE FLUX MODEL

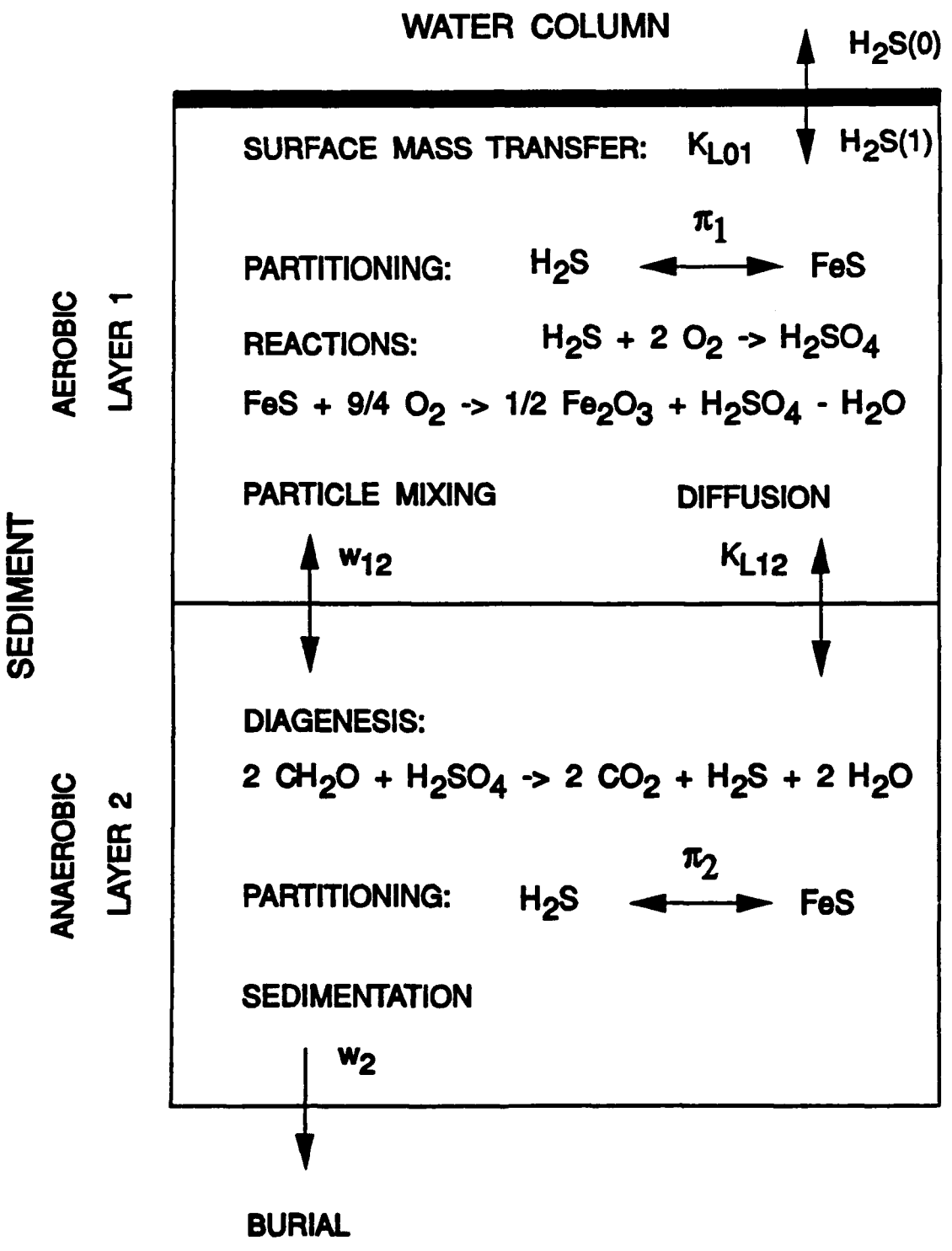

CHAP51L

Figure 5.1

where $k_{H2S.dl}$ and $k_{H2S.pl}$ are the reaction rate constants for dissolved and particulate oxidation, respectively. The equivalent reaction velocities are:

$$\kappa_{H2S.dl} = \sqrt{D_1 k_{H2S.dl}} \tag{3}$$

$$\kappa_{H2S.pl} = \sqrt{D_1 k_{H2S.pl}} \tag{4}$$

so that the fraction reacted in layer 1, $fr_{re.1}$, which will be denoted by fr_{ox}, is:

$$fr_{ox} = \frac{(\kappa^2_{H2S.dl} f_{dl} + \kappa^2_{H2S.pl} f_{pl})\theta^{(T-20)}_{H2S}}{s} \frac{[O_2(1)]}{K_{M.H2S.O2}}$$

$$= \frac{(\kappa^2_{H2S.dl} f_{dl} + \kappa^2_{H2S.pl} f_{pl})\theta^{(T-20)}_{H2S}}{s} \frac{[O_2(0)]}{2K_{M.H2S.O2}} \tag{5}$$

where the relationship: $O_2(1) = O_2(0)/2$, eq.(II-23), relates the aerobic layer oxygen concentration to the overlying water.

D. Solutions

The flux of sulfide oxidized in layer 1, J_{ox}, is found using eq.(IV-32):

$$J_{ox} = J_{re.1} = J_{T2} \frac{fr_{re.1}}{fr_{re.1} + fr_{aq} + fr_{br}} \tag{6}$$

The diffusion and burial fluxes are given by eqs. (IV-28) and (IV-30).

$$J_{aq} = J_{T2} \frac{fr_{aq}}{fr_{re.1} + fr_{aq} + fr_{br}} \tag{7}$$

$$J_{br} = J_{T2} \frac{fr_{br}}{fr_{re.1} + fr_{aq} + fr_{br}} \tag{8}$$

E. Flux Apportionment

The distribution of carbon diagenesis among the various pathways is controlled by the magnitude of the sulfide partition coefficients and the oxidation reaction velocities. The partition coefficients determine the fraction of sulfide that is either in the dissolved or particulate fraction of the sediment. An example which illustrates the importance of the extent of partitioning of sulfide into a solid phase is shown in Fig. 5.2A. This is a cumulative plot of the proportion of carbon diagenesis that is either oxidized in the aerobic zone via sulfide oxidation, J_{ox}, the diffusive flux of sulfide to the overlying water, J_{aq}, and the burial flux, J_{br}. The parameters used in the computation are listed in Table 5.1. These coefficients are justified subsequently. For this example only dissolved sulfide is allowed to oxidize. For low partition coefficients, $\pi_1 = \pi_2 < 10^3$ L/kg, the burial is insignificant and only SOD and diffusive flux are important (Fig. 5.2A). As the partition coefficient increases the SOD and diffusive flux decrease and the burial flux increases. This is a consequence of the decrease in dissolved sulfide concentration so that less is available either for oxidation or for escape as an aqueous flux. Since there is no particulate oxidation, the only remaining possibility is loss by burial.

Fig. 5.2B illustrates the behavior of the fluxes at a fixed partition coefficient (10^4 L/kg) as a function of overlying water DO concentration, $O_2(0)$. As DO decreases the oxygen flux decreases and both the diffusive flux and the burial flux increase. The reason is that as the oxygen concentration decreases the oxidation rate and, therefore the flux of oxygen to the sediment decreases. As a consequence, the dissolved sulfide concentration increases. The result is that the aqueous flux of sulfide increases. The increased dissolved sulfide concentration also causes an increase in the particulate sulfide concentration - the ratio is the constant partition coefficient - which increases the loss of sulfide by burial.

The effect of increasing the oxidation rate of particulate sulfide is illustrated in Fig. 5.2C,D. A small particulate reaction velocity (Fig. 5.2C) increases the oxygen flux but the effect of lowering

Flux Apportionment

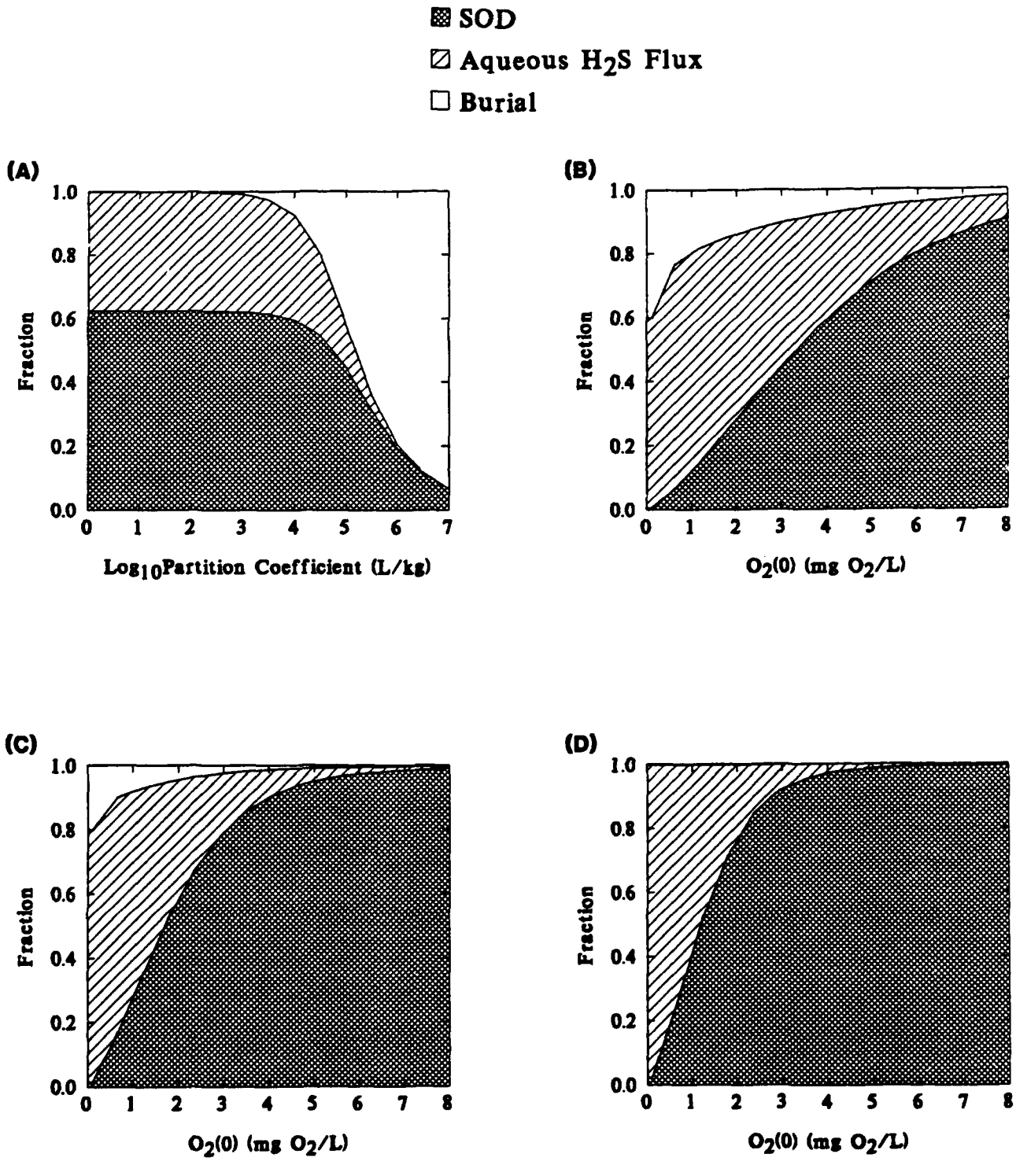

CHSOD2

Figure 5.2

overlying water DO is similar to that in the above example. Further increasing the particulate sulfide oxidation velocity (Fig. 5.2D) increases the oxidation flux until quite low DO, when the aqueous flux begins. For this case the burial flux is small enough to be negligible.

F. Sediment Oxygen Demand

Sediment oxygen demand is the common term for the flux of oxygen to the sediment. By convention, it is a positive number. The convention used in this report is that positive fluxes are from the sediment to the overlying water. Therefore, $SOD = -J[O_2]$. The flux of oxygen to the sediment is the result of the oxidation reactions in the aerobic layer. These reactions are presented below.

1. Sulfide Oxidation

The oxygen consumed by the oxidation of sulfide is one component of the total oxygen flux to the sediments. Carbon diagenesis, J_C, produces sulfide via the reaction given in eq.(1). If oxygen equivalents, denoted by O_2^*, are adopted as the units for sulfide concentrations and fluxes, then the stoichiometric coefficient relating the flux of carbon diagenesis and sulfide production is: $J_{T2} = \alpha_{O2,H2S} J_C$, where $\alpha_{O2,H2S} = 2.67$ (mg O_2^*/mg C). The oxygen flux that results from the oxidation of sulfide is:

$$J_{ox} = \alpha_{O2,H2S} J_C \frac{fr_{ox}}{fr_{ox} + fr_{aq} + fr_{br}} = CSOD \qquad (9)$$

Since the source of this oxygen flux is carbon diagenesis, it can be termed the carbonaceous sediment oxygen demand, CSOD.

2. Ammonia Oxidation and Denitrification

Oxygen is also consumed as a result of the oxidation of NH_4 to NO_3. The stoichiometry is $\alpha_{O2.NH4}$ = 4.57 gm O_2 / gm N. The quantity of ammonia that is nitrified is equal to the quantity of nitrate produced: $S[NO_3]$. It can be calculated by evaluating the nitrification sink term in the mass balance equation (II-1):

$$S[NO_3] = K_{NH4,1}[NH_4(1)] = \frac{\kappa^2_{NH4,1}}{s}\theta^{(T-20)}_{NH4}[NH_4(1)] \qquad (10)$$

where $[NH_4(1)]$ is given by eq.(II-18). The equivalent term for Michaelis Menton kinetics is:

$$S[NO_3] = \left(\frac{K_{M,NH4}}{K_{M,NH4} + [NH_4(1)]}\right)\left(\frac{[O_2(0)]}{2K_{O2,NH4} + [O_2(0)]}\right) \cdot \frac{\kappa^2_{NH4,1}}{s}\theta^{(T-20)}_{NH4}[NH_4(1)] \qquad (11)$$

where $[NH_4(1)]$ is given by the solution of eq.(II-22). The oxygen consumed by nitrification is can be termed the nitrogenous sediment oxygen demand, NSOD:

$$NSOD = \alpha_{O2,NH4} S[NO_3] \qquad (12)$$

The SOD of the sediment is the sum of the CSOD and NSOD:

$$SOD = CSOD + NSOD \qquad (13)$$

3. Carbon Requirement for Denitrification

A final issue needs to be addressed. The denitrification of nitrate to nitrogen gas requires a carbon source. The reaction is:

$$\frac{10}{8}CH_2O + HNO_3 \rightarrow \frac{10}{8}CO_2 + \frac{1}{2}N_2(g) + \frac{7}{4}H_2O \qquad (14)$$

and the carbon to nitrogen stoichiometric coefficient is α_{C,N_2} = 10/8 (mol C/mol N) = 1.25 (gm C/gm N). This requirement must be satisfied from carbon diagenesis since it is the only source of reactive carbon. Hence, the carbon diagenesis that reacts to form sulfide is that which remains: $J_C - \alpha_{C,N_2} J[N_2(g)]$.

The rate of denitrification is equal to the flux of nitrogen gas, $J[N_2(g)]$, which can be calculated by evaluating the denitrification sink term in the mass balance equation (III-1, III-2). The result, which is equivalent to the rate at which nitrogen gas is produced, eq.(III-46) is:

$$J[N_2(g)] = -K_{NO3,1}H_1[NO_3(1)] + K_{NO3,2}H_2[NO_3(2)]$$

$$= \frac{\kappa^2_{NO3,1}}{s}[NO_3(1)] + \kappa_{NO3,2}[NO_3(2)] \qquad (15)$$

where $[NO_3(1)]$ and $[NO_3(2)]$ are given by eqs. (III-3, III-4).

4. Final Equation

The equation for SOD is made up of the sum of the carbonaceous and nitrogenous components, with the former corrected for the denitrification sink of carbon diagenesis:

$$SOD = \alpha_{O2,H2S}(J_C - \alpha_{C,N_2}J[N_2(g)])\frac{fr_{ox}(s)}{fr_{ox}(s) + fr_{aq}(s) + fr_{br}(s)} + NSOD \qquad (16)$$

This nonlinear equation can be solved for SOD. The nonlinearity arises from the fact that the right hand side of the equation contains terms that are functions of $s = SOD/[O_2(0)]$ so that SOD appears on both sides of the equation. This problem is easily solved using standard root finding algorithms such as successive substitution (Di Toro et al., 1990). The remaining fluxes follow from the above equations.

G. Data Analysis

A commonly used technique to analyze sediment nutrient and oxygen fluxes is to examine the variation of one with respect to another (Nixon et al., 1975). This procedure is ideally suited for analyzing data using the models developed above because they predict ammonia flux as well the oxygen flux within a comprehensive framework.

The idea is as follows. One of the flux measurements is used to estimate the diagenesis flux. For example, the ammonia flux, $J[NH_4]$ is used to estimate J_N. Then carbon diagenesis, J_C, is estimated from nitrogen diagenesis using a suitable stoichiometric ratio. Once carbon diagenesis is known, the SOD can be computed, eq.(16), and compared to the ammonia flux. Thus any set of laboratory or field measurements that include simultaneous measurements of ammonia and oxygen fluxes can be compared to model predictions.

1. Methodology

The procedure uses the equation that relates ammonia flux to ammonia diagenesis eq.(II-25):

$$J_N = \left(\frac{K_{M,NH4}}{K_{M,NH4}+[NH_4(1)]}\right)\left(\frac{[O_2(0)]}{2K_{O2,NH4}+[O_2(0)]}\right)\frac{\kappa^2_{NH4,1}}{s}\theta^{(T-20)}_{NH4}[NH_4(1)] + s([NH_4(1)]-[NH_4(0)]) \quad (17)$$

where $[NH_4(1)]$ is computed from the ammonia flux, eq.(II-9):

$$[NH_4(1)] = \frac{J[NH_4]}{s} + [NH_4(0)] \quad (18)$$

Using the stoichiometric ratio, $\alpha_{C,N}$, determined below, the carbon diagenesis flux, J_C, is determined. This is substituted into the SOD equation (16). The resulting nonlinear equation can be solved for SOD which corresponds to the starting ammonia flux.

In fact, this computation can be thought of as being indexed by the ammonia flux. That is, given an ammonia flux, the corresponding SOD is computed. In order to make the calculation, however, all the exogenous variables required in the computation of SOD are also required as a function of $J[NH_4]$. These relationships are established in the next section.

2. Exogenous Variables

Both the SOD and ammonia flux are strongly influenced by the overlying water oxygen concentration, $[O_2(0)]$. Lowering the oxygen concentration decreases the SOD and increases the ammonia flux. Hence it is necessary to stratify the data with respect to $[O_2(0)]$. A division at $[O_2(0)] = 2$ mg/L is chosen as a compromise between a suitably low DO concentration and the presence of a sufficient number of flux measurements in the Chesapeake Bay data set below that concentration.

Within the two subsets of observations, there may still be a systematic variation of the exogenous variables: overlying water concentrations, $[O_2(0)]$, $[NH_4(0)]$, $[NO_3(0)]$, and temperature, T, with respect to ammonia flux. Fig. 5.3 presents the data versus $J[NH_4]$ for the variables with the most impact on the calculation: $[O_2(0)]$ and temperature. The data set is averaged over 0.2 $\log_{10}$ units of ammonia flux. The histograms are the number of data points in each interval. For the subset $[O_2(0)] > 2$ mg/L, overlying water DO varies from 10 to 5 mg/L as the ammonia flux increases, Fig. 5.3A. This is a reflection of the increasing water temperature as shown in Fig. 5.3C. For the subset $[O_2(0)] < 2$ mg/L, overlying water DO is between 1 and almost 0 mg/L over the range of ammonia fluxes, Fig. 5.3B. The water temperature is high and almost constant, Fig. 5.3D.

3. Diagenesis Stoichiometry

The method being employed to calculate the SOD associated with an ammonia flux requires that the carbon diagenesis be estimated from the ammonia diagenesis. A convenient approximation is that the ratio of carbon to nitrogen diagenesis fluxes follows Redfield

stoichiometry (Redfield et al., 1963): $\alpha_{C,N,} = J_C / J_N$ = 5.68 (gm C/gm N). This approximation is shown below in Chapter VIII to be applicable to Chesapeake Bay sediments. Although a stoichiometric ratio is not necessary when the sediment model is used as part of a coupled water column - sediment model, it provides a necessary relationship for the calculation of SOD from ammonia flux since it relates nitrogen diagenesis to carbon diagenesis.

4. SOD and Ammonia Fluxes

The calculations presented below are performed using the complete time variable model in steady state mode. The parameter values and formulations employed in the calculation are presented in Chapters VIII to X. Since the complete model is forced by the depositional fluxes, the depositional flux of particulate nitrogen is back computed from the ammonia flux. The stoichiometric ratios are used to compute the other depositional fluxes. Rather than giving a brief and incomplete summary of the complete model formulation, it is more illuminating to examine the results of the calculation, using the insights and formulas obtained above.

The comparison of SOD and ammonia flux is shown in Fig. 5.4. The means and the standard errors of the mean are shown. The histograms display the number of data points in each interval. The relationship between SOD and $J[NH_4]$ for the two subsets is quite different and the model qualitatively reproduces the different behavior. The SOD for the low overlying water oxygen data set, $[O_2(0)] < 2$ mg/L, Fig. 5.4B, is smaller than the high DO data set, Fig. 5.4A, and the model successfully reproduces the trend. However, the model results are quantitatively less satisfactory. For the higher oxygen concentration, Fig. 5.4A, the data indicate a relationship that is less steep than the model predicts. And the model consistently over predicts the observed SOD for the low DO data set, Fig. 5.4B.

H. Commentary

The behavior of the SOD model can be understood as follows. The model apportions carbon diagenesis to the three terminal sinks: oxidation, sulfide flux to the overlying water, and

Overlying Water Data

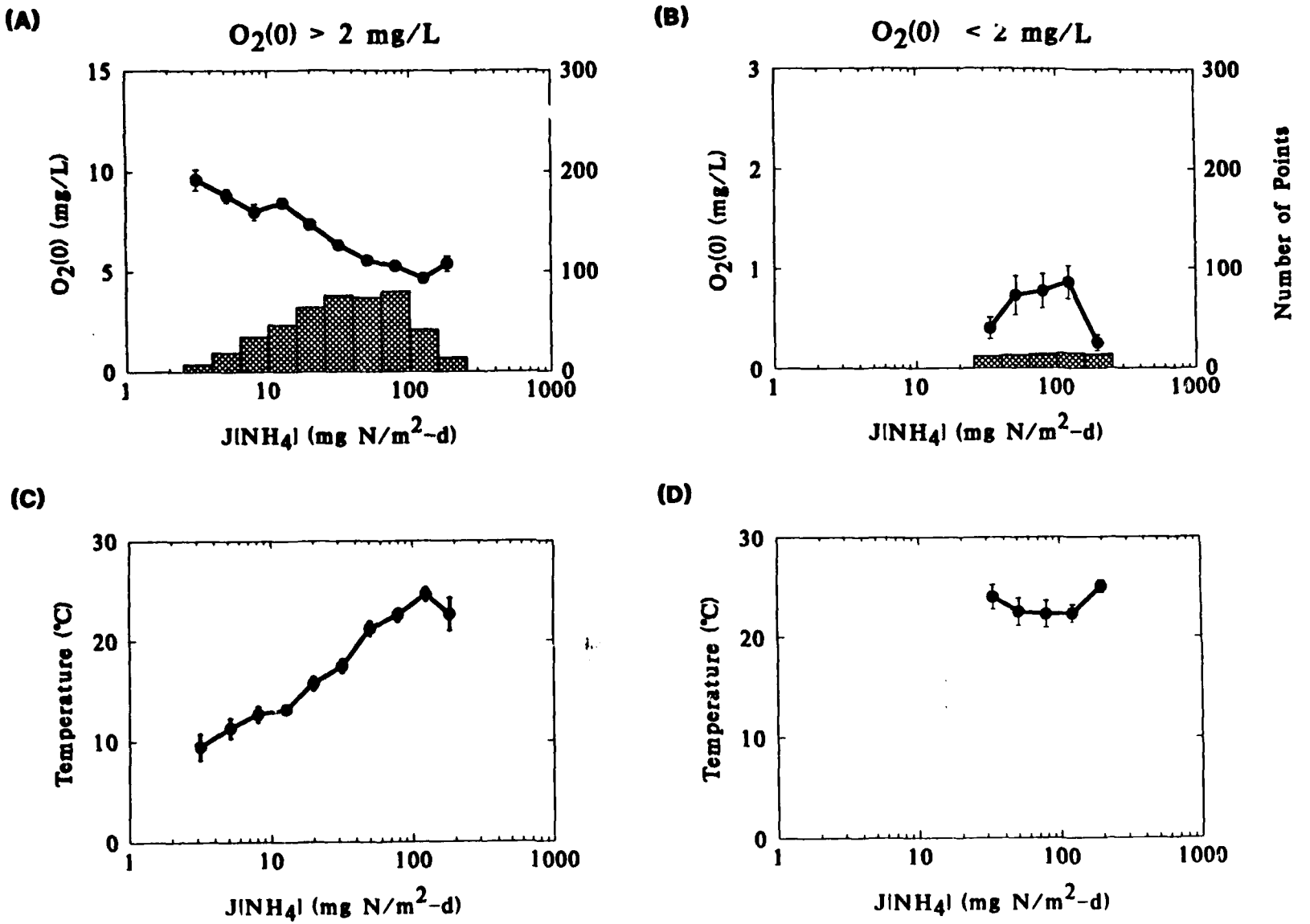

SODSS1

Figure 5.3

Comparison of Model and Data

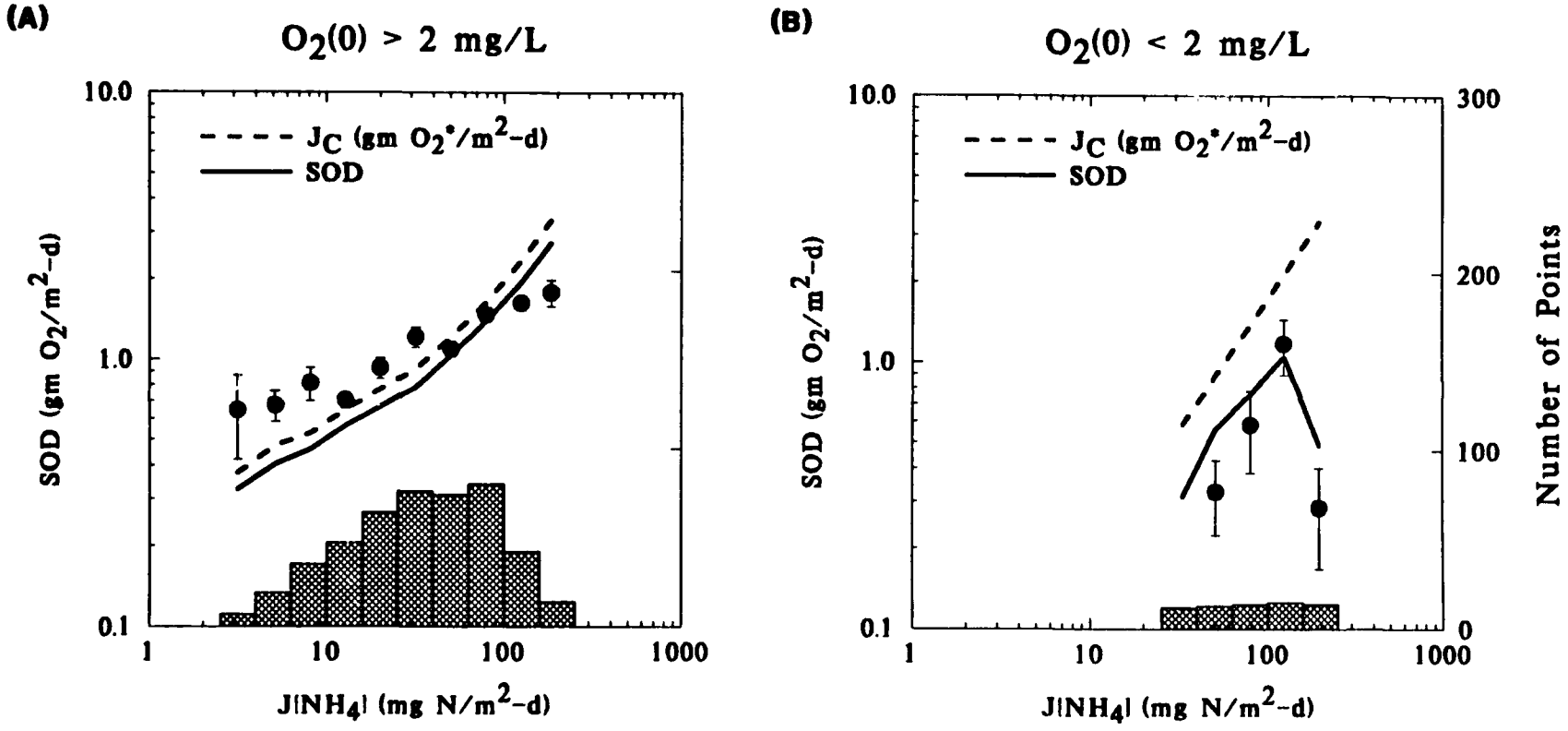

SODSS2

Figure 5.4

burial. For the subset $[O_2(0)] > 2$ mg/L, the overlying water DO is actually greater than 5 mg/L (Fig. 5.3A), and essentially all the carbon diagenesis is oxidized, (Fig. 5.2D). For $[O_2(0)] < 2$ mg/L, a substantial quantity is released as a sulfide flux (Fig. 5.2D) thereby lowering the SOD.

The models inability to obtain the correct slope of the relationship between SOD and ammonia flux for the high DO data set points to a fundamental deficiency. Since the ammonia flux model appears to successfully reproduce the observations (Fig. 2.5), the problem must be with the SOD model. The SOD is over predicted for the high ammonia fluxes. This could be remedied by choosing model parameters that apportion more of the diagenesis to burial, for example. But the under prediction of SOD for the small ammonia fluxes cannot be remedied in any way. All of the carbon diagenesis is being converted to SOD and it is *still* not enough. There is no remedy within the context of a steady state model.

In fact, what we are seeing is a direct manifestation of a non steady state effect. It is possible for the SOD to be larger than carbon diagenesis if it is due to the oxidation of previously stored particulate sulfide. In order for this to be the case, there must be periods where carbon diagenesis exceeds SOD. The excess production causes an increase in particulate sulfide which is stored in the sediment. This occurs during the time of rapid carbon diagenesis. As a consequence, larger SODs can be supported during periods of lower carbon diagenesis by the oxidation of the stored particulate sulfide.

For this explanation to be correct it must be true that the average SOD is correctly computed. The comparison is shown in Table 5.2 where the arithmetic average SODs are listed.

Table 5.2
Average SOD

SOD ($gm\ O_2/m^2$-d)	Observations (Std. Err)	Model (Std. Err)
Without weighting	1.06 (0.126)	0.966 (0.233)
With weighting	1.14 (0.015)	1.01 (0.025)

The computation is performed both without weighting - each bin average in Fig. 5.4 in treated equally - and with weighting where the bin averages are weighted by the number of points in each bin average. The result is indeed that the average SODs are similar. Thus, it is the steady state assumption that is in error and this can only be remedied by employing a time variable calculation which is presented in Chapter X.

Table 5.1

Parameters for Flux Apportionment Calculation

Parameter	Description	Value	Units
m_1	Aerobic layer solids concentration	0.5	kg/L
m_2	Anaerobic layer solids concentration	0.5	kg/L
w_2	Sedimentation velocity for the stand alone calibration.	0.25	cm/yr
w_{12}	Particle mixing velocity	0.001	m/d
K_{L12}	Diffusive mass transfer coefficient	0.01	m/d
$\kappa_{H2S,d1}$	Reaction velocity for dissolved sulfide oxidation in the aerobic layer	0.20	m/d
$\kappa_{H2S,p1}$	Reaction velocity for particulate sulfide oxidation in the aerobic layer	(A) 0.00 (B) 0.00 (C) 0.01 (D) 0.40	m/d
$K_{M,H2S,O2}$	Sulfide oxidation normalization constant for oxygen	4.0.	mg O_2/L
$\pi_{H2S,1}$ $\pi_{H2S,2}$	Partition coefficient for sulfide in the aerobic and anaerobic layers	(B) 10^4 (C) 10^4 (D) 10^2	L/kg

I. References

Almegren, T. and Hagstrom, I. (1974): The oxidation rate of sulfide in sea water. Wat. Res. 8: pp. 395-400.

Barnes, R.O. and Goldberg, E.D. (1976): Methane production and consumption in anoxic marine sediments. Geology 4: pp. 297-300.

Boudreau, B.P. (1991): Modelling the sulfide-oxygen reaction and associated pH gradients in porewaters. Geochim. Cosmochim. Acta 55: pp. 145-159.

Cline, J.D. and Richards, F.A. (1969): Oxygenation of hydrogen sulfide in seawater at constant salinity, temperature, and pH. Environ. Sci. Tech. 3: pp. 838-843.

Howarth, R.W. and Jorgensen, B.B. (1984): Formation of ^{35}S-labelled elemental sulfur and pyrite in coastal marine sediments (Limfjorden and Kysing Fjord, Denmark) during short-term 35SO4 reduction experiments. Geochim. Cosmochim. Acta 48: pp. 1807-1818.

Jorgensen, B.B. (1977): The sulfur cycle of a coastal marine sediment (Limfjorden, Denmark). Limnol. Oceanogr. 22: pp. 814-832.

Jorgensen, B.B. (1982): Ecology of the bacteria of the sulphur cycle with special reference to anoxic-oxic interface environments. Phil. Trans. R. Soc. Lond. B 298: pp. 543-561.

Jorgensen, B.B., Revsbech, N.P. and Cohen, Y. (1983): Photosynthesis and structure of benthic microbial mats: microelectrode and SEM studies of four cyanobacterial communities. Limnol. Oceanogr. 28: pp. 1075-1093.

Jorgensen, B.B. and Revsbech, N.P. (1990): Oxygen uptake, bacterial distribution, and carbon-nitrogen-sulfur cycling in sediments from the Baltic Sea - North Sea transition. Ophelia 31(1): pp. 29-49.

Martens, C.S. and Berner, R.A. (1977): Interstitial water chemistry of anoxic Long Island Sound sediments. I. Dissolved gases. Limnol. and Oceanogr. 22(1): pp. 10-25.

Millero, F.J. (1986): The thermodynamics and kinetics of the hydrogen sulfide system in natural waters. Mar. Chem. 18: pp. 381-391.

Millero, F.J. (1991): The oxidation of H_2S in the Chesapeake Bay. Estuarine, Coastal and Shelf Sci. 33: pp. 521-527.

Millero, F.J., Hubinger, S., Fernandez, M. and Garnett, S. (1987): Oxidation of H_2S in seawater as a function of temperature, pH, and ionic strength. Environ. Sci. Technol 21: pp. 439-443.

Morse, J.W., Millero, F.J., Cornwell, J.C. and Rickard, D. (1987): The Chemistry of the Hydrogen Sulfide and Iron Sulfide Systems in Natural Waters. Earth Science Reviews 24: pp. 1-42.

Nelson, M.B. (1978): Kinetics and mechanisms of the oxidation of ferrous sulfide. Ph.D Thesis. Stamford University, Palo Alto, CA. pp. 1-288.

Nixon, S.W., Oviatt, C.A. and Hale, S.S. (1975): Nitrogen regeneration and the metabolism of coastal marine bottom communities. In: The Role of Terrestrial and Aquatic Organisms in Decomposition Processes, pp. 269-283. Editors: J.M. Anderson and A. Macfadyen. Blackwell Scientific Pubs., Oxford, England.

O'Brien, D.J. and Birkner, F.B. (1977): Kinetics of oxygenation of reduced sulfur species in aqueous solution. Environ. Sci. Technol. 11(12): pp. 1114-1120.

Redfield, A.C., Ketchum, B.H. and Richards, F.A. (1963): The influence of organisms on the composition of seawater. In: The Sea, pp. 26-77. Editor: M.N. Hill. Wiley-Interscience, N.Y.

Reeburgh, W.S. and Heggie, D.T. (1974): Depth Distributions of Gases in Shallow Water Sediments. In: Natural Gases in Marine Sediments, pp. 27-46. Editor: I.R. Kaplan. Plenum Press, N.Y.

Wilmot, P.D., Cadee, K., Katinic, J.J. and Kavanagh, B.V. (1988): Kinetics of sulfide oxidation by dissolved oxygen. J. Water Pollut. Control Fed. 60(7): pp. 1264-1270.

Zhang, J.Z. and Millero, F.J. (1991): The rate of sulfite oxidation in seawater. Geochim. Cosmochim. Acta 55: pp. 677-685.

VI. PHOSPHORUS

A. Introduction

The search for an understanding of the mechanisms that control the flux of phosphorus from sediments has a long history. For lake sediments, the classical experiments and their interpretation by Mortimer (1941, 1942) provided a framework within which to understand the profound effect of the overlying water dissolved oxygen concentration. He posited that a barrier to phosphate exists in the aerobic layer of the sediment due to the formation of iron oxyhydroxide precipitate via the oxidation of ferrous iron. The stoichiometry for this amorphous precipitate is reported to be $Fe_2O_3 \cdot n\ H_2O$ with n = 1 to 3 (Dzombak and Morel, 1990), which is abbreviated as Fe_2O_3 for simplicity. This particulate species strongly sorbs phosphate and prevents its escape to the overlying water via diffusion. When the overlying water oxygen concentration decreased to zero, the ferric oxyhydroxide is reduced to soluble ferrous iron, the barrier no longer exists, and phosphate escapes unimpeded. This mechanism has been invoked in many models of phosphate flux.

For marine sediments, the focus has been more on models for the interstitial water concentration distribution of phosphate (Berner, 1974; Berner, 1980; van Cappellen and Berner, 1988). These relate the diagenetic production of phosphate to the resulting pore water concentration distribution, usually as a one dimensional steady state vertical model.

Models that are specifically designed to compute phosphate fluxes have been proposed as well. Empirical models relate phosphate flux to an extracted fraction of the phosphorus concentration of the sediment (Kamp-Nielsen, 1975; Jorgensen et al., 1975; Nurnberg, 1988). More detailed, vertically segmented models have also been proposed (Kamp-Nielsen et al., 1982; Berner, 1974; Berner, 1980; Ishikawa and Nishimura, 1989; Jorgensen et al., 1975; Kamp-Nielsen, 1975; Kamp-Nielsen et al., 1982; Nurnberg, 1988; van Cappellen and Berner, 1988; Van der Molen,

1991; Yoshida, 1981.) The model developed below is based on both of these approaches. It incorporates the diagenetic production of phosphate and it uses the mechanism of iron oxyhydroxide trapping.

B. Model Components

The phosphate flux model is constructed using the solutions for the steady state model equations developed in Chapter IV. The schematic is presented in Fig. 6.1. The production of phosphate is via the diagenetic breakdown of particulate organic matter. The result is a flux of phosphate, J_P, to the anaerobic layer. A portion of the liberated phosphate remains in the dissolved form and a portion becomes particulate phosphate, either via precipitation of phosphate containing minerals (Troup, 1974), e.g. vivianite, $Fe_3(PO_4)_2(s)$, or by partitioning to phosphate sorption sites (Lijklema, 1980; Barrow, 1983; Dzombak and Morel, 1990). The extent of particulate formation is determined by the magnitudes of the partition coefficients π_1 and π_2 in layer 1 and 2 respectively. The interaction between layer 1 and 2 is via diffusion of dissolved chemical and particle mixing. The rate of burial is determined by the sedimentation velocity, w_2. Finally the flux into or out of the sediment is via diffusive exchange with the overlying water. Thus, the phosphate flux model has a structure that is similar to the models discussed in the previous chapters.

C. Solutions

The mass balance equations for phosphate are the same as eqs. (IV-1) to (IV-4) but without the reaction terms. For simplicity the case for zero overlying water phosphate concentration is considered. The solution is obtained from eq.(IV-19):

$$[PO_4(1)]_T = \frac{J_P}{s f_{d1} + w_2 r_{21}} \qquad (1)$$

where r_{21} is given by eq.(IV-9) and (IV-12):

$$r_{21} = \frac{w_2 + w_{12} f_{p1} + K_{L12} f_{d1} + s f_{d1}}{w_{12} f_{p2} + K_{L12} f_{d2}} \quad (2)$$

The phosphate flux to the overlying water is, eq.(IV-21):

$$J[PO_4] = J_P \frac{s f_{d1}}{s f_{d1} + w_2 r_{21}} \quad (3)$$

Because this is the steady state solution, the phosphate released by particulate organic matter diagenesis can either escape to the overlying water, or be buried. The extent of partitioning in layer 1 and layer 2 affects f_{d1} and r_{21} which, in turn, control the fraction of mineralized phosphorus that is either recycled to the overlying water or is buried.

1. Effect of Partitioning and Particle Mixing

It has been observed that the phosphate flux from sediments is strongly affected by the overlying water oxygen concentration, $[O_2(0)]$ (Mortimer, 1941, 1942, 1971; Bostrom et al., 1988). It has been suggested that the phosphate transferred to the aerobic layer is sorbed to freshly precipitated iron oxyhydroxides which prevents it from diffusing into the overlying water. At low oxygen concentrations, the iron oxyhydroxides are reduced and dissolve, the sorption barrier is removed, and the phosphate flux escapes unimpeded (Mortimer, 1941, 1942, 1971; Baccini, 1985; Sundby, 1986; Bostrom et al., 1988; Chambers and Odum, 1990). This suggests that the dissolved fraction in the aerobic layer, f_{d1}, is changing as a function of overlying water DO.

At first glance, it is not clear that this mechanism - a partition coefficient that is larger in the aerobic layer than in the anaerobic layer - can account for the variation of phosphate flux as a function of overlying water DO. How is it possible that, at steady state, a difference in partitioning in layer 1 and 2 can reduce the flux to the overlying water? Would not the aerobic layer barrier eventually be saturated? Consider the following progression in time. At any point, the sorbed phosphate equilibrates with the dissolved phosphate concentration in both layers. If a gradient of dissolved phosphate exists between the layer 1 and 2, then pore water diffusion will tend to

PHOSPHORUS FLUX MODEL

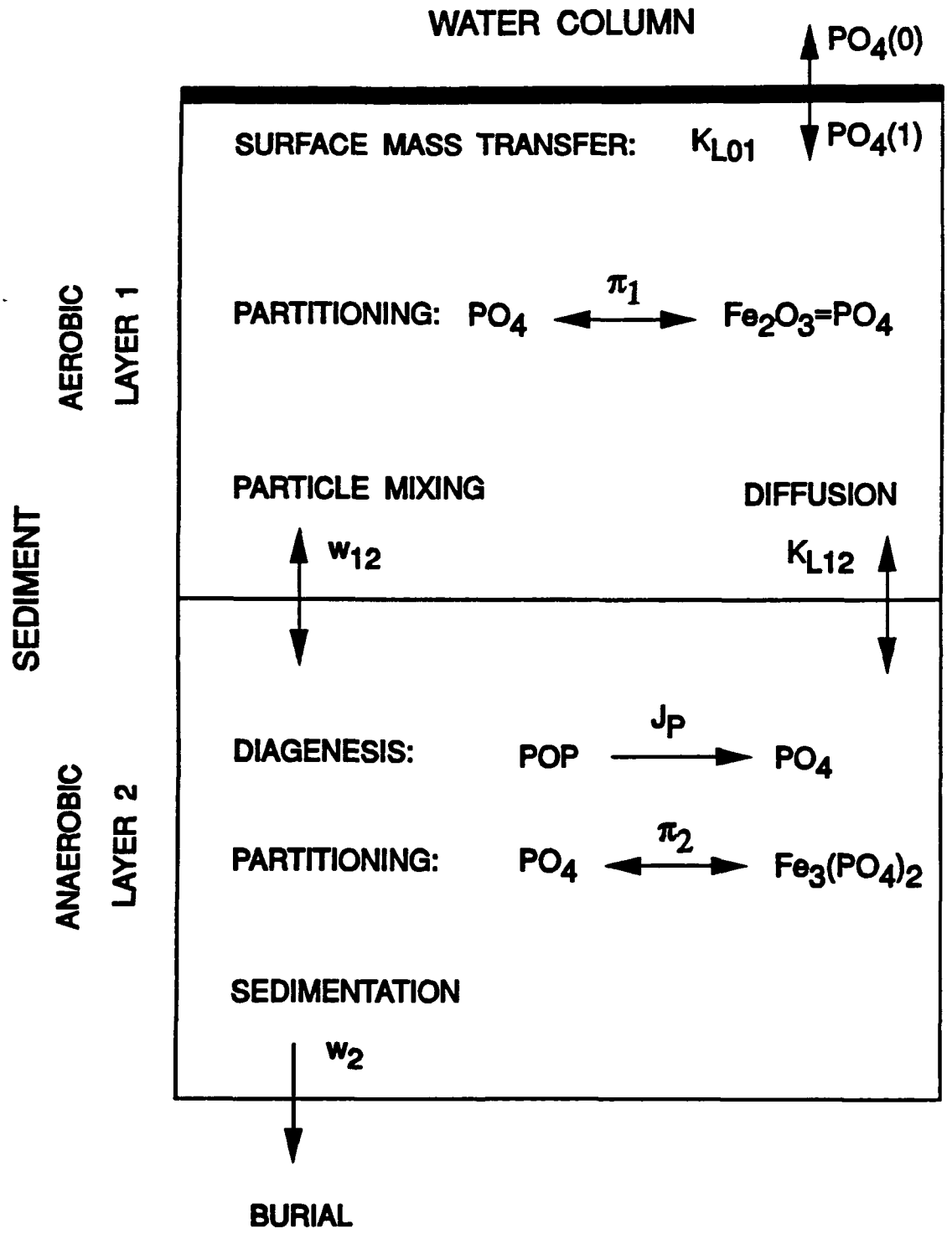

CHAP61L

Figure 6.1

equalize the pore water concentrations. The solid phase phosphate concentrations will adjust to accommodate the new dissolved concentrations. The process of pore water diffusion and solid phase adjustment will continue until the pore water concentrations are equal in both layers. At that point the dissolved concentrations in the aerobic and anaerobic layers are the same, the barrier is saturated, and the phosphate flux would be equal to the phosphate flux from an entirely anaerobic sediment. The presence of an aerobic layer would no longer reduce the dissolved phosphate concentration at the sediment-water interface, and, therefore, would no longer reduce the flux from the aerobic layer.

This line of reasoning depends on the assumption that the pore water concentrations will eventually equilibrate in both layers due to diffusion of dissolved phosphate. However, it is not clear that this will occur, particularly in the presence of particle mixing between layers 1 and 2. An examination of the flux equation (3), indicates that if r_{21} is reasonably constant, then increasing the partitioning in layer 1 decreases f_{d1}, and thereby decreases the phosphate flux to the overlying water.

However, decreasing f_{d1} may also decrease r_{21}, see eq.(2). Consider the limiting cases. Without particle mixing, eq.(2) becomes:

$$r_{21} = \frac{w_2 + K_{L12} f_{d1} + s f_{d1}}{K_{L12} f_{d2}} \tag{4}$$

and the phosphate flux becomes:

$$J[PO_4] = J_P \frac{s f_{d1}}{s f_{d1} + w_2 \left(\frac{w_2 + K_{12} f_{d1} + s f_{d1}}{K_{12} f_{d2}} \right)}$$

$$\approx J_P \frac{s f_{d1}}{s f_{d1} + w_2 \left(\frac{K_{12} f_{d1} + s f_{d1}}{f_{d2}} \right)}$$

$$= J_P \frac{s}{s + w_2 \left(\frac{K_{12} + s}{f_{d2}} \right)} \qquad (5)$$

The approximation in the second line follows from the assumption that the burial is small relative to the other transport terms, $w_2 \ll K_{12} f_{d1} + s f_{d1}$. For this case, the phosphate concentration is indeed independent of the layer 1 partition coefficient and the trapping mechanism will not reduce phosphate flux at steady state.

With intense particle mixing, eq.(2) becomes:

$$r_{21} = \frac{w_2 + w_{12} f_{p1}}{w_{12} f_{p2}} \approx \frac{f_{p1}}{f_{p2}} \approx 1 \qquad (6)$$

since, for any realistic partition coefficient, the fraction of phosphate that is in the particulate form is essentially unity so that $f_{p1} \approx 1$ and $f_{p2} \approx 1$. Thus the particulate concentrations in the two layers equalize, and the phosphate flux to the overlying water becomes:

$$J[PO_4] = J_P \frac{s f_{d1}}{s f_{d1} + w_2} \qquad (7)$$

which varies with f_{d1} and, therefore, with aerobic layer partitioning. Hence, the intensity of particle mixing determines whether the trapping mechanism can be effective in varying phosphate flux as a function of overlying water DO.

A quantitative examination is presented in Fig. 6.2. The parameters used in the calculation are given in Table 6.1.

Steady State Phosphate Flux Model

With Particle Mixing

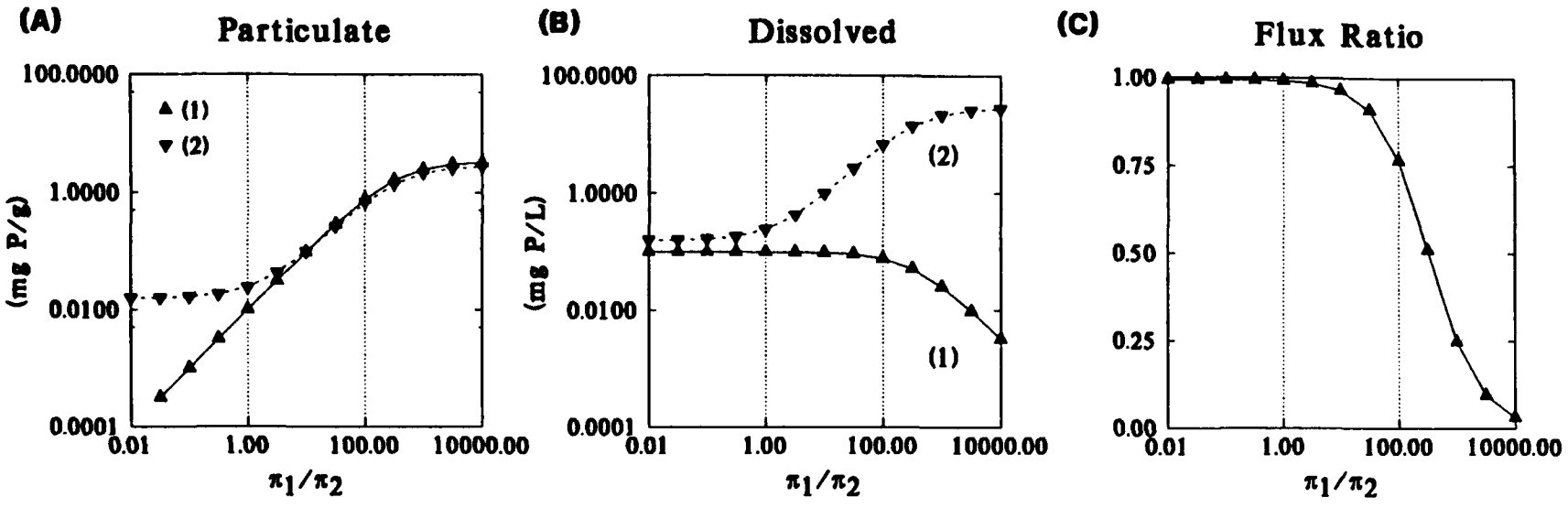

Without Particle Mixing

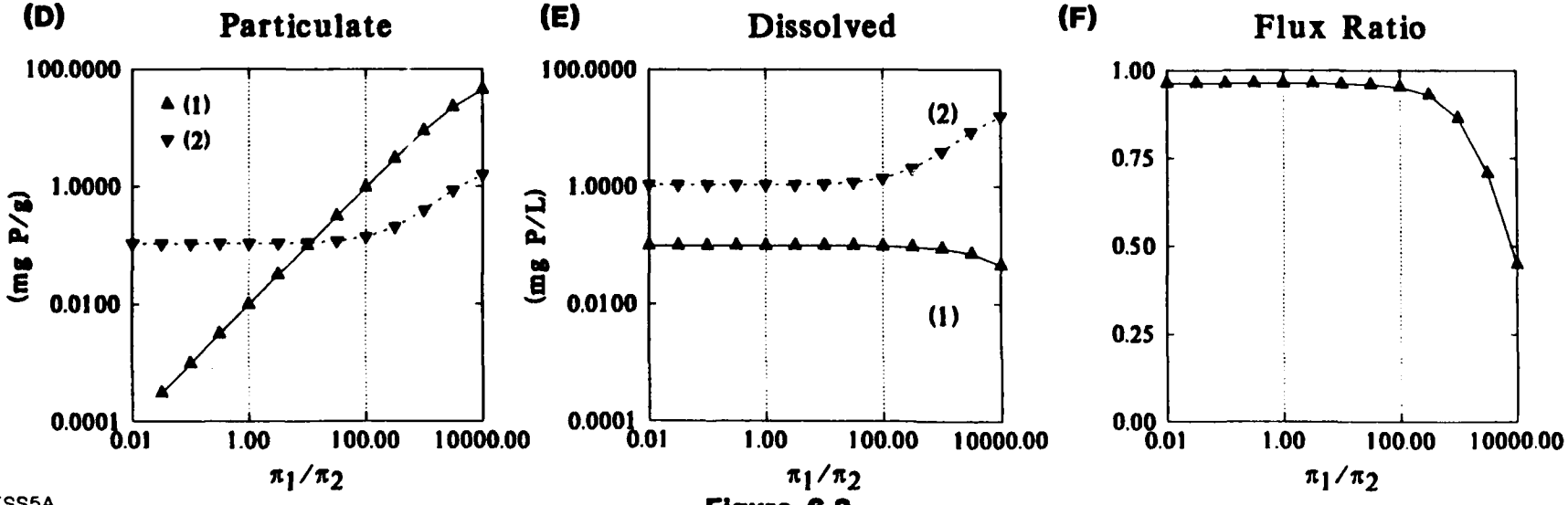

TSS5A

Figure 6.2

Table 6.1
Phosphate Flux Model Parameters
Effect of Partition Coefficient Ratio

Parameter	With Particle Mixing	Without Particle Mixing
w_2	0.25 (cm/yr)	0.25 (cm/yr)
w_{12}	0.0012 (m/d)	0.0
K_{L12}	0.01 (m/d)	0.01 (m/d)
m_1	0.5 (kg/L)	0.5 (kg/L)
m_2	0.5 (kg/L)	0.5 (kg/L)
J_p	10 (mg P/m^2-d)	10 (mg P/m^2-d)

The particulate and dissolved concentrations, and the ratio of flux to the overlying water to the diagenesis flux, $J[PO_4]/J_P$, are plotted versus the ratio of layer 1 to layer 2 partition coefficient, π_1/π_2. The top panels present the case with particle mixing. For equal partition coefficients, $\pi_1 = \pi_2$, the layer 1 and 2 particulate and dissolved concentrations are essentially equal and virtually all the diagenesis flux is escaping to the overlying water as indicated by the flux ratio = 1, Fig. 6.2C. As π_1/π_2 increases, particle mixing equilibrates the particulate concentrations, and the dissolved concentrations become quite different in the two layers. For $\pi_1/\pi_2 > 100$, the aerobic layer concentration is sufficiently reduced so that the flux ratio begins to decline. Note that the particulate concentration begins to increase as well since less phosphate is being lost to the overlying water, Fig. 6.2A.

The Fig. 6.2 results for no particle mixing indicate that if the partition coefficient ratio approaches 10^4 then the phosphate flux is again reduced, Fig. 6.2F. The reason for this behavior can be seen from eq.(5):

$$J[PO_4] = J_P \frac{s f_{d1}}{s f_{d1} + w_2 \left(\frac{w_2 + K_{L12} f_{d1} + s f_{d1}}{K_{L12} f_{d2}} \right)}$$

$$\rightarrow J_P \frac{s f_{d1}}{s f_{d1} + w_2 \left(\frac{w_2}{K_{L12} f_{d2}} \right)} \qquad (8)$$

as $K_{L12} f_{d1} + s f_{d1}$ becomes small relative to w_2. Now burial can become significant and the trapping mechanism operates. The interesting question is: why is there no equilibration of the dissolved concentrations as suggested above? This can be determined by examining the ratio of dissolved concentrations:

$$\frac{c_{d2}}{c_{d1}} = \frac{f_{d2}}{f_{d1}} r_{21} = \left(\frac{f_{d2}}{f_{d1}} \right) \frac{w_2 + K_{L12} f_{d1} + s f_{d1}}{K_{L12} f_{d2}}$$

$$= \frac{\frac{w_2}{f_{d1}} + K_{L12} + s}{K_{L12}} \qquad (9)$$

Therefore, only if the diffusive exchange, K_{L12}, is larger than the other terms, will the dissolved concentrations equilibrate. Thus, although particle mixing if not essential for the trapping mechanism to operate, it is effective at a considerably lower partition coefficient ratio if it is present, compare Fig. 6.2C to 6.2F.

D. Simplified Phosphate Flux Model

Since the aerobic layer trapping mechanism can reduce the aerobic layer phosphate flux, it is instructive to compare its predictions to observed phosphate fluxes. The total phosphate concentration in layer 1 is:

$$[PO_4(1)]_T = \frac{J_P + s[PO_4(0)]}{s f_{d1} + w_2 r_{21}} \qquad (10)$$

where the source due to diffusive exchange from the overlying water has been added to the diagenesis source. Strictly speaking, this equation is not valid since diagenesis is a source to the anaerobic layer and the flux from the overlying water is a source to the aerobic layer. However, the analysis in Chapter IV indicates that the approximation is reasonable if $r_{12} \approx 1$. As this is also the condition for which the trapping mechanism is most effective, the approximation is useful for this analysis.

Using equation (10) the phosphate flux is given by:

$$\begin{aligned} J[PO_4] &= s([PO_4(1)]-[PO_4(0)]) \\ &= s(f_{d1}[PO_4(1)]_T-[PO_4(0)]) \\ &= s\left(\frac{J_P+s[PO_4(0)]}{s+w_2\left(\frac{r_{21}}{f_{d1}}\right)}-[PO_4(0)]\right) \\ &= s\left(\frac{J_P+s[PO_4(0)]}{s+\Omega}-[PO_4(0)]\right) \end{aligned} \tag{11}$$

where:

$$\Omega = \frac{w_2 r_{21}}{f_{d1}} \tag{12}$$

which is the parameter group that controls the extent of burial.

Since this solution is approximate - the aerobic layer source from the overlying water is treated as an anaerobic layer source - it is appropriate to check the solution's limiting behavior. With only the overlying water as a source of phosphate, $J_P = 0$, and no burial flux $\Omega = 0$, it is easy to see that eq.(11) predicts a zero net flux as it should.

A more interesting case occurs as $s \to \infty$ and the aerobic layer thickness approaches zero. The limit in this case can be found as follows:

$$J[PO_4] = s\left(\frac{J_P + s[PO_4(0)]}{s+\Omega} - [PO_4(0)]\right)$$

$$= s\left(\frac{J_P - \Omega[PO_4(0)]}{s+\Omega}\right)$$

$$\to J_P - \Omega[PO_4(0)] \qquad (13)$$

as $s \to \infty$. And, from eq.(10) it can be seen that the layer 1 dissolved concentration approaches the overlying water concentration as the aerobic layer shrinks to zero thickness: $[PO_4(1)]_T f_{d1} \to [PO_4(0)]$, and this substitution can be made in eq.(13). Therefore:

$$J[PO_4] \to J_P - \Omega f_{d1}[PO_4(1)]_T$$

$$= J_P - w_2 r_{21}[PO_4(1)]_T$$

$$= J_P - w_2[PO_4(2)]_T \qquad (14)$$

where the definition of $r_{21} = C_{T2}/C_{T1}$ (eq. IV-9) is used to obtain the final result. This equation is a correct expression of mass balance. The flux to the overlying water is the difference between the diagenesis flux and the burial flux.

1. Numerical Analysis

The phosphate flux equation (11) has only one unknown parameter, Ω. The remaining terms are either measured: s and $[PO_4(0)]$, or for the diagenesis source, J_P, it can be estimated from nitrogen diagenesis, J_N, using the Redfield ratio: $J_P/J_N = 1/7.228$ (mg P/mg N). A regression analysis yields $\Omega = 0.10$ (m/d). The comparison of observed and computed

fluxes are shown in Fig. 6.3A. The result is not satisfactory. The measured fluxes bare almost no relation to the modeled fluxes. This suggests that the burial fraction, Ω, is varying with respect to the overlying water DO, $[O_2(0)]$.

The required variation can be estimated by computing Ω directly from the data. Solving for Ω in eq.(11) yields:

$$\Omega = s\left(\frac{J_P + s[PO_4]_0}{J[PO_4] + s[PO_4]_0} - 1\right) \tag{15}$$

The result is shown in Fig. 6.3B. The ordinate scale, based on an arcsech transformation, is discussed in detail in Chapter X, Section F, eq.(X-11). Note that Ω is roughly constant (~ 0.1 m/d = 10 cm/d) for $[O_2(0)] > 2$ mg/L and decreases as $[O_2(0)]$ approaches zero. In fact, negative Ω's are required to fit the observed phosphate fluxes at low dissolved oxygen concentrations. This is an indication that, in fact, this model is incapable of reproducing these observed fluxes.

E. Steady State Model

Perhaps the failure of the simplified model is due to the approximations introduced, namely replacing the transport and partitioning terms with the lumped parameter, Ω. In this section, the results of the steady state version of the full sediment model are examined. The trapping mechanism is included by varying the aerobic layer partition coefficient as a function of the overlying water DO.

A simple way to implement this mechanism is to make the aerobic layer partition coefficient larger than in the anaerobic layer during oxic conditions. These are defined to occur when the overlying water oxygen concentration exceeding some critical oxygen concentration, i.e. $[O_2(0)] > [O_2(0)]_{crit,PO4}$. The additional sorption would be removed as $[O_2(0)]$ decreases below $[O_2(0)]_{crit,PO4}$. Hence if $[O_2(0)] > [O_2(0)]_{crit,PO4}$ sorption in the aerobic layer is

enhanced by an amount $\Delta\pi_{PO4,1}$:

$$\pi_1 = \pi_2(\Delta\pi_{PO4,1}) \qquad [O_2(0)] > [O_2(0)]_{crit,PO4} \qquad (16)$$

However, if oxygen falls below a critical concentration, $[O_2(0)] < [O_2(0)]_{crit,PO4}$, then:

$$\pi_1 = \pi_2(\Delta\pi_{PO4,1})^{([O_2(0)]/[O_2(0)]_{crit,PO4})} \qquad [O_2(0)] \leq [O_2(0)]_{crit,PO4} \qquad (17)$$

which smoothly reduces the aerobic layer partition coefficient to that in the anaerobic layer as $[O_2(0)]$ goes to zero.

The steady state model is used to compare the variation of the ammonia and phosphate fluxes. This is the same technique that was applied to the analysis of the oxygen fluxes, as discussed in Chapter V, Section G. The ammonia flux is used to compute the depositional flux of particulate nitrogen. The depositional flux of particulate organic phosphorus is obtained using the Redfield ratio. Then the full model equations are solved at steady state to obtained the predicted phosphate flux. In order to complete the calculation, the variation in overlying water phosphate concentration with respect to ammonia flux is shown in Fig. 6.4A,B.

The results are examined in Fig. 6.4C,D. The model successively predicts the variation in phosphate flux as ammonia flux increases for $[O_2(0)] > 2$ mg/L, Fig. 6.4C. However, for $[O_2(0)] < 2$ mg/L the predicted flux is substantially less than the observations, Fig. 6.4D. The model behavior can be understood by examining the relationship of computed phosphate flux, $J[PO_4]$, and phosphorus diagenesis, J_P. For the cases where $[O_2(0)] > 2$ mg/L, the model predicts a phosphate flux that is a constant fraction (~ 0.88) of the phosphorus diagenesis as shown in Fig. 6.4C. For $[O_2(0)] < 2$ mg/L, however, the model predicts that $J[PO_4] = J_P$, Fig. 6.4D. This is not unexpected since at steady state, the maximum flux possible is that generated by diagenesis. Apparently this is insufficient.

Simplified Phosphorus Flux Model

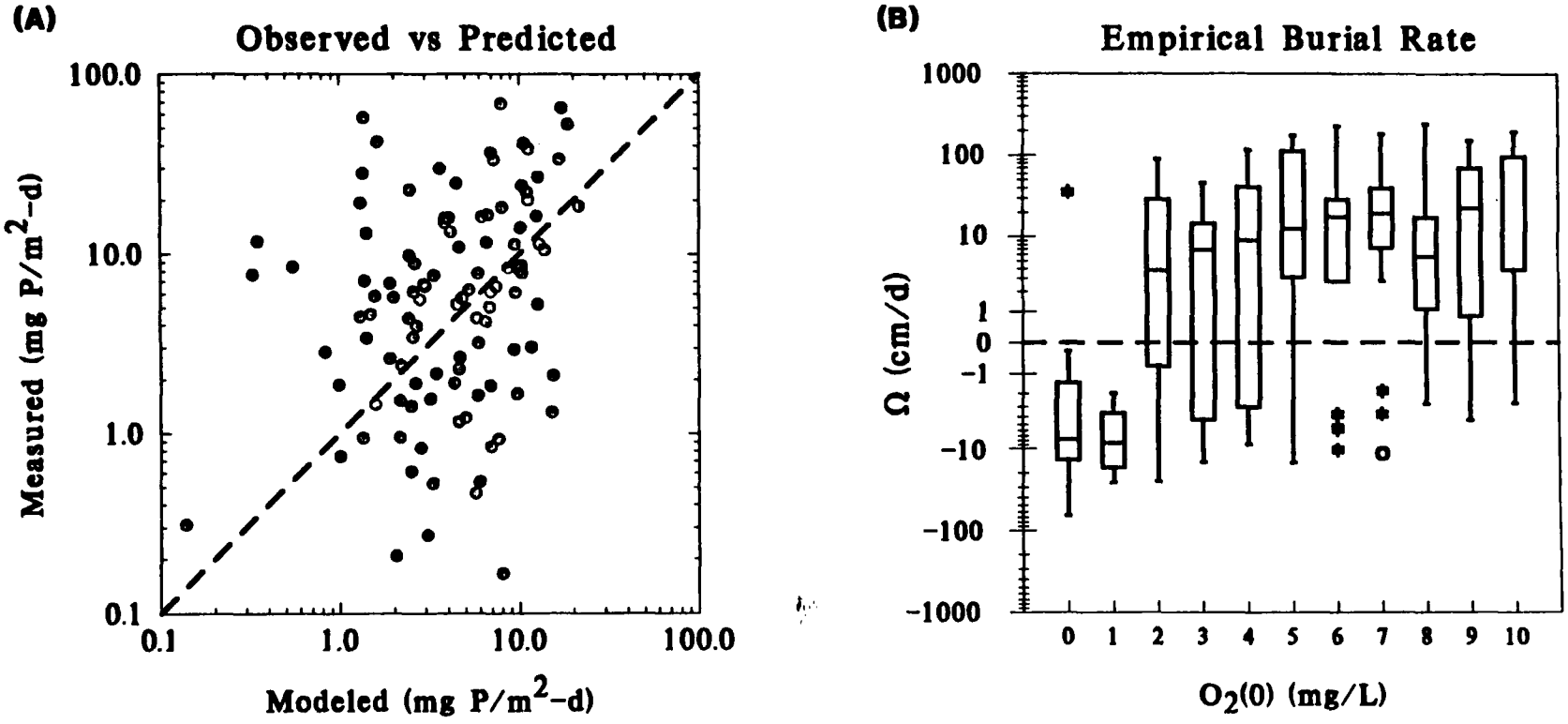

PCLX3

Figure 6.3

Overlying Water Phosphate

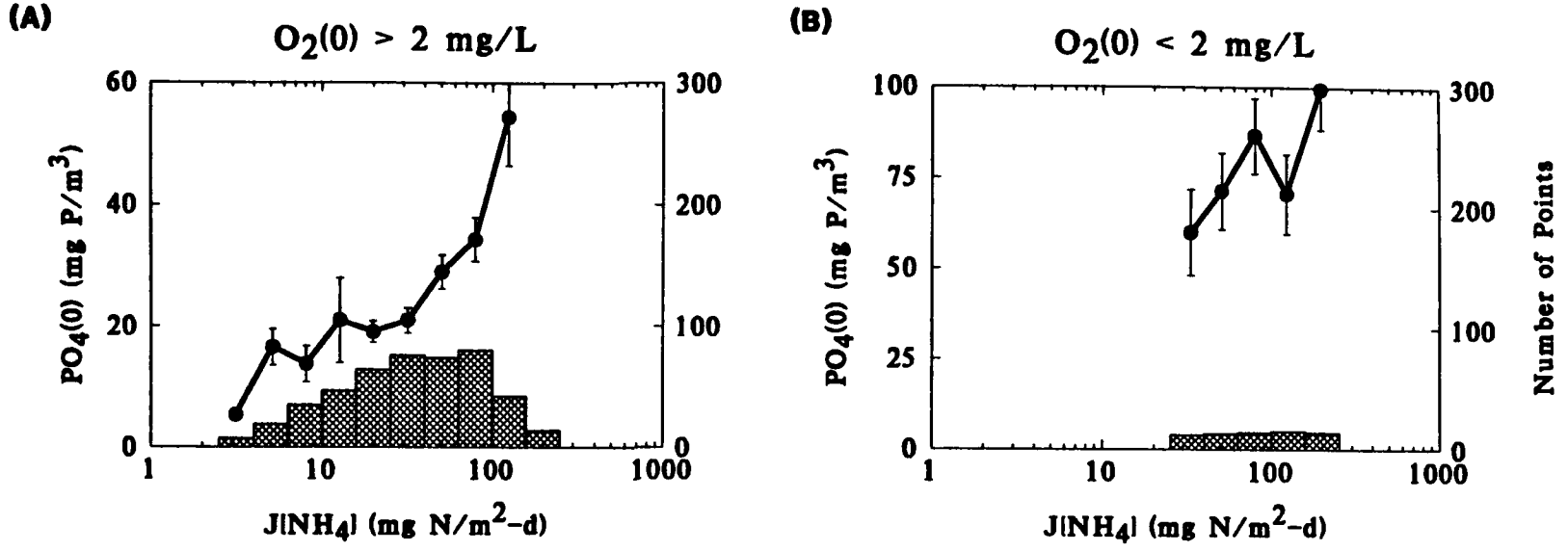

Comparison of Model and Data

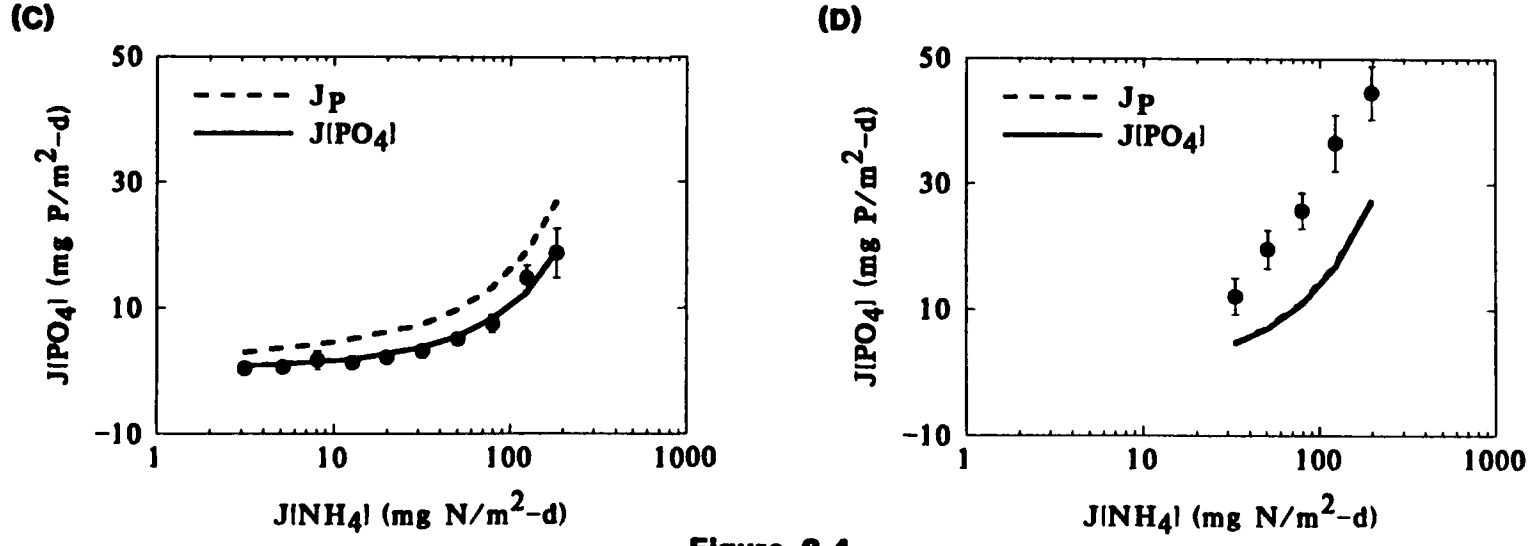

PO4SS3

Figure 6.4

This can clearly be seen in Fig. 6.5A which compares the phosphate flux to phosphorus diagenesis, where phosphorus diagenesis is estimated from ammonia diagenesis, eq.(V-17), and the Redfield ratio, $a_{C:P} = 106$ (mol C/mol P) = 41 (gC/gP). A significant fraction of the phosphate fluxes are in excess of phosphorus diagenesis. This occurs when the overlying water DO is low as shown in Fig. 6.5B, a plot of $J[PO_4]/J_P$ versus $O_2(0)$. At high overlying water DO concentrations the phosphate flux is less than phosphorus diagenesis. The difference is removed by burial. However when $O_2(0)$ approaches zero, the phosphate flux is larger than J_P. As can be seen from eq.(14), this cannot occur in a steady state model.

What is actually happening is that during the period of high overlying water DO a portion of the phosphate produced by diagenesis is not being buried but is actually going into storage in the anaerobic layer. This corresponds to a positive derivative in the mass balance equation for phosphate in the anaerobic layer:

$$H_2 \frac{d[PO_4(2)]_T}{dt} > 0 \tag{18}$$

In this case, storage mimics a sink in the mass balance equation. This can be seen if the derivative is included as part of the right hand side of the mass balance equation:

$$0 = -w_{12}(f_{p2}[PO_4]_{T2} - f_{p1}[PO_4]_{T1}) - K_{L12}(f_{d2}[PO_4]_{T2} - f_{d1}[PO_4]_{T1})$$
$$+ w_2([PO_4]_{T1} - [PO_4]_{T2}) + J_{T2} - H_2 \frac{d[PO_4]_{T2}}{dt} \tag{19}$$

The positive derivative corresponds to a loss term in the equation.

During periods of low overlying water DO, this stored phosphate, together with the phosphate generated by diagenesis, is released to the overlying water. Then the derivative is negative and the term acts as a source to the mass balance equation. Since this fluctuating derivative is a non-steady state phenomena, it cannot be reproduced by a steady state model. The only solution is a time variable simulation. This is presented in Chapter X.

F. Conclusions

The simplified steady state model is completely unsuccessful in simulating the range of observed phosphate fluxes. The problem is traced to the magnitude of the fluxes when the overlying water DO is less than 2 mg/L. The steady state results from the complete model reinforce this observation. The relationship between phosphate and ammonia fluxes is well reproduced for $[O_2(0)] > 2$ mg/L, but the anaerobic fluxes are underestimated. In fact, they exceed the phosphorus diagenesis flux. The source of the extra phosphate is from storage. Since this is not possible for the steady state model, only a time variable simulation will suffice.

Analysis of Phosphorus Flux

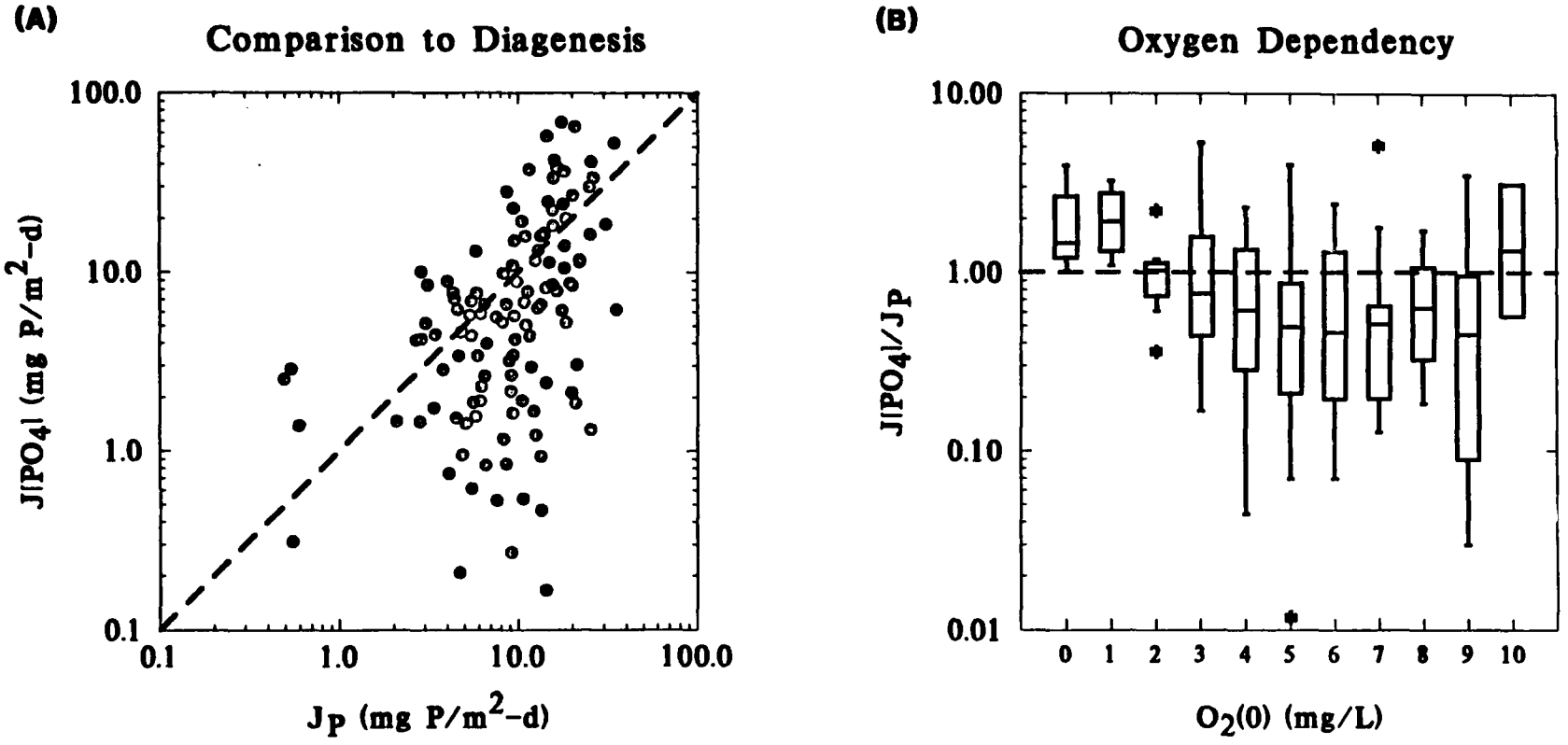

PCLX4

Figure 6.5

G. References

Baccini, P. (1985): Phosphate interactions at the sediment-water interface. In: Chemical Processes in Lakes, pp. 189-205. Editor: W. Stumm. J. Wiley & Sons, New York.

Barrow, N.J. (1983): A mechanistic model for describing the sorption and desorption of phosphate by soil. Journal of Soil Science 34: pp. 733-750.

Berner, R.A. (1974): Kinetic models for the early diagenesis of nitrogen, sulfur, phosphorus and silicon in anoxic marine sediments. In: The Sea Vol. 5, pp. 427-450. Editor: E.D. Goldberg. J. Wiley and Sons, N.Y..

Berner, R.A. (1980): Early Diagenesis. A Theoretical Approach. Princeton Univ. Press, Princeton, N.J.

Bostrom, B., Andersen, J.M., Fleischer, S. and Jansson, M. (1988): Exchange of phosphorus across the sediment-water interface. Hydrobiologia 170: pp. 229-244.

Chambers, R.M. and Odum, W.E. (1990): Porewater oxidation, dissolved phosphate and the iron curtain. Biogeochemistry 10: pp. 37-52.

Dzombak, D.A. and Morel, F.M.M. (1990): Surface Complexation Modeling. Hydrous Ferric Oxide. John Wiley & Sons, New York, NY. pp. 1-393.

Ishikawa, M. and Nishimura, H. (1989): Mathematical model of phosphate release rate from sediments considering the effect of dissolved oxygen in overlying water. Wat. Res. 23(3): pp. 351-359.

Jorgensen, S.E., Kamp-Nielsen, L. and Jacobsen, O.S. (1975): A submodel for anaerobic mud-water exchange of phosphate. Ecol. Modelling 1: pp. 133-146.

Kamp-Nielsen, L. (1975): A kinetic approach to the aerobic sediment-water exchange of phosphorus in Lake Estrom. Ecol. Modelling 1: pp. 153-160.

Kamp-Nielsen, L., Mejer, H. and Jorgensen, S.E. (1982): Modelling the influence of bioturbation on the vertical distribution of sedimentary phosphorus in L. Esrom. Hydrobiologia 91: pp. 197-206.

Lijklema, L. (1980): Interaction of ortho-phosphate with iron(III) and aluminum hydroxides. Environ. Sci. Technol. 14: pp. 537-541.

Mortimer, C.H. (1941): The exchange of dissolved substances between mud and water. I and II. J. Ecol 29: pp. 280-329.

Mortimer, C.H. (1942): The exchange of dissolved substances between mud and water in lakes. III and IV. J. Ecol 30: pp. 147-201.

Mortimer, C.H. (1971): Chemical exchanges between sediments and water in the Great Lakes - Speculations on probable regulatory mechanisms. Limnology and Oceanography 16(2): pp. 387-404.

Nurnberg, G.K. (1988): Prediction of phosphorus release rates from total and reductant-soluble phosphorus in anoxic lake sediments. Can. J. Fish. Aquat. Sci. 45: pp. 453-462.

Sundby, D., Anderson, L.G., Hall, P.O.J., Iverfeldt, A., Rutgers, L., Michiel, M. and Westerlund, S.F.G. (1986): The effect of oxygen on release and uptake of cobalt, manganese, iron and phosphate at the sediment-water interface. Geochim. Cosmochim. Acta 50(6): pp. 1281-1288.

Troup, R. (1974): The Interaction of Iron with Phosphate, Carbonate and Sulfide in Chesapeake Bay Interstitial Waters: A Thermodynamic Interpretation. Ph.D. Thesis. Johns Hopkins Univ., Baltimore, Md.

van Cappellen, P. and Berner, R.A. (1988): A mathematical model for the early diagenesis of phosphorus and fluorine in marine sediments: apatite precipitation. Am. J. Sci. 288: pp. 289-333.

Van der Molen, D.T. (1991): A simple, dynamic model for the simulation of the release of phosphorus from sediments in shallow, eutrophic systems. Wat. Res. 25(6): pp. 737-744.

Yoshida, T. (1981): Mathematical model of phosphorus release from lake sediment. Verh. Internat. Verein. Limnol. 21: pp. 268-274.

VII. SILICA

A. Introduction

The production of ammonia, sulfide, and phosphate in sediments is the result of the mineralization of particulate organic matter by bacteria. The production of dissolved silica in sediments occurs via a different mechanism which is thought to be independent of bacterial processes. It occurs as the result of the dissolution of particulate biogenic or opaline silica (Hurd, 1973). The dissolution releases silica to the pore water.

Two classes of models have been proposed for the vertical distribution of silica in sediment pore waters. The first consider only dissolved silica and neglect the solid phase (Anikouchine, 1967; Hurd, 1973; Berner, 1974; Lerman, 1975; Vanderborght et al., 1977). This approach is used initially for the simplified steady state model presented below. The more complete models consider both the solid phase and dissolved silica, and their interactions (Schink et al., 1975; Wong and Grosch, 1978; Schink and Guinasso 1980; Boudreau, 1990; Rabouille and Gaillard, 1990). The final model presented below includes both these phases.

B. Model Components

The schematic is presented in Fig. 7.1. The dissolution of particulate silica produces dissolved silica in the pore water of the sediment. However, silica has only a limited solubility in water, $[Si]_{sat}$. It has been determined that the rate of biogenic silica dissolution is proportional to the silica solubility deficit: $[Si]_{sat} - [Si(aq)]$ where $[Si(aq)]$ is the dissolved silica concentration. To see that this is a reasonable formulation, consider the sequence of events as biogenic silica dissolves into water that is free of dissolved silica. Initially, biogenic silica dissolves at its maximum rate, unimpeded by limited solubility. As the concentration of silica in pore water increases, however, the reverse reaction, the precipitation of opaline silica, begins to take place. This retards the overall rate of dissolution. As the pore water concentration continues to increase,

the concentration eventually approaches the solubility limit of opaline silica and the reaction reaches a steady state where the rate of dissolution equals the rate of precipitation. The result is that there is no further increase of dissolved silica.

This formulation can be expressed as follows. Let S_{Si} be the rate of production of dissolved silica. The rate of biogenic silica dissolution is proportional to the silica solubility deficit: $[Si]_{sat} - [Si(aq)]$, and also the concentration of particulate biogenic silica, P_{Si}. Thus:

$$S_{Si} = k_{Si}\theta_{Si}^{(T-20)} P_{Si}([Si]_{sat} - [Si(aq)]) \qquad (1)$$

where k_{Si} is the specific reaction rate for silica dissolution; θ_{Si} is the coefficient of temperature dependence; P_{Si} is the concentration of particulate biogenic silica; $[Si]_{sat}$ is the saturation concentration of silica in the pore water, and $[Si(aq)]$ is the dissolved silica concentration.

For the initial steady state modeling analysis it is convenient to replace the product: $k_{Si}P_{Si}$, with an overall first order reaction rate, K_{Si}. With this simplification eq.(1) becomes:

$$\begin{aligned} S_{Si} &= K_{Si}\theta_{Si}^{(T-20)}([Si]_{sat} - [Si(aq)])H_2 \\ &= K_{Si}\theta_{Si}^{(T-20)}[Si]_{sat}H_2 - K_{Si}\theta_{Si}^{(T-20)}[Si(aq)]H_2 \end{aligned} \qquad (2)$$

This simplifies the analysis since the mass balance equation is now linear and an equation for P_{Si} not required. This simplification, however, should be viewed only as an expedient. The basic principle guiding the development of these models is the principle of mass balance and, clearly, an adherence to this principle requires an explicit accounting of the source of silica. It is included in the numerical steady state calculations presented below, and in the time variable model discussed in Chapter X.

SILICA FLUX MODEL

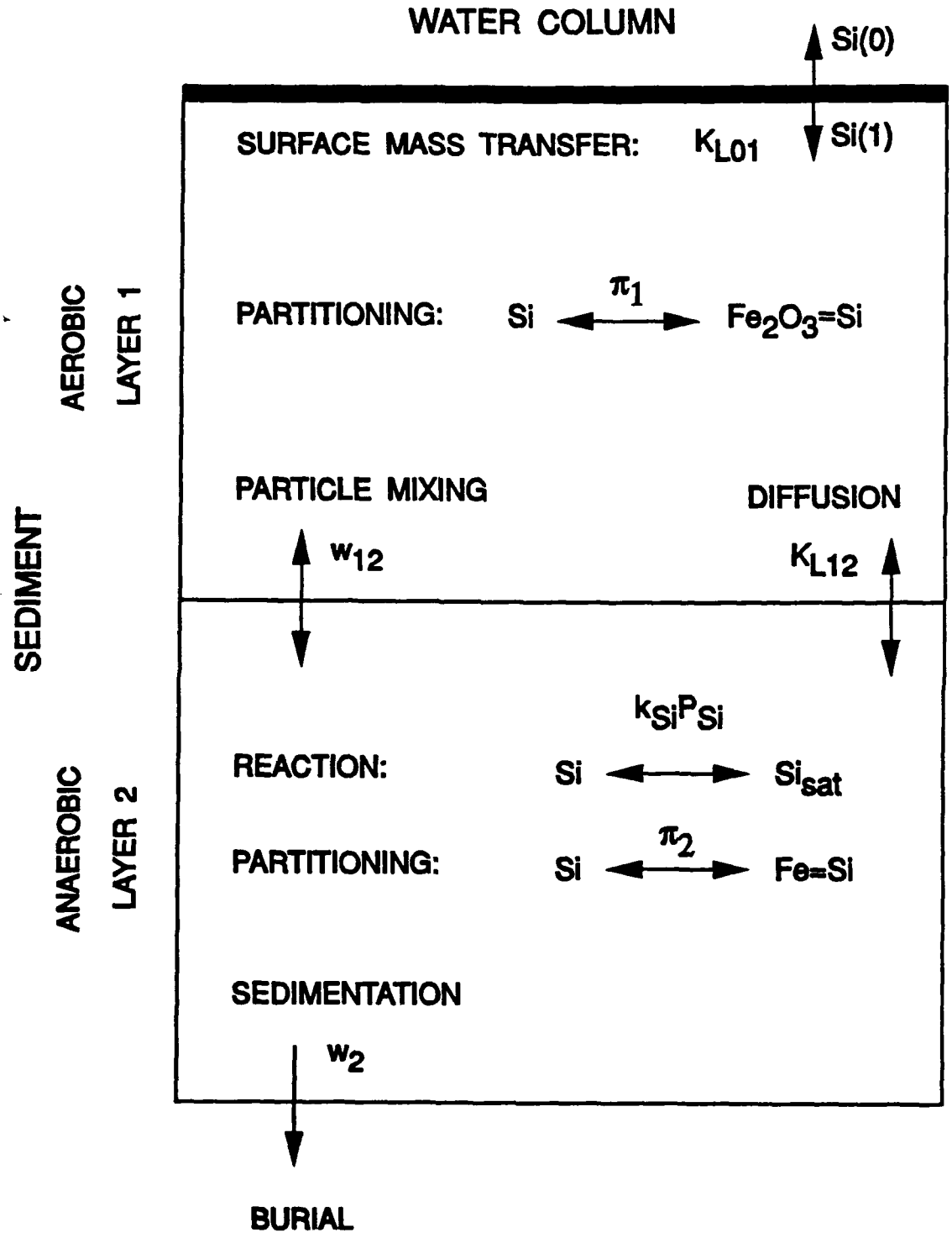

CHAP71L

Figure 7.1

C. Solutions

In order to use the general solutions obtained in Chapter IV, the two terms in this expression need to be related to their counterparts in the general solution. They represent, respectively, the source term in layer 2: J_{T2}; and a layer 2 reaction rate, K_2. Thus:

$$J_{T2} = K_{Si}\theta_{Si}^{(T-20)}[Si]_{sat}H_2 \tag{3}$$

$$K_2 = K_{Si}\theta_{Si}^{(T-20)}f_{d2} \tag{4}$$

Note that the source term is the dissolution reaction and the sink is the precipitation reaction. The dissolved fraction, f_{d2}, is included to allow for the possibility that a fraction of the dissolved silica is sorbed to the particles in the sediment. In addition to the dissolution source, the source from the overlying water, $s[Si(0)]$, must be included. This is considered below in the simplified solutions.

The solutions follow from the general equations given in Chapter IV. The layer 1 concentration of total dissolved silica is (eq.IV-19):

$$[Si(1)]_{T1} = \frac{J_{T2}}{sf_{d1} + (\kappa_{Si,2}f_{d2} + w_2)r_{21}} \tag{5}$$

where $\kappa_{Si,2} = K_2H_2$, eq.(4). The net flux of silica to the overlying water is:

$$J[Si] = s(f_{d1}[Si(1)] - [Si(0)]) \tag{6}$$

The result is:

$$J[Si] = sf_{d1}\frac{K_{Si}\theta_{Si}^{(T-20)}[Si]_{sat}H_2}{sf_{d1} + (w_2 + \kappa_{Si,2}f_{d2})r_{21}} - s[Si(0)] \tag{7}$$

where:

$$r_{21} = \frac{w_2 + f_{d2}\kappa_{Si,2} + w_{12} f_{p1} + K_{L12} f_{d1}}{w_{12} f_{p2} + K_{L12} f_{d2}} \tag{8}$$

and:

$$\kappa_{Si,2} = K_{Si}\theta_{Si}^{(T-20)} H_2 \tag{9}$$

the reaction velocity in layer 2.

1. Simplified Solution

In addition to the dissolution source in layer 2, there is the source of dissolved silica that is transferred from the overlying water to layer 1. This can be included as though it were a layer 2 source for the sake of convenience. This approximation is discussed in Chapter IV and used in the simplified phosphate flux model in Chapter VI, Section D. Hence, eq.(7) becomes:

$$J[Si] = s\left(\frac{K_{Si}\theta_{Si}^{(T-20)}[Si]_{sat} H_2 + s[Si(0)]}{s + \frac{f_{d2} r_{21}}{f_{d1}} K_{Si}\theta_{Si}^{(T-20)} H_2 + \frac{w_2 r_{21}}{f_{d1}}} - [Si(0)]\right) \tag{10}$$

This equation can be further simplified by assuming that:

$$\frac{f_{d2}}{f_{d1}} r_{21} \approx 1 \tag{11}$$

which corresponds to assuming that the silica partition coefficient is the same in both layers, $f_{d1} = f_{d2}$, and that particle mixing is sufficiently intense so that $r_{21} \approx 1$. The result is:

$$J[Si] = s\left(\frac{K_{Si}\theta_{Si}^{(T-20)}[Si]_{sat} H_2 + s[Si(0)]}{s + K_{Si}\theta_{Si}^{(T-20)} H_2 + \Omega} - [Si(0)]\right) \tag{12}$$

where

$$\Omega = \frac{w_2 r_{21}}{f_{d1}} \tag{13}$$

the equivalent burial rate. These simplifications render the equation suitable for fitting to the silica flux data using nonlinear regression.

2. Data Analysis

The parameters remaining to be estimated in eq.(12) are the reaction rate parameters: K_{Si}, θ_{Si}, and the equivalent burial rate, Ω. Table 7.1 presents the results of a nonlinear regression fit to observed silica fluxes and compares them to values reported in the literature. The measured versus predicted fluxes are compared in Fig. 7.2A. Although there is substantial scatter, the comparison suggests that the simplified steady state model is capable of reproducing the general behavior of silica fluxes.

A common analysis procedure for fluxes is to correlate them to temperature variation. Fig. 7.2B presents the data and model results versus temperature. The approximately exponential variation is captured reasonably well by the model. This is due to the temperature dependency of the silica dissolution kinetics, eq.(1). However, the predicted dependency is not exactly exponential. The relationship levels off at the higher temperatures. This is due to the appearance of the temperature correction term in both the numerator and denominator of the flux equation (12).

The model also predicts the magnitude of the silica flux. This is determined by the overall reaction rate for silica dissolution and the saturation concentration. The magnitude of the rate constant, K_{Si}, in turn depends on the quantity of particulate biogenic silica in the sediment and the specific rate constant, k_{Si}. Thus the concentration of the particulate biogenic silica is required.

D. Final Model

The final model for silica flux includes a mass balance for particulate biogenic silica:

$$H_2 \frac{dP_{Si}}{dt} = -S_{Si} H_2 - w_2 P_{Si} + J_{PSi} \qquad (14)$$

where P_{Si} is the concentration of particulate biogenic silica in the sediment and J_{PSi} is the depositional flux of particulate biogenic silica to the sediment. The loss terms are that due to dissolution, eq.(1), and burial. This equation can be thought of as the analog of the diagenesis equations for particulate organic carbon, nitrogen, and phosphorus. It specifies the rate at which particulate biogenic silica becomes dissolved silica.

The original formulation of the dissolution reaction was as a linear function of P_{Si} (Hurd, 1973). Recent data (Conley, 1989) suggests that the rate of silica dissolution is not linear in particulate silica concentration but rather that the dependency saturates at higher concentrations. Data from Lake Michigan sediments indicating that such a dependency is required, is shown in Fig. 7.3A. A Michaelis Menton expression, which is fitted to the data is also shown. Biogenic silica concentrations in Chesapeake Bay sediments range from less than 10 to 100 mg Si/g, Fig. 7.3B which is similar to these sediments from Lake Michigan.

The expression which includes the Michaelis Menton dependency of silica dissolution rate on particulate silica, P_{Si}, is:

$$S_{Si} = K_{Si} \theta_{Si}^{(T-20)} \frac{P_{Si}}{P_{Si} + K_{M,PSi}} ([Si]_{sat} - f_{d2}[Si(2)]) \qquad (15)$$

where the dissolution rate constant, K_{Si}, is now a first order constant with units of 1/day. The relationship between the specific rate constant, k_{Si}, and the first order rate constant, K_{Si}, is:

Simplified Silica Flux Model

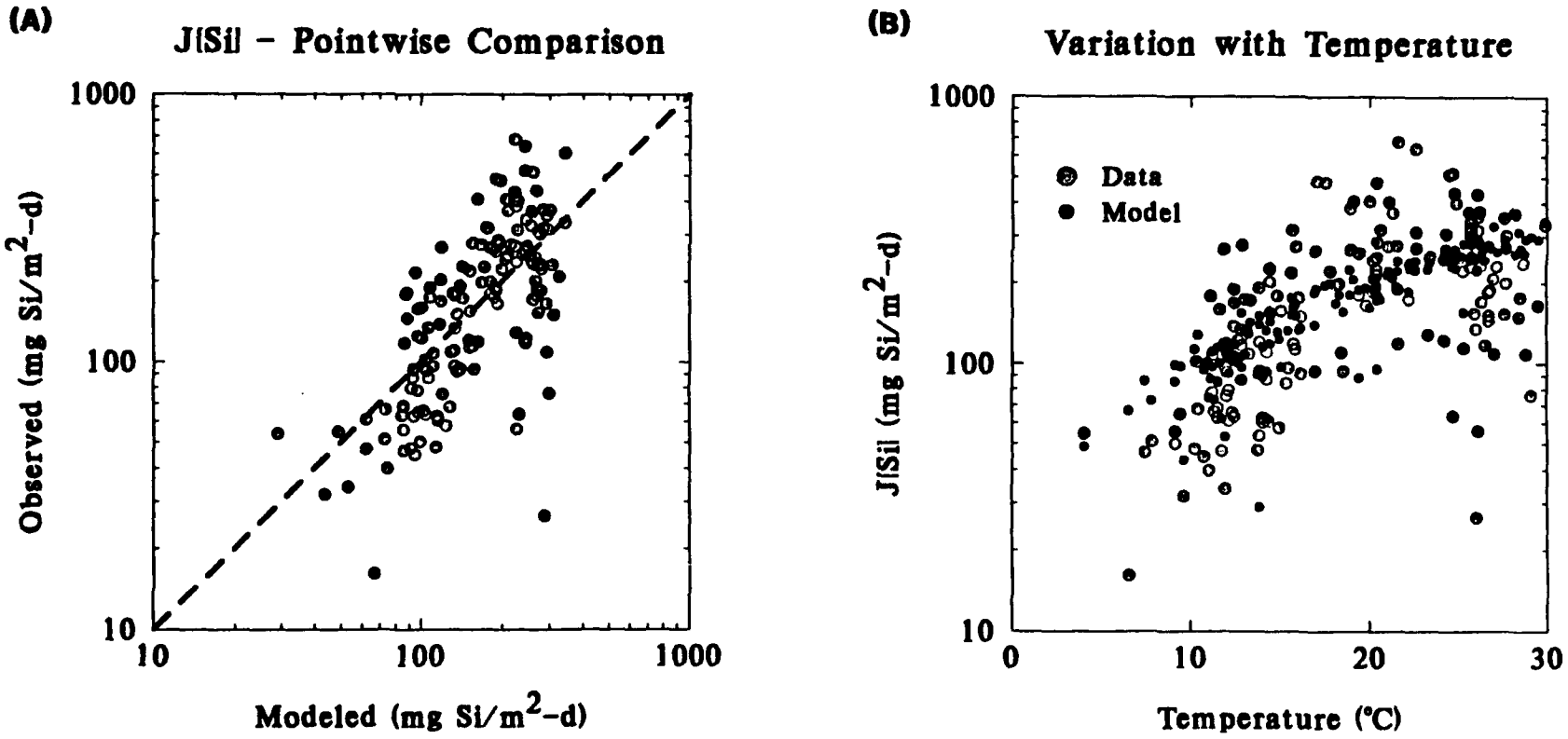

SIFLX2

Figure 7.2

Silica Flux and Biogenic Silica

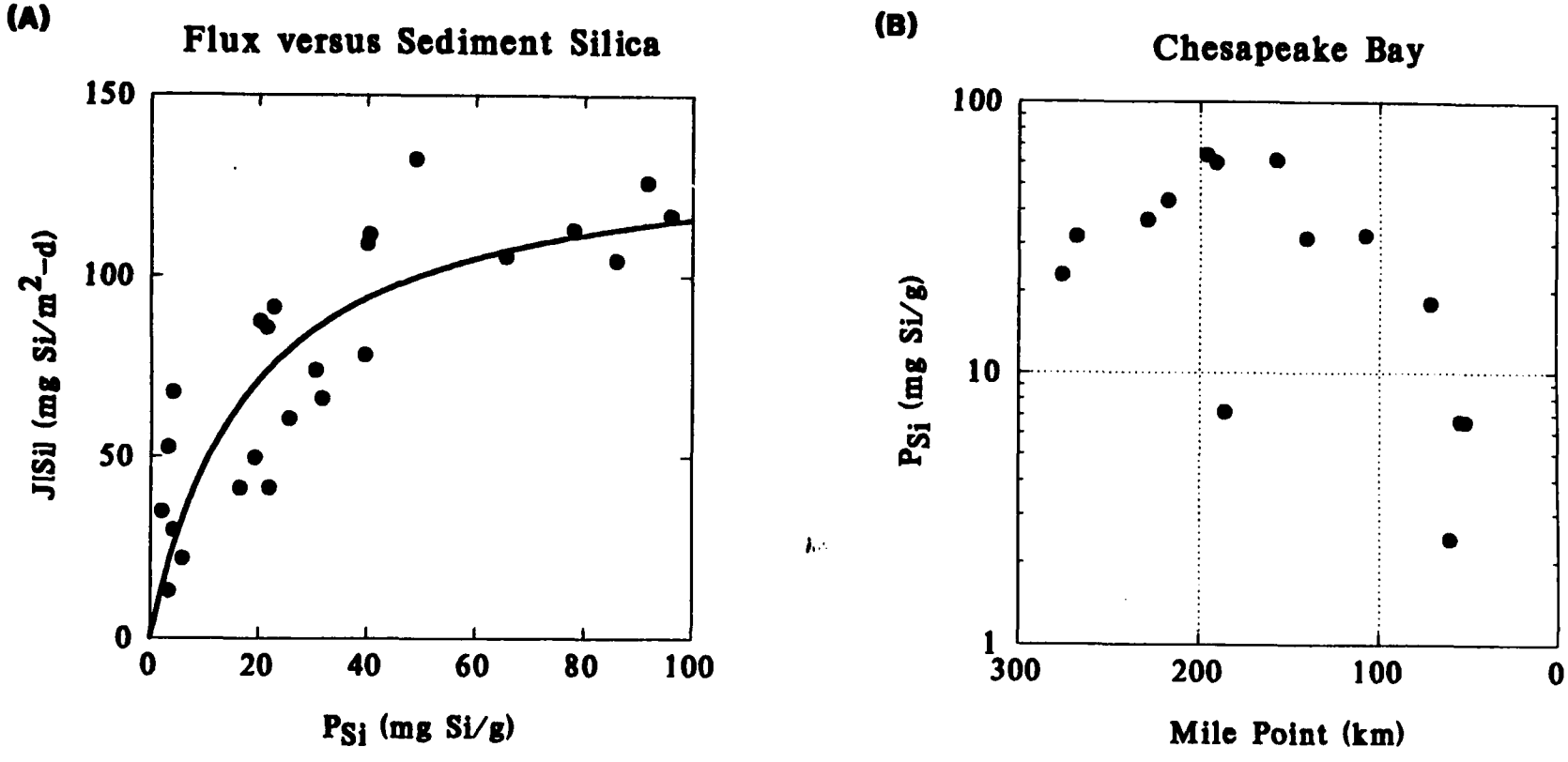

SIFLX3A

Figure 7.3

$$k_{Si} = \frac{K_{Si}}{P_{Si} + K_{M,PSi}} \qquad (16)$$

which follows from the definitions of the constants.

1. Steady State Model Results

The silica steady state model is evaluated by comparing the variation of the silica flux with respect to the ammonia flux. This is the same technique that was applied to the analysis of the oxygen (Chapter V, Section G) and phosphate fluxes (Chapter VI, Section E). The ammonia flux is used to compute ammonia diagenesis. Carbon diagenesis is obtained using the Redfield ratio. The silica to carbon ratio is established using water column particulate data. The full model equations are solved at steady state to obtain the predicted silica flux.

In order to perform this computation, the exogenous variables are required as a function of ammonia flux, since it indexes the computation. The variation in overlying water silica concentration with respect to ammonia flux is shown in Fig. 7.4A,B. The other exogenous variables that are necessary for the calculation have been presented in the previous chapters.

As in the case of phosphate flux model, the partitioning of silica in the aerobic layer is larger than in the anaerobic layer. The reason that partitioning is included is that silica is known to sorb to iron oxyhydroxide as shown in Fig. 7.5 (Sigg and Stumm, 1980). The magnitude of the partition coefficients are determined using the time variable model as discussed subsequently.

The results are compared to observed fluxes in Fig. 7.4C,D. Both the computed flux (solid line) and the estimated depositional flux (dashed line) are shown. The data and model for both the high and low DO subsets exhibit essentially the same behavior. Silica flux increases as ammonia flux increases. There appears to be no pronounced effect of overlying water DO on silica flux although the anaerobic fluxes are slightly larger than the corresponding aerobic fluxes. This can be seen by comparing the observed and computed fluxes to the depositional fluxes. For the computed fluxes, less silica is trapped and buried in the low DO subset, Fig. 7.4D, than the high

DO subset, Fig. 7.4C. This occurs for the same reason as for phosphate fluxes, except that the magnitude is smaller due to the smaller aerobic layer partition coefficient. The observations also appear to exhibit a slightly larger silica flux relative to the ammonia flux for the low DO subset although the effect is small.

The lack of a strong dissolved oxygen dependency is somewhat surprising because silica and phosphate sorb to iron oxyhydroxide to roughly the same extent as shown in Fig. 7.5. A somewhat stronger dependency is exhibited by the time variable model, for the same reasons as the phosphate flux model, namely the effect of storage and release of sorbed silica.

E. Conclusions

The silica fluxes can be computed with reasonable accuracy by the simplified steady state model which relates the flux to temperature. The primary disadvantage is that the model does not consider particulate silica. Thus there is no tie to the depositional flux, as is required by mass balance considerations. Further the dissolution kinetics do not reflect the variation in particulate silica.

These deficiencies are corrected in the final model. The results of steady state computations, indexed by the ammonia flux, are in reasonable agreement with the observations, grouped in this way. A small effect of overlying water DO is both computed and observed, which is somewhat surprising since the partitioning of silica to iron oxyhydroxide almost as strong as for phosphate.

Overlying Water Silica

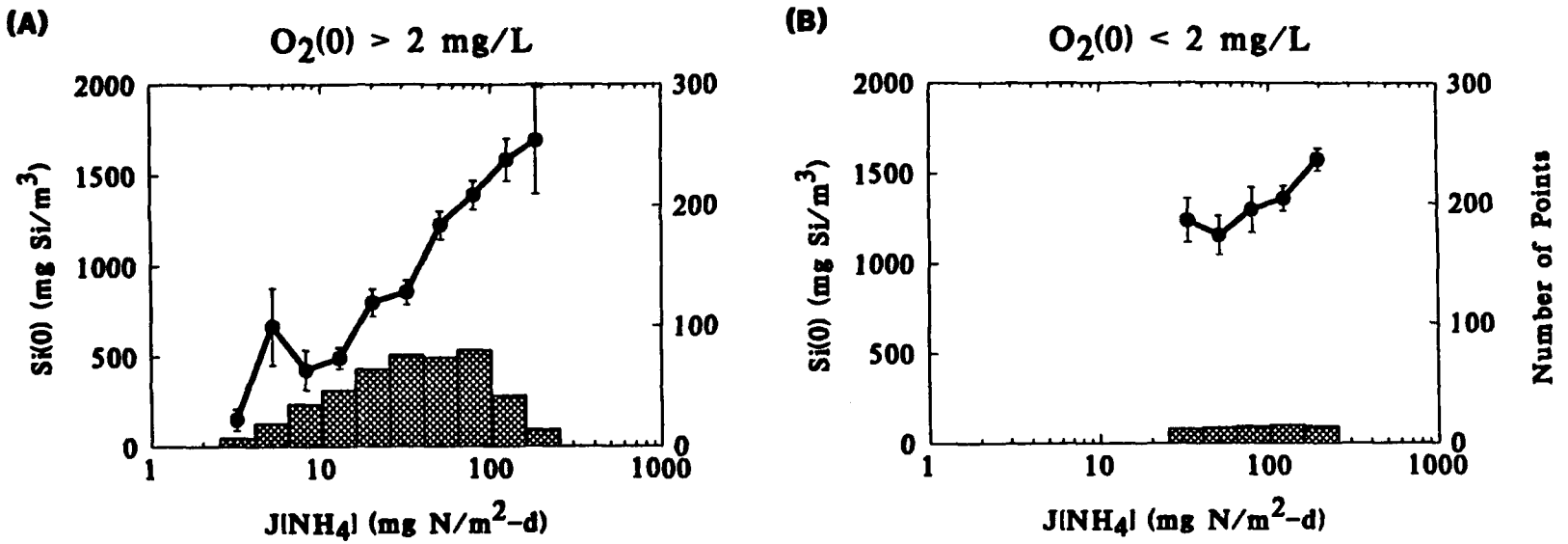

Comparison of Model and Data

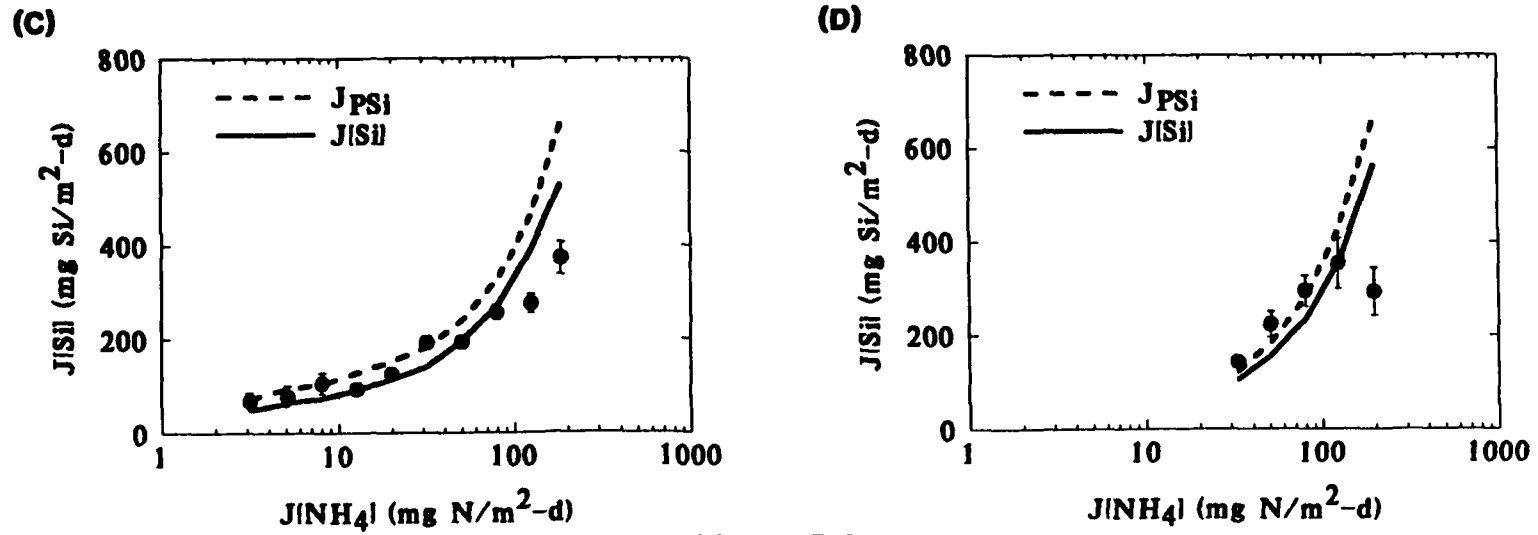

SISS3

Figure 7.4

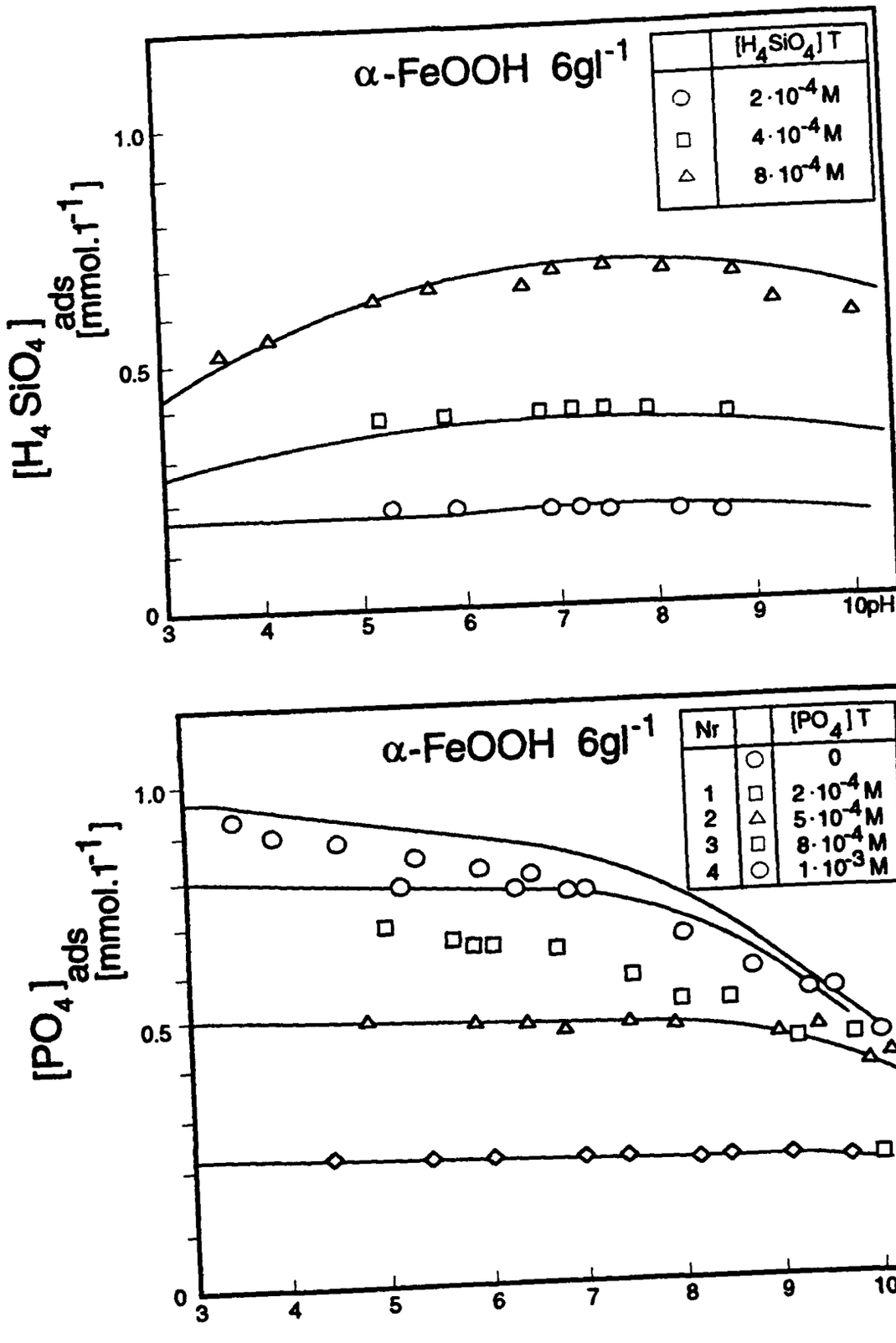
α-FeOOH 6gl-1
[H4SiO4]T
2·10-4M
4·10-4M
8·10-4M
[H4SiO4]ads [mmol.l-1]
1.0
0.5
0
3
4
5
6
7
8
9
10pH
α-FeOOH 6gl-1
Nr
[PO4]T
0
1 2·10-4M
2 5·10-4M
3 8·10-4M
4 1·10-3M
[PO4]ads [mmol.l-1]
1.0
0.5
0
3
4
5
6
7
8
9
10pH

Figure 7.5

Table 7.1
Silica Model Parameters

Parameter	Symbol	(a)	(b)	(c)	(d)	(e)
First order reaction rate (20 °C)	K_{Si} (/day)	0.103	0.039	0.2	0.09	0.02-0.2
Temperature coefficient	θ_{Si}	1.059	1.059*	1.08	-	1.0836
Saturation concentration	$[Si]_{sat}$ (mg Si/L)	26.5*	26.5*	26.5	33.7	39
Equivalent burial velocity	Ω (m/d)	0.0322	-	-	-	-
Half saturation constant	$K_{M,PSi}$ (mg Si/g)	-	19.8	100	-	-

*Assigned

(a)Nonlinear regression analysis using eq.(12)

(b)Nonlinear regression analysis of data from Conley et al., (1986), Conley and Schelske (1989).

(c)Steady state model parameters

(d)Ullman and Aller (1989)

(e)Lawson and Hurd (1978)

F. References

Boudreau, B.P. (1990). Asymptotic forms and solutions of the model for silica-opal diagenesis in bioturbated sediments. J. Geophysical Res. 95(C5): pp. 7367-7379.

Conley, D.J., Schelske, C.L., Dempsey, B.G. and Campbell, C.D. (1986). Distribution of biogenic silica in the surficial sediments of Lake Michigan. Can. J. Earth Sci. 23: pp. 1442-1449.

Conley, D.J. and Schelske, C.L. (1989). Processes controlling the benthic regeneration and sedimentary accumulation of biogenic silica in Lake Michigan. Arch. Hydrobiol. 116(1): pp. 23-43.

D'Elia, C.F. (1983). Chesapeake Bay nutrient and plankton dynamics: III. The annual cycle of dissolved silicon. Geochim. Cosmochim. Acta 47: pp. 1945-1955.

Hurd, D.C. (1973). Interactions of biogenic opal, sediment, and seawater in the central equatorial Pacific. Geochim. Cosmochim. Acta 37: pp. 2257-2282.

Hurd, D.C. (1983). On producing a more general model for biogenic silica dissolution. Am. J. Sci. 283: pp. 1-28.

Lawson, D.S., Hurd, D.C. and Pankratz, H.S. (1978). Silica dissolution rates of decomposing phytoplankton assemblages at various temperatures. Am. J. Sci. 278: pp. 1373-1393.

Lerman, A. (1975). Maintenance of steady state in oceanic sediments. Am. J. Sci. 275: pp. 609-635.

Rabouille, C. and Gaillard, J. (1990). The validity of steady-state flux calculations in early diagenesis: a computer simulation of deep-sea silica diagenesis. Deep-Sea Res. 37(4): pp. 625-646.

Schink, D.R. and Guinasso Jr., N.L. (1980). Processes affecting silica at the abyssal sediment-water interface. Biogeochimie de la Matiere Organique a l'Interface Eau-Sediment Marin. Colloq. Int. du CNRS. pp. 81-92.

Schink, D.R., Guinasso Jr., N.L. and Fanning, K.A. (1975). Processes affecting the concentration of silica at the sediment-water interface of the Atlantic Ocean. J. Geophys. Res. 80: pp. 3013-3031.

Sigg, L. and Stumm, W. (1980). The interaction of anions and weak acids with the hydrous goethite (a-FeOOH) surface. Colloids and Surfaces 2: pp. 101-117.

Ullman, W.J. and Aller, R.C. (1989). Nutrient release rates from the sediments of Saginaw Bay, Lake Huron. Hydrobiologia 171: pp. 127-140.

Wong, G.T.F. and Grosch, C.E. (1978). A mathematical model for the distribution of dissolved silicon in interstitial waters - an analytical approach. J. Mar. Res. 36: pp. 735-750.

VIII. DIAGENESIS

A. Introduction

The sediment flux modeling framework, diagrammed in Fig. 1.1, incorporates three processes. First, the sediment receives depositional fluxes of particulate organic carbon, nitrogen, phosphorus, and silica from the overlying water. Second, the mineralization of POM produces soluble intermediates which are quantified as diagenesis fluxes. Third, the intermediates react in the aerobic and anaerobic layers of the sediment and portions are returned to the overlying water as sediment fluxes.

The principal focus of the previous chapters has been on the last of these processes that leads to sediment fluxes. However, the computation of sediment fluxes requires that the magnitude of the diagenesis fluxes be known. In the previous chapters, ammonia diagenesis is estimated from the ammonia flux corrected for the fraction that is nitrified. Carbon, phosphorus, and silica diagenesis fluxes are estimated using stoichiometric ratios.

In this chapter, the diagenesis fluxes are explicitly computed using mass balance equations for the POM deposited to the sediment. A model for the diagenesis reaction is explicitly formulated. The source terms are the depositional fluxes of particulate C, N, and P to the sediment. The diagenesis fluxes result from the rate and extent of decay of particulate organic matter in the sediment. Since the mass balance equation and the kinetics of particulate silica mineralization have been formulated in Chapter VII Section D, they are not considered in this chapter.

The integration of the mass balance equations for POC, PON, and POP provides the time variable diagenesis fluxes that are the inputs for the NH_4, NO_3, H_2S, and PO_4 mass balance equations. These equations are integrated to compute the sediment fluxes as a function of time.

Because the model is no longer at steady state, the time variable model is capable of simulating the critical mechanism that modifies the temporal behavior of the fluxes, namely the storage and release of POM and diagenetically produced intermediates.

B. Mass Balance Equations

The mass balance equations for POC, PON, and POP, include an expression for the diagenesis reaction which specifies the rate and extent of breakdown of particulate organic matter. The earliest model for this reaction employed a single first order kinetic reaction rate (Berner, 1970). However, it was found subsequently to be incomplete. Particulate organic matter initially mineralizes rather rapidly, but then the reaction slows down. This has been successfully modeled by assigning a fraction of the POM to various reactivity classes (Westrich and Berner, 1984). These are termed "G classes" after the symbols used to identify POM in each class.

Each class represents a portion of the organic material that reacts at a specific rate. The reaction rates for each class are approximately an order of magnitude smaller than the previous class. For this sediment model application three G classes are chosen representing three scales of reactivity: G_1, rapidly reactive (20 day half life); G_2, more slowly reactive (1 year half life); and G_3, which, for this model, is taken to be non-reactive.

The varying reactivity of the G classes control the time scale over which changes in depositional fluxes will be reflected in changes in diagenesis fluxes. If the reactive POM fractions were reacting rapidly, then the diagenesis flux would equal the reactive fraction of the depositional flux since there would be no time lag introduced by mineralization.

The mass balance equations for particulate organic carbon, nitrogen, and phosphorus are similar. Consider POC, and let $G_{POC,i}$ be the concentration of POC in the i^{th} diagenesis class ($i = 1, 2$ or 3). The mass balance equation for $G_{POC,i}$ in the anaerobic layer is:

$$H_2 \frac{dG_{POC,i}}{dt} = -K_{POC,i}\theta_{POC,i}^{(T-20)} G_{POC,i} H_2 - w_2 G_{POC,i} + f_{POC,i} J_{POC} \qquad (1)$$

where:

$G_{POC,i}$ concentration of particulate organic carbon in reactivity class i in layer 2; [M/L^3]

$K_{POC,i}$ first order reaction rate coefficient: [T^{-1}]

$\theta_{POC,i}$ temperature coefficient

w_2 sedimentation velocity (L/T)

J_{POC} depositional flux of POC from the overlying water to the sediment. [M/L^2-T]

$f_{POC,i}$ fraction of J_{POC} that is in the ith G class

The aerobic layer is not included because of its small depth relative to the anaerobic layer: H_1 ~ 0.1 cm relative to H_2 = 10 cm. Even if aerobic diagenesis were occurring at a more rapid rate, say ten times faster, the contribution would still be small (1/10) relative to the anaerobic layer:

The kinetic coefficients are:

$K_{POC,1}$	reaction rate constant for $G_{POC,1}$	3.50E-02	day^{-1}
$\theta_{POC,1}$	temperature coefficient for $G_{POC,1}$	1.100	-
$f_{POC,1}$	fraction in G_1	0.65	
$K_{POC,2}$	reaction rate constant for $G_{POC,2}$	1.80E-03	day^{-1}
$\theta_{POC,2}$	temperature coefficient for $G_{POC,2}$	1.150	-
$f_{POC,2}$	fraction in G_2	0.20	
$K_{POC,3}$	reaction rate constant for $G_{POC,3}$	0.0	day^{-1}
$\theta_{POC,3}$	temperature coefficient for $G_{POC,3}$	-	-
$f_{POC,3}$	fraction in G_3	0.15	

The reaction rates and temperature coefficients for $G_{POC,1}$ and $G_{POC,2}$ are representative of values reported in the literature, see Table 8.1. The G fractions are derived from the calibration as discussed below.

Once the mass balance equations for $G_{POC,1}$ and $G_{POC,2}$ are solved, the carbon diagenesis flux, J_C, is computed from the rate of mineralization of the two reactive G classes:

$$J_C = \sum_{i=1}^{2} K_{POC,i}\theta_{POC,i}^{(T-20)} G_{POC,i} H_2 \tag{2}$$

The mass balance equations for particulate nitrogen and phosphorus are completely analogous.

$$H_2 \frac{dG_{PON,i}}{dt} = -K_{PON,i}\theta_{PON,i}^{(T-20)} G_{PON,i} H_2 - w_2 G_{PON,i} + f_{PON,i} J_{PON} \tag{3}$$

$$H_2 \frac{dG_{POP,i}}{dt} = -K_{POP,i}\theta_{POP,i}^{(T-20)} G_{POP,i} H_2 - w_2 G_{POP,i} + f_{POP,i} J_{POP} \tag{4}$$

as are the equations for the diagenesis fluxes:

$$J_N = \sum_{i=1}^{2} K_{PON,i}\theta_{PON,i}^{(T-20)} G_{PON,i} H_2 \tag{5}$$

$$J_P = \sum_{i=1}^{2} K_{POP,i}\theta_{POP,i}^{(T-20)} G_{POP,i} H_2 \tag{6}$$

The reaction rates and temperature coefficients for particulate organic nitrogen and phosphorus are identical to those listed above for particulate organic carbon. The appropriate G fractions are discussed below.

C. Diagenesis Stoichiometry

As pointed out by Berner (1977), the ratio of the changes in depth of two constituents in pore water can be used to deduce the stoichiometry of the decaying organic matter. This can be seen by examining the solution of a one dimensional model for organic matter decay and end-product accumulation. Consider two reactive G classes. Each class, $G_i(z)$, is assumed to be

decaying following first order kinetics. The vertical transport term represents the burial by sedimentation. For simplicity, no other particle transport terms are considered. The mass balance equation for POC is:

$$w_2 \frac{dG_{POC,i}}{dz} = -K_{POC,i} G_{POC,i} \tag{7}$$

with the analogous equation for PON:

$$w_2 \frac{dG_{PON,i}}{dz} = -K_{PON,i} G_{PON,i} \tag{8}$$

The solutions are:

$$G_{POC,i}(z) = G_{POC,i}(0) e^{-K_{POC,i} z / w_2} \tag{9}$$

and

$$G_{PON,i}(z) = G_{PON,i}(0) e^{-K_{PON,i} z / w_2} \tag{10}$$

where $G_{POC,i}(0) = J_{POC,i}/w_2$ and $G_{PON,i}(0) = J_{PON,i}/w_2$, the concentrations at $z = 0$. The depositional fluxes are $J_{POC,i}$ and $J_{PON,i}$.

The decay of PON produces ammonia and the decay of POC consumes sulfate. Thus the relationship between ammonia generation and sulfate depletion should be a measure of the nitrogen to carbon ratio of the decaying organic matter. The mass balance equation for pore water ammonia is:

$$-D_{NH4} \frac{d^2[NH_4(z)]}{dz^2} + w_2 \frac{d[NH_4(z)]}{dz} = \sum_{i=1}^{2} K_{PON,i} G_{PON,i} \tag{11}$$

and for pore water sulfate is:

$$-D_{SO4}\frac{d^2[SO_4(z)]}{dz^2}+w_2\frac{d[SO_4(z)]}{dz}=-\alpha_{SO4,C}\sum_{i=1}^{2}K_{POC,i}G_{POC,i} \qquad (12)$$

where D_{NH4} and D_{SO4} are the pore water diffusion coefficients for ammonia and sulfate respectively, and $\alpha_{SO4,C}$ is the stoichiometric ratio of SO_4 reduced to POC oxidized. The solutions of these equations are:

$$[NH_4(z)]=[NH_4(0)]+\frac{G_{PON,1}(0)}{1+D_{NH4}K_{PON,1}/w_2^2}[1-e^{-K_{PON,1}z/w_2}]$$

$$+\frac{G_{PON,2}(0)}{1+D_{NH4}K_{PON,2}/w_2^2}[1-e^{-K_{PON,2}z/w_2}] \qquad (13)$$

and:

$$[SO_4(z)]=[SO_4(0)]-\alpha_{SO4,C}\{\frac{G_{POC,1}(0)}{1+D_{SO4}K_{POC,1}/w_2^2}[1-e^{-K_{POC,1}z/w_2}]$$

$$+\frac{G_{POC,2}(0)}{1+D_{SO4}K_{POC,2}/w_2^2}[1-e^{-K_{POC,2}z/w_2}]\} \qquad (14)$$

The key to evaluating the stoichiometry of the decaying POM is to find the ratio of sulfate to ammonia change: $d[SO_4(z)]/d[NH_4(z)]$. This can be found by dividing $d[SO_4(z)]/dz$ by $d[NH_4(z)]/dz$. The result is:

$$\frac{d[SO_4(z)]}{d[NH_4(z)]}=-\alpha_{SO4,C}$$

$$\cdot\frac{\left\{\frac{G_{POC,1}(0)K_{POC,1}e^{-K_{POC,1}z/w_2}}{w_2^2+D_{SO4}K_{POC,1}}+\frac{G_{POC,2}(0)K_{POC,2}e^{-K_{POC,2}z/w_2}}{w_2^2+D_{SO4}K_{POC,2}}\right\}}{\left\{\frac{G_{PON,1}(0)K_{PON,1}e^{-K_{PON,1}z/w_2}}{w_2^2+D_{NH4}K_{PON,1}}+\frac{G_{PON,2}(0)K_{PON,2}e^{-K_{PON,2}z/w_2}}{w_2^2+D_{NH4}K_{PON,2}}\right\}} \qquad (15)$$

As it stands, this ratio does not provide a useful result. However, for most situations, the following simplification is available: $w_2^2 \ll DK$ for each of the denominator terms. This follows from order of magnitude estimates of the various parameters:

Table 8.2
Diagenesis Parameters

w_2	$\sim 10^{-5}$	m/d
D_{SO4}	$\sim 10^{-4}$	m^2/d
D_{NH4}	$\sim 10^{-4}$	m^2/d
$K_{POC,1}$	$\sim 10^{-2}$	/d
$K_{POC,2}$	$\sim 10^{-3}$	/d
w_2^2	$\sim 10^{-10}$	$(m/d)^2$
$D_{SO4}K_{POC,1}$	$\sim 10^{-6}$	$(m/d)^2$
$D_{SO4}K_{POC,2}$	$\sim 10^{-7}$	$(m/d)^2$

A comparison of the last three rows demonstrates that the approximation is valid. The sedimentation velocity used in the analysis corresponds to ~ 0.4 cm/yr, and an order of magnitude increase would not change the conclusion. Thus, eq.(16) becomes:

$$\frac{d[SO_4(z)]}{d[NH_4(z)]} = -a_{SO4,C}\left\{\frac{D_{NH4}}{D_{SO4}}\right\}\left\{\frac{G_{POC,1}(0)e^{-K_{POC,1}z/w_2} + G_{POC,2}(0)e^{-K_{POC,2}z/w_2}}{G_{PON,1}(0)e^{-K_{PON,1}z/w_2} + G_{PON,2}(0)e^{-K_{PON,2}z/w_2}}\right\} \quad (17)$$

Define the ratio of carbon to nitrogen in POM as:

$$a_{C,N} = \frac{G_{POC,1}(0)}{G_{PON,1}(0)} = \frac{G_{POC,2}(0)}{G_{PON,2}(0)} \quad (18)$$

SEDIMENT FLUX MODEL

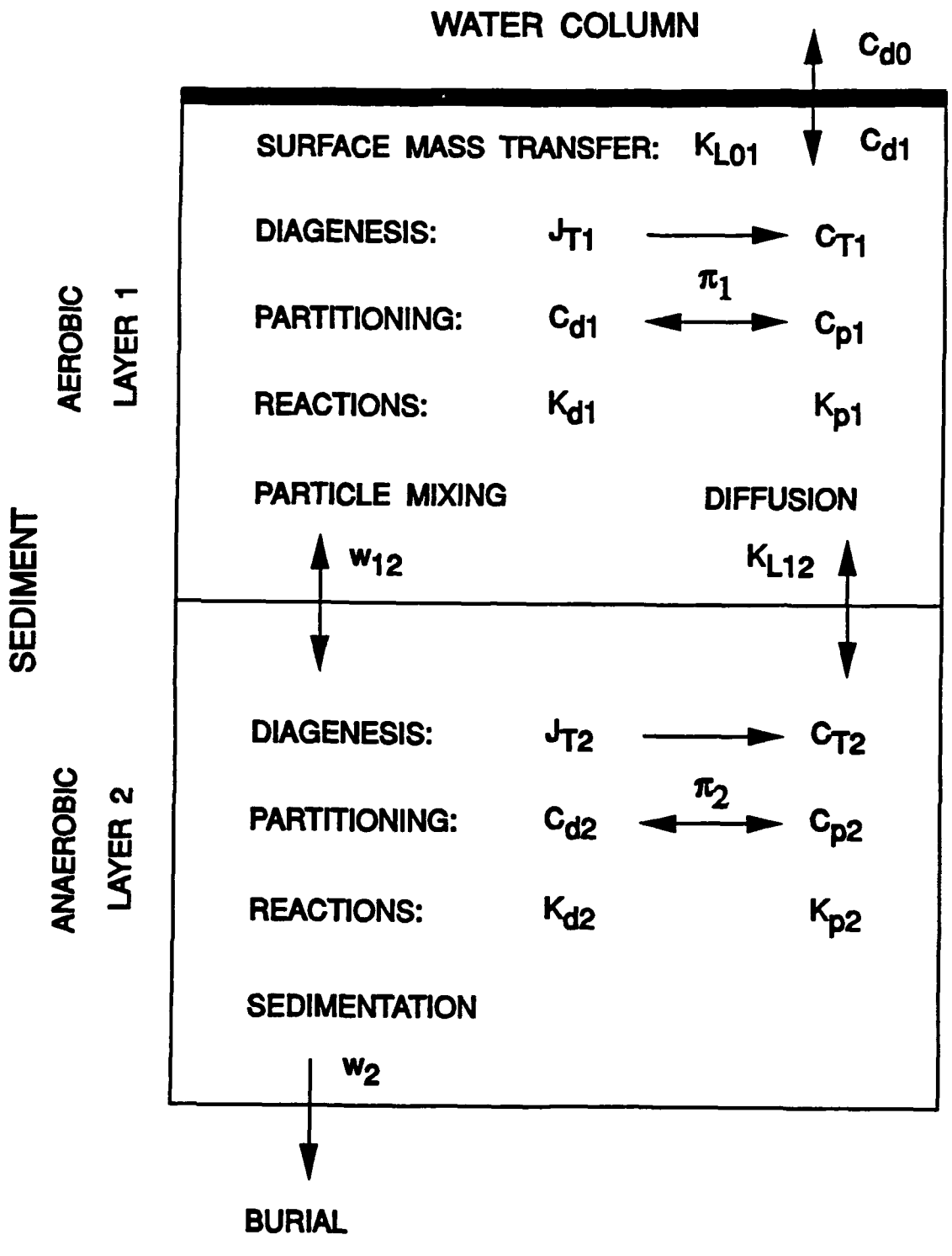

CHAP41L

Figure 4.1

where we assume for simplicity that G_1 and G_2 organic matter have the same C to N stoichiometry. Then eq.(17) becomes:

$$\frac{d[SO_4(z)]}{d[NH_4(z)]} = -\alpha_{SO4,C}\left\{\frac{D_{NH4}}{D_{SO4}}\right\}\alpha_{C,N} \cdot \left\{\frac{G_{PON,1}(0)e^{-K_{POC,1}z/w_2} + G_{PON,2}(0)e^{-K_{POC,2}z/w_2}}{G_{PON,1}(0)e^{-K_{PON,1}z/w_2} + G_{PON,2}(0)e^{-K_{PON,2}z/w_2}}\right\} \quad (19)$$

If the decay rates are the same for carbon and nitrogen than the term in braces equals one and:

$$\alpha_{C,N} = -\alpha_{C,SO4}\left\{\frac{D_{SO4}}{D_{NH4}}\right\}\frac{d[SO_4(z)]}{d[NH_4(z)]} \quad (20)$$

where $\alpha_{C,SO4} = \alpha^{-1}_{SO4,C}$.

Thus the carbon to nitrogen ratio $\alpha_{C,N}$ can be found from an analysis of the ratio of vertical changes in sulfate and ammonia, eq.(20). Similarly, $\alpha_{C,P}$ can be found using the phosphate and sulfate pore water profiles. Since the data set to be analyzed also includes alkalinity, the relationship between sulfate consumption and alkalinity generation can also be investigated.

The data are processed as follows. The changes in sulfate, ammonia, phosphate, and alkalinity over a depth interval z_1 to z_2 are computed from formulas of the form:

$$\Delta[SO_4(\bar{z}_{12})] = [SO_4(z_2)] - [SO_4(z_1)] \quad (21)$$

where $\bar{z}_{12} = \frac{1}{2}(z_1 + z_2)$, the average depth. They are multiplied by the ratio of the diffusion coefficients, listed in Table 8.3.

Table 8.3
Diffusion Coefficients, D.
(from Berner, 1980)

Ion	D (10^{-6} cm^2/sec)
$SO_4^=$	4.5
NH_4^+	9.8
$HPO_4^=$	3.6
Cl^-	10.2
HCO_3^-	~4.5

In addition, the sulfate to carbon stoichiometry, $\alpha_{C,SO4}$, is required. The stoichiometric equation that describes sulfate reduction eq.(V-1), indicates that 2 moles of CH_2O react with 1 mole of sulfate, so that $\alpha_{C,SO4}$ = 2 mol C/mol SO_4. Hence:

$$\alpha_{C,N} = -2\frac{D_{SO4}}{D_{NH4}}\frac{\Delta[SO_4(\bar{z}_{12})]}{\Delta[NH_4(\bar{z}_{12})]} \tag{22}$$

$$\alpha_{C,P} = -2\frac{D_{SO4}}{D_{PO_4}}\frac{\Delta[SO_4(\bar{z}_{12})]}{\Delta[PO_4(\bar{z}_{12})]} \tag{23}$$

$$\alpha_{SO4,Alk} = -\frac{D_{SO4}}{D_{HCO3}}\frac{\Delta[SO_4(\bar{z}_{12})]}{\Delta[Alk(\bar{z}_{12})]} \tag{24}$$

for concentrations in molar units. The results are estimates of the ratio of the carbon to nitrogen and phosphorus, and the ratio of sulfate consumed to alkalinity produced by diagenesis, in this depth interval in the sediment.

The full Bricker pore water data set is used, with the exception of the measurements that were affected by hurricane Agnes - the steady state assumption is questionable - and any pore water interval for which the sulfate concentration at z_1 is < 5mM. The latter restriction is to insure that sulfate is the primary electron acceptor for the change that occurs in the interval z_1 to z_2, which is assumed in the analysis.

The stoichiometry that results of this analysis are plotted versus $\bar{z}_{12}$ in Fig. 8.1. The symbols represent the mean ± the standard error of the mean. The number of data points are nearly 100 in the 0 - 1 cm interval to approximately 10 at the lower depths. The decrease in number of points to due to the decrease of sulfate below 5mM at the lower depths of the sediment. The computed ratios are compared to the stoichiometry suggested by Redfield (1963) to represent phytoplankton:

$$C_{106}H_{263}O_{110}N_{16}P_1 = (CH_2O)_{106}(NH_3)_{16}(H_3PO_4) \qquad (25)$$

Thus, Redfield stoichiometry is: $\alpha_{C:N}$ = 6.62 mol C/mol N = 5.68 gC/gN, and $\alpha_{C:P}$ = 106 mol C/mol P = 41 gC/gP. The alkalinity stoichiometry is the same as the sulfate - carbon stoichiometry.

As shown in Fig. 8.1, the observed C/N ratios and the alkalinity stoichiometry are reasonably close to Redfield stoichiometry. The carbon to phosphorus stoichiometry is slightly enriched in P relative to the Redfield ratio. This may be due to an additional source of inorganic phosphorus that is settling to the sediment. However, the results are close enough to justify the assumption of Redfield stoichiometry in the analysis that follows.

D. Diagenesis Kinetics

The rate at which organic material mineralizes can also be determined by measuring the rate at which reactants are consumed and end-products accumulate in a closed reaction vessel. The situation is first analyzed theoretically and then the results are applied to a set of data from Chesapeake Bay sediments.

1. Theory

Consider an experiment in which a sample of sediment is retrieved, an anaerobic incubation is started at t = 0, and the production of ammonia is monitored. The initial concentrations of reactive PON are $G_{PON,1}(0)$ and $G_{PON,2}(0)$. The decay of each PON fraction follows first order kinetics:

$$\frac{dG_{PON,i}}{dt} = -K_{PON,i}G_{PON,i} \tag{26}$$

so that:

$$G_{PON,i}(t) = G_{PON,i}(0)e^{-K_{PON,i}t} \tag{27}$$

The mass balance equation for ammonia is:

$$\frac{d[NH_4]}{dt} = K_{PON,1}G_{PON,1} + K_{PON,2}G_{PON,2} \tag{28}$$

so that:

$$[NH_4(t)] = [NH_4(0)] + G_{PON,1}(0)(1 - e^{-K_{POC,1}t}) + G_{PON,2}(0)(1 - e^{-K_{POC,2}t}) \tag{29}$$

Ammonia increases as both G_1 and G_2 mineralize at their individual rates.

Diagenesis Stoichiometry

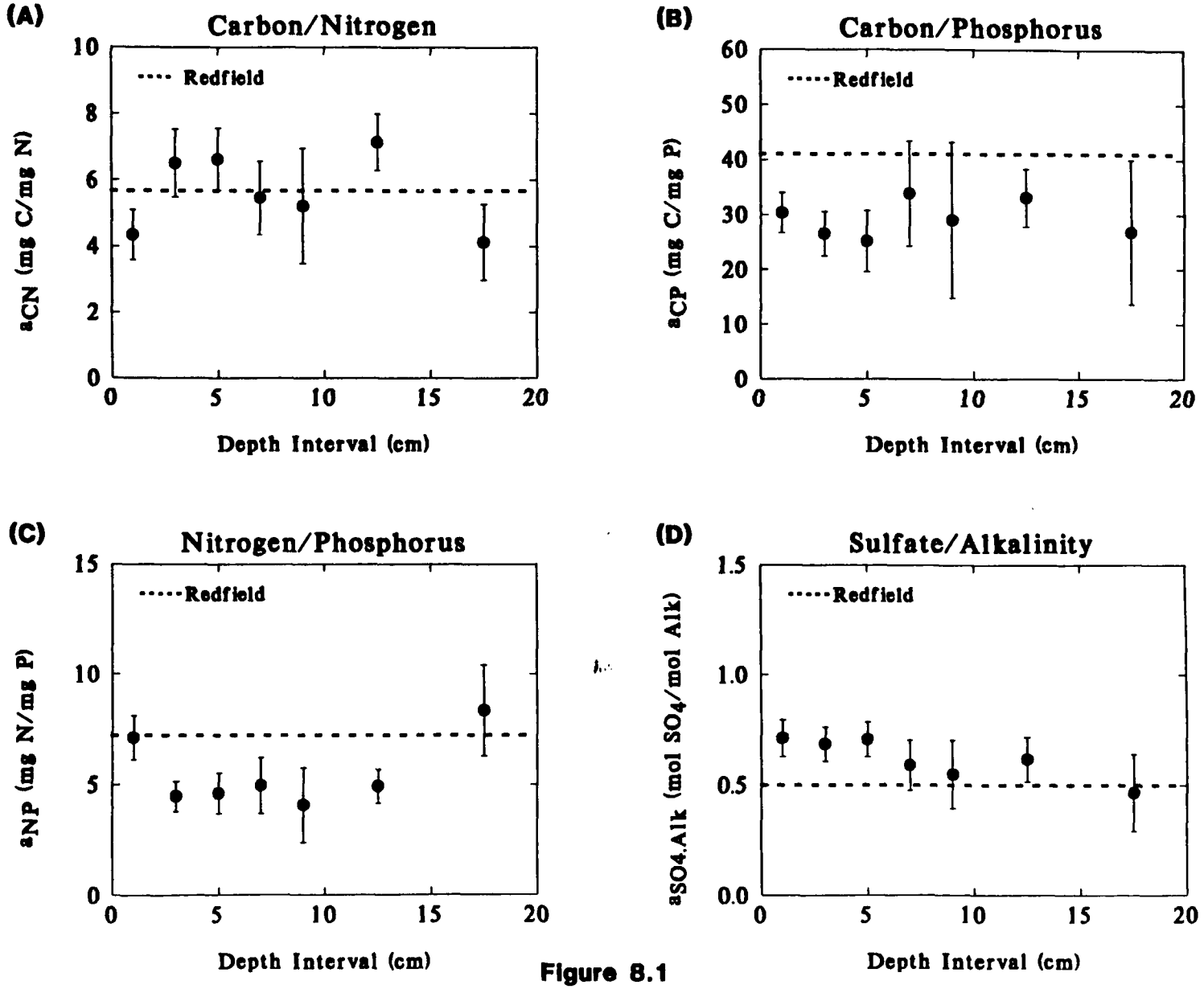

BRICKH2D

Figure 8.1

It is interesting to examine which G component contributes the majority of the ammonia released. It depends on the relative amounts in the sediment. This can be approximated by solving the PON mass balance equation (3) at steady state:

$$G_{PON,i} = \frac{f_{PON,i} J_{PON}}{K_{PON,i} H_2 + w_2} \tag{30}$$

where a constant T = 20 ℃ is assumed. Substituting this result in eq.(29) and noting that $K_{PON,i} H_2 \gg w_2$ yields:

$$[NH_4(t)] = [NH_4(0)] + \frac{J_{PON}}{H_2}\left\{ f_{PON,1} \frac{(1 - e^{-K_{PON,1} t})}{K_{PON,1}} + f_{PON,2} \frac{(1 - e^{-K_{PON,2} t})}{K_{PON,2}} \right\} \tag{31}$$

where $f_{PON,i}$ is the fraction of PON in component G_i.

Two points of interest emerge. Initially t is small and:

$$\frac{1 - e^{-K_{PON,1} t}}{K_{PON,1}} \approx \frac{1 - (1 - K_{PON,1} t + \cdots)}{K_{PON,1}} \approx t \tag{32}$$

so that:

$$[NH_4(t)] \approx [NH_4(0)] + \frac{J_{PON}}{H_2}\{ f_{PON,1} t + f_{PON,2} t \} \tag{33}$$

Each G component contributes to the ammonia increase in proportion to its PON fraction, $f_{PON,i}$, in the sediment.

This is also what is occurring when the sediments are continuously receiving depositional fluxes of PON and generating ammonia fluxes. To see this, consider the formula for ammonia diagenesis, eq.(5):

$$J_N = K_{PON,1} H_2 G_{PON,1} + K_{PON,2} H_2 G_{PON,2} \tag{34}$$

and substituting the steady state concentrations, eq.(30), yields:

$$\begin{aligned} J_N &= K_{PON,1} H_2 \frac{f_{PON,1} J_{PON}}{K_{PON,1} H_2 + w_2} + K_{PON,2} H_2 \frac{f_{PON,2} J_{PON}}{K_{PON,2} H_2 + w_2} \\ &\approx f_{PON,1} J_{PON} + f_{PON,2} J_{PON} \end{aligned} \tag{35}$$

so that each component contributes in proportion to its fractional composition in J_{PON}

By contrast, as $t \to \infty$ eq.(31) becomes

$$[NH_4(\infty)] = [NH_4(0)] + \frac{J_{PON}}{H_2}\left\{\frac{f_{PON,1}}{K_{PON,1}} + \frac{f_{PON,2}}{K_{PON,2}}\right\} \tag{36}$$

Now the fractional contribution includes the inverse of the reaction rates of the components. Since $K_{PON,2} \ll K_{PON,1}$ the G_2 component dominates the contribution. The reason is that G_2 is the most plentiful reactive component in the sediment and it all eventually reacts to produce ammonia.

The difference between the two extremes can be understood as follows. Initially the results are analogous to the field situation where the depositional flux continuously supplies PON to the sediment. In a kinetics experiment, however, the depositional flux is not present and as time passes the fractions contribute in proportion to their concentrations in the sediment at the time of collection.

A numerical computation can clarify the situation. For a depositional flux of J_{PON} = 50 mg N/m^2-d and a sedimentation velocity of w_2 = 0.25 cm/yr and m_2 = 0.5 kg/L, the sediment composition is given in Table 8.4:

Table 8.4
Kinetic Parameters and Sediment Components

	G_1	G_2	G_3
$f_{PON,i}$	0.65	0.25	0.10
$K_{PON,i}$ (d^{-1})	0.035	0.0018	0
$G_i(0)$ (mg N/g)	0.019	0.136	1.46
$G_i(0)$ (%)	1.2	8.4	90.4

where $G_1(0)$ is computed as follows, eq.(30):

$$G_1(0) = [J_{PON} f_{PON,1}]/[K_{PON,1} H_2 m_2] = [(50 mg N/m^2 - d)(0.65)]/[(0.035 d^{-1})(0.1 m)(0.5 kg/L)]$$

The sediment is ~ 90% G_3, ~ 10% G_2, and ~ 1%, G_1. The fractional contributions to diagenesis flux and total ammonia release are:

Table 8.5
Fractional Contributions

	G_1	G_2
J_N (eq.35)	72%	28%
$NH_4(\infty)$ (eq.36)	12%	88%

The difference between the two cases is entirely due to the lack of a depositional flux in the kinetics experiment. This does not diminish the utility of kinetic experiments, it just clarifies the analysis to which the data should be subjected.

2. Application to Chesapeake Bay Sediments

A set of sediment mineralization experiments have been performed using sediments from lower Chesapeake Bay (Burdige, 1989). This section presents an analysis of the results of these experiments. A more detailed analysis has subsequently been presented (Burdige, 1991).

Sediment from five stations were retrieved. Three depth intervals were chosen to represent various ages of sediment organic material: 0-2 cm; 5-7 cm; and 12-15 cm. Samples from each depth interval were composited. A slurry was made with additional seawater and a series of 50 mL vessels were filled and incubated at 25 °C. At various times during a 180 day incubation, a vessel was centrifuged and the concentrations of NH_4, CO_2, SO_4, and PO_4 in the filtrate were measured. Data from the surface layer incubations are presented in Fig. 8.2 for four stations. The decrease in sulfate and the increases in the other constituents is the result of POM mineralization.

a. Reaction Rates

With two reactive G components, it is expected that the concentrations would increase or decrease following equations of the form:

$$c(t) = c(0) \pm \frac{J_{POM}}{H_2}\left\{ f_{POM,1}\frac{(1-e^{-K_{POM,1}t})}{K_{POM,1}} + f_{POM,2}\frac{(1-e^{-K_{POM,2}t})}{K_{POM,2}} \right\} \qquad (37)$$

where POM represents POC, PON, POP as appropriate and the minus sign applies to sulfate consumption. Fig. 8.2E presents a cumulative plot of the two terms representing the contributions of G_1 and G_2, eq.(31). The parameters are listed in Table 8.4.

In principle, this equation should be fit to the data from each station and depth interval to determine the relevant parameters: $c(0)$, J_{POM}, $f_{POM,1}$, $K_{POM,1}$, $f_{POM,2}$, and $K_{POM,2}$. Unfortunately, there are an insufficient number of data points to reliably estimate this many parameters. As a consequence, a simplified equation is fit to the data:

Diagenesis Kinetics

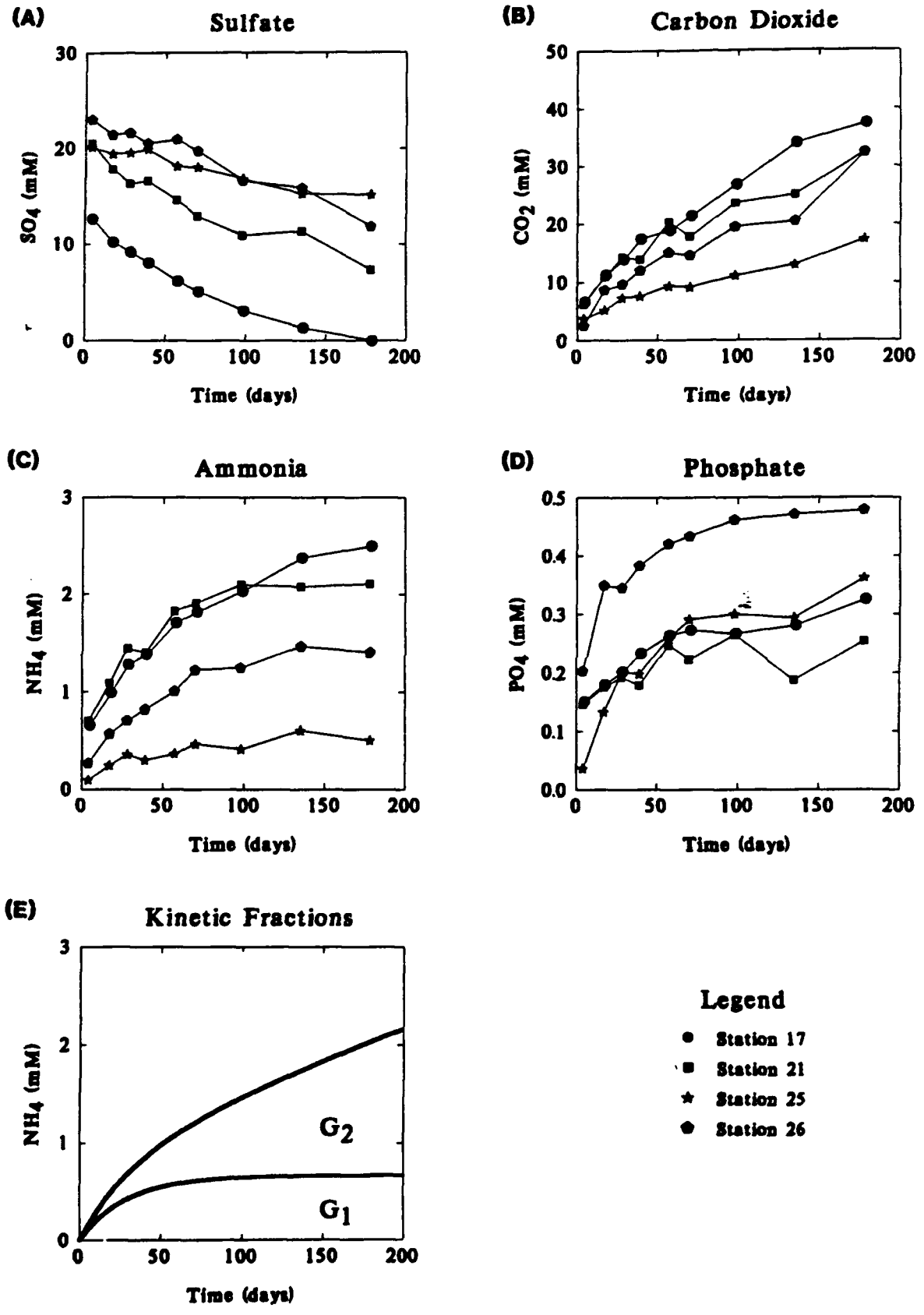

BURDGKP3

Figure 8.2

$$c(t) = c(0) \pm m_2 G(0)(1 - e^{-K_{POM,1} t}) \quad (38)$$

where m_2 is the solids concentration in the slurry and $G(0)$ is the reactive organic matter on a dry weight basis. Fig. 8.3 presents the results (Burdige, 1989) as probability plots. The mineralization rates basically span the range from G_1 to G_2 reactivity. The rates decrease from the 0-2 cm interval, Fig. 8.3A, to the 5-7 cm interval, Fig. 8.3B, and are quite low - below the G_2 mineralization rate - in the 12-15 cm interval, Fig. 8.3C. The low reactivity in the 12-15 cm depth interval supports the use of H_2 = 10 cm for the depth of the active layer. Also, the nitrogen and phosphorus mineralization rates are systematically larger than the carbon mineralization rates. It has been previously observed that nitrogen mineralization seems to occur relatively more rapidly than carbon mineralization (e.g. Berner, 1970).

In addition to the reaction rate, an estimate of the fraction of the sediment that can be mineralized, $G(0)$, is made. This can be compared to the expected fraction of G_1 + G_2 in a sediment sample. In the previous section this was estimated to be ~ 10%, the remaining 90% is the G_3 component, Table 8.4. The comparison to the results of the experiment is made in Fig. 8.4. The reactive fraction declines with depth and it is quite small in the 12-15 cm interval. The composited data for the 0-2 and 5-7 cm intervals (Depths < 10 cm) is also shown, Fig. 8.4D. The median reactive fraction is on the order of 10% which confirms the model results.

Thus, although kinetic experiments of this sort cannot be used to determine the reaction rates and reactive fractions to be used in a multi-G diagenesis model, they can be used to confirm that the choices made for these parameters are not drastically contradicted by the experimental information.

b. Stoichiometry

One additional analysis is possible using these data. Since the various end-products of diagenesis are measured simultaneously, it is possible to examine the stoichiometry of the decaying organic matter. This is similar to the analysis of pore water profiles presented in the previous section. Any pair of variables can be chosen.

Consider the relationship between sulfate reduced and carbon oxidized. The concentrations are given by:

$$[CO_2(t)] = [CO_2(0)] + \frac{J_{POC}}{H_2}\left\{ f_{POC,1}\frac{(1-e^{-K_{POC,1}t})}{K_{POC,1}} + f_{POC,2}\frac{(1-e^{-K_{POC,2}t})}{K_{POC,2}} \right\} \qquad (39)$$

and

$$[SO_4(t)] = [SO_4(0)] - \alpha_{SO4,C}\frac{J_{POC}}{H_2}\left\{ f_{POC,1}\frac{(1-e^{-K_{POC,1}t})}{K_{POC,1}} + f_{POC,2}\frac{(1-e^{-K_{POC,2}t})}{K_{POC,2}} \right\} \qquad (40)$$

Since the bracketed terms are equal, eq.(39) can be used to substitute for the bracketed term into eq.(40):

$$[SO_4(t)] = [SO_4(0)] - \alpha_{SO4,C}\frac{J_{POC}}{H_2}\left\{ \frac{[CO_2(t)] - [CO_2(0)]}{\frac{J_{POC}}{H_2}} \right\} \qquad (41)$$

so that:

$$[SO_4(t)] = -\alpha_{SO4,C}[CO_2(t)] + [SO_4(0)] + \alpha_{SO4,C}[CO_2(0)] \qquad (42)$$

This suggests that a plot of $SO_4(t)$ versus $CO_2(t)$ can be used to determine the POM stoichiometry: $-\alpha_{SO4,C}$. In order for one straight line to apply, each station is analyzed individually and the y intercept, $[SO_4(0)] + \alpha_{SO4,C}[CO_2(0)]$, is found from a linear regression. This concentration is subtracted from $SO_4(t)$ so that the initial concentration is zero for each

Mineralization Rates

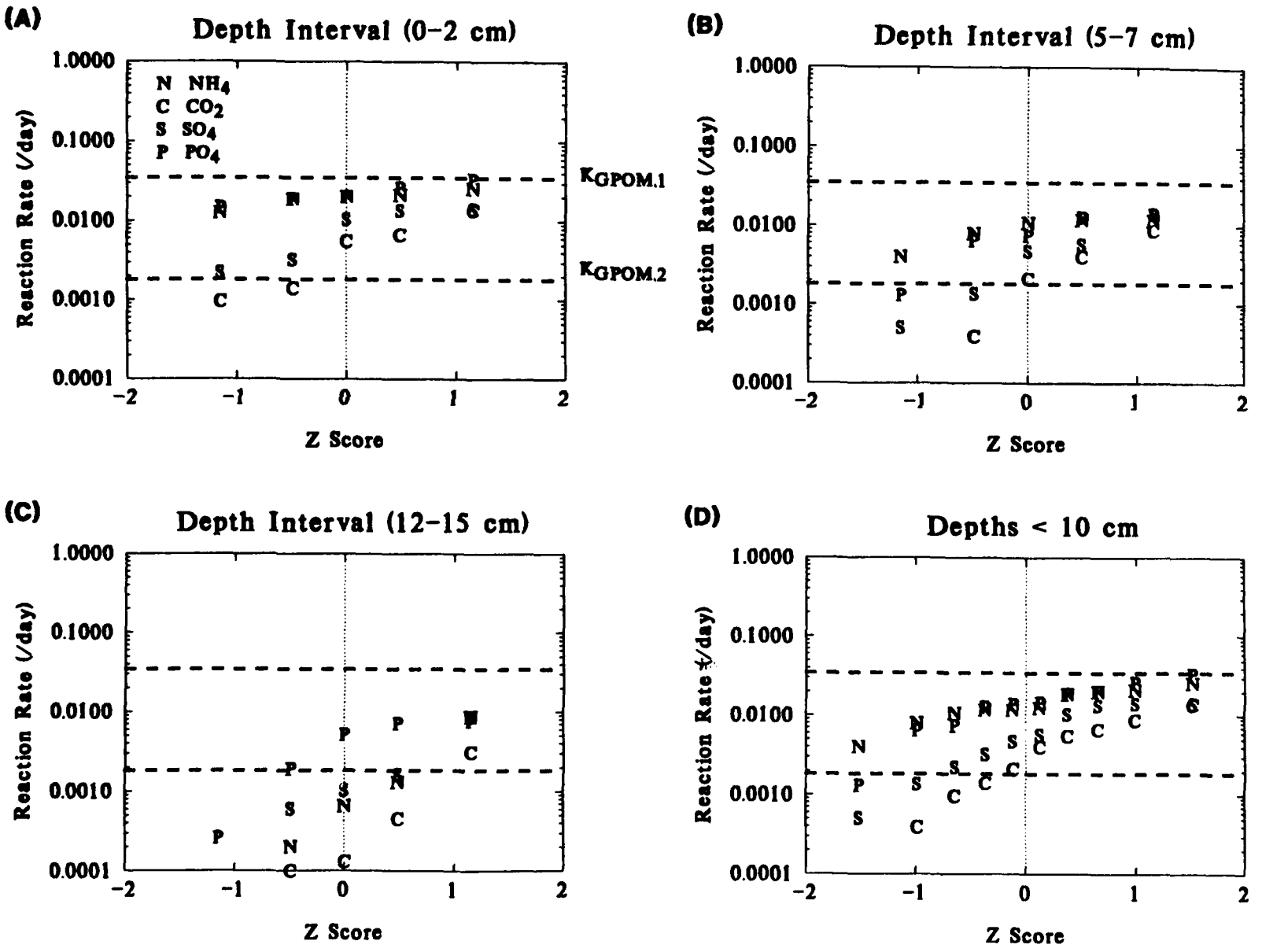

DIAGENP6

Figure 8.3

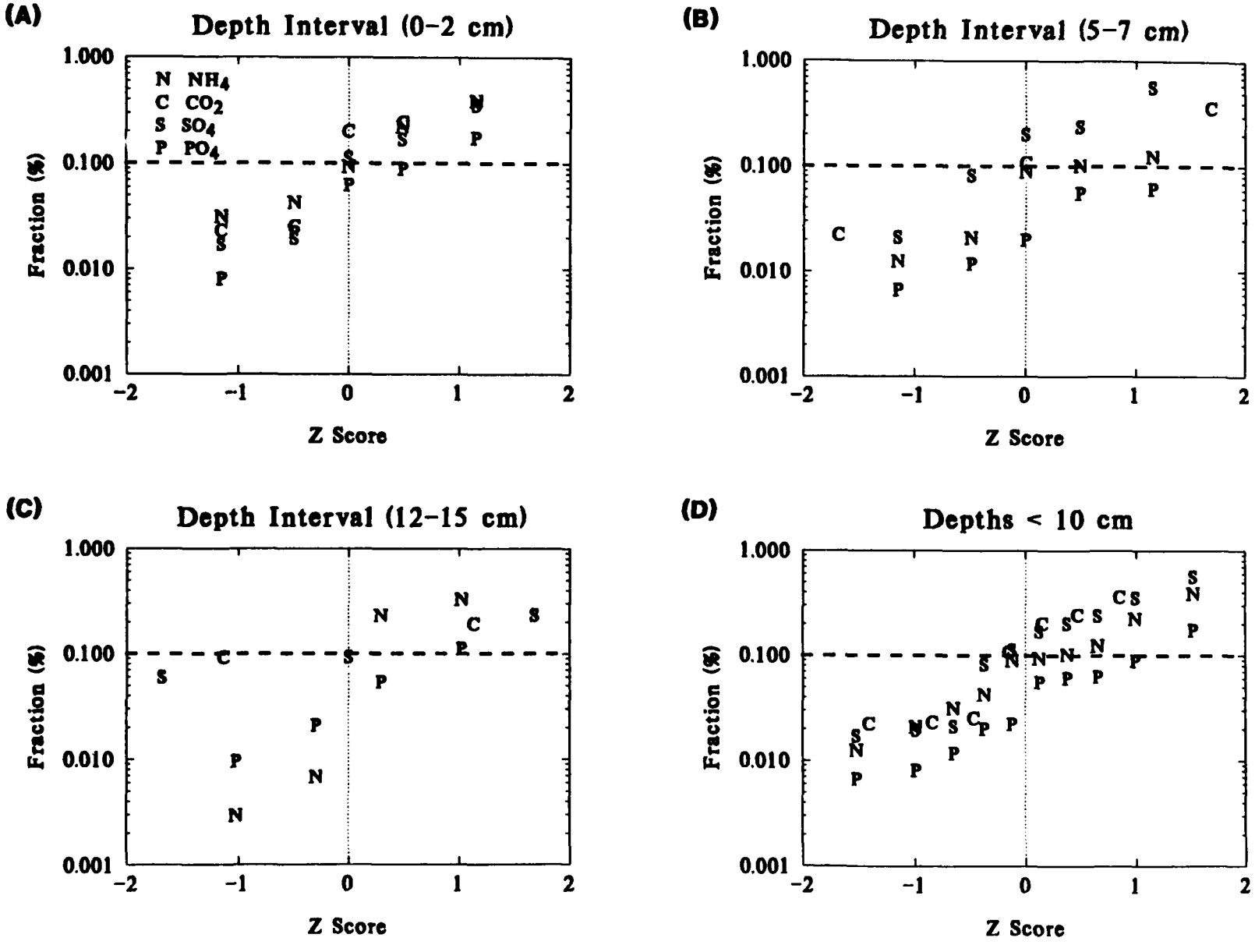

DIAGENP7

Figure 8.4

station. Fig. 8.5. presents the data from the 0-2 cm and 5-7 cm intervals. They are compared to a slope = 1/2 straight line. Note that all the data conform to this relationship. These data justify the use of eq.(V-1) to represent the stoichiometry of sulfate reduction.

The comparison of NH_4 and PO_4 to CO_2 produced are also presented in Fig. 8.5B,C. The analysis procedure is the same. The lines correspond to Redfield stoichiometry. The ammonia concentrations are adjusted for ammonia sorption (Burdige, 1989) since the concentration representing the total ammonia production is required. The nitrogen to carbon stoichiometry, Fig. 8.5B, is approximately Redfield as indicated by the approximate conformity with the straight lines. However, there is a clear bias: the shallow depths are comparatively nitrogen rich and the deeper depth interval are comparatively nitrogen poor. As pointed out above, this is a common observation - the nitrogen component mineralizes more rapidly than the carbon component. A more refined diagenesis model would account for this behavior explicitly.

The carbon to phosphorus stoichiometry, Fig. 8.5C, also appears to be roughly Redfield although some significant departures are observed. However, these data are more difficult to interpret since the extent of phosphorus partitioning to solid phases during the experiment is unknown. It is not known how to correct the concentrations to reflect this and other chemical phenomena. Hence, it could be that the lack of a uniform stoichiometry is a reflection of chemical reactions which are occurring. Therefore, on balance, a Redfield stoichiometry seems an acceptable approximation.

E. Depositional Flux

The following sections presents the results of the calibration of the diagenesis portion of the sediment model to the Chesapeake Bay data set. The diagenesis model receives the depositional fluxes of particulate organic carbon, nitrogen, and phosphorus, and computes the quantity of the solutes that are liberated by mineralization. These diagenesis fluxes are the source terms for the flux model equations. The diagenesis model also computes the concentrations of G_1 through G_3 carbon, nitrogen, and phosphorus, which can be compared to appropriate observations.

The object of the calibration is to estimate the magnitudes of the depositional fluxes. They are assumed to vary from station to station and from year to year. But they are assumed to be constant within the year. This rather unrealistic choice is made for two reasons. First, there is no obvious way to include a seasonal variation. Second, in spite of a constant depositional flux, there is a strong seasonal modulation that is imposed on the resulting diagenesis fluxes due to the temperature dependency of the diagenesis rate constants. Thus, the effect of assuming a constant versus a time varying depositional flux is greatly diminished. As shown below, the seasonal variation of diagenesis is reasonably well reproduced using a constant yearly average depositional flux.

The PON depositional flux, J_{PON}, is estimated by fitting the ammonia diagenesis flux. Estimates of ammonia diagenesis can be made from the observations of ammonia flux and the other necessary variables as follows (eq.II-25):

$$J_N = J[NH_4] + \left(\frac{K_{M,NH4}\theta_{K_{M,NH4}}^{(T-20)}}{K_{M,NH4}\theta_{K_{M,NH4}}^{(T-20)} + [NH_4(1)]}\right)\left(\frac{[O_2(0)]}{2K_{O2,NH4} + [O_2(0)]}\right) \cdot \frac{\kappa_{NH4,1}^2 \theta_{NH4}^{(T-20)}}{s}[NH_4(1)] \qquad (43)$$

Ammonia diagenesis is the sum of the ammonia flux and the quantity of ammonia that is nitrified to nitrate. The aerobic layer ammonia concentration is estimated using (eq.II-34):

$$[NH_4(1)] = \frac{J[NH_4]}{s} + [NH_4(0)] \qquad (44)$$

The kinetic coefficients are listed in Table 2.1 and 2.2. These equations can be applied pointwise to each ammonia flux observation. The result is a time series of estimates of ammonia diagenesis that can serve as the calibration data for estimating the depositional fluxes.

Stoichiometry

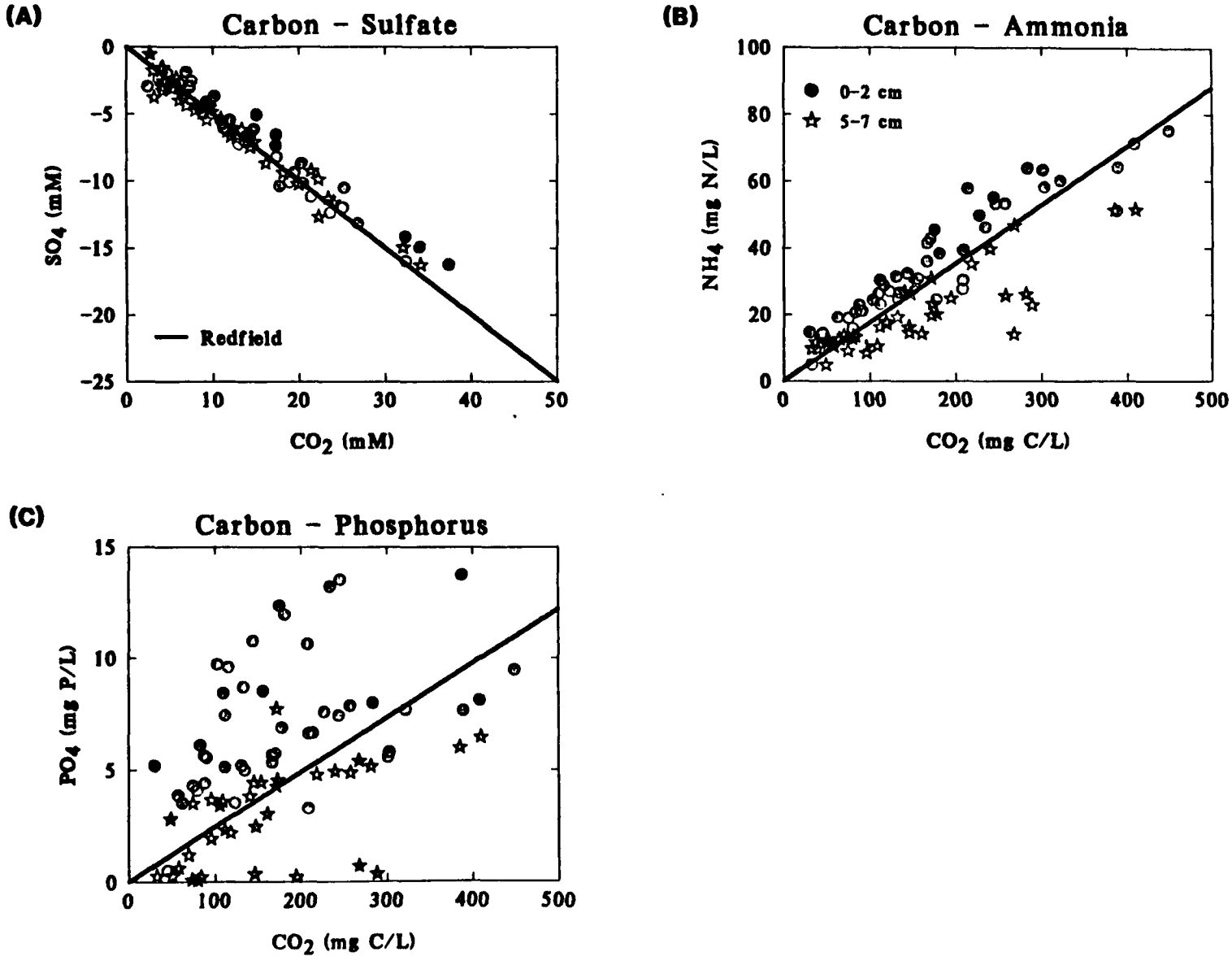

BURDGKPC

Figure 8.5

The ammonia diagenesis flux is computed from the diagenesis model by integrating the mass balance equation (3) and using eq.(5) for J_N. The model results are compared to the estimates in Fig. 8.6. The depositional fluxes of PON are listed in Table 8.6. The seasonal variation of ammonia diagenesis appears to be reasonably well reproduced with low rates during the cold periods of the year and maximal rates during mid year. There appears to be no systematic problem that can be attributed to the use of yearly average depositional fluxes.

The depositional flux of carbon, phosphorus, and silica are established using constant stoichiometric ratios. If $J_{PON}(i,j)$ is the depositional flux of PON for station i during year j, then the carbon depositional flux is given by:

$$J_{POC}(i,j) = \alpha_{C,N} J_{PON}(i,j) \tag{45}$$

and equivalently for phosphorus and silica:

$$J_{POP}(i,j) = \alpha_{C,P}^{-1} J_{POC}(i,j) \tag{46}$$

$$J_{PSi}(i,j) = \alpha_{C,Si}^{-1} J_{POC}(i,j) \tag{47}$$

The depositional fluxes are apportioned into the three G classes using the stoichiometric coefficients which are listed in Table 8.7. For carbon and phosphorus, these are the Redfield stoichiometries. The carbon to silica ratio is based on a limited amount of overlying water particulate biogenic silica data. The fractions of the depositional fluxes in the G_1, G_2, and G_3 classes are listed in Table 8.8. Note that there is slightly less nitrogen in G_3 relative to carbon and phosphorus. This nitrogen poor G_3 is necessary to reproduce the nitrogen poor stoichiometry of the sediment organic matter as shown below.

F. Sediment Composition

The most important calibration of the diagenesis model is to compare the resulting diagenesis fluxes to estimates derived from observations. They are critical since diagenesis fluxes

are the inputs to the mass balance equations that determine the sediment fluxes. It is essential that they be correctly specified if realistic fluxes are to be computed. This is the reason that ammonia diagenesis is used to establish the magnitude of the nitrogen depositional fluxes. There are, however, additional data which can be used for calibration, namely the sediment composition.

It is important to note that the gross sediment composition is almost entirely due to G_3 POM. The reason is that the reactive fractions have decayed to produce the diagenesis flux (Table 8.4). The comparisons are presented in Fig. 8.7 for the four main stem SONE stations. Remarkably, the agreement with the observed PON is almost perfect. However, the POC data shows an enrichment at the upstream stations. This may be due to an additional source of POM from the Susquehana river which is terrigenous and relatively poor in PON relative to POC.

The phosphorus measurements are total phosphorus, TP, the sum of particulate organic phosphorus, POP, and particulate inorganic phosphorus, PIP. Both the computed TP and PIP are shown. The agreement for TP is quite reasonable. At the upper bay station (Still Pond), a substantial fraction of TP is PIP, as shown. However, at the further downstream stations, the majority is POP. The causes of the variation of the forms of phosphorus is discussed in the next chapter where the results of the phosphate flux model are presented.

G. Sediment Algal Carbon

The primary source of POC to the sediments of Chesapeake Bay is algal POC. Hence, the sediment should have a corresponding concentration of chlorophyll$_a$ (Chl_a). The utility of sediment Chl_a has been demonstrated using data obtained from Long Island Sound (Sun, Aller, and Lee, 1991). The decay kinetics of Chl_a in sediments has been found to be relatively independent of temperature with a first order decay constant of approximately 0.03 day^{-1}. It is fortuitous that this is also the average rate constant for the mineralization of G_1 carbon. Hence, the concentration of sediment Chl_a should be a direct measure of the concentration of G_1 carbon in the sediment.

Ammonia Diagenesis

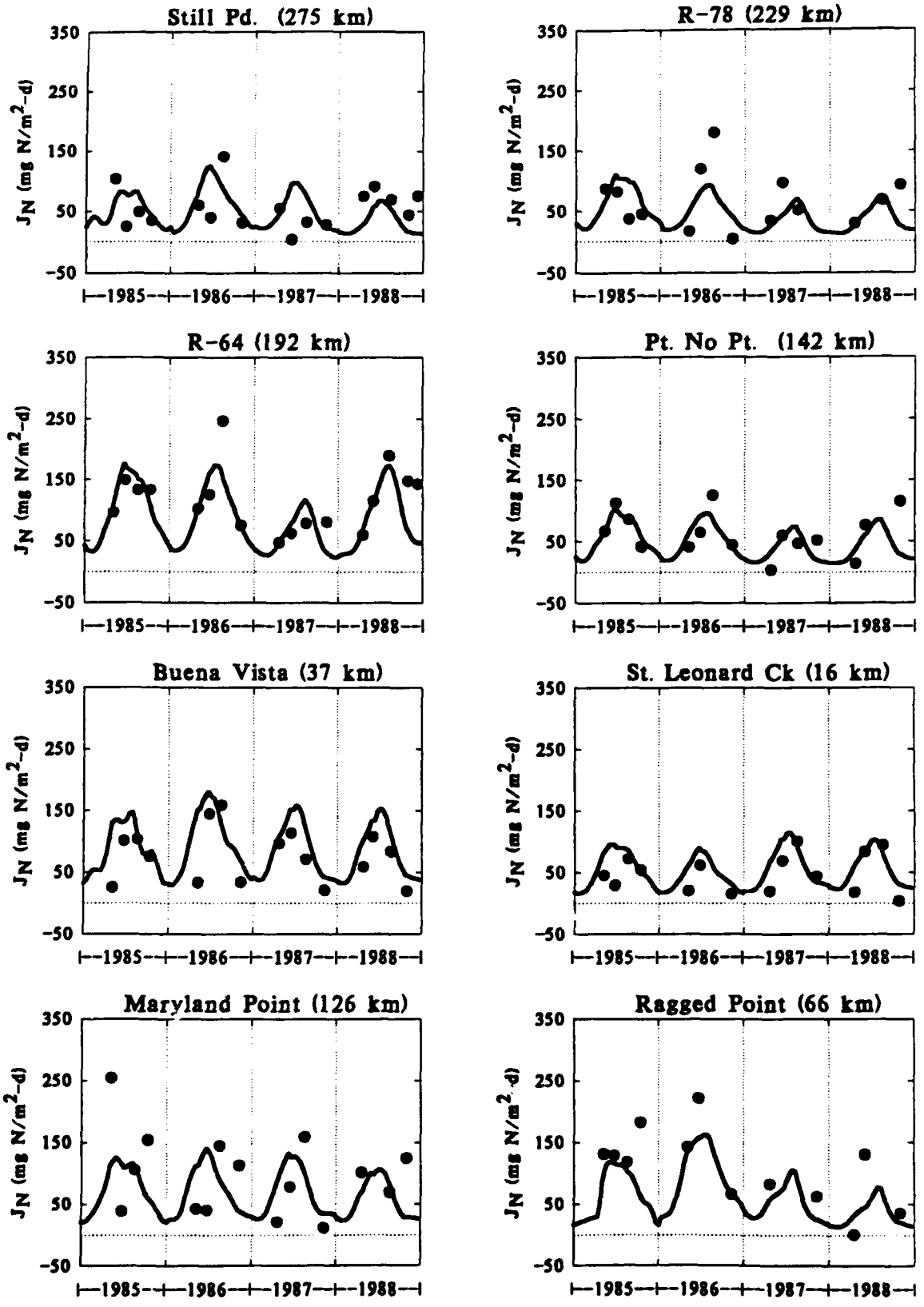

RUN104 - PLTVJN1

Figure 8.6

Sediment Composition

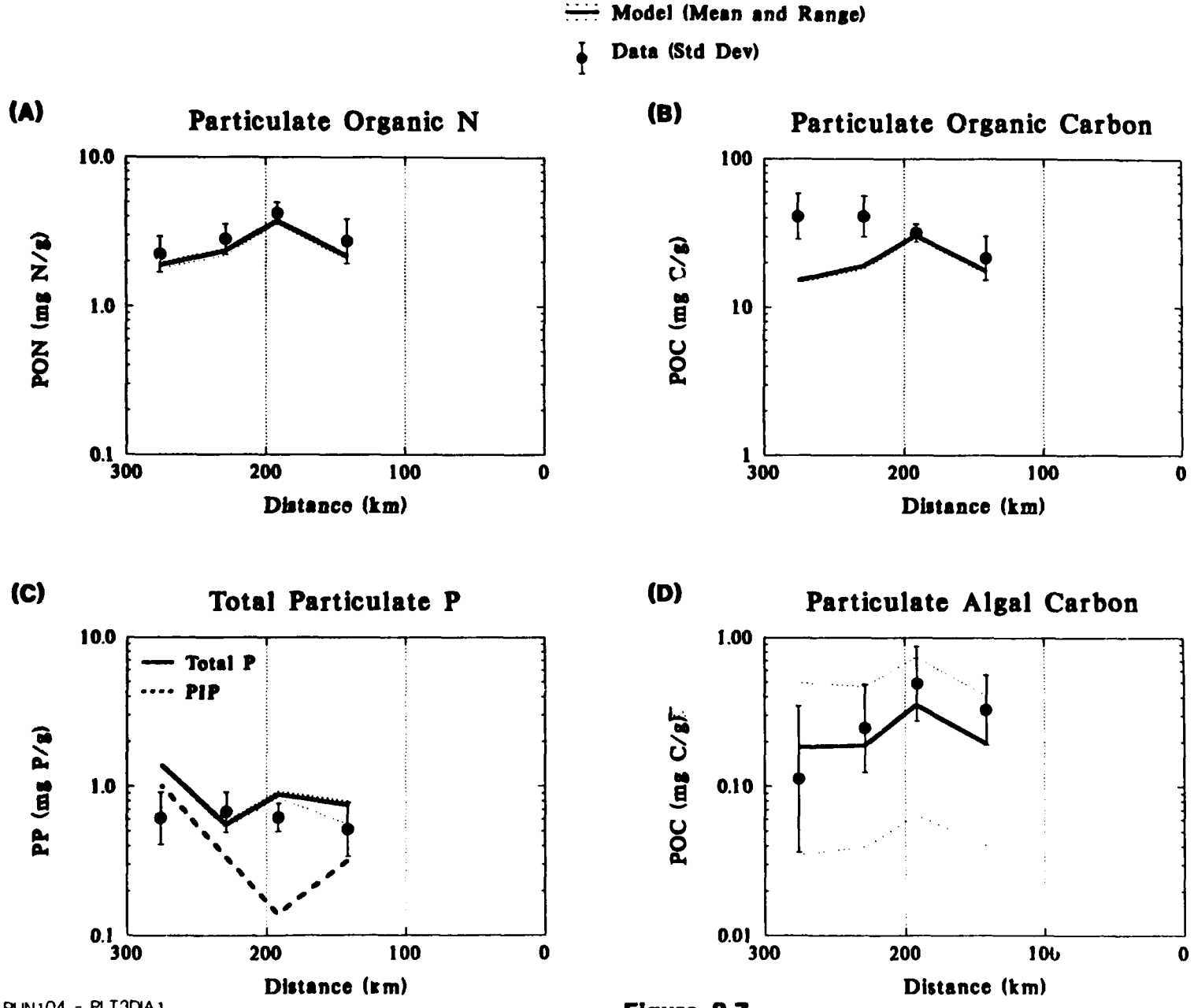

RUN104 - PLT3DIA1

Figure 8.7

The measurements that are available for Chesapeake Bay are for the top one-half to one centimeter of the sediment. The model computations are for the average concentrations in the active sediment layer of 10 cm depth. Hence it is necessary to convert the surface chlorophyll$_a$ measurements to depth averages. The data presented by Sun, Aller and Lee for Long Island Sound can be used to compute the ratio of surface (0-1 cm) chlorophyll, Chl_s, to depth averaged (0-10 cm) chlorophyll, Chl_{av}. The results are presented in Fig. 8.8. The cosine fit to Chl_{av}/Chl_s, Fig. 8.8B, is used to convert the Chesapeake Bay surface chlorophyll data to the ten centimeter depth average.

The resulting average particulate algal chlorophyll concentration is converted to carbon using a carbon to chlorophyll ratio of 60 mg C/mg Chl_a which has been found to be representative of Chesapeake Bay plankton. The results are compared to the computed G_1 carbon concentration in Fig. 8.7D. Note that the G_1 concentration is approximately two orders of magnitude less than the total POC in accord with the analysis presented in the previous section (Table 8.4). The magnitudes and spatial distribution are well reproduced by the model. This result provides additional support that the depositional fluxes are reasonable and that the diagenesis model appropriately describes POM mineralization.

The seasonal variation of total and algal POC are examined in Fig. 8.9. The data are from four main bay SONE stations which have been averaged by month in order to detect seasonal variations. Total POC, Fig. 8.9A, exhibits no discernable seasonable variation and the model computes no variation. This is not unexpected since there is no mechanism in the model by which G_3 carbon can vary. The depositional flux and the sedimentation velocity are both constants.

The comparison of the seasonal variation of algal POC and G_1, Fig. 8.9B, reveals a systematic difference. Computed G_1 carbon peaks in the spring while the temperature is still low and then declines as the loss by diagenesis exceeds the rate of supply. Algal POC appears to exhibit a different pattern with the maximum occurring in summer. This may be a reflection of the

differing temperature dependencies between G_1 carbon and algal POC. The former has a large temperature coefficient: $\theta_{POC,1} = 1.10$, while the latter is reported to be practically temperature independent (Sun, Aller and Lee, 1991).

Nevertheless, the extent of the agreement as exhibited in the spatial distribution, Fig. 8.7D, demonstrates the utility of sediment chlorophyll as a measure of G_1 carbon. More detailed vertical profiles can also be used to quantify the rate of particle mixing (Sun, Aller and Lee, 1991). If the ratio of surface to depth averaged chlorophyll is large, then little particle mixing is occurring. However, if the ratio approaches unity, then the mixing is intense. Such data would be ideally suited for quantification of the particle mixing velocity.

H. Conclusions

The diagenesis of POM deposited to the sediment is formulated as a three G component reaction. The depositional flux is assumed to be a constant within each year, at each station. The yearly average depositional fluxes are chosen to reproduce the average ammonia diagenesis that is estimated from the observed ammonia fluxes. The comparison to the annual cycle of ammonia diagenesis indicates that the use of constant within year depositional fluxes produces acceptable results.

The stoichiometry of the deposited POM can be deduced in a number of ways. The changes in pore water concentrations reflect the composition of organic matter that has mineralized. This is also the case for the anaerobic incubation experiments. The results indicate that the assumption of Redfield stoichiometry is an adequate approximation.

The validity of the diagenesis model component is examined in a number of ways. The most important is the comparison to ammonia diagenesis. However, the composition of the sediment POM is also important. The comparison is reasonable for carbon, nitrogen and phosphorous. This basically validates the G_3 components since they dominate the gross sediment composition. The anaerobic mineralization experiments can be used to estimate the quantity of G_2 in the

Sediment Chlorophyll Concentrations

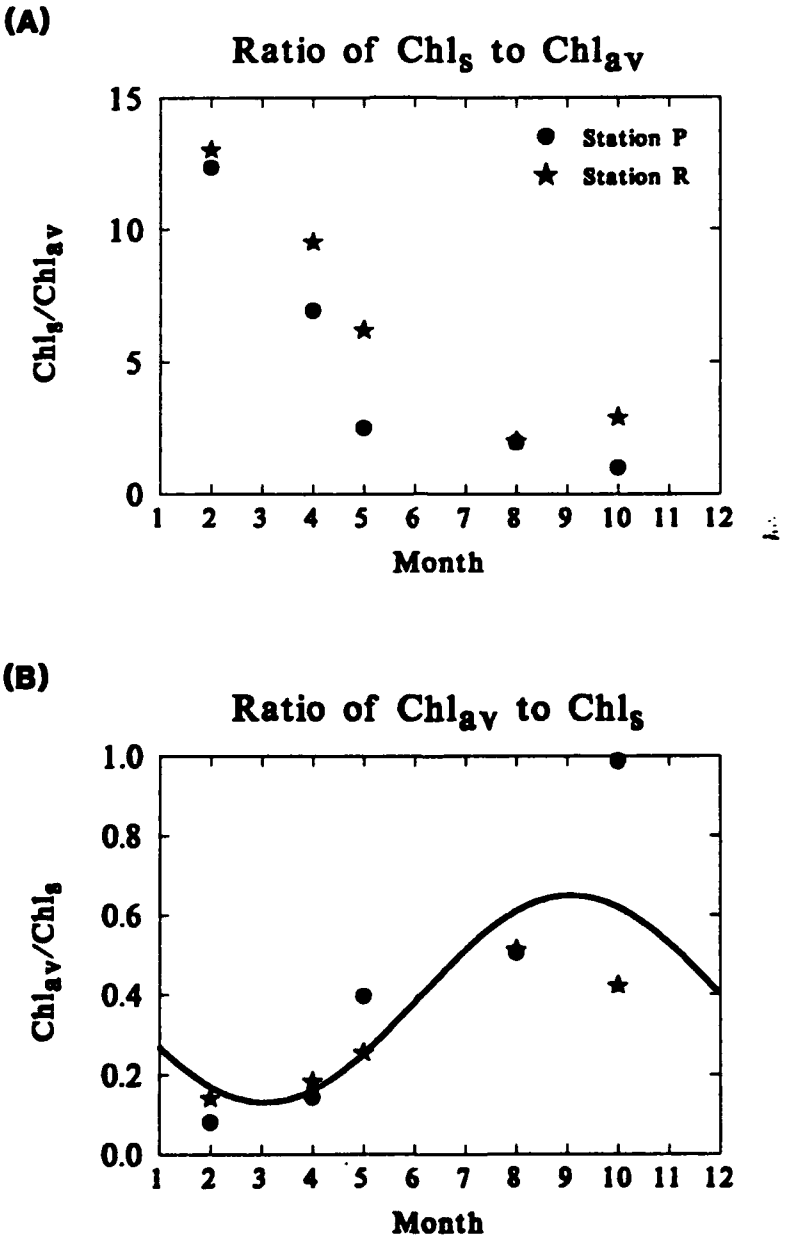

ALLER1

Figure 8.8

Seasonal POC Variation

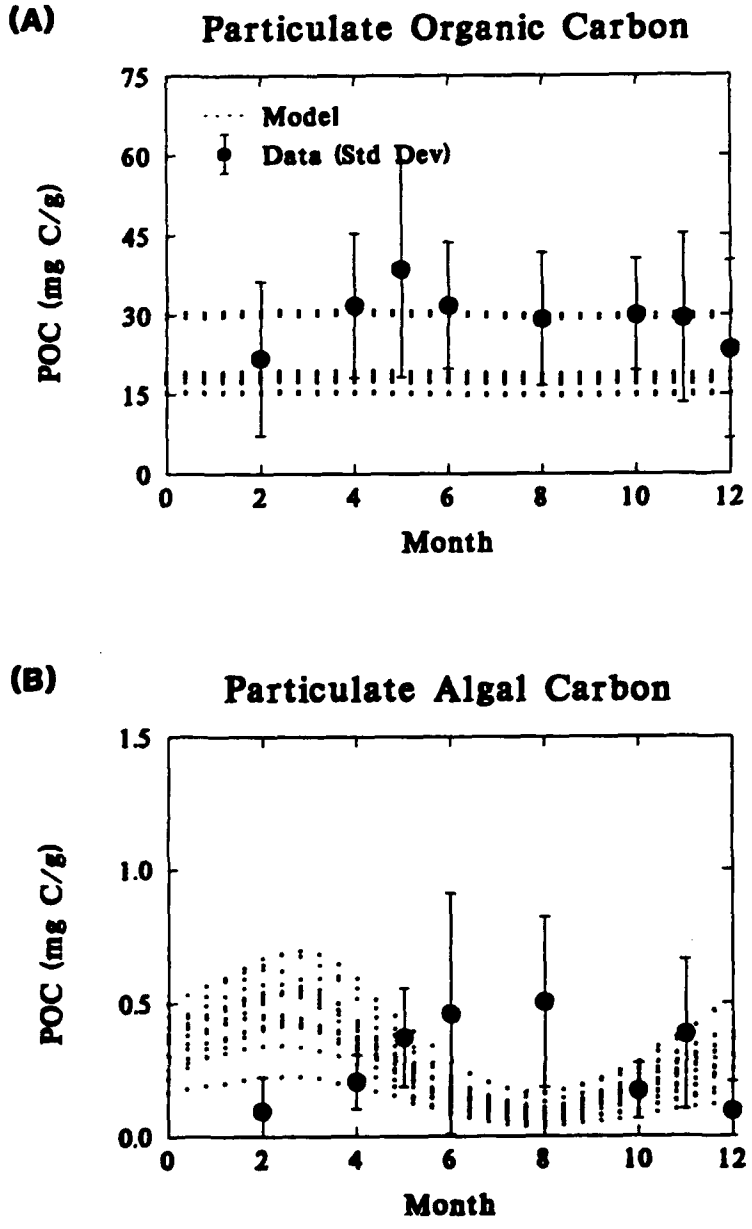

RUN104 - PLT3POCS

Figure 8.9

sediment, since it dominates the reactive portion. They also compare favorably with the model results. The final validation is the comparison of G_1 carbon to the quantity of algal carbon in the sediment, which is estimated from the sediment chlorophyll. Again the comparison is satisfactory.

These comparisons indicate that the parameters used for the diagenesis model component are realistic. They duplicate the available observations with reasonable fidelity. Therefore, the diagenesis model is used to drive the sediment flux model so that time variable fluxes can be computed. This is the subject of the next chapter.

I. References

Abodollahi, H. and Nedwell, D.B. (1979): Seasonal temperature as a factor influencing bacterial sulfate reduction in a saltmarsh sediment. Micro. Ecol. 5: pp. 73-79.

Aller, R.C. and Benninger, L.K. (1981): Spatial and temporal patterns of dissolved ammonium, manganese, and silica fluxes from bottom sediments of Long Island Sound, USA. J. Mar. Res 39: pp. 295-314.

Aller, R.C. and Yingst, J.Y. (1980): Relationships between microbial distributions and the anaerobic decomposition of organic matter in surface sediment of Long Island Sound, USA. Mar. Biol. 56: pp. 29-42.

Berner, R.A. (1977): Stoichiometric models for nutrient regeneration in anoxic sediments. Limnol. Oceanog. 22(5): pp. 781-786.

Berner, R.A. (1980): Early Diagenesis. A Theoretical Approach. Princeton Univ. Press, Princeton, N.J. p.40

Berner, R.A. (1980): A rate model for organic matter decomposition during bacterial sulfate reduction in marine sediments. In: Biogeochemistry of organic matter at the sediment-water interface, pp. 35-44. Editor:. Comm. Natl. Recherche Scientific, France.

Billen, G. (1982): An idealized model of nitrogen recycling in marine sediments. Am. J. Sci. 282: pp. 512-541.

Burdige, D.J. (1989). Sediment Monitoring Program for Southern Chesapeake Bay. Old Dominion Univ. ODURF Technical Report 89-6

Burdige, D.J. (1991). The kinetics of organic matter mineralization in anoxic marine sediments. J. Mar. Res. 49: pp. 727-761.

Fallon, R.D. and Brock, T.D. (1979): Decomposition of blue-green algal (cyanobacteria) blooms in Lake Mendota, Wisconsin. Appl. Environ. Microbiol. 37: pp. 820-830.

Goldhaber, M.B., Aller, R.C., Cochran, J.K., Rosenfeld, J.K., Martens, C.S. and Berner, R.A. (1977): Sulfate reduction diffusion and bioturbation in Long Island Sound sediments: reports of the FOAM group. Am. J. Sci. 277: pp. 193-237.

Grill, E.V. and Richards, F.A. (1964): Nutrient regeneration from phytoplankton decomposing in seawater. J. Mar. Res 22: pp. 51-59.

Jewell, W.J. and McCarty, P.L. (1971): Aerobic decomposition of algae. Environ. Sci. Technol. 5: pp. 1023-1031.

Jorgensen, B.B. (1977): The sulfur cycle of a coastal marine sediment (Limfjorden, Denmark). Limnol. Oceanogr. 22: pp. 814-832.

Kaplan, I.R. and Rittenberg, S.C. (1964): Microbiological fractionation of sulfur isotopes. J. Gen. Microbiol. 34: pp. 195-212.

Klump, J.V. (1980): Benthic nutrient regeneration and the mechanisms of chemical sediment-water exchange in an organic-rich coastal marine sediment Ph.D. Thesis. Univ. of North Carolina, Chapel Hill, NC.

Klump, J.V. and Martens, C.S. (1981): Biogeochemical cycling in an organic rich coastal marine basin. II. Nutrient sediment-water exchange processes. Geochim. Cosmochim. Acta 45: pp. 101-121.

Klump, J.V. and Martens, C.S. (1983): Benthic Nitrogen Regeneration. In: Nitrogen in the Marine Environment, pp. 411-457. Editors: E.J. Carpenter and D.G. Capone. Academic Press, New York.

Klump, J.V. and Martens, C.S. (1989): The seasonality of nutrient regeneration in an organic-rich sediment: Kinetic modeling of changing pore-water nutrient and sulfate distributions. Limnol. Oceanogr. 34(3): pp. 559-577.

Nixon, S.W., Oviatt, C.A. and Hale, S.S. (1976): Nitrogen regeneration and the metabolism of coastal marine bottom communities. In: The Role of Terrestrial and Aquatic Organisms in Decomposition Processes, pp. 269-283. Editors: J. Anderson and A. MacFayden. Blackwell, Oxford.

Nedwell, D.B. and Abram, J.W. (1979): Relative influence of temperature and electron donor and electron acceptor concentrations on bacterial sulfate reduction in saltmarsh sediment. Micro. Ecol. 5: pp. 67-72.

Nedwell, D.B. and Floodgate, G.D. (1972): Temperature-induced changes in the formation of sulfide in a marine sediment. Mar. Biol. 14: pp. 18-24.

Otsuki, A. and Hanya, T. (1972): Production of dissolved organic matter from dead green algal cells. 1. Aerobic microbial decomposition. Limnol. Oceanogr. 17: pp. 248-257.

Redfield, A.C., Ketchum, B.H. and Richards, F.A. (1963): The influence of organisms on the composition of seawater. In: The Sea, pp. 26-77. Editor: M.N. Hill. Wiley-Interscience, N.Y.

Sun, M., Aller, R.C. and Lee, C. (1991). Early diagenesis of chlorophyll-a in Long Island Sound sediments: A measure of carbon flux and particle reworking. J. Marine Res. 49: pp. 379-401.

Turekian, K.K., Benoit, G.J. and Benninger, L.K. (1980): The mean residence time of plankton-derived carbon in a Long Island Sound sediment core: A correction. Est. Coast. Mar. Sci. 11: pp. 583-587.

Vosjan, J.H. (1974): Sulfate in water and sediment of the Dutch Wadden Sea. J. Mar. Res. 1: pp. 15-21.

Westrich, J.T. and Berner, R.A. (1984): The role of sedimentary organic matter in bacterial sulfate reduction: The G model tested. Limnol. Oceanogr. 29(2): pp. 236-249.

Westrich, J.T. (1983): The consequences and controls of bacterial sulfate reduction in marine sediments Ph.D. Thesis. Yale University, New Haven, CN.

Westrich, J.T. and Berner, R.A. (1988): The effect of temperature on rates of sulfate reduction in marine sediments. Geomicrobiology J. 6: pp. 99-117.

Wheatland, A.B. (1954): Factors affecting the formation and oxidation of sulphides in a polluted estuary. J. Hyg. 52: pp. 194-210.

Table 8.1
Three G Model Reaction Rates, K, and Fractional Composition, f
(Westrich and Berner, 1984)

Aerobic Algae Decay - (T = 20-22 °C)

	f_1 (%)	K_1 (day^{-1})	f_2 (%)	K_2 (day^{-1})	Reference
Marine	-	0.038	-	0.0088	Grill and Richards (1964)
Fresh	50	0.019-0.06	-	-	Jewell and McCarty (1971)
"	-	0.030-0.071	-	0.0049	Otsuki and Hanya (1972)
"	-	0.041	-	-	Fallon and Brock (1979)
Marine	50	0.066	16	0.0038	Westrich (1983)
Average	**50**	**0.046**	**16**	**0.0058**	
Half Life (days)		**15**		**120**	

Anaerobic Sediment Decay - Sulfate Reduction

Marine	-	0.024	-	0.0023	Westrich (1983)
"		0.020	-	0.0030	"
"	-	-	-	0.0016	Berner (1980)
"	-	-	-	0.0012	Turekian et al., (1980)
"	-	-	-	0.0026	Billen (1982)
Average		**0.022**		**0.002**	
Half Life (days)		**32**		**345**	

Temperature Dependence
(Klump and Martens, 1983; Westrich, 1983)

Reaction	ΔH (kcal/mol)	θ	Reference
Ammonia Flux	22	1.138	Klump, 1980; Klump and Martens, 1981
"	19	1.118	Aller and Benninger, 1981
"	24	1.151	Nixon et al., 1976
Ammonia Diagenesis	23	1.144	Klump, 1980; Klump and Martens, 1981
"	19	1.118	Aller and Yingst, 1980
"	23	1.144	Klump and Martens, 1989
Sulfate Reduction	21	1.131	"
"	19	1.118	"
Sulfate Reduction	17	1.104	Wheatland (1954)
"	24	1.150	Kaplan and Rittenberg, 1964
"	16	1.098	Nedwell and Floodgate, 1972
"	22	1.137	Vosjan, 1974
"	25.1	1.158	Goldhaber et al., 1977
"	17.9-20.1	1.111-1.125	Jorgensen, 1977
"	18.6-26.3	1.115-1.166	Abdollahi and Nedwell, 1977
"	75-84	1.111-1.125	Aller and Yingst, 1980
Sulfate Reduction Depth $\leq$ 10 cm	13.5 (8.6-16.3)	1.082 (1.052-1.100)	Westrich and Berner (1988)
Sulfate Reduction Depth > 10 cm	21.7 (16.0-31.5)	1.136 (1.098-1.203)	"
G_1	**16.3**	**1.10**	**This work**
G_2	**23.9**	**1.15**	**This work**

Table 8.6

Particulate Organic Nitrogen Depositional Fluxes

J_{PON} (mg N/m^2-d)

Station	1985	1986	1987	1988
Point No Pt.	66.6	61.3	34.1	50.0
R-64	114.2	110.0	50.0	110.0
R-78	71.7	52.2	30.0	40.0
Still Pond	57.0	80.0	47.4	30.0
St. Leo	64.0	47.1	72.3	57.9
Buena Vista	97.5	120.0	90.0	90.0
Ragged Pt.	75.0	125.0	40.0	30.0
Maryland Pt.	82.5	81.0	77.9	60.0

Table 8.7

Depositional Flux Stoichiometry

(mg/mg)

Carbon/Nitrogen $\alpha_{C,N}$	Carbon/Phosphorus $\alpha_{C,P}$	Carbon/Silica $\alpha_{C,Si}$
5.68	41.0	2.0

Table 8.8

Depositional Flux - G Classes Fractions

Fractions $f_{POM,i}$	G_1	G_2	G_3
Carbon	0.65	0.20	0.15
Nitrogen	0.65	0.25	0.10
Phosphorus	0.65	0.20	0.15

IX. TIME VARIABLE MODEL

A. Introduction

The flux models presented in the previous chapters are all steady state solutions of the mass balance equations. In this chapter, the additional information that is necessary for constructing the time variable model will be presented. The simplified steady state solutions used a lumped parameter, Ω, which included the mass transfer and particle mixing coefficients between the aerobic and anaerobic layers. However, these parameters are explicitly required for the time variable calculations. The anaerobic layer depth is also essential. Finally, the numerical methods for specifying the overlying water concentrations, the initial conditions for the sediment state variables, and the finite difference algorithm, are presented.

B. Transport Parameters

The particulate and dissolved phase mixing coefficients between the two layers determine the rate at which solutes stored in the anaerobic layer are transferred to the aerobic layer and potentially to the overlying water. They influence the time variable model results more than they do the steady state solutions. Therefore, a more detailed description of these processes is required.

1. Particulate Phase Mixing

The rate of mixing of sediment particles by macrobenthos (bioturbation) is quantified in this model by estimating the apparent particle diffusion coefficient, D_p. It has been found that the variation appears to be proportional to the biomass of the benthos, as shown in Fig. 9.1A (Matisoff, 1982). In addition, it has been found that benthic biomass is correlated to the carbon input to the sediment (Maughan, 1986; Robbins et al., 1989). In order to make the sediment model self consistent - that is, to use only internally computed variables in the parameterizations -

Particle Mixing

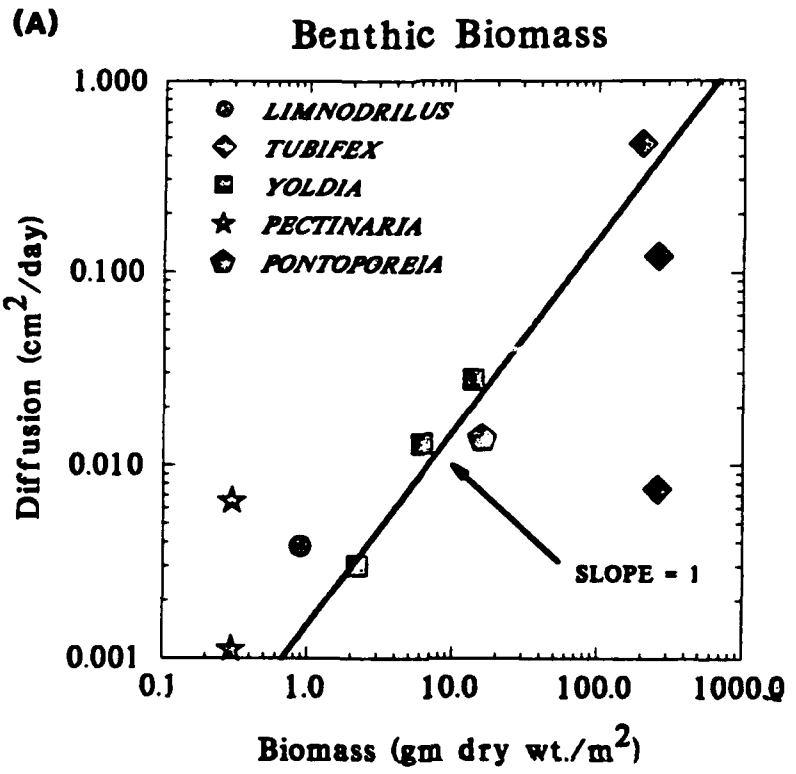

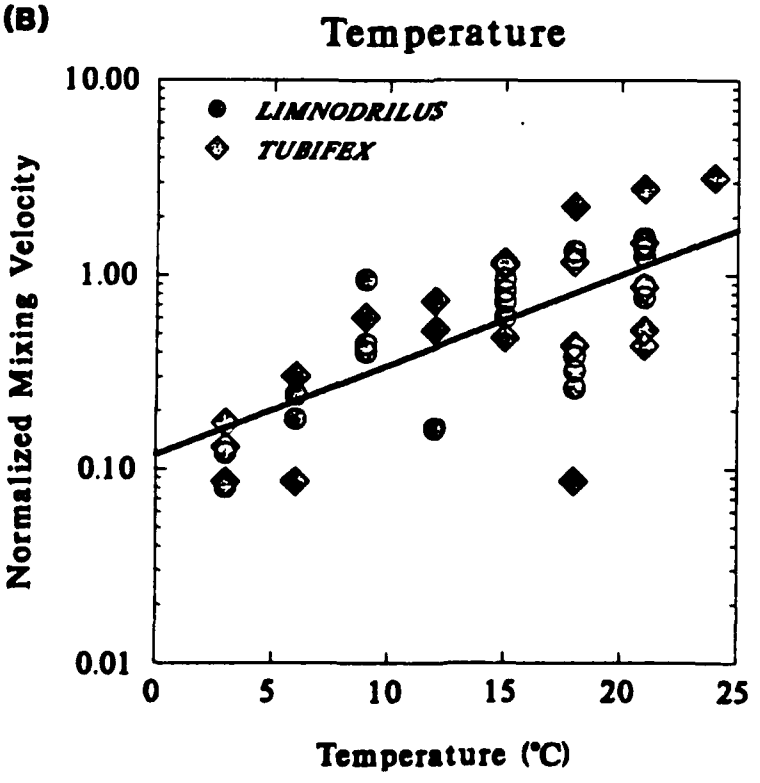

WORMP1

Figure 9.1

it seems reasonable to assume that benthic biomass is proportional to the labile carbon in the sediment which is calculated by the model as $G_{POC,1}$. While this is not as satisfactory a solution as modeling the benthic biomass directly, it appears to be a reasonable first step.

The temperature dependency of particle mixing has also been investigated (McCall and Tevesz, 1982). The results are presented in Fig. 9.1B. The data sets are all normalized with respect to the mixing velocity at T = 20 °C. The straight line corresponds to an Arrhenius temperature dependency with $\theta_{Dp} = 1.117$. Hence, the particle mixing velocity, w_{12}, can be expressed as:

$$w_{12}^{*} = \frac{D_p \theta_{Dp}^{(T-20)}}{H_2} \frac{G_{POC,1}}{G_{POC,R}} \qquad (1)$$

where $G_{POC,R}$ is the reference G_1 concentration at which $w_{12}^{*} = D_p / H_2$ at 20 °C. The superscript * is used to distinguish this formulation from the final expression for w_{12} that is developed below.

A series of experiments have examined the relationship between particle mixing due to benthic organisms and the overlying water oxygen concentration, (Robbins et al., 1984). The results of four experiments are shown in Fig. 9.2, a plot of particle reworking rate versus DO. The solid symbols denote the data during the initial declining phase of the DO, and the open symbols denote the data during the subsequent increase. There is a general dependency of mixing rate on DO, with the lower rates occurring at the lower DO concentrations. This dependency will be modeled using a Michaelis Menton expression. Note, however, that there is a hysteresis in the results. The particle mixing rate does not return to the same magnitude when the DO is increased following the decrease. This behavior is addressed in the next section.

The particle mixing mass transfer coefficient that includes the temperature dependence, the benthic biomass dependence, and the Michaelis Menton oxygen dependency is:

$$w_{12}^{*} = \frac{D_p \theta_{Dp}^{(T-20)}}{H_2} \frac{G_{POC,1}}{G_{POC,R}} \frac{[O_2(0)]}{K_{M,Dp} + [O_2(0)]} \qquad (2)$$

with units [L/T]. The parameter values are:

D_p	Diffusion coefficient for particle mixing	1.2E-04	m^2/d
θ_{Dp}	Temperature coefficient for D_p	1.117	-
$G_{POC,R}$	Reference concentration for $G_{POC,1}$	0.1	mg C/g
$K_{M,Dp}$	Particle mixing half saturation constant for oxygen	4.0	mg/L

The particle diffusion coefficient is established via calibration as described subsequently in Chapter X. The particle mixing half saturation constant, $K_{M,Dp}$ appears to be representative of the data in Fig. 9.2 although it is by no means a precise representation. One difficulty is discussed next.

2. Benthic Stress

In addition to the reduction in particle mixing velocity due to the instantaneous oxygen concentration, it has been found necessary to include a more lasting effect. In particular, if anoxia occurs, then the benthic faunal population is reduced or eliminated and cannot recover. This cannot be modeled using a functional relationship between particle mixing rate and DO. Fig. 9.3 presents the time history of the particle mixing rate and DO for the results analyzed in Fig. 9.2. As the DO declines the particle mixing rate also declines. But as the DO subsequently increases, the particle mixing rate either increases more slowly, experiments A and B, or not at all, experiments C and D.

The same type of behavior is exhibited by the benthic populations in Chesapeake Bay. Fig. 9.4 presents the bottom water DO and the mean abundance of benthic organisms at a station in the deep trough (Versar, 1990). Benthic abundance increases as the summer progresses. However, the occurrence of anoxia reduces the population dramatically. After overturn, the DO

Stylodrilus Sediment Reworking Rate

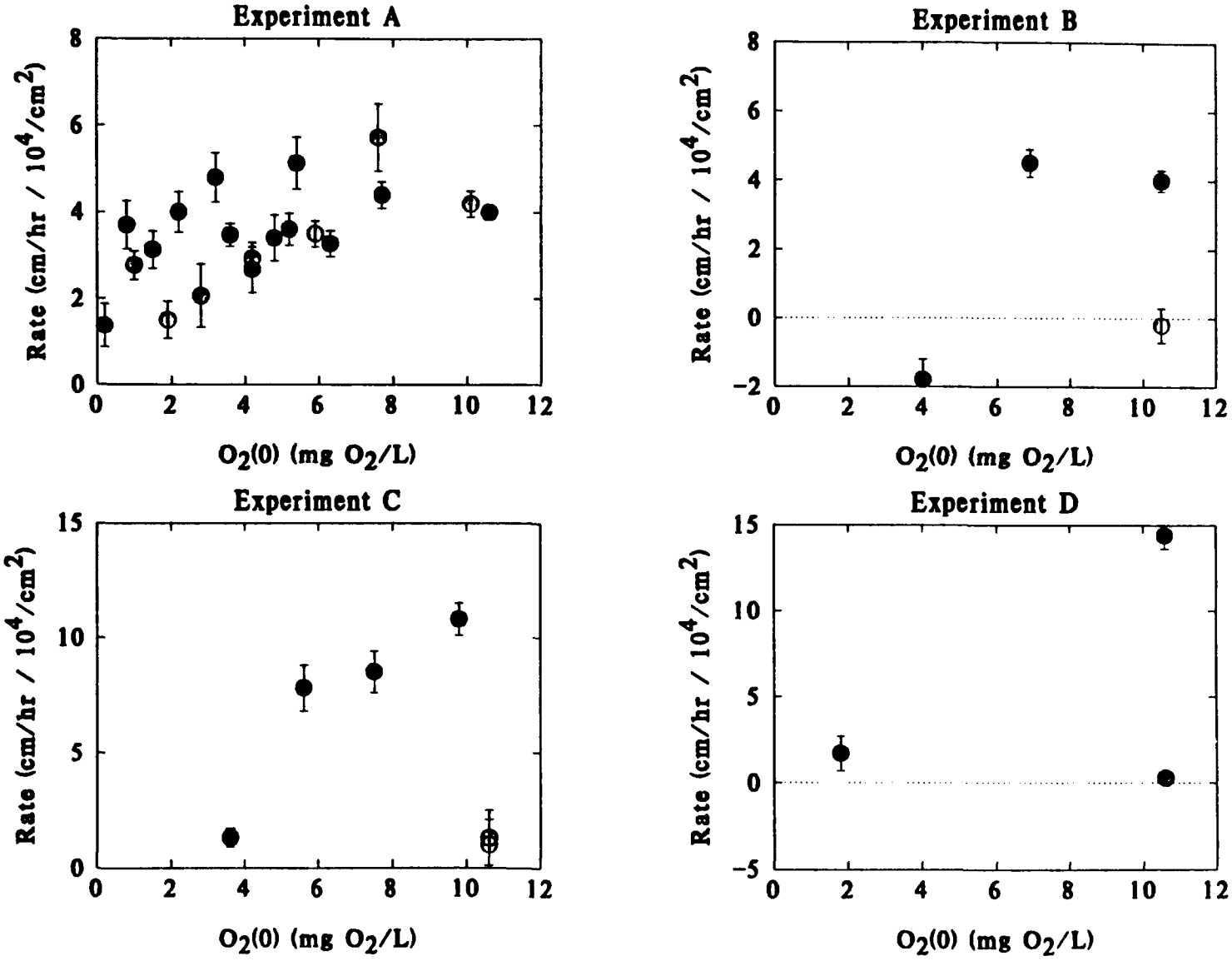

ROBBINP4

Figure 9.2

Stylodrilus Sediment Reworking Rate

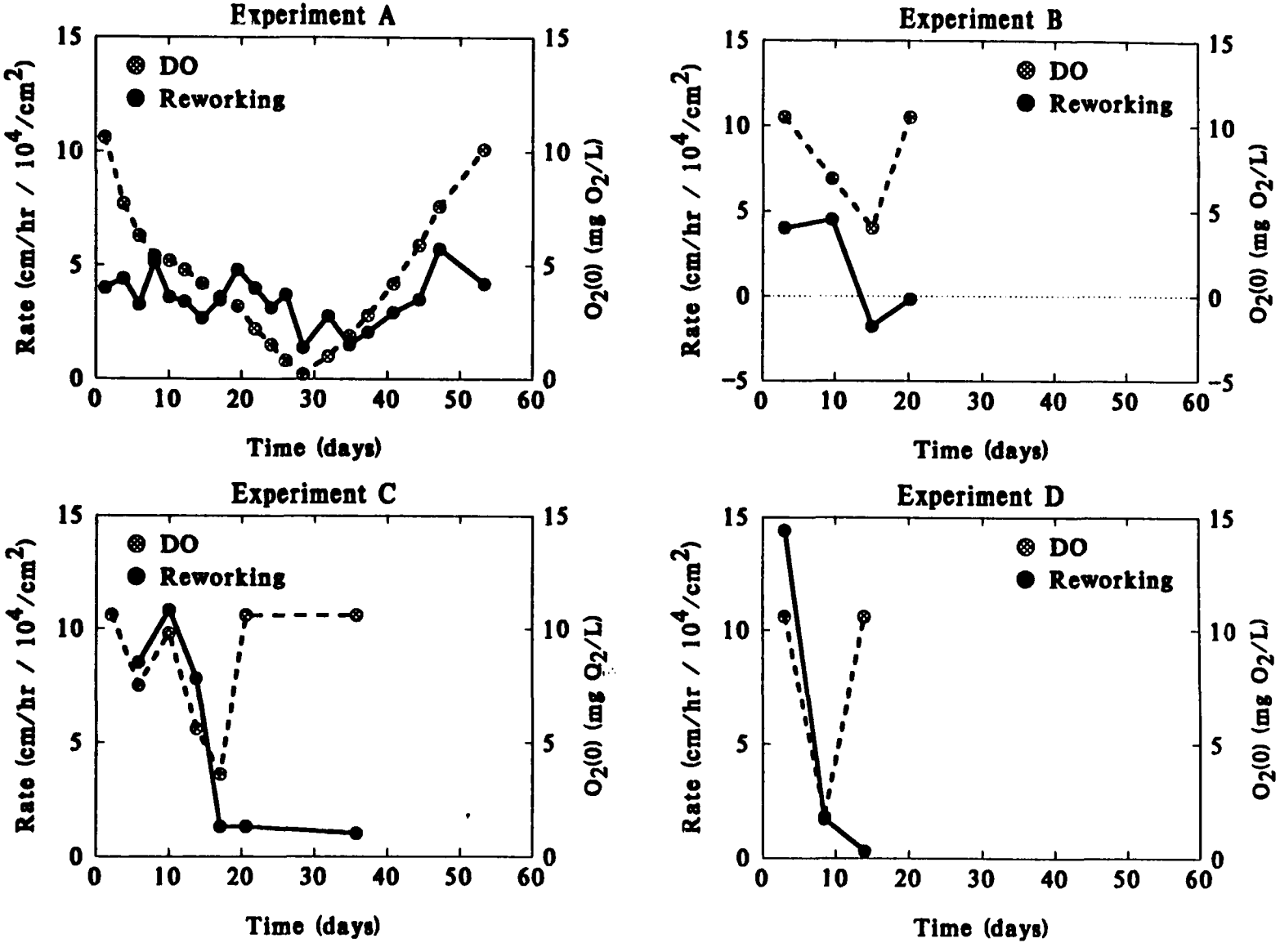

ROBBINP5

Figure 9.3

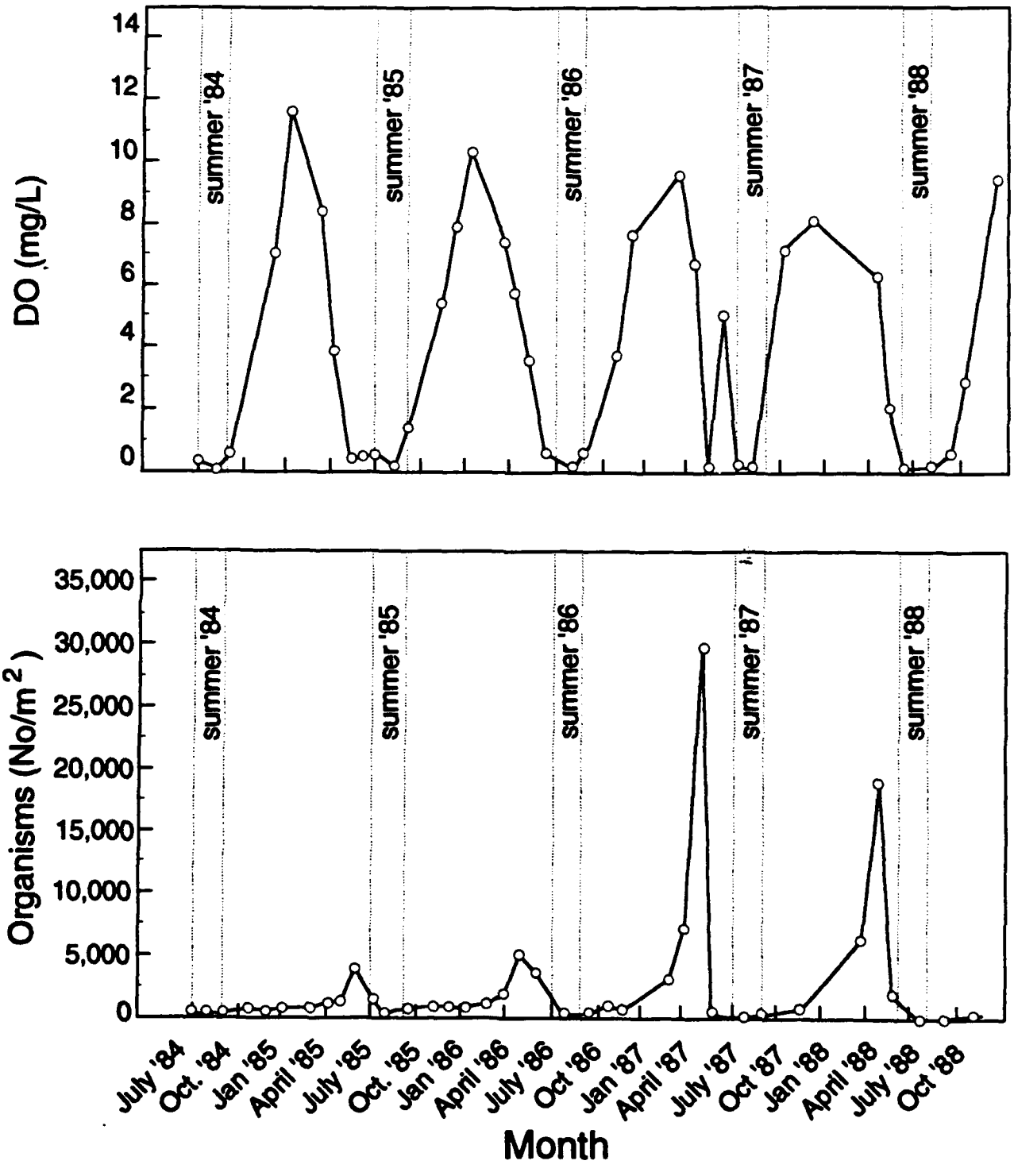
DO (mg/L)
14
12
10
8
6
4
2
0
summer '84
summer '85
summer '86
summer '87
summer '88
Organisms (No/m 2)
35,000
30,000
25,000
20,000
15,000
10,000
5,000
0
summer '84
summer '85
summer '86
summer '87
summer '88
July '84
Oct. '84
Jan '85
April '85
July '85
Oct. '85
Jan '86
April '86
July '86
Oct '86
Jan '87
April '87
July '87
Oct '87
Jan '88
April '88
July '88
Oct '88
Month

Figure 9.4

increases but the population does not recover. Since the particle mixing rate is proportional to the population abundance, Fig. 9.2, it presumably also does not increase in response to the increased DO. The same information is presented for a station near the deep trough in Fig. 9.5. The DO decline is not as pronounced at this station and the population does exhibit some recovery, but not to the levels before the DO decline.

A simple model of this phenomena can be based on the idea of modeling the stress that low DO imposes on the population. The model is analogous to the formulation employed in modeling the toxic effect of chemicals on organisms (Mancini, 1983). A first order differential equation is employed that accumulates stress, S, when overlying water dissolved oxygen is below the particle mixing half saturation constant for oxygen, $K_{M.Dp}$. Stress accumulates as the oxygen concentration decreases, and is dissipated at a first order rate with rate constant, K_S, when conditions improve. Thus:

$$\frac{dS}{dt} = -K_S S + \frac{K_{M.Dp}}{K_{M.Dp} + [O_2(0)]} \tag{3}$$

where:

S	Accumulated benthic stress	[T].
K_S	First order decay coefficient for accumulated stress	$[T^{-1}]$

The behavior of this formulation can be understood by evaluating the steady state stresses at the two oxygen extremes:

$$[O_2(0)] \to 0 \qquad K_S S \to 1 \qquad (1 - K_S S) \to 0 \tag{4}$$

$$[O_2(0)] \to \infty \qquad K_S S \to 0 \qquad (1 - K_S S) \to 1 \tag{5}$$

As $[O_2(0)]$ approaches zero at the onset of anoxia, the term $(1 - K_S S)$ also approaches zero, eq.(4). This suggests that $(1 - K_S S)$ is the proper variable to quantify the degree of benthic

stress. The expression is unitless and requires no additional parameter - for example a half saturation constant for benthic stress. The final formulation for the particle mixing velocity which includes the benthic stress is:

$$w_{12} = w_{12}^{*} \min_{\text{each year}} (1 - K_S S) \tag{6}$$

where w_{12}^{*} is defined above, eq.(2). The stress is continued at its minimum value through the end of the year, in order to conform to the observation that once the benthic population has been suppressed by low oxygen, it does not recover until the next year, Fig. 9.4.

3. Dissolved Phase Mixing

Dissolved phase mixing between layers 1 and 2 is via passive molecular diffusion which is enhanced by the mixing activities of the benthic organisms (bio-irrigation). This is modeled by increasing the diffusion coefficient relative to the molecular diffusion coefficient. The mass transfer coefficient can be expressed in terms of the diffusion coefficient via:

$$K_{L12} = \frac{D_d \theta_{Dd}^{(T-20)}}{H_2} \tag{7}$$

Since it has been demonstrated that the pore water ammonia concentrations are primarily determined by K_{L12}, eq.(II-40), the dissolved phase mixing can be calibrated directly. The result is:

D_d	Pore water diffusion coefficient	1.0E-3	m^2/d
θ_{Dd}	Temperature coefficient for D_d	1.08	-

The resulting diffusion coefficient is roughly ten times the molecular diffusivity, an indication of the importance of benthic enhancement. The temperature coefficient is chosen to be typical of biological reactions.

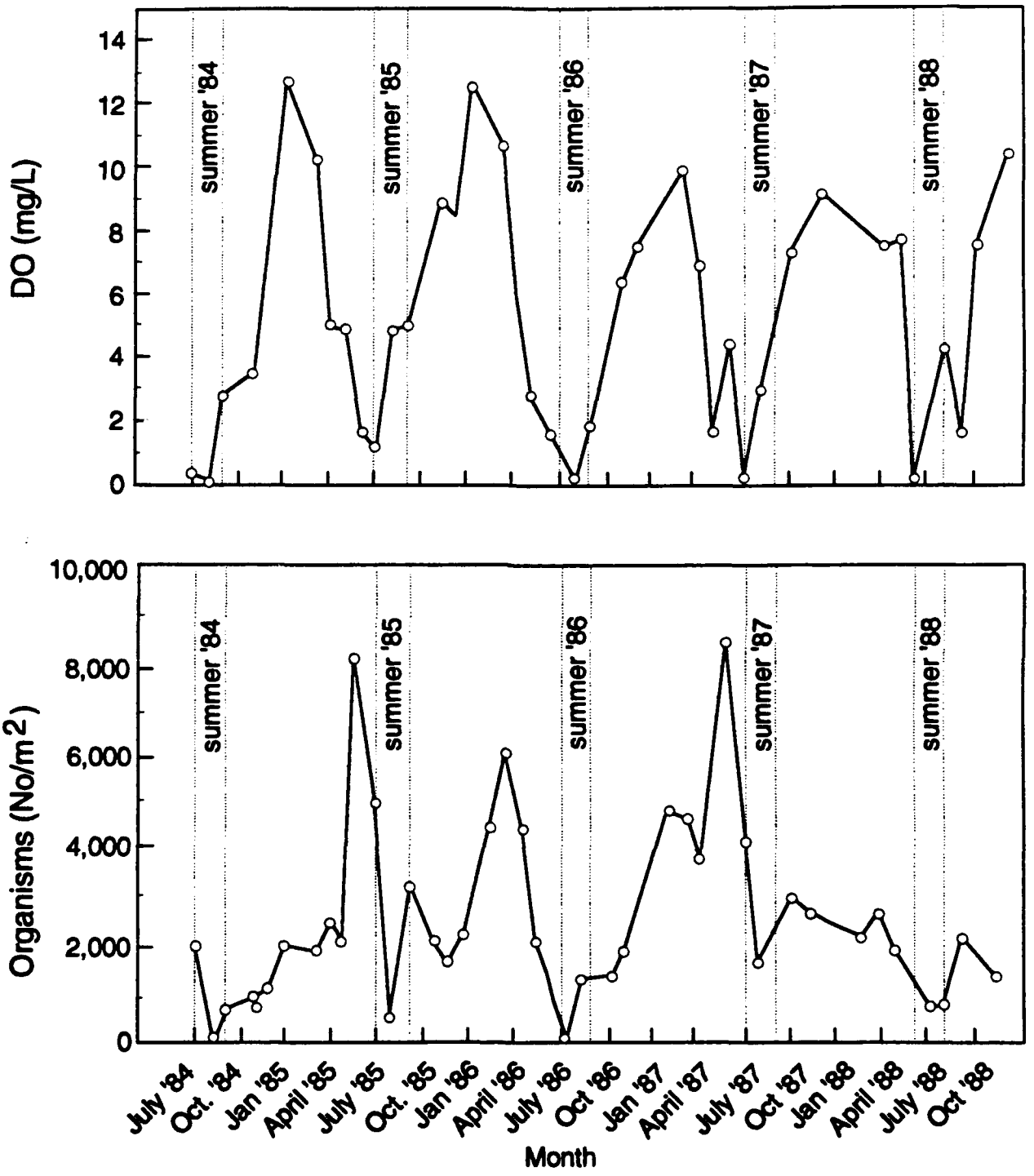
DO (mg/L)
14
12
10
8
6
4
2
0
summer '84
summer '85
summer '86
summer '87
summer '88
Organisms (No/m2)
10,000
8,000
6,000
4,000
2,000
0
summer '84
summer '85
summer '86
summer '87
summer '88
July '84
Oct. '84
Jan '85
April '85
July '85
Oct. '85
Jan '86
April '86
July '86
Oct '86
Jan '87
April '87
July '87
Oct '87
Jan '88
April '88
July '88
Oct '88
Month

Figure 9.5

4. Active Layer Depth

The depth of the active layer, H_2, does not appear as a parameter in the steady state solutions for the general sediment model, eqs. (IV-18, IV-19). It is implicitly included in the layer 2 reactions rates, via the definition of the reaction velocity: $\kappa_2 = K_2 H_2$. However, since κ_2 is the parameter estimated from the data and used in the equations, the value of H_2 does not appear. Hence, its value has no direct effect on the steady state fluxes.

However, H_2 directly influences the time variable behavior of the model. This occurs because it multiplies the time derivative of the layer 2 POM eqs.(VIII-1) and the layer 2 solute eq.(IV-2). Its importance can be understood as follows. At any instant in time, the magnitude of the product, $H_2 dC_{T2}/dt$, is fixed by the magnitude of the terms on the right hand side of the layer 2 mass balance equation. Hence, H_2 and dC_{T2}/dt are inversely related. Consider the case where H_2 is small. Then, since the product has a fixed magnitude, dC_{T2}/dt must be large. Therefore, C_{T2} changes rapidly and the model responds quickly to changes. Conversely, a large H_2 produces a smaller dC_{T2}/dt and changes occur more slowly.

The physical reason for the importance of H_2 is that it controls the volume of the anaerobic layer reservoir. The quantity of solute stored in the layer determines the time it takes for changes in inputs to be reflected in changes in stored solute. Changes in stored solute are eventually reflected in changes in fluxes. Thus the magnitude of H_2 controls the long term response time of the sediment. This is just a restatement of the more mathematical reasoning presented in the previous paragraph. The computational consequences are examined in Chapter XI where the transient response of the model is considered.

The mechanisms that determine the active layer depth are those that influence the depth to which sediment solids are mixed. These mixing mechanisms establish a homogeneous layer within which the diagenesis and other reactions take place. The principal agents of deep sediment mixing

are the larger benthic organisms. Hence H_2 is chosen to represent the depth of organism mixing. Active layer depths of 5 to 15 cm have been reported for estuaries (Aller, 1982). A value of 10 cm seems appropriate.

H_2	Depth of the anaerobic layer	0.1	m

Particles below this depth cannot be recycled into the active layer of the sediment. They are assumed to be permanently buried and lost from the system.

C. Sediment Solids

The most important feature of the sediment that is directly related to the solid fraction of the sediment is the rate at which solids accumulate in the sediment. Of secondary importance is the concentration of solids in the sediment which is related to the volume fraction of solids in a sediment, i.e. the porosity.

1. Solids Sedimentation and Burial

The deposition of solids from the water column to the sediment causes an increase in the depth of the sediment relative to a fixed datum - say the depth of bedrock. Consider a layer of fixed depth measured from the sediment - water interface, for example, the active layer. As sediment solids are deposited, the new solids increase the overall depth of sediment. From the point of view of the active layer, which is a constant depth from the sediment - water interface, this layer moves upward as the sediment depth increases. The velocity at which the layer moves is termed the sedimentation velocity.

The reason this phenomena is important is that it causes a loss of mass from the active layer. This is related to the fact that the sediment layer is moving vertically as the sediment depth increases. The vertical motion causes sediment solids to be lost from the bottom of the active layer.

To see this in another way, consider what happens as new solids enter the layer. Either the concentration of solids in the layer increases and the depth remains the same, or the depth increases and the concentration of solids remains constant. Since the concentration of solids is constant - it is determined by the volume fraction of solids in the active layer of the sediment - then solids must be lost from the bottom of the active layer. The magnitude of the loss per unit area is $w_2 m_2$ where w_2 is the sedimentation velocity, the velocity at which the sediment depth is increasing, and m_2 is the sediment solids concentration. Using a similar argument, any constituent of the active layer with concentration C_{T2} will also be lost from the active layer with magnitude $w_2 C_{T2}$. This is the origin of the loss terms in the mass balance equation (IV-1,IV-2).

The sedimentation velocity for Chesapeake Bay has been measured using a number of methods. The results are displayed in Fig. 9.6B. There is considerable variability in the estimates. This is not unexpected since the rate at which solids are deposited can depend on site specific features. For the stand alone calibration, an average value of 0.25 cm/yr is selected.

w_2	Sedimentation velocity for the stand alone calibration.	6.85E-06 (0.25)	m/d (cm/yr)

For the coupled Chesapeake Bay water column - sediment model, the sedimentation velocities are spatially variable consistent with the observations.

2. Solids Concentrations

The partitioning model which is used to determine the fraction of the solutes that are in the particulate or dissolved form requires the concentration of sorbing solids. Figs. 9.6A and 9.6C present observed 0-10 cm average sediment porosity and solids data for the main stem SONE and BEST stations. A solids concentration of m_2 = 0.5 kg/L seems representative of the upper bay SONE stations. Since m_1 and m_2 appear as a product with the partition coefficients that are determined by calibration, it is reasonable to use sediment solids concentrations that are representative of the upper bay stations.

m_1	Aerobic layer solids concentration	0.5	kg/L
m_2	Anaerobic layer solids concentration	0.5	kg/L

The product of the sedimentation velocity and the solids concentration is the mass flux of solids to the sediment. The results are shown in Fig. 9.6D. It is interesting to note that the solids mass flux is more nearly constant along the axis of the bay. The reason is that lower sedimentation velocities are associated with higher solids concentrations.

D. Numerical Considerations

The time variable solutions of the sediment mass balance equations IV-1 and IV-2 are computed using numerical integration methods. These require that the exogenous variables in the equations, e.g. the overlying water concentration and temperature, be available as smooth functions of time. In addition, the initial conditions - the values of the concentrations at the start of the integration - are required. Finally, a finite difference scheme for the differential equations is required. These three topics are discussed next.

1. Boundary Conditions

In order to calibrate the sediment model it is necessary to specify the overlying water concentrations and temperature as a function of time at each station for the four years. This is done using a four term Fourier series:

$$C_{do}(t) = a_0 + \sum_{k=1}^{4} \left\{ a_k \sin\left(\frac{2\pi k t}{T}\right) + b_k \cos\left(\frac{2\pi k t}{T}\right) \right\} \qquad (8)$$

The data for each year are fit separately. Since the data are not sampled at regular intervals, the usual formulas for the Fourier coefficients (e.g. Hamming, 1962) are not applicable. Rather, a straightforward multiple linear regression can be used to estimate the nine coefficients:

Sediment Solids

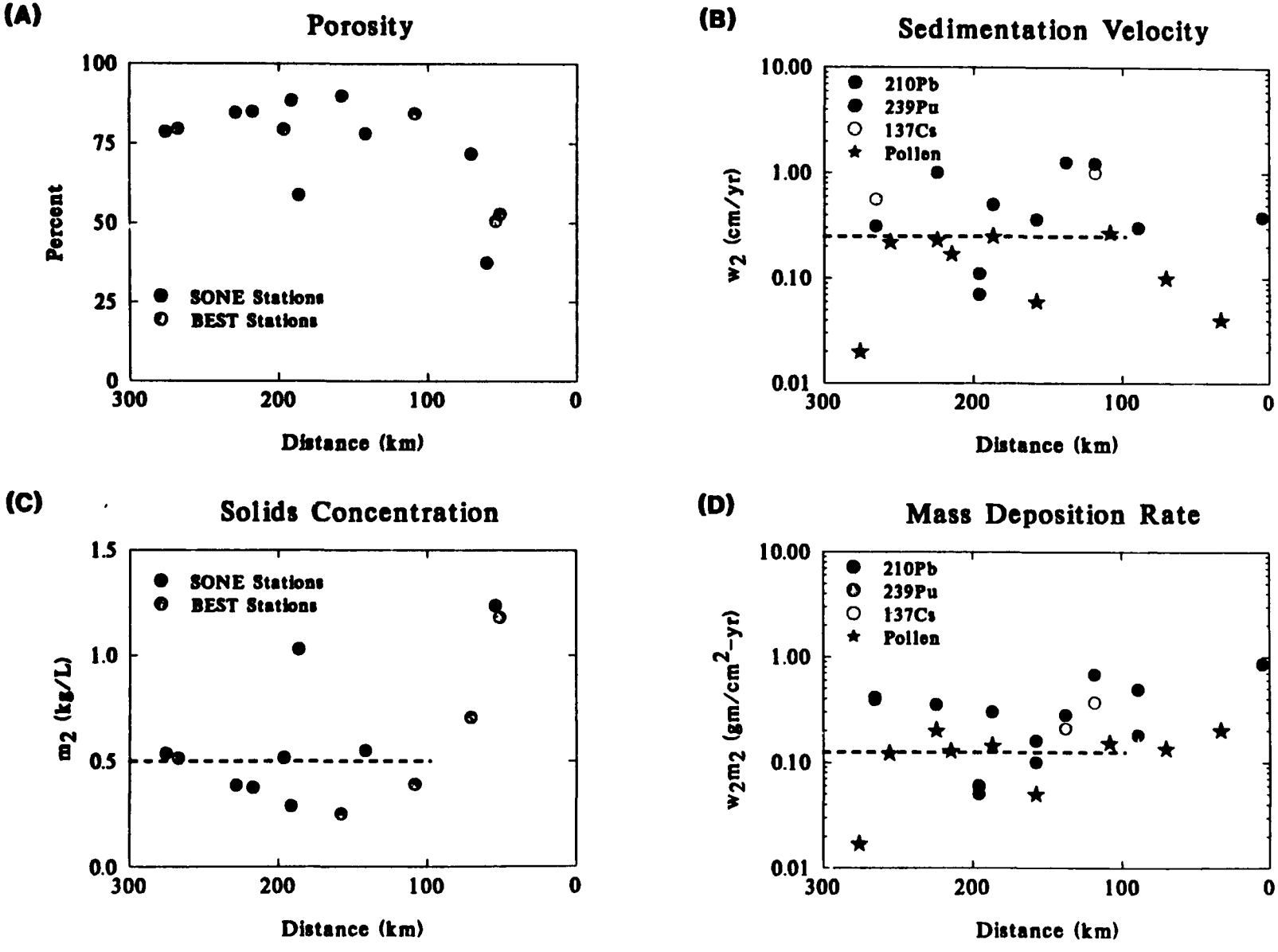

ROBBINP5

Figure 9.6

$a_0, \ldots, a_4; b_1, \ldots, b_4$. Fig. 9.7 presents an example of the result: the overlying water DO data and the Fourier series fit. The graphical displays for all the other variables follow, Fig. 9.8 to 9.12, at the chapter's end.

2. Sediment Initial Conditions

The solution of the diagenesis and sediment model equations require initial conditions, the concentrations at t = 0: $G_{POC,i}(0)$, $P_{Si}(0)$, and the total concentrations for ammonia, nitrate, sulfide, phosphate, and silica: $C_{T1}(0)$, and $C_{T2}(0)$, to start the computations. Strictly speaking these initial conditions should reflect the past history of the depositional fluxes and overlying water conditions. Since this is impractical owing to lack of data for these earlier years it is necessary to adopt some other strategy to obtain initial conditions.

Two possibilities are available. The first is to assign these initial conditions. However, there appears to be no unique way to establish these concentrations. Therefore, the results can be quite arbitrary and subject to a large uncertainty.

The alternate is to equilibrate the model using the 1985 information, the first year for which inputs and overlying water data are available. The procedure is as follows. The model equations can be solved using an arbitrary set of initial conditions. In order to speed up the convergence, the first set of initial conditions are chosen to be the steady state solution for the 1985 average conditions. This insures that the initial conditions are reasonable. The model is then integrated for one year. The final concentrations at the end of the first year are then used as the initial conditions and the equations are solved again for the first year. This procedure is repeated until the final conditions at the end of the year are equal, within a tolerance, to the initial conditions. At this point the model is at periodic steady state. The solution represents the situation that would be reached if the conditions for 1985 had repeatedly occurred and the sediment had equilibrated to these conditions.

The utility of this method is that the initial conditions result from a well specified requirement - that of periodic steady state - rather than a more arbitrary procedure. When changes are made in the kinetic parameters to improve the calibration, the initial conditions are recalculated with the new model coefficients. This removes the initial conditions from the parameters that require calibration. They are always set at the concentrations that produce a periodic steady state for the 1985 inputs.

3. Finite Difference Equations

The most convenient method of solution for the sediment model equations is to use an implicit integration scheme. This is due to the similarity of the equations that result to the steady state equations for which a simple solution algorithm is available. Given the concentrations at t, the finite difference equations are solved for the unknown concentrations at $t + \Delta t$. Since layer 1 is quite thin, $H_1 \sim 1$ mm = 10^{-3} m, and the surface mass transfer coefficient is of order $s \sim 0.1$ (m/d), the residence time in the layer is: $H_1/s \sim 10^{-2}$ days. Hence, it can be assumed to be at steady state without any loss of accuracy. The layer 1 equation is:

$$0 = H_1 \frac{dC_{T1}^{(t+\Delta t)}}{dt} = s(f_{d1}C_{T1}^{(t+\Delta t)} - C_{d0}^{(t+\Delta t)}) + w_{12}(f_{p2}C_{T2}^{(t+\Delta t)} - f_{p1}C_{T1}^{(t+\Delta t)})$$

$$+ K_{L12}(f_{d2}C_{T2}^{(t+\Delta t)} - f_{d1}C_{T1}^{(t+\Delta t)}) - \frac{\kappa_1^2}{s}C_{T1}^{(t+\Delta t)} + J_{T1} \qquad (9)$$

The layer 2 mass balance finite difference equation which is implicit in time is:

$$H_2 \frac{C_{T2}^{(t+\Delta t)} - C_{T2}^{(t)}}{\Delta t} = -w_{12}(f_{p2}C_{T2}^{(t+\Delta t)} - f_{p1}C_{T1}^{(t+\Delta t)}) - K_{L12}(f_{d2}C_{T2}^{(t+\Delta t)} - f_{d1}C_{T1}^{(t+\Delta t)})$$

$$- \kappa_2 C_{T2}^{(t+\Delta t)} - w_2 C_{T2}^{(t+\Delta t)} + J_{T2}^{(t+\Delta t)} \qquad (10)$$

which can be put into a form that is similar to the steady state equations:

Overlying Water Dissolved Oxygen

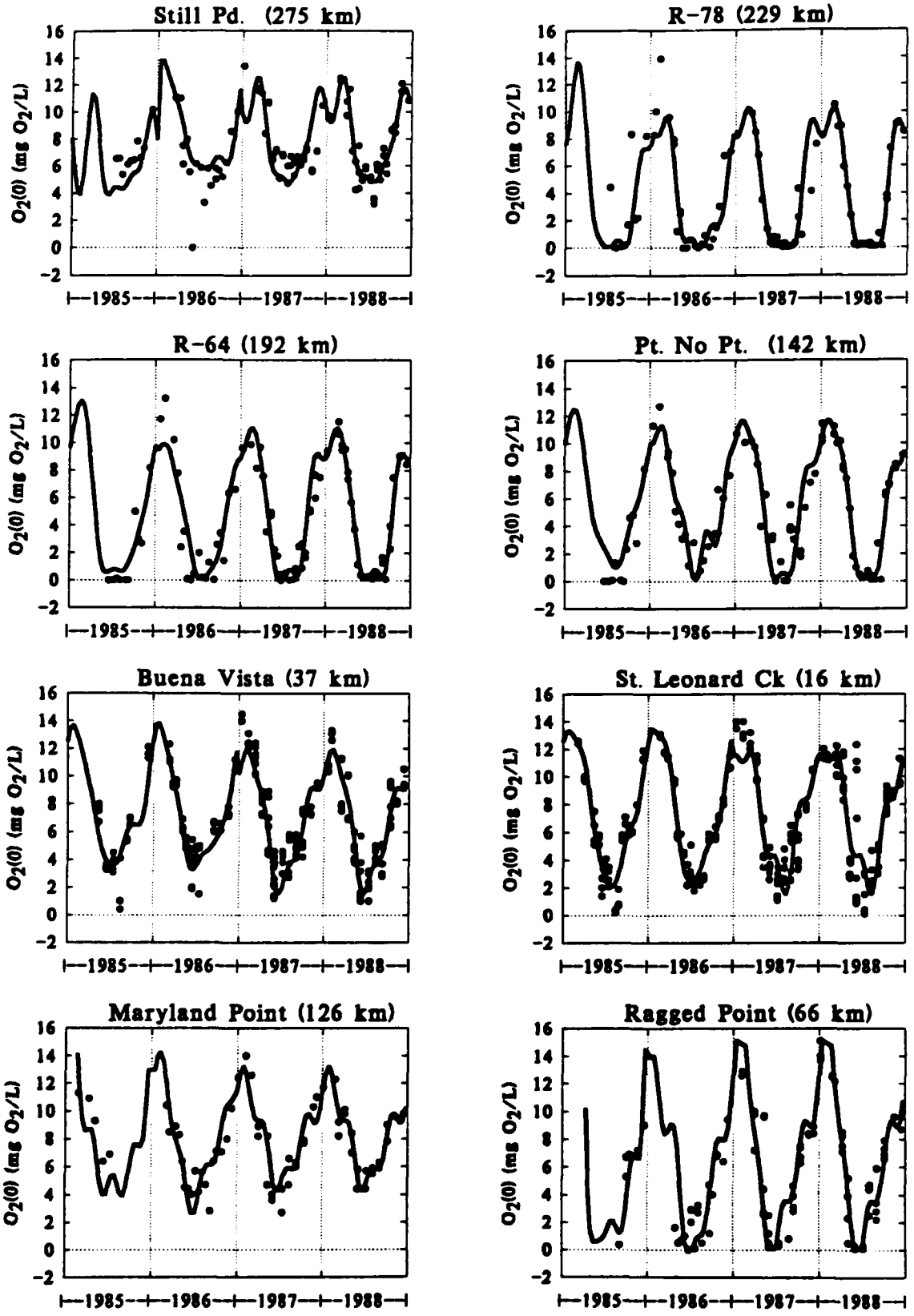

RUN104 - PLTVO20

Figure 9.7

Overlying Water Ammonia

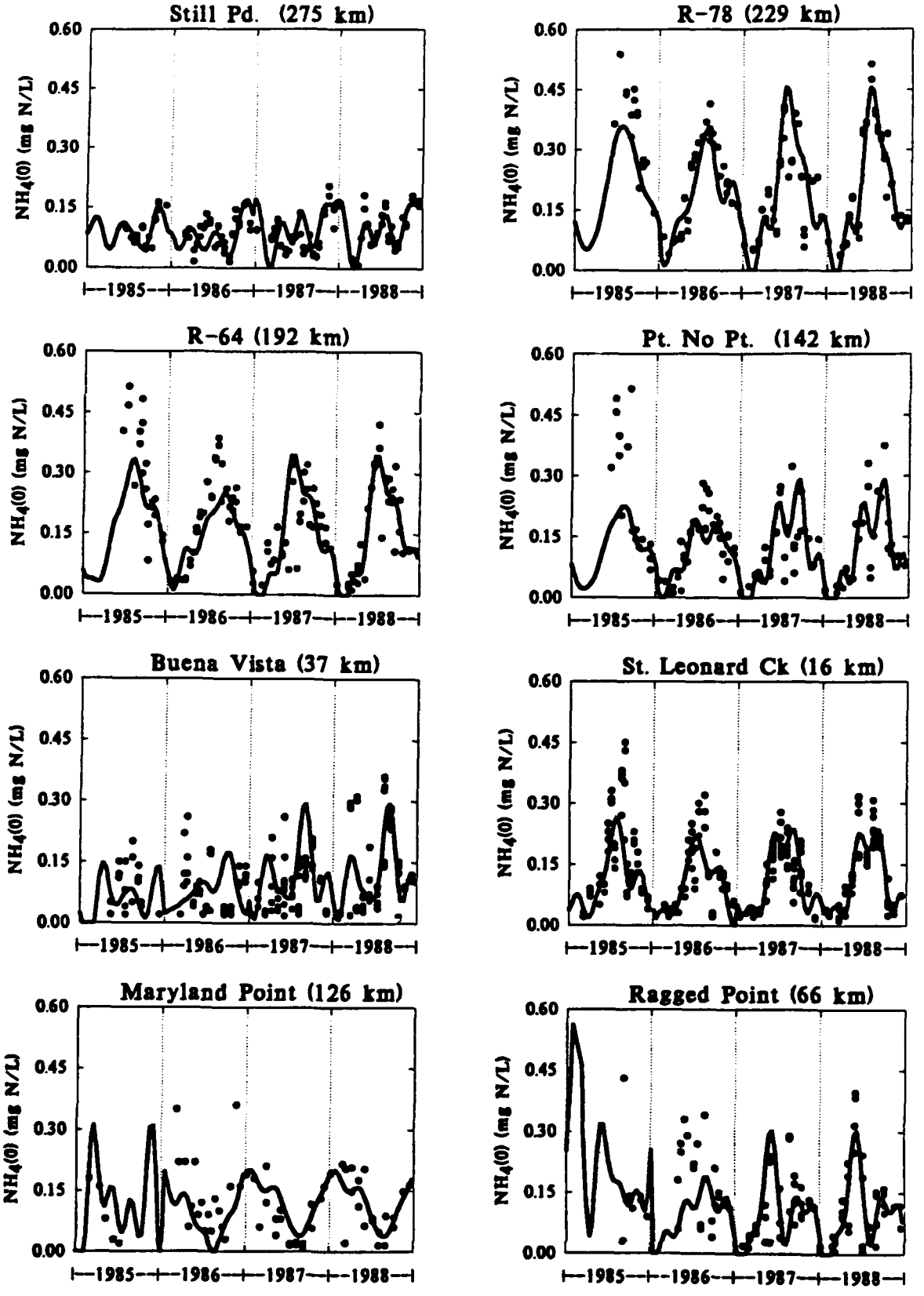

RUN104 - PLTVNH40

Figure 9.8

Overlying Water Nitrate

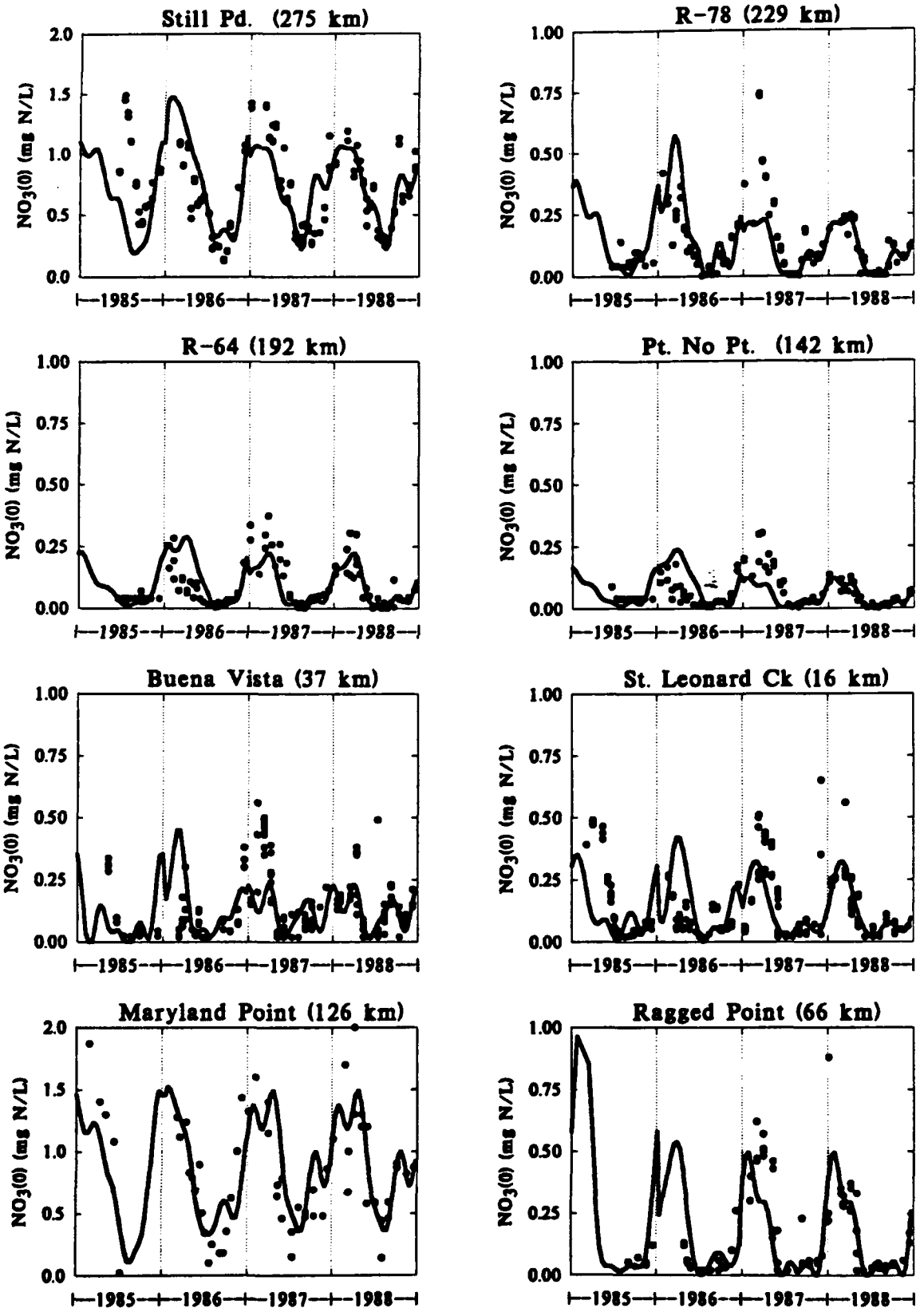

RUN104 - PLTVNO30

Figure 9.9

Overlying Water Phosphate

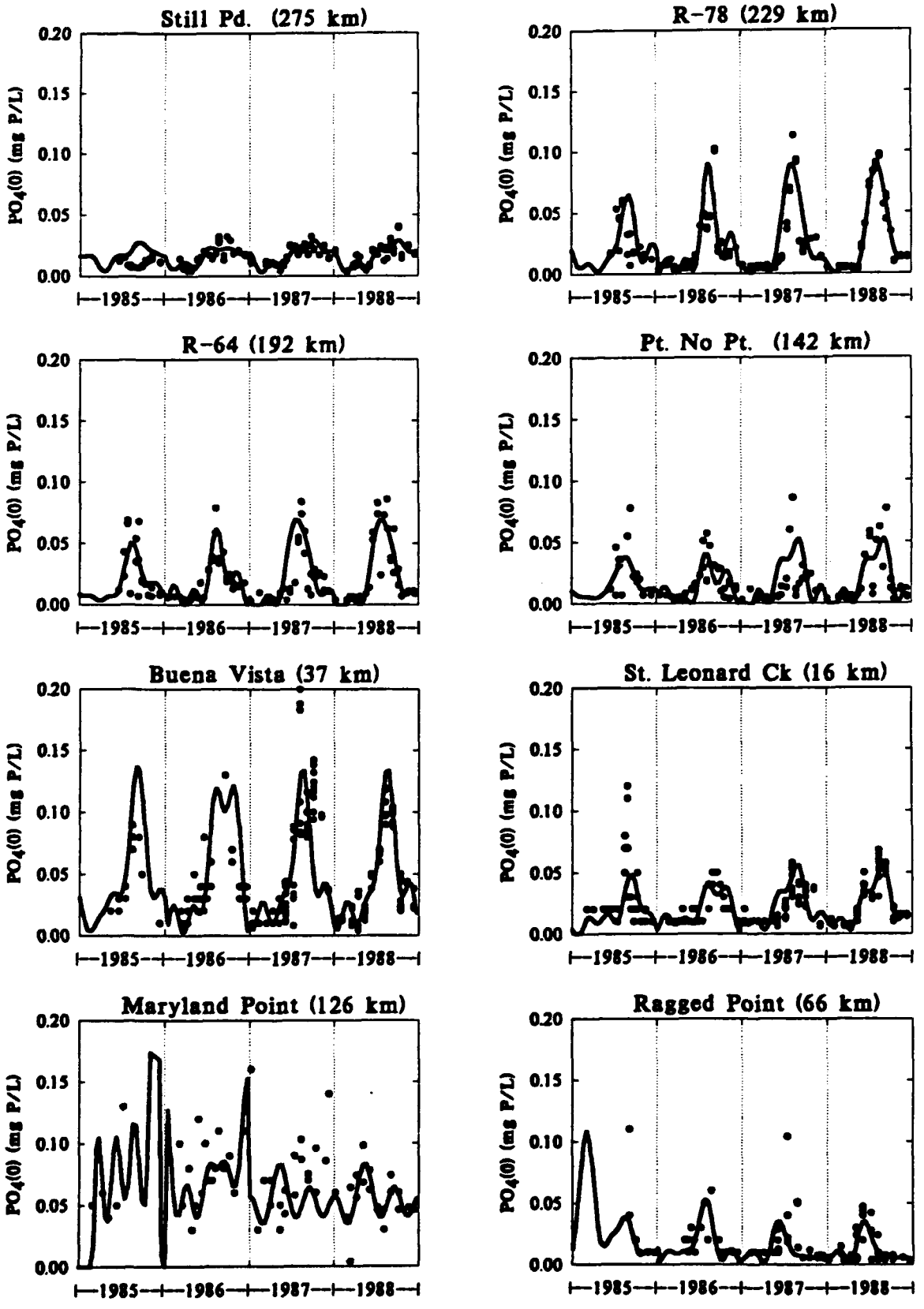

RUN104 - PLTVPO40

Figure 9.10

Overlying Water Silica

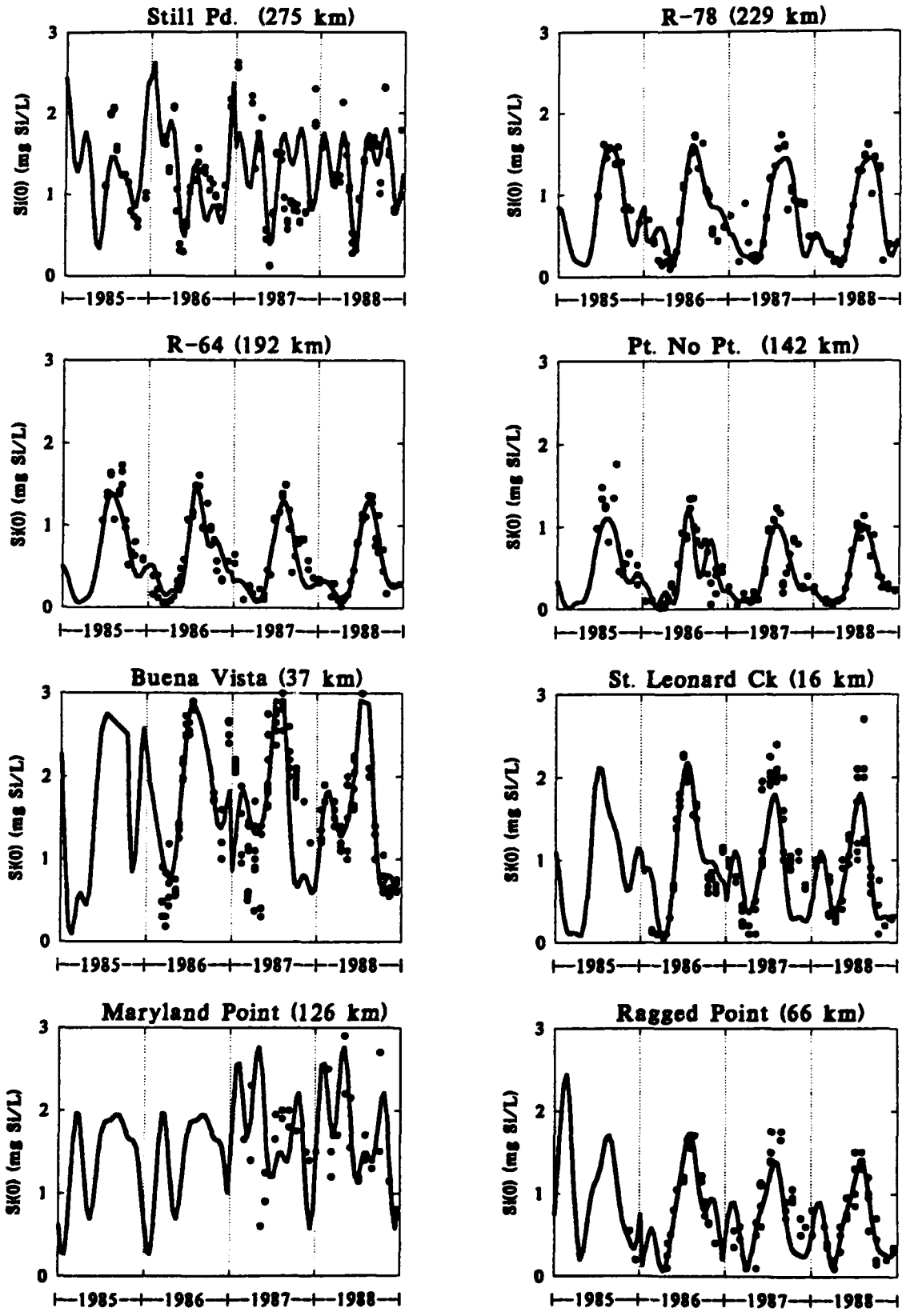

RUN104 - PLTVSIO

Figure 9.11

Overlying Water Temperature

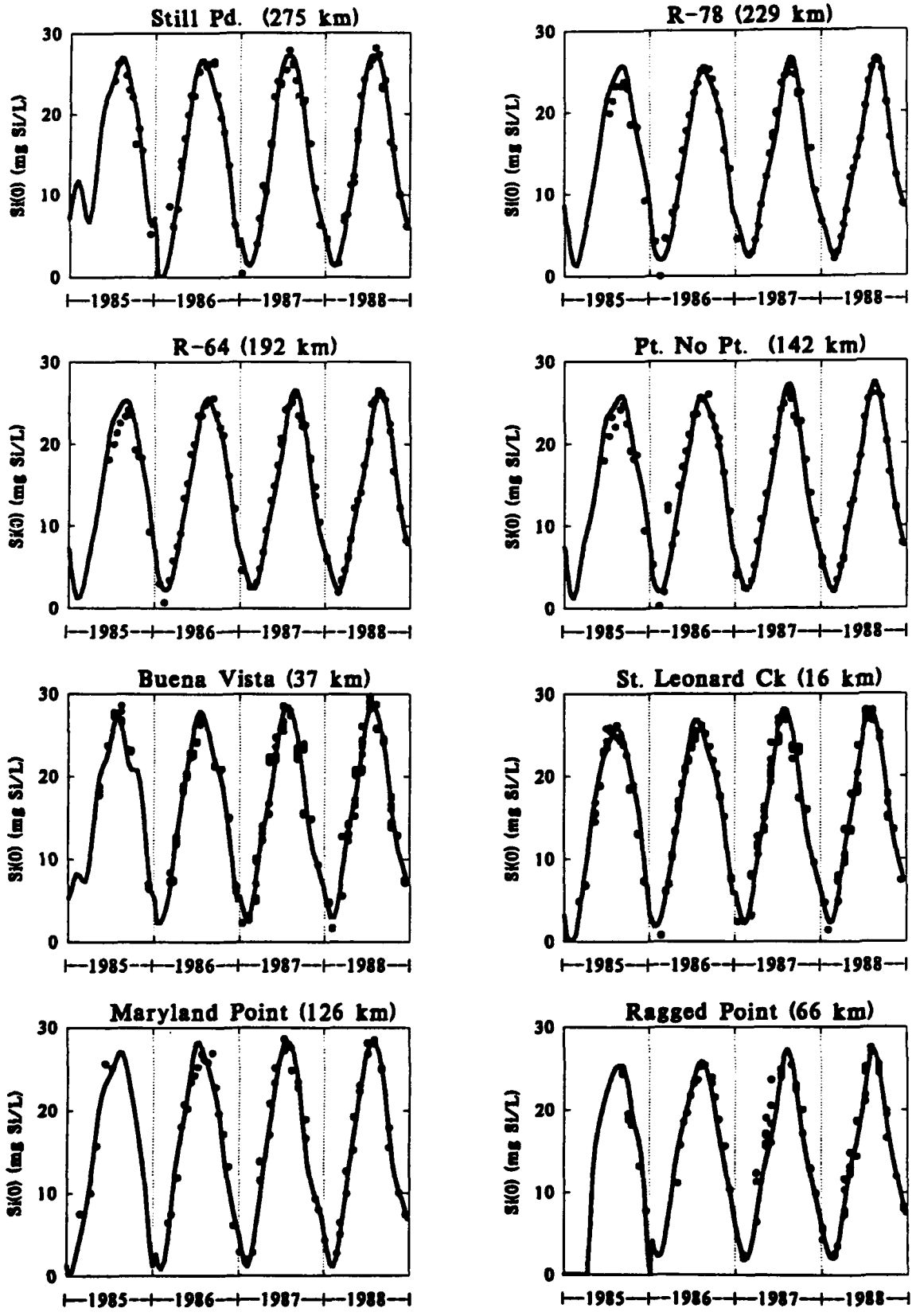

RUN104 - PLTVTEMO

Figure 9.12

$$0 = -w_{12}(f_{p2}C_{T2}^{(t+\Delta t)} - f_{p1}C_{T1}^{(t+\Delta t)}) - K_{L12}(f_{d2}C_{T2}^{(t+\Delta t)} - f_{d1}C_{T1}^{(t+\Delta t)})$$

$$-\kappa_2 C_{T2}^{(t+\Delta t)} - w_2 C_{T2}^{(t+\Delta t)} - \frac{H_2 C_{T2}^{(t+\Delta t)}}{\Delta t} + J_{T2}^{(t+\Delta t)} + \frac{H_2 C_{T2}^{(t)}}{\Delta t} \qquad (11)$$

The terms corresponding to the derivatives: $H_2 C_{T2}^{(t+\Delta t)}/\Delta t$ and $H_2 C_{T2}^{(t)}/\Delta t$, simply add to the layer 2 removal rate and the forcing function respectively. Hence the solution algorithm for these equations is the same as the steady state model. $C_{T1}^{(t+\Delta t)}$ and $C_{T2}^{(t+\Delta t)}$ are the two unknowns in the two equations which are solved at every time step.

For the sake of symmetry the diagenesis equations are also solved in implicit form:

$$H_2 \frac{G_{POC,i}^{(t+\Delta t)} - G_{POC,i}^{(t)}}{\Delta t} = -K_{G,i}\theta_{G,i}^{(T-20)} G_{POC,i}^{(t+\Delta t)} H_2 + J_{GPOC,i} \qquad (12)$$

so that:

$$G_{POC,i}^{(t+\Delta t)} = \left[G_{POC,i}^{(t)} + \frac{\Delta t}{H_2} J_{GPOC,i} \right] [1 + \Delta t K_{G,i}\theta_{G,i}^{(T-20)}]^{-1} \qquad (13)$$

Similarly, the particulate biogenic silica equation becomes:

$$P_{Si}^{(t+\Delta t)} = \left[P_{Si}^{(t)} + \frac{\Delta t}{H_2} J_{PSi} \right] \left[1 + \frac{w_2 \Delta t}{H_2} + K_{Si}\theta_{Si}^{(T-20)} \Delta t \frac{[Si]_{sat} - f_{d2}[Si(2)]^{(t)}}{P_{Si}^{(t)} + K_{M,PSi}} \right]^{-1} \qquad (14)$$

where P_{Si} in the Michaelis Menton term has been kept at time level t to simplify the solution.

The solution of the layer 1 and layer 2 mass balance equations require an iterative technique since the surface mass transfer coefficient, $s = SOD/[O_2](0)$, is a function of the SOD which, in turn, is a function of the ammonia and sulfide mass balance equations. A simple back substitution method can be used to solve the equations at each time step. The procedure is:

(1). Start with an initial estimate of SOD. For example: $SOD = a_{o2,c} J_c$, or the previous time step SOD.

(2). Solve layer 1 and 2 equations for ammonia, nitrate, and sulfide.

(3). Compute the SOD that results: SOD = NSOD + CSOD.

(4). Refine the estimate of SOD. A root finding method is used to make the new estimate (Press et al., 1989).

(5). Go to (2) if no convergence.

(6). Compute the phosphate and silica fluxes

This method has been found to be quite reliable. Since it is implicit it can be used to compute the steady state solution very easily by setting Δt to a large number. And, by comparison to an explicit scheme it adds only a small amount of additional computation.

E. References

Aller, R.C. (1982). The effects of macrobenthos on chemical properties of marine sediment and overlying water. Animal-Sediment Relations. The Biogenic Alteration of Sediments. New York, Plenum Press. pp. 53-102

Hamming, R.W. (1962). Numerical Methods for Scientists and Engineers. New York, McGraw-Hill Book Company, Inc.

Mancini, J.L. (1983). A method for calculating effects on aquatic organisms of time varying concentrations. Water Res. 17: pp. 1355-1362.

Matisoff, G. (1982). Mathematical Models of Bioturbation. Animal-Sediment Relations. The Biogenic Alteration of Sediments. New York, Plenum Press. pp. 289-330.

Maughan, J.T. (1986). Relationship between macrobenthic infauna and organic carbon. Ph.D. Thesis. University of Rhode Island.

McCall, P.L. and Tevesz, M.J.S. (1982). The effects of benthos on physical properties of freshwater sediments. Animal-Sediment Relations. The Biogenic Alteration of Sediments. New York, Plenum Press. pp. 105-176.

Press, W.H., Flannery, B.P., Teukolsky, S.A. and Vetterling, W.T. (1989). Numerical Recipes. The Art of Scientific Computing. (FORTRAN Version). New York, NY, Cambridge University Press.

Robbins, J.A., Husby-Coupland, K. and White, D.S. (1984). Precise radiotracer measurement of the rate of sediment reworking by *Stylodrilus Heringianus* and the effects of variable dissolved oxygen concentrations. J. Great Lakes Res. 10(4): pp. 335-347.

Robbins, J.A., Keilty, T.J., White, D.S. and Edgington, D.N. (1989). Relationships between tubificid abundances, sediment composition and accumulation rates in Lake Erie. Canadian J. Fish. Aquatic Sci. 46(2): pp. 223-231.

Versar, Inc. (1990). Impact assessment of Craighill Channel Dredged Material Placement in the Deep Trough. Versar, Inc. ESM Operations 9200 Rumsery Rd. Columbia, MD 21045.

X. MODEL CALIBRATION

A. Introduction

This chapter presents the results of the calibration of the time variable sediment flux model to the Chesapeake Bay data set. The primary calibration data are the observed sediment fluxes. However, the model also computes the organic and inorganic particulate and dissolved concentrations in t'ıe anaerobic layer. These are compared to observed pore water and particulate phase measurements.

The calibration of the time variable model is constrained by the interrelationships between the fluxes. These arise from the stoichiometric dependencies of the depositional fluxes, which supply nitrogen, carbon, phosphorus and silica in fixed proportions. In addition, the mechanisms that determine the fluxes are interdependent. The depth of the aerobic layer, which regulates the extent of all oxidation reactions, is a function of the SOD and the overlying water DO. The fluxes of ammonia, nitrate, sulfide, oxygen, phosphate, and silica are computed using the difference in overlying water and computed aerobic layer concentrations, and the surface mass transfer coefficient, s. But s itself is computed using the ratio of computed oxygen flux and the observed overlying water DO concentration. Hence, the model fluxes are interrelated due to their implicit dependency on s.

The calibration involves choosing model parameters that best reproduce the observations. Some of the model parameters have been established using the steady state version of the model. Others are the result of fitting the time variable model fluxes to the observations as discussed below.

The model kinetic formulations are presented below for each solute. The model parameters and their values are also listed. Although these equations have been presented in the previous chapters, they are grouped together in this chapter for convenience of presentation. The notation is consistent with the general equations presented in Chapter IX.

The model computation is performed as follows. For each station the model is equilibrated to the 1985 inputs as discussed in Chapter IX. Then using the equilibrated 1985 initial conditions, and the depositional fluxes listed in Chapter VIII, the model equations are integrated for the four year period: from 1985 to 1988. The resulting fluxes and concentrations are displayed in the figures that follow.

B. Ammonia

1. Model parameters

Ammonia is nitrified in the aerobic layer. A Michaelis Menton expression is used for the ammonia concentration dependency and for the oxygen dependency of the nitrification rate. The temperature dependence is applied to κ^2 since this is proportional to the first order reaction rate constants. The aerobic layer reaction velocity is:

$$\kappa_1^2 = \kappa_{NH4,1}^2 \theta_{NH4}^{(T-20)} \left(\frac{K_{M,NH4} \theta_{K_{M,NH4}}^{(T-20)}}{K_{M,NH4} \theta_{K_{M,NH4}}^{(T-20)} + [NH_4(1)]} \right) \left(\frac{[O_2(0)]}{2K_{M,NH4,O2} + [O_2(0)]} \right) \quad (1)$$

Partitioning is included although it has a negligible effect on the computation. No anaerobic layer reactions occur. The parameters values are:

$\kappa_{NH4,1}$	Reaction velocity for nitrification	0.131	m/d
θ_{NH4}	Temperature coefficient for nitrification	1.123	-
$K_{M,NH4}$	Nitrification half saturation constant for ammonia	728	mg N/m^3
$\theta_{K_{M,NH4}}$	Temperature coefficient for nitrification half saturation constant	1.125	-
$K_{M,NH4,O2}$	Nitrification half saturation constant for oxygen	0.37	mg O_2/L

$\pi_{NH4,1}$	Aerobic layer partition coefficient	1.0	L/kg
$\pi_{NH4,2}$	Anaerobic layer partition coefficient	1.0	L/kg
κ_2	Anaerobic layer reaction velocity	0.0	m/d
J_{T1}	Aerobic layer ammonia source	0.0	mg N/m^2-d
J_{T2}	Nitrogen diagenesis, J_N, eq.(VIII-3)	-	mg N/m^2-d

2. Diagnostic Results

In order to illuminate the inner workings of the model, plots of various concentrations and fluxes for station R-78 are presented in Fig. 10.1. The depositional flux of PON provides the source to the diagenesis model. The flux is apportioned to the three G classes which react at the appropriate reaction rates (Chapter VIII). The concentrations for the three classes are shown in Fig. 10.1A. Note that almost all of the PON in the sediment is the nonreactive G_3 component consistent with previous analysis. Since the decay rates for the two reactive classes are temperature dependent, an annual variation occurs with maxima in the spring and minima in the fall. This occurs because the mineralization reactions are slow in the early part of the year and PON builds up. Then, during the high temperature periods, mineralization exceeds production and the PON concentration decreases.

The diagenesis flux that results is shown in Fig. 10.1B, a plot of the components of J_N due to G_1, and G_2, denoted by $J_{N,G1}$ and $J_{N,G2}$, and J_N itself. The majority of the flux is produced by G_1, followed by G_2. The fractions are in proportion to $f_{PON,1}$ and $f_{PON,2}$, the fractions of J_{PON} that are in the two G classes. The reason is that essentially all of G_1 and G_2 react away in the active layer so that the fraction buried is negligible. Hence, by mass balance each component must be converted to J_N. G_3, on the other hand, does not react. It just passes through the layer and is buried.

Station R-78

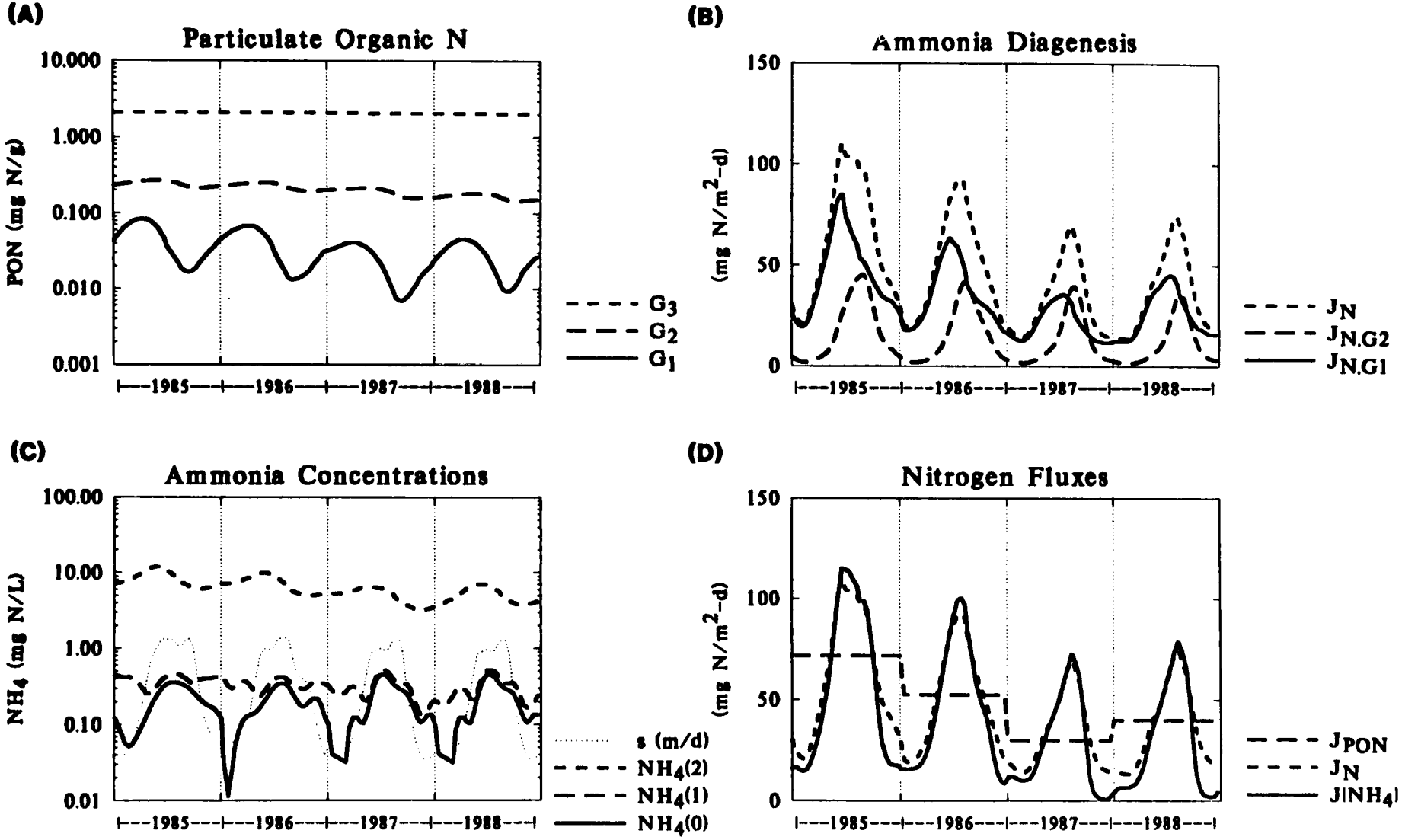

RUN104 - PLT3JND

Figure 10.1

The ammonia concentrations in the overlying water and the aerobic and anaerobic layers are shown in Fig. 10.1C. In addition, the surface mass transfer coefficient, s, is plotted. It is important to realize that the magnitude of the aerobic and anaerobic layer ammonia concentrations do not determine the magnitude of the ammonia flux to the overlying water. Rather, they are determined by the magnitude of the mixing coefficients. This is clear from the steady state solutions, eq.(II-7,II-8). The magnitude of the ammonia flux is determined by the rate of production by diagenesis and the fraction that is nitrified. Therefore, it is misleading to interpret the layer concentrations as causing the flux. Note that even though the ammonia flux peaks in the summer, the gradient between the overlying water and aerobic layer concentrations is smallest. This is due to the large surface mass transfer coefficient that reduces the aerobic layer concentration. Conversely, the gradient is maximum in the winter, which corresponds to the smallest ammonia fluxes, but also to the smallest s.

A comparison of the three fluxes representing the input, J_{PON}, the result of mineralization, J_N, and the output, $J[NH_4]$, is shown in Fig. 10.1D. The depositional flux, J_{PON}, is assumed to be constant within the year, as shown. The diagenesis flux varies seasonally due to the temperature dependence of the reaction rate. The ammonia flux is also shown. During the cold periods, the ammonia flux is substantially below the diagenesis flux. The difference is being nitrified or is increasing the anaerobic layer ammonia concentration. During the summer, the peak ammonia flux actually slightly exceeds the diagenesis flux. The extra ammonia is being supplied from storage in the anaerobic layer.

3. Data Comparisons

The ammonia flux data are compared to observations in Fig. 10.2. The top two rows are the Chesapeake Bay main stem stations. The third row are the Patuxent estuary stations and the bottom row are the Potomac estuary stations. The locations are shown in Fig. 1.2. The mean of the triplicated measurement is shown, together with the range of the measurements, denoted by the vertical line. If no line is shown, the range is smaller than the symbol. In general, the model

reproduces the very small fluxes during the cold periods and the peaks in the summer. The temporal variation is due primarily to the variation in ammonia diagenesis (Fig. 10.1), and to a lesser extent by the variation in the fraction of ammonia diagenesis that is nitrified.

The sediment nitrogen data are examined in Fig. 10.3. The longitudinal profiles of particulate organic nitrogen (PON) and pore water ammonia concentrations for the main stem of the Chesapeake Bay are compared to the computations for the four main bay stations (Fig. 10.3A,B). The data are for the top 10 cm, corresponding to the anaerobic layer of the model. The model computations for the four years are averaged and the mean and range are presented.

The spatial variation of increasing and then decreasing PON concentrations is reproduced by the model computations, Fig. 10.3A. This is a direct result of the variation in the depositional fluxes for the four stations. In addition, the magnitude of the PON concentrations computed by the model depends on the fraction of the depositional flux that is in the G_3 component, $f_{PON,3}$, and the sedimentation velocity, ω_2. The agreement suggests that these parameters are consistent with the observations.

The spatial variation of anaerobic layer ammonia concentration is compared to the pore water data from the Bricker data set (Bricker et al., 1977) in Fig. 10.3C. As pointed out in Chapter II, the anaerobic layer ammonia concentration is used to estimate the layer 1 - 2 diffusive mass transfer coefficient, K_{L12}. The pore water data exhibits more variability than the computations. However, these measurements are from many stations, not just the four SONE stations. Also, these data are from the mid 1970s. Therefore, the comparison should be viewed more as an order of magnitude check that the diffusive exchange coefficient is reasonable. Some pore water data for the SONE stations are available for 1988. These are compared to the model computations in Fig. 10.3B,D. The model correctly reproduces the smaller concentrations at Still Pond, Fig. 10.3B, corresponding to a smaller depositional flux, than at R-64, Fig. 10.3D. Also the temporal variation seems to be reasonably well reproduced.

Ammonia Flux

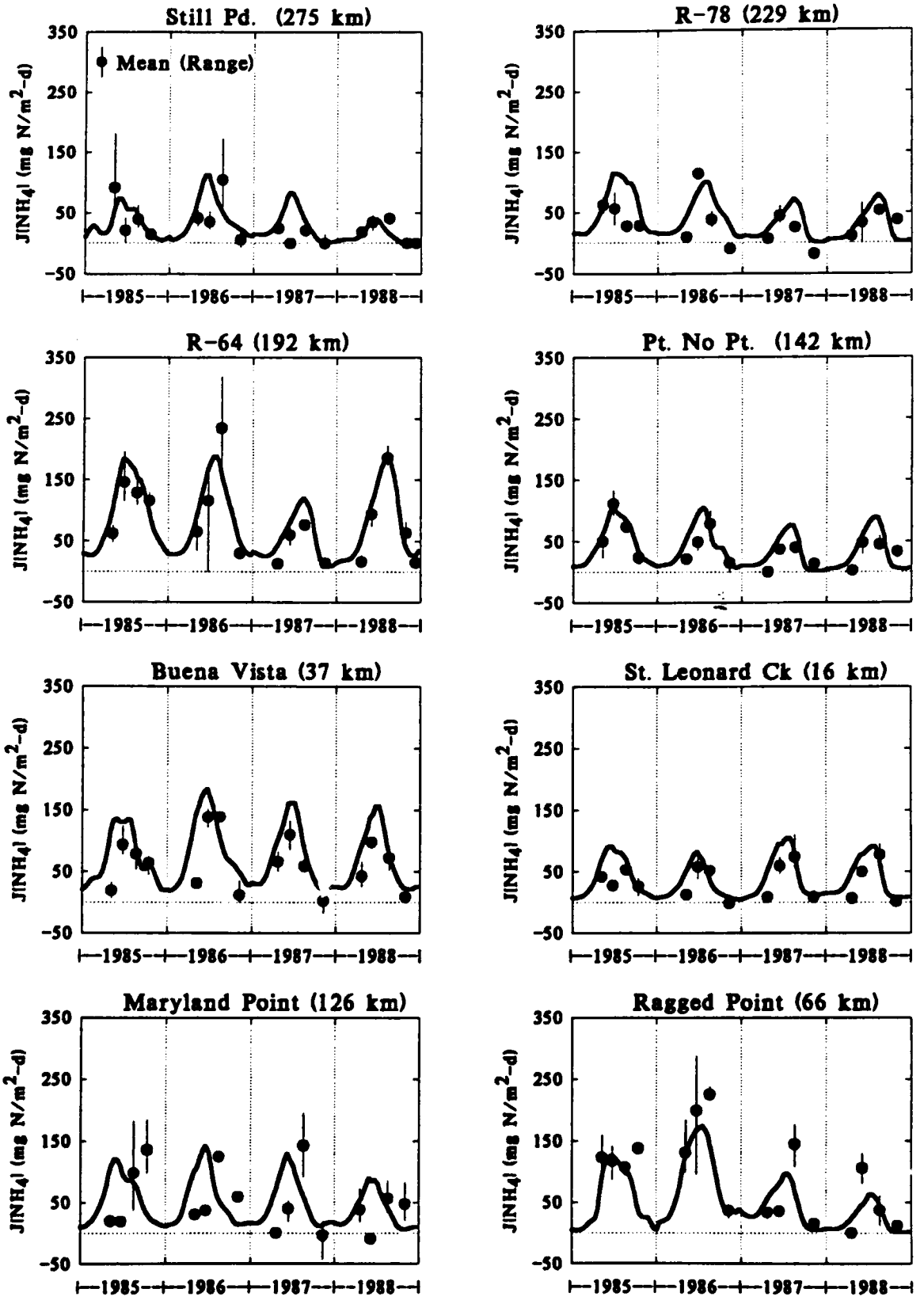

RUN104 - PLTVNH41

Figure 10.2

Sediment Composition - Nitrogen

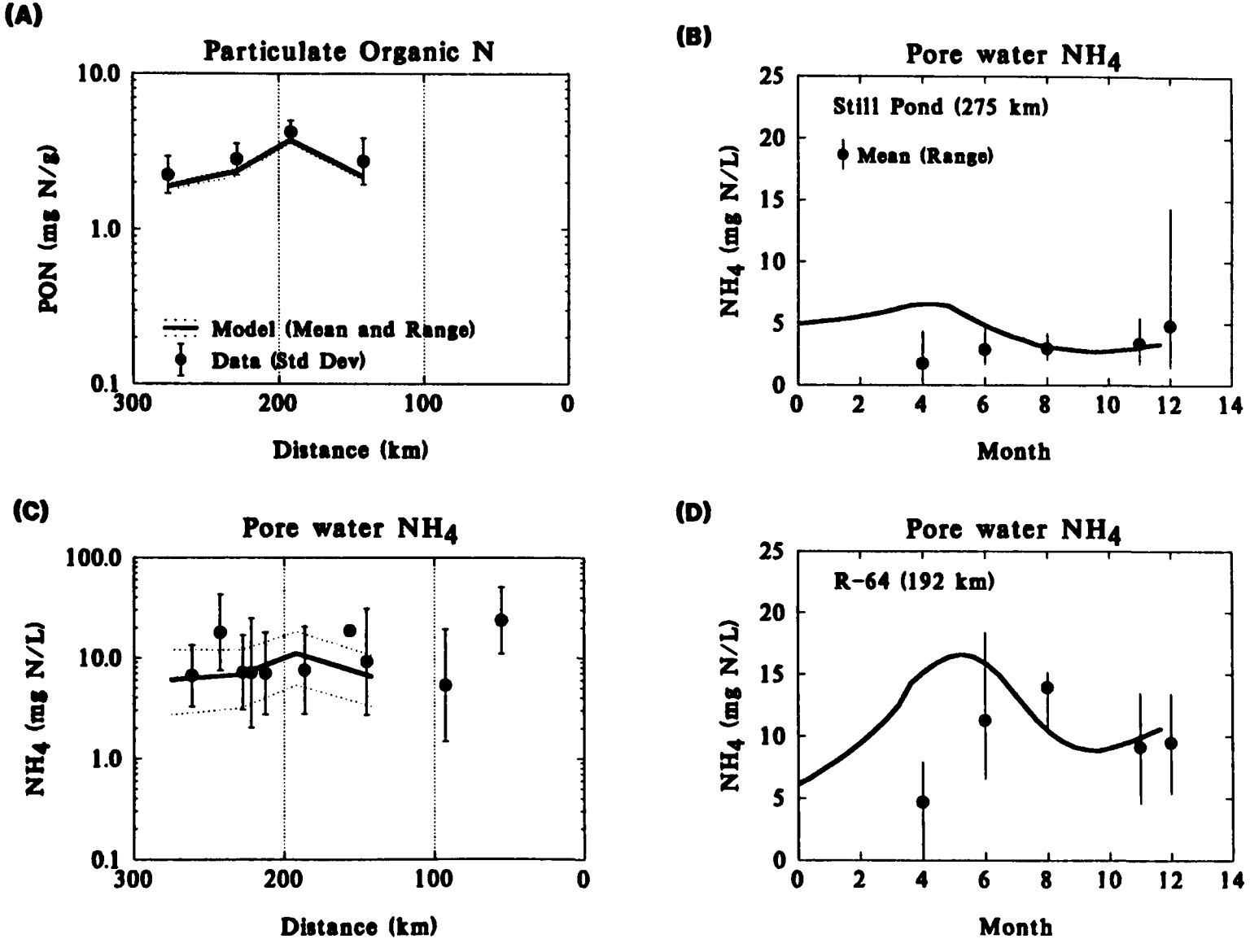

RUN104 - PLT3IPWN

Figure 10.3

Fig. 10.4 compares the measured and modeled fluxes in four ways. Figure 10.4A is a pointwise comparison. The plot is an alternate presentation of the data and computation in Fig. 10.2. The different symbols represent main stem and tributary station with overlying water DO greater than 2 mg/L, and all samples less than 2 mg/L. There is considerable scatter in the comparison, especially at the lower ammonia fluxes. This appears to be mostly a matter of mismatches in timing between the data and the model. A more rigorous statistical analysis of the goodness of fit is presented below.

Figure 10.4B is a comparison of the probability distributions of the data and model values. It compares the ordered set of observations to the ordered set of model predictions. The plot is constructed as follows. The model values are ordered from lowest to highest. The data are also ordered from lowest to highest. Then the ordered model values and data are plotted against each other. Thus, the lowest computed model flux is plotted against the lowest observed flux. Then the next in order are plotted against each other, and so on until the largest values are plotted. This type of plot is called a quantile plot (Wilkinson, 1990) since it compares the quantiles (the ordered values) of two samples.

The main stem data are analyzed separately from the tributaries and both data sets are plotted in Fig. 10.4B. The modeled fluxes are slightly larger, in general, from the observed fluxes. However, the range of values are well represented. This comparison indicates that, considered as whole without regard to station or time, the distribution of the main stem and tributary ammonia fluxes are reproduced by the model. Since this is quite a weak form of calibration it is reassuring that this comparison is reasonable.

The bottom plots compare averages: yearly averages for each station on the left, Fig. 10.4C, and station averages (4 year averages for each station) on the right, Fig. 10.4D. The model averages are computed using the model output at every ten days. The data averages are either four points for the yearly averages, or sixteen points for the station averages. The symbols are the means ± standard error of the mean. It is interesting to note that the yearly average comparisons

seems to indicate that the observed fluxes are slightly larger than the modeled fluxes whereas the quantile plot indicates the opposite. The difference is that the yearly average model fluxes are computed using the full year computation, whereas the quantiles compare only pointwise observations and model output. The station averages are presented in Fig. 10.4D. The stations are identified by a two letter code identified in Table 10.1.

Table 10.1
Plotting Symbols for Station Averages

Station	Symbol
Still Pond	SP
R-78	R78
R-64	R64
Point No Pt.	PP

Station	Symbol
Buena Vista	BV
St. Leonard Ck.	SL
Maryland Pt.	MP
Ragged Pt.	RP

The comparison indicates that the model correctly reproduces the station averages with one exception, Ragged Point, for which the standard error of the mean is quite large.

Fig. 10.5 presents a side by side comparison of the observed and modeled distribution of fluxes as a function of temperature, overlying water oxygen concentration, and the surface mass transfer coefficient, $s = SOD/[O_2(0)]$. The temperature dependence is expected since all the mass transport coefficients and reaction rates are temperature dependent. Note, however, that there is considerable spread, particularly at low temperatures, and the model reproduces that behavior.

The middle plots in Fig. 10.5 present the observed and modeled fluxes versus overlying water dissolved oxygen concentration. The distributions appear to be reasonably similar. Both the model and the data display a rough relationship between ammonia flux and overlying water oxygen concentration, but the scatter in both model and data relationship is quite large.

Ammonia Flux Calibration

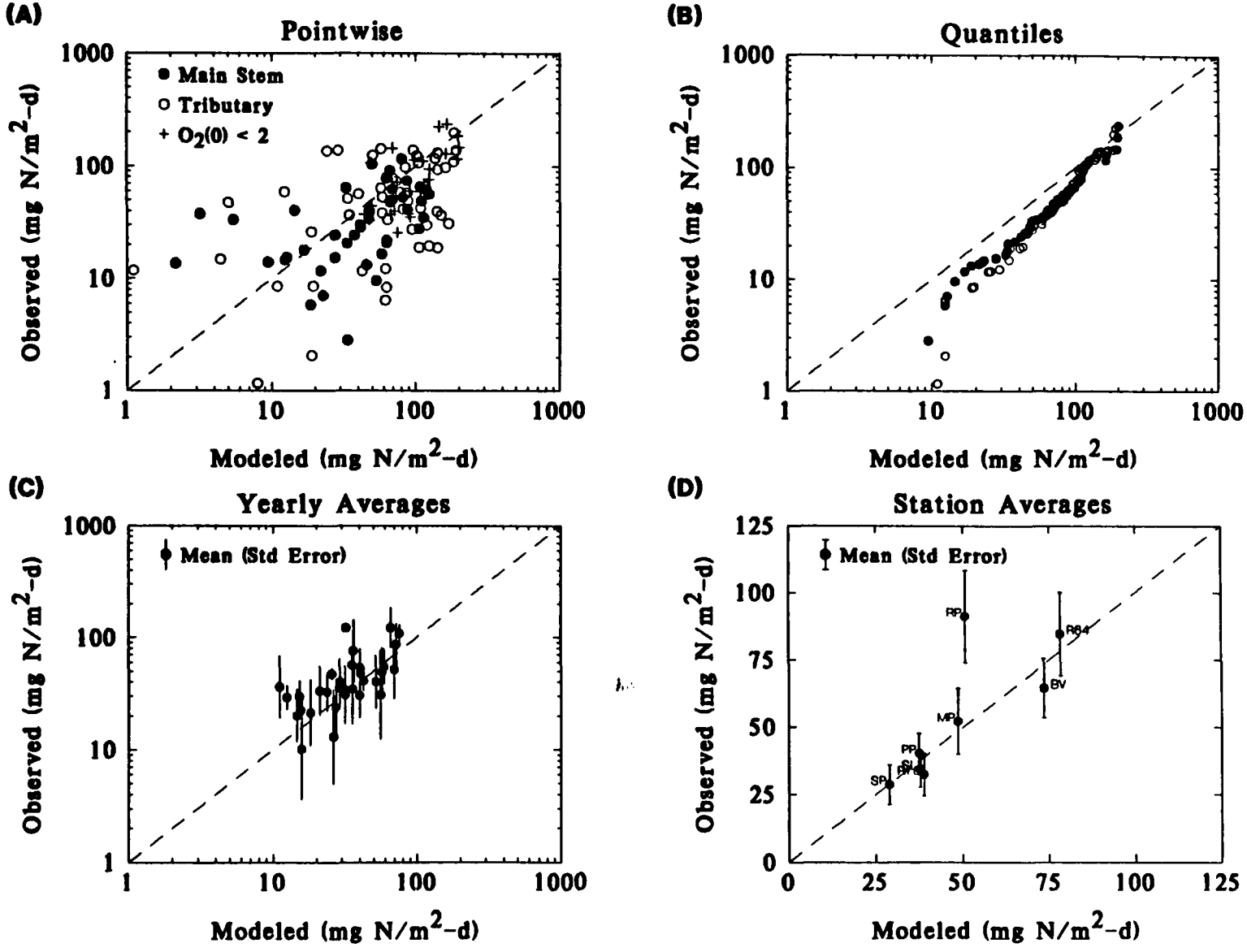

RUN104 - PLT3CMA

Figure 10.4

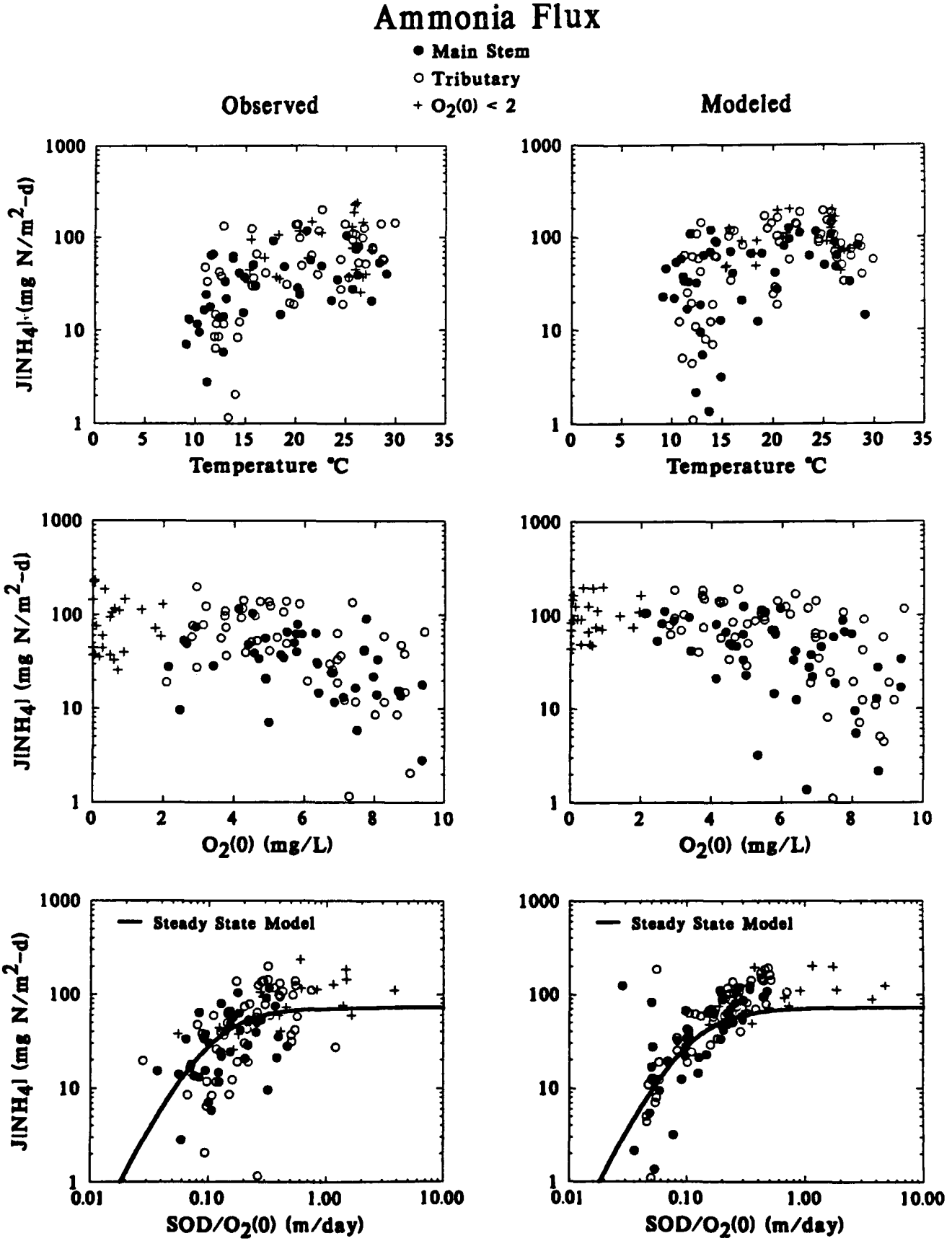

RUN104 - PLT3MOA

Figure 10.5

The bottom plots in Fig. 10.5 compare the ammonia fluxes to the surface mass transfer coefficient. The simplest steady state model, eq.(II-26), is included as well. The time variable model results show a strong relationship to s as might be expected whereas there is more scatter in the observations. It is interesting that the time variable model results conform reasonably closely to the steady state model, in spite of the significantly more complex kinetics, and the varying diagenesis fluxes.

The ammonia flux - temperature relationship is examined more closely in Fig. 10.6. It has been pointed out (Boynton et al.,, 1990) that ammonia fluxes are not a single function of temperature, but rather display a hysteresis behavior. The observed average monthly fluxes for two main stem stations, Fig. 10.6AB, are plotted versus temperature. The ammonia fluxes are generally higher in the spring months than in the fall months at the same temperature. The lines in the bottom plots, Fig. 10.6CD, are the ammonia fluxes for the four years of model calculations. The hysteresis effect is qualitatively reproduced by the ammonia flux model. The cause is the seasonal variation of G_1 carbon as illustrated in Fig. 10.1A. The spring concentrations are much higher than the fall concentrations corresponding to the same temperature. Therefore, ammonia diagenesis will exhibit some hysteresis and, consequently, so will ammonia flux.

The flux components are presented in Fig. 10.7. The depositional flux, J_{PON}, the loss of PON by sedimentation, $w_2 PON$, the loss via nitrification, labeled as κ_{NH4}, and the ammonia flux, $J[NH_4]$, are shown for each main stem, Fig. 10.7A, and tributary, Fig. 10.7B, station. Note that burial flux is roughly comparable to the loss via nitrification. The influence of overlying water anoxia is also apparent, with the aerobic stations exhibiting greater loss. The overall loss of deposited nitrogen can be quantified by comparing the ammonia flux to the depositional flux, Fig. 10.7C. Approximately 24% of the depositional flux is lost either as PON buried or via nitrification. As shown below, very little of the nitrified ammonia is returned to the overlying water. Therefore, this component is also a permanent sink of nitrogen.

C. Nitrate

1. Model Parameters

Nitrate is produced by nitrification in the aerobic layer. The nitrate source in the aerobic layer is the ammonia produced by diagenesis decremented by the ammonia that escapes to the overlying water. Thus:

$$J_{T1} = J_N - J[NH_4] \tag{2}$$

There is no anaerobic layer source. Nitrate is removed by denitrification in both the aerobic and anaerobic layers.

$$\kappa_1^2 = \kappa_{NO3,1}^2 \theta_{NO3}^{(T-20)} \tag{3}$$

$$\kappa_2 = \kappa_{NO3,2} \theta_{NO3}^{(T-20)} \tag{4}$$

The carbon required by denitrification is supplied by carbon diagenesis. No other reactions occur. The parameters are:

$\kappa_{NO3,1}$	Reaction velocity for denitrification in the aerobic layer	0.10	m/d
$\kappa_{NO3,2}$	Reaction velocity for denitrification in the anaerobic layer	0.25	m/d
θ_{NO3}	Temperature coefficient for denitrification	1.08	-

2. Data Comparisons

The observed and computed time series of nitrate fluxes are shown in Fig. 10.8. Still Pond, the station nearest the head of the bay, exhibits a strong seasonal distribution of nitrate fluxes to the sediment. This is due to the large overlying water nitrate concentrations at this station ranging from 0.5 to 1.5 mg N/L. The other main bay stations are characterized by almost zero nitrate

Ammonia Flux vs Temperature

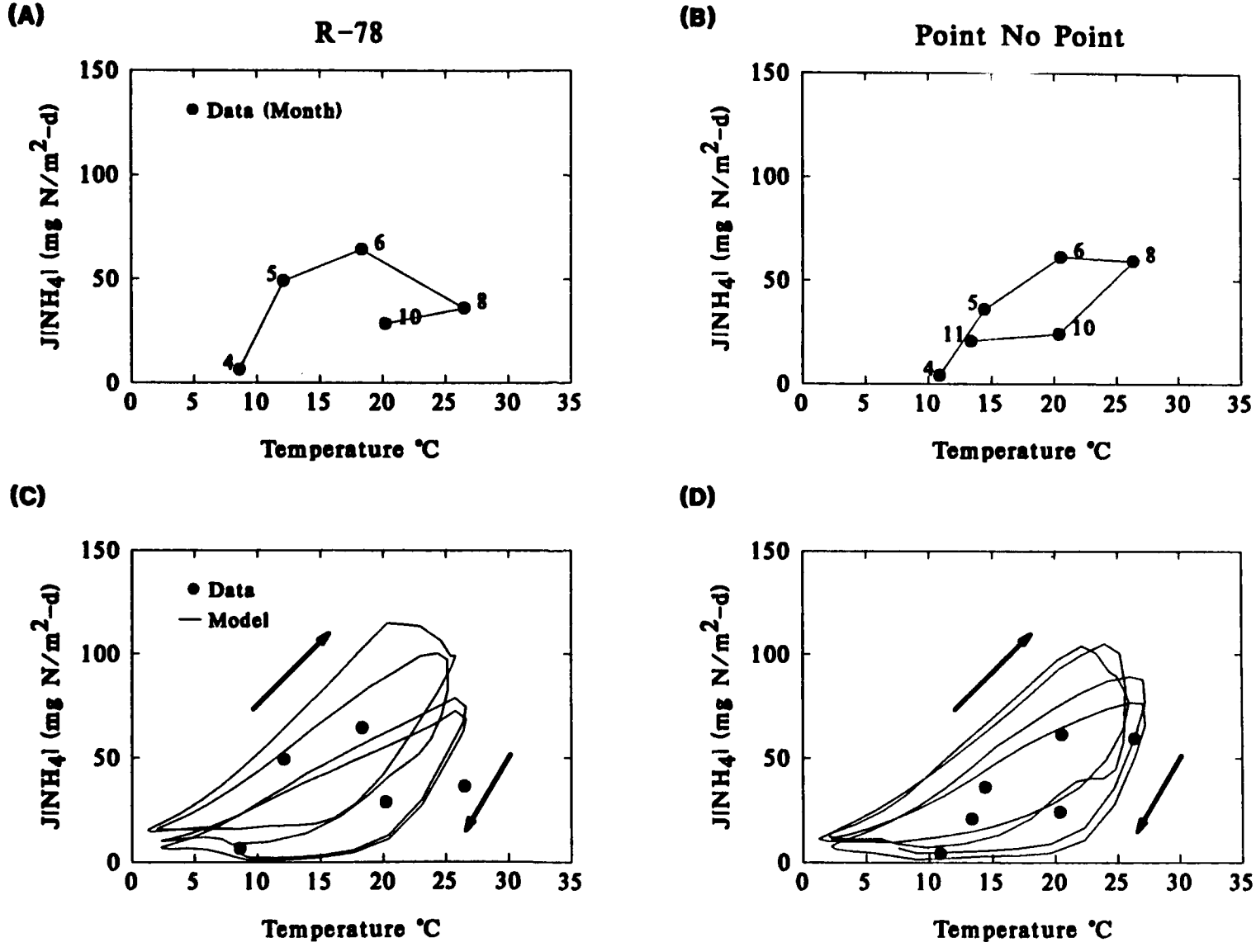

RUN104 - PLT3JNH

Figure 10.6

Flux Components

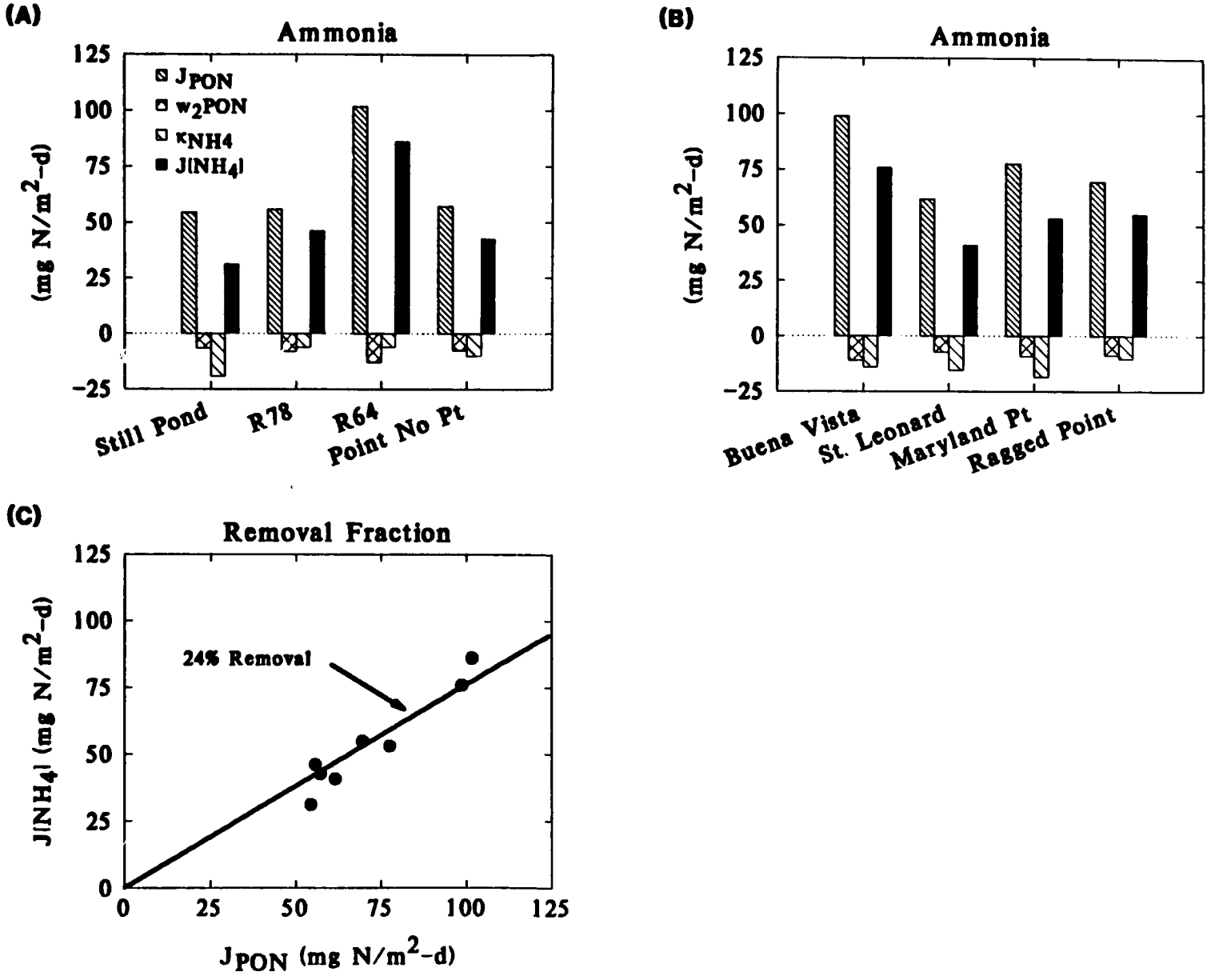

RUN104 - PLT3FR9A

Figure 10.7

Nitrate Flux

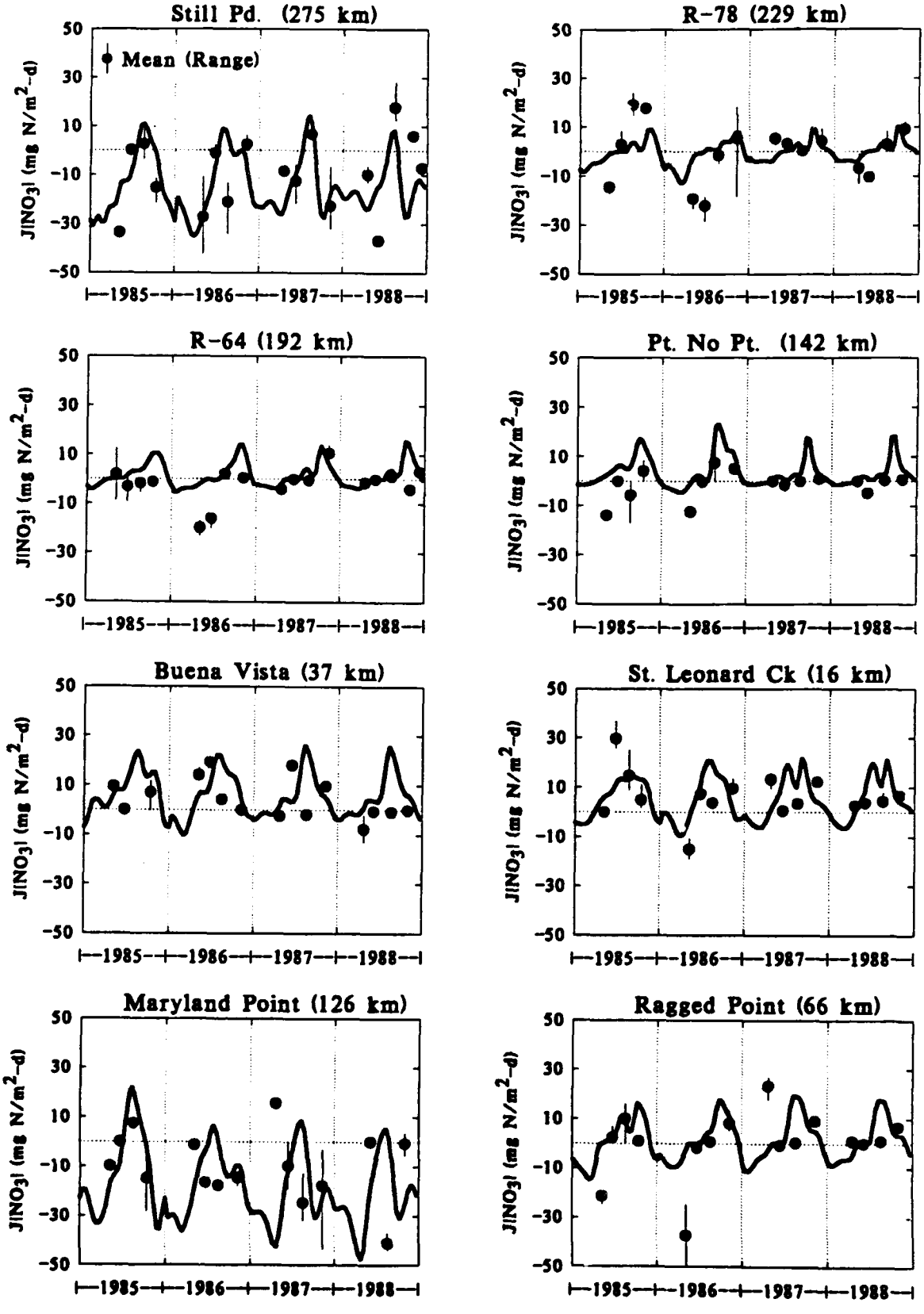

RUN104 - PLTVNO31

Figure 10.8

fluxes throughout the year which the model reproduces. The overlying water nitrate concentrations are typically less than 0.25 mg N/L and these stations have significant periods of anoxia in the summer. There appear to be infrequent positive or negative spikes which the model is unable to capture.

The Patuxent river stations, the third row in Fig. 10.8, are computed to have nitrate fluxes that are slightly positive and the data seem to reflect that behavior. The Potomac river stations, bottom row, are quite different. The upstream station at Maryland Point is predicted to have substantial fluxes to the sediment, due to a high overlying water nitrate concentration (0.5 to 1.5 mg N/L). The Ragged Point station is predicted to have zero flux during the period of anoxia and slightly positive fluxes in the fall. The time series of observations appear to reflect this behavior.

The pointwise comparison, Fig. 10.9A, indicates that the model has almost no ability to predict a particular nitrate flux at a specific time and station. However the quantile comparison, Fig. 10.9B, is satisfactory, indicating that the model reproduces the observed distribution of fluxes. This suggests that the global behavior of the model is correct, but that the pointwise predictions are very noisy. The following observations may help to explain this result. The nitrate flux is determined by the difference of two processes: the flux of overlying water nitrate into the sediment, and the flux of nitrate produced by ammonia nitrification out of the sediment. Errors in either of the fluxes is magnified in the difference of the fluxes because the net flux is reduced in magnitude while the magnitude of the error remains the same. Hence, any individual flux prediction has a relatively large error associated with it.

The comparison of the yearly averages, Fig. 10.9C, suggests that the model can roughly reproduce the observations. However, the comparison of the stations averages, Fig. 10.9D, indicates that the model can indeed capture the salient features that distinguish stations. The two stations with the largest fluxes to the sediment are distinguished from the stations with essentially zero fluxes, and from the two with slightly positive fluxes. At this level of averaging, the model is quite successful.

The relationship between nitrate flux and temperature, surface mass transfer coefficient, and overlying water nitrate concentration are examined in Fig. 10.10. Neither the data nor the model show any strong systematic pattern with respect to temperature or s. The relationship with overlying water nitrate concentration is more apparent. The pattern of positive nitrate fluxes associated with small overlying water nitrate concentrations and negative fluxes associated with large overlying water nitrate concentrations is apparent in the modeled fluxes and less strongly evident in the observed fluxes. The model also predicts that for low overlying water DO concentrations (the + symbol) the nitrate flux is essentially zero and almost all of the observations conform. The reason for the zero fluxes is the low overlying water nitrate concentrations at these stations and also that the low overlying water DO concentrations reduces ammonia nitrification and, therefore, the production of nitrate in the sediment.

The flux components are presented in Fig. 10.11. They are: the source of nitrate due to nitrification, $S[NO_3]$, the source due to surface mass transfer from the overlying water, $s[NO_3(0)]$, the loss due to denitrification in both the aerobic and anaerobic layers, denoted by κ_{NO3}, the sink to surface mass transfer to the overlying water, $s[NO_3(1)]$, and the net nitrate flux, $J[NO_3] = s([NO_3(1)]-[NO_3(0)])$. From these results, it is possible to understand what controls the nitrate flux. The two stations with significant nitrate fluxes to the sediment (Still Pond and Maryland Pt.) have large inputs from the overlying water, $s[NO_3(0)]$. The stations with essentially zero fluxes (R-78, R-64, Ragged Pt.) have an intermediate overlying water source. The remaining stations with the positive fluxes to the overlying water have small overlying water sources.

Nitrate Flux Calibration

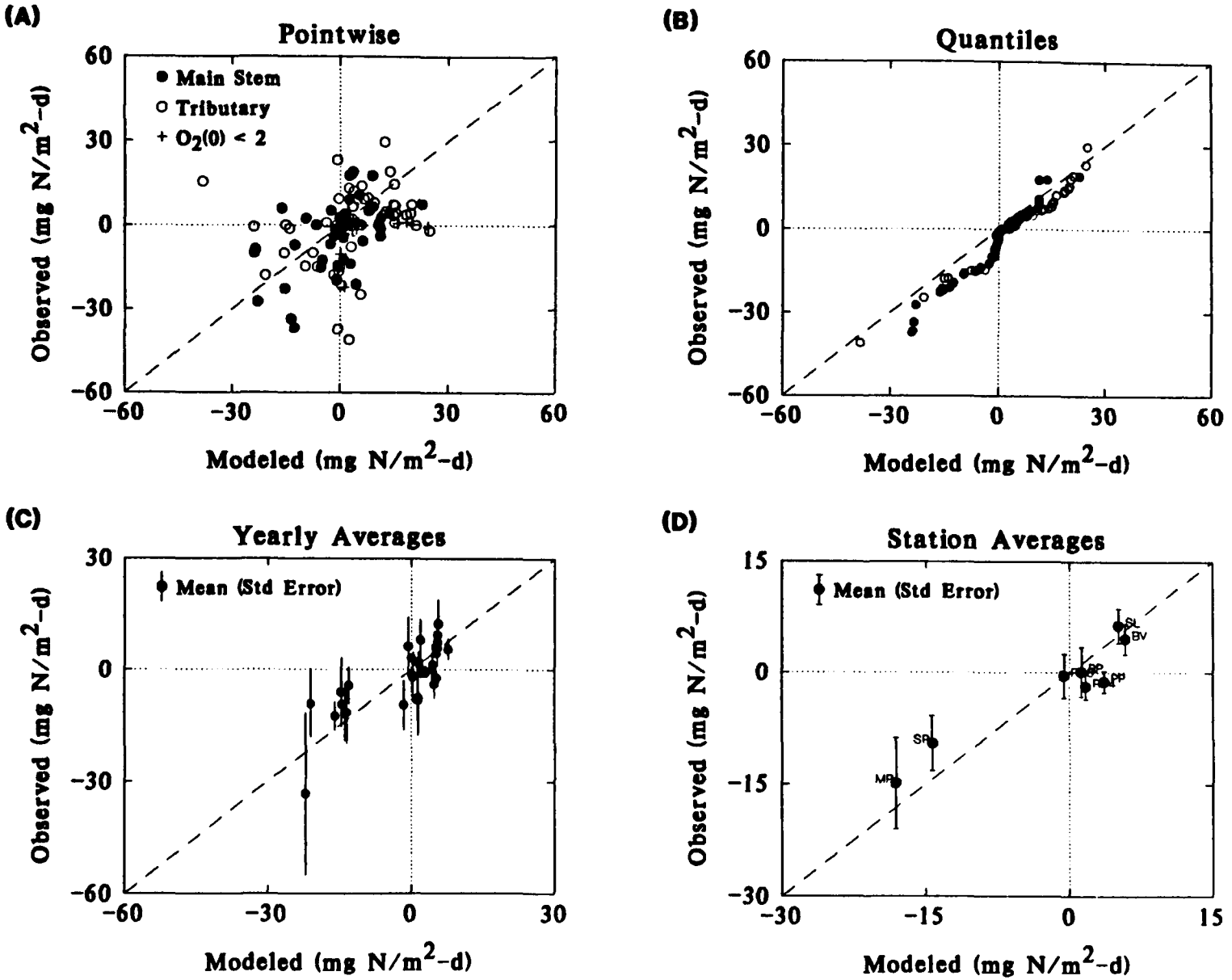

RUN104 - PLT3CMN

Figure 10.9

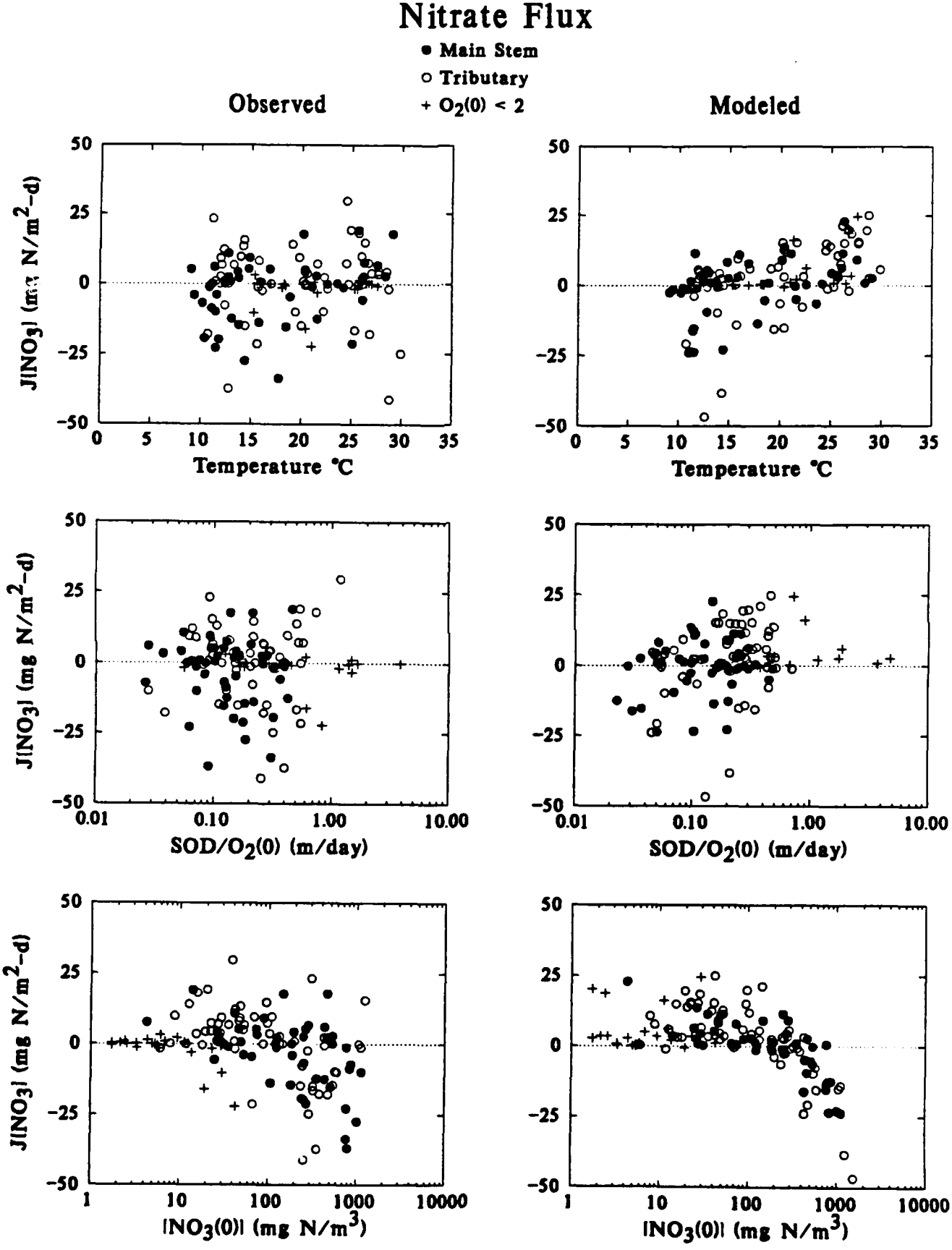

RUN104 - PLT3MON

Figure 10.10

Flux Components

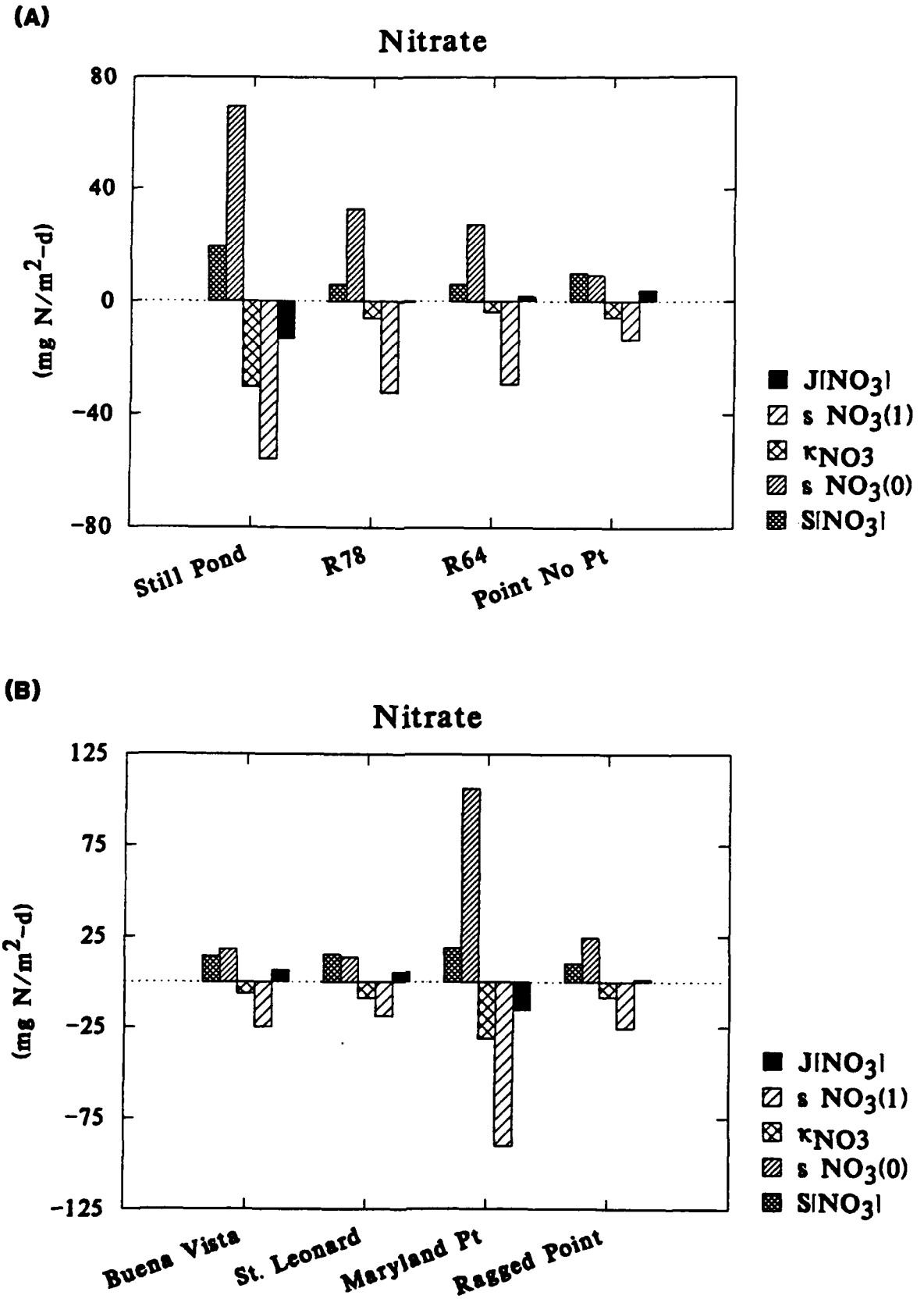

RUN104 - PLT3FR10

Figure 10.11

D. Sulfide

1. Model Parameters

Sulfide is produced by carbon diagenesis, decremented by the organic carbon consumed by denitrification.

$$J_{T2} = J_C - \alpha_{O2,NO3}\left(\frac{\kappa^2_{NO3,1}}{s}[NO_3(1)] + \kappa_{NO3,2}[NO_3(2)]\right) \quad (5)$$

where:

$\alpha_{O2,NO3}$	diagenesis (in O_2 equivalents) consumed by denitrification	2.8571	g O_2^*/g N

Dissolved and particulate sulfide are oxidized in the aerobic layer only. The reaction rate is linear in oxygen concentration, consistent with reported formulations for these reactions. The constant $K_{M,H2S,O2}$ scales the overlying water oxygen concentration. It is included for convenience only. At $[O_2(0)] = K_{M,H2S,O2}$ the sulfide oxidation reaction velocity is at its nominal value. The aerobic layer reaction velocity is given by:

$$\kappa^2_1 = (\kappa^2_{H2S,dl} f_{dl} + \kappa^2_{H2S,pl} f_{pl})\theta^{(T-20)}_{H2S} \frac{[O_2(0)]}{K_{M,H2S,O2}} \quad (6)$$

Partitioning between dissolved and particulate sulfide represents the formation of iron sulfide, FeS. This is parameterized using partition coefficients in the aerobic, $\pi_{H2S,1}$, and anaerobic $\pi_{H2S,2}$, layer. No other reactions occur. The parameters are:

$\kappa_{H2S,dl}$	Reaction velocity for dissolved sulfide oxidation in the aerobic layer	0.20	m/d
$\kappa_{H2S,pl}$	Reaction velocity for particulate sulfide oxidation in the aerobic layer	0.40	m/d

θ_{H2S}	Temperature coefficient for sulfide oxidation	1.08	-
$K_{M,H2S,O2}$	Sulfide oxidation normalization constant for oxygen	4.0.	mg O_2/L
$\pi_{H2S,1}$	Partition coefficient for sulfide in the aerobic layer	100	L/kg
$\pi_{H2S,2}$	Partition coefficient for sulfide in the anaerobic layer	100	L/kg

2. Data Comparisons

The time series of observed and computed sulfide fluxes are presented in Fig. 10.12. The overlying water DO is also plotted for reference. Only two observations are available for main stem stations (R-64 and Point No Point) and the model computes fluxes of comparable magnitudes. The sulfide fluxes occur when the overlying water DO is sufficiently low to limit the oxidation of sulfide in the aerobic layer. The result is that sulfide is transferred to the overlying water by surface mass transfer.

Fig. 10.13 compares the sediment data for organic carbon and particulate sulfide to the model computations. The particulate organic, Fig. 10.13A, and algal, Fig. 10.13C, carbon results have been discussed in Chapter VIII. The comparison of the sulfide data, Fig. 10.13B, highlights the fact that the sulfur cycle in the model is not complete. The model computations are substantially in excess of the observations for acid volatile sulfide, AVS, which is a measure of iron monosulfide, FeS. The model forms FeS using a partitioning equilibria. FeS is considered to be reactive and can be oxidized. This is the only reaction considered in the model. However, iron monosulfide can also react with elemental sulfur to form iron pyrite, FeS_2, which is much less reactive. The result would be a buildup of FeS_2 in the sediment. The chromate reducible sulfide (CRS) plotted in Fig. 10.13B is a measure of both FeS and FeS_2. Including the reaction for the formation of pyrite would lower the concentration of FeS computed by the model and bring it into closer agreement with the observations, and allow a buildup of FeS_2, to match the observed total inorganic sulfide in the sediment.

Sulfide Flux

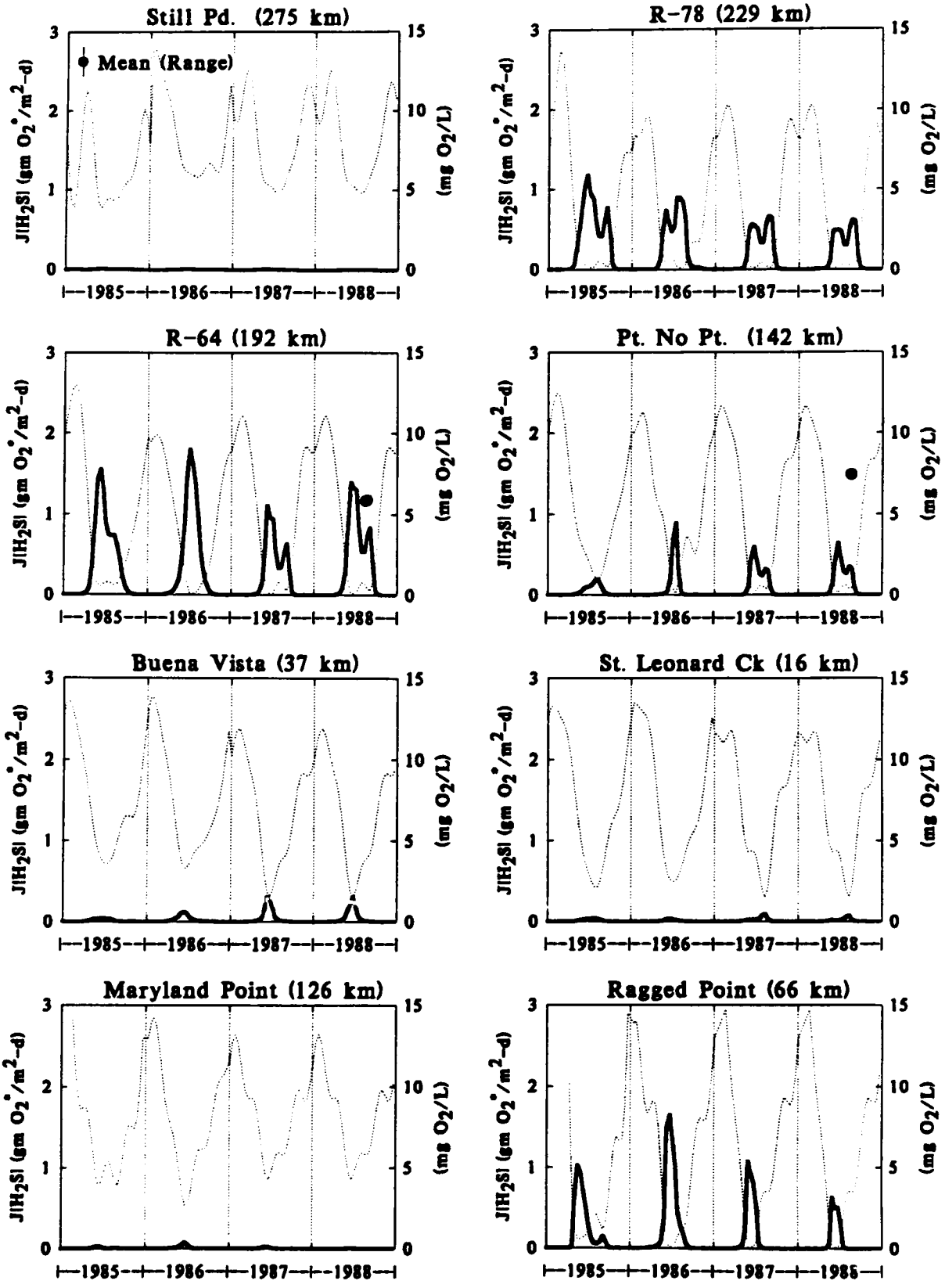

RUN104 - PLTVHS1

Figure 10.12

Sediment Composition - Carbon, Sulfur

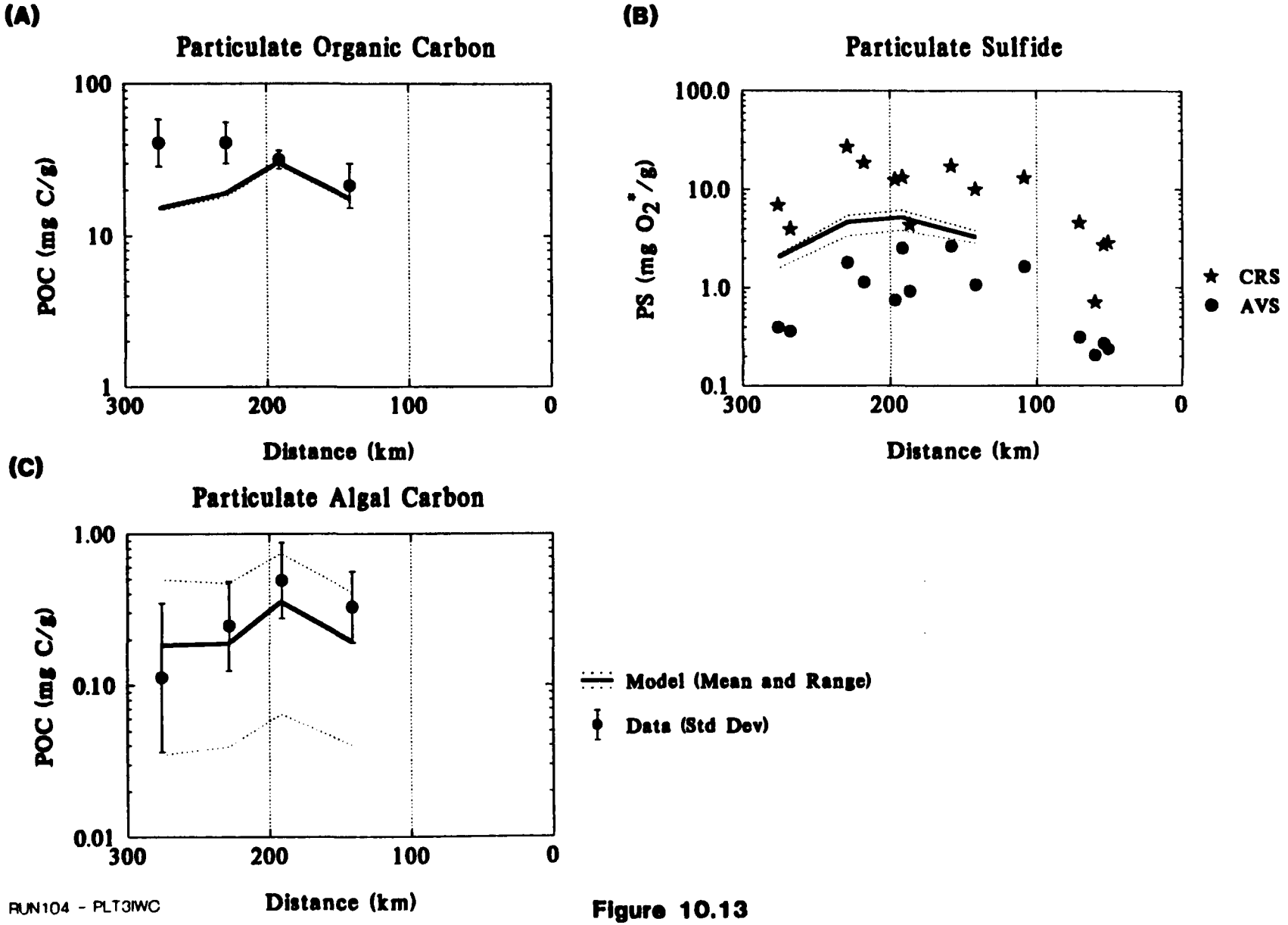

Figure 10.13

Fig. 10.14 examines the seasonal variation of solid phase sulfide , Fig. 10.14A,B and pore water sulfide concentrations, Fig. 10.14C,D. The model predicts almost no seasonal variation, whereas the pore water data, Fig. 10.14C, appear to indicates a seasonal variation. However, the model does capture the difference in pore water concentrations at Still Pond, Fig 10.14D, and R-64, Fig. 10.14C.

It is apparent that a price has been paid for simplifying the sulfide cycle and using linear partitioning to determine the particulate and dissolved species. The model calculates solid phase sulfide concentrations that are between the observed FeS and FeS_2 concentrations. The fact that the FeS pool is too large prevents it from responding to the seasonal variations of the sources and sinks. As a consequence, pore water sulfide concentrations cannot vary either. Finally, while constant linear partitioning is convenient, it cannot reproduce the variation to be expected in partitioning due to, for example, the variation in iron content of the sediment. Considering these deficiencies, it is somewhat surprising that the sulfide model is at all representative.

The flux components are presented in Fig. 10.15. They are: the depositional flux of POC in oxygen equivalents, J_{POC}, the loss of POC via sedimentation, $w_2 POC$, the loss via consumption by denitrification, $S[NO_3]$, the loss via oxidation of sulfide, denoted by κ_{H2S}, the loss of particulate sulfide via sedimentation, $w_2 PS$, and the sulfide flux, $J[H_2S]$. The significant removal component is the loss of POC by burial. The burial of inorganic sulfide is small, as is the denitrification consumption. This is confirmed by the comparison given in Fig. 10.15C of the relationship between the depositional flux, J_{POC}, and the amount that is either oxidized, CSOD, or escapes to the overlying water, $J[H_2S]$. The results indicates that 18% of the depositional flux is not recycled as either carbonaceous SOD (via the oxidation of sulfide) or as a sulfide flux to the overlying water. This is slightly in excess of the 15% of POC that is G_3 carbon which is inert and, therefore, is completely removed by burial. The remaining 3% is lost by burial of particulate sulfide.

E. Oxygen

1. Model Parameters

Oxygen is consumed by the oxidation reactions in the aerobic layer. Carbonaceous sediment oxygen demand (CSOD) - so named because it originates with carbon diagenesis - is computed from the rate of oxygen utilization during sulfide oxidation. No stoichiometric coefficient is needed because the sulfide concentrations are computed in oxygen equivalents. The nitrogenous sediment oxygen demand (NSOD) is the consumption of oxygen due to nitrification with the indicated stoichiometry. No other oxygen consuming reactions are considered.

$$CSOD = \frac{(\kappa_{H2S,dl}^2 f_{dl} + \kappa_{H2S,pl}^2 f_{pl})\theta_{H2S}^{(T-20)}}{s} \frac{[O_2(0)]}{K_{M,H2S,O2}} [\Sigma H_2S(1)] \qquad (7)$$

$$NSOD = \alpha_{O2,NH4} \kappa_{NH4,1}^2 \theta_{NH4}^{(T-20)} \left(\frac{K_{M,NH4} \theta_{K_{M,NH4}}^{(T-20)}}{K_{M,NH4} \theta_{K_{M,NH4}}^{(T-20)} + [NH_4(1)]} \right)$$

$$\left(\frac{[O_2(0)]}{2K_{M,NH4,O2} + [O_2(0)]} \right) [NH_4(1)] \qquad (8)$$

where:

$[\Sigma H_2S(1)]$	Total aerobic layer sulfide concentration	-	$g\ O_2^*/m^3$
$\alpha_{O2,NH4}$	oxygen consumed by nitrification	4.5714	$g\ O_2/g\ N$

2. Data Comparisons

The time series of observed and computed oxygen fluxes are shown in Fig. 10.16. There is a different pattern of oxygen fluxes from the stations which are aerobic throughout the year and those which experience hypoxia or anoxia, which are identified with an asterisk (*). The aerobic stations, Still Pond in the main bay, and all but Ragged Point in the tributaries, exhibit a seasonal distribution that is similar to the ammonia fluxes. However, the stations that experience anoxia,

Seasonal Variation - Sulfide

Solid Phase

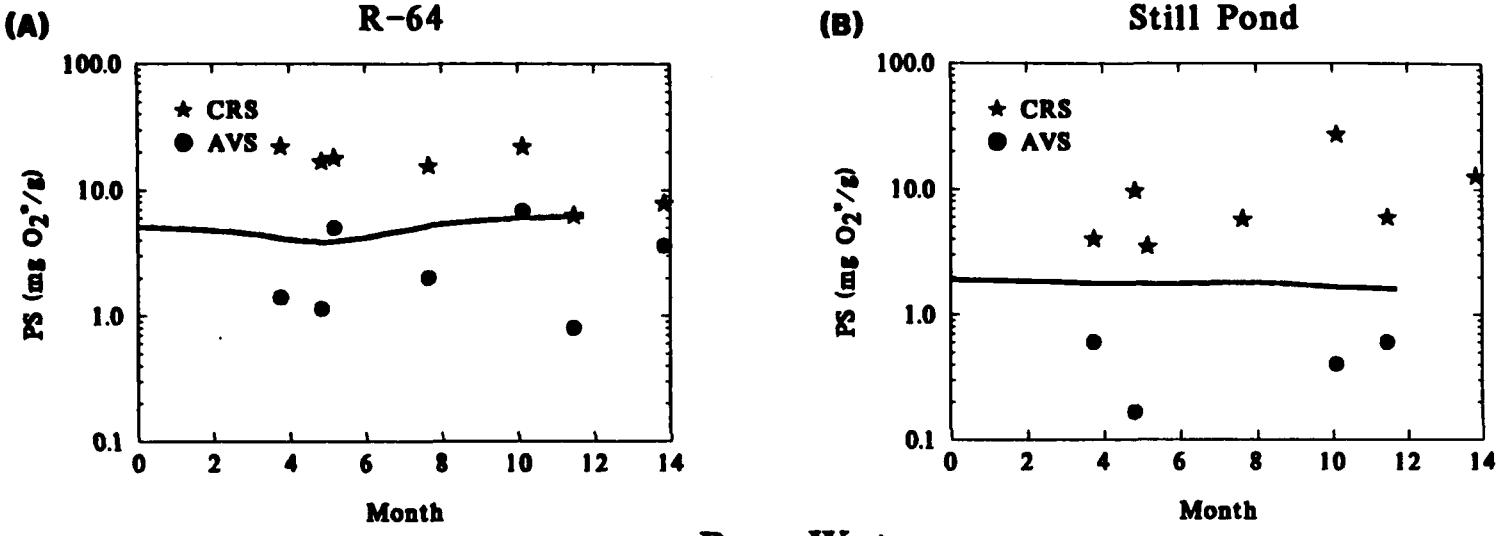

Pore Water

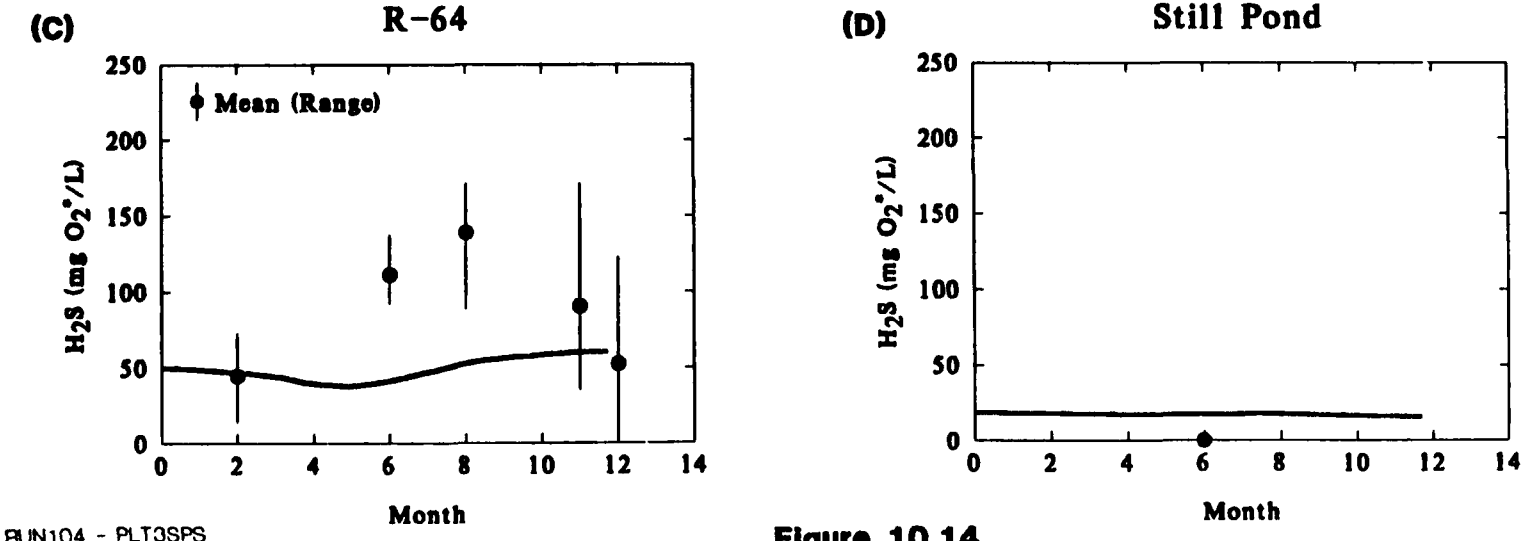

RUN104 - PLT3SPS

Figure 10.14

Flux Components

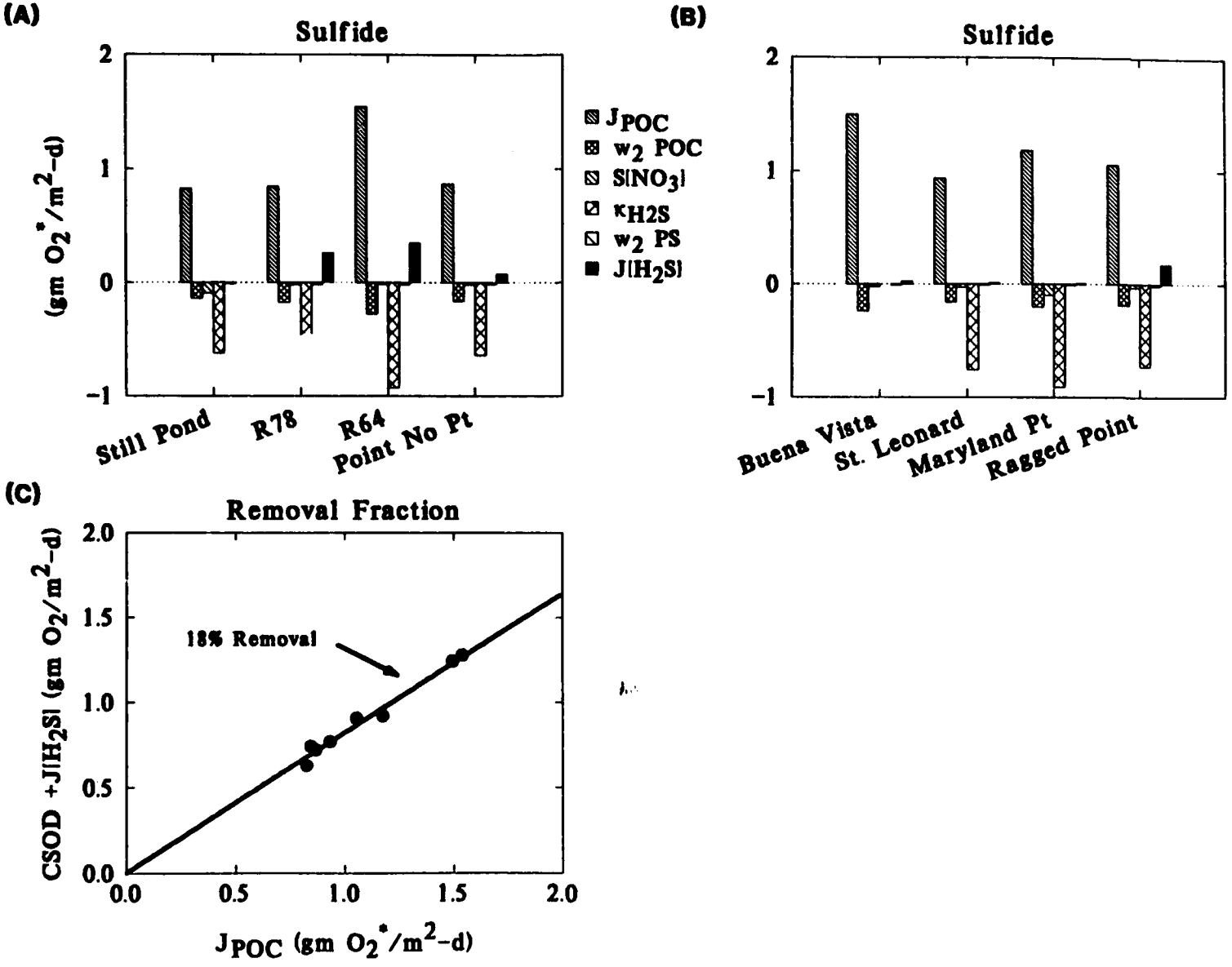

RUN104 - PLT3FR3A

Figure 10.15

Oxygen Flux

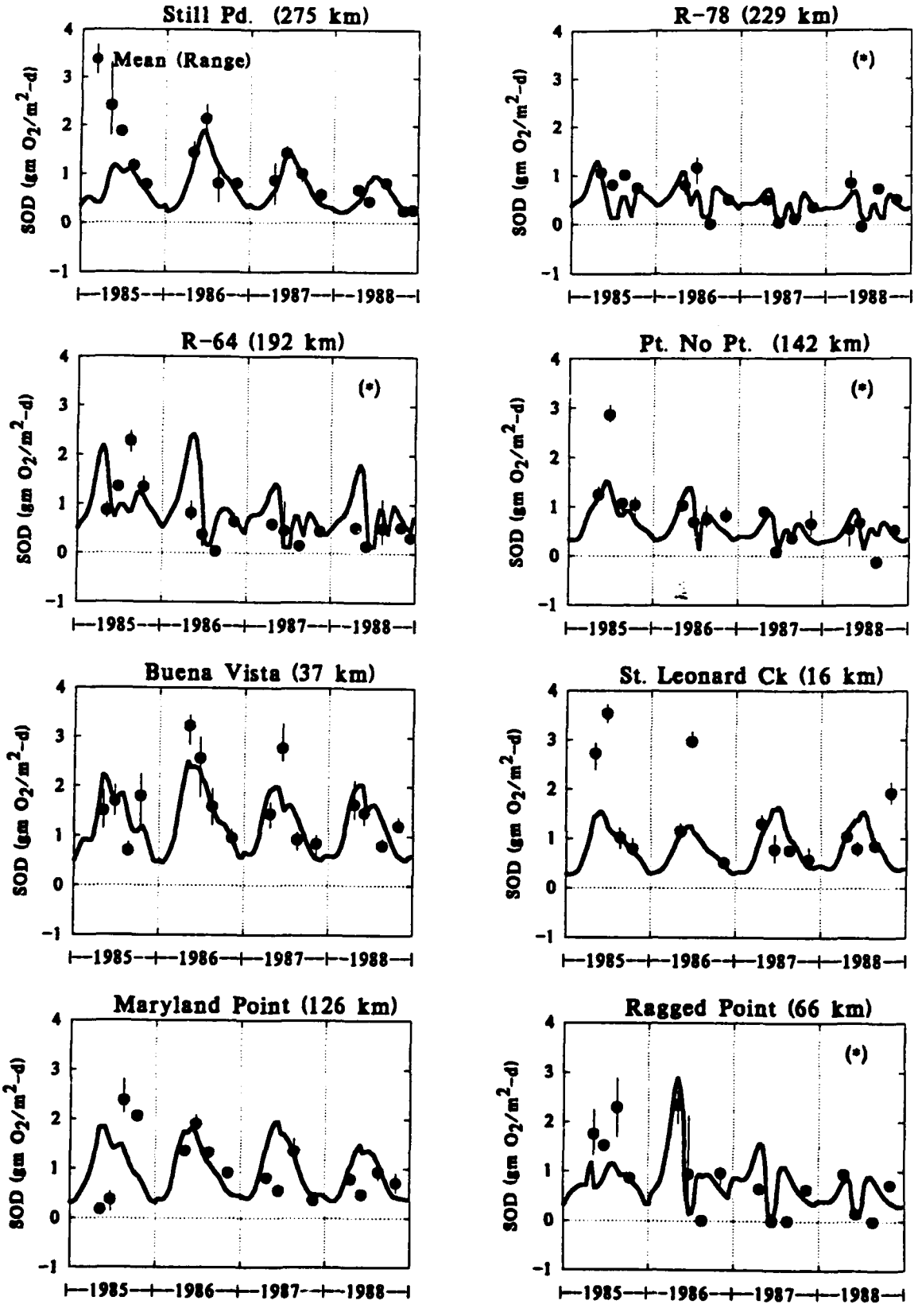

RUN104 - PLTVSOD1

Figure 10.16

the remaining main stem stations and Ragged Point, lack a strong seasonal cycle. The model reproduces this contrasting behavior reasonably well. The mechanisms involved are the lack of overlying water oxygen which prevents oxidation, directly reduces particle mixing, and produces benthic stress.

Fig. 10.17 displays the particle mixing velocity with, w_{12} eq.(IX-6), and without, w_{12}^{*} eq.(IX-2), the effect benthic stress. For the anoxic stations (*), the particle mixing is strongly inhibited - compare the light and dark shaded curves. As a consequence, the particulate sulfide is not mixed into the aerobic layer where oxidation can occur. Hence, the summer peak of SOD does not occur. Rather the SOD is spread out over the year.

Fig. 10.18 presents the pointwise, quantile, and average comparisons. The results are similar to the ammonia and nitrate fluxes. The pointwise comparison, Fig. 10.18A, is scattered, whereas the quantile distributions, Fig. 10.18B, are comparable. The yearly average comparison, Fig. 10.18C, is less scattered than the pointwise comparison. The station average comparison, Fig. 10.18D, indicates that the observations are slightly larger than the model results. This may be due to the unexplained spikes of SOD, see Fig. 10.16, that increase the average observed SOD.

Fig. 10.19 presents the relationship between SOD and temperature, overlying water DO and ammonia flux. Neither the data nor the model show any strong temperature dependence (top panel). There is a consistent dependency of SOD on overlying water DO in both the observations and the model results (middle panels). It is reasonable to expect that SOD will decrease as the overlying water oxygen decreases, since, in the limit as $O_2(0)$ approaches zero, the SOD must also approach zero, there being no oxygen to consume.

The relationship between SOD and ammonia flux for aerobic cases, Fig. 10.19 (bottom), is more consistent in the model results than in the observations. However, both the model and the observations indicate that low oxygen concentration favors a lowered SOD and an increased ammonia flux.

The components of sediment oxygen demand are shown in Fig. 10.20. The nitrogenous component, NSOD, is a small fraction of the carbonaceous (i.e. sulfide oxidation) component, CSOD. The two make up the direct oxygen uptake, the SOD, of the sediment. The sulfide flux, $J[H_2S]$, is also shown, which for the anoxic stations can be a significant component. The sum of NSOD, CSOD, and J[H_2S], is the total oxygen equivalent sediment flux, J[O_2^*], is as indicated.

Benthic Particle Mixing

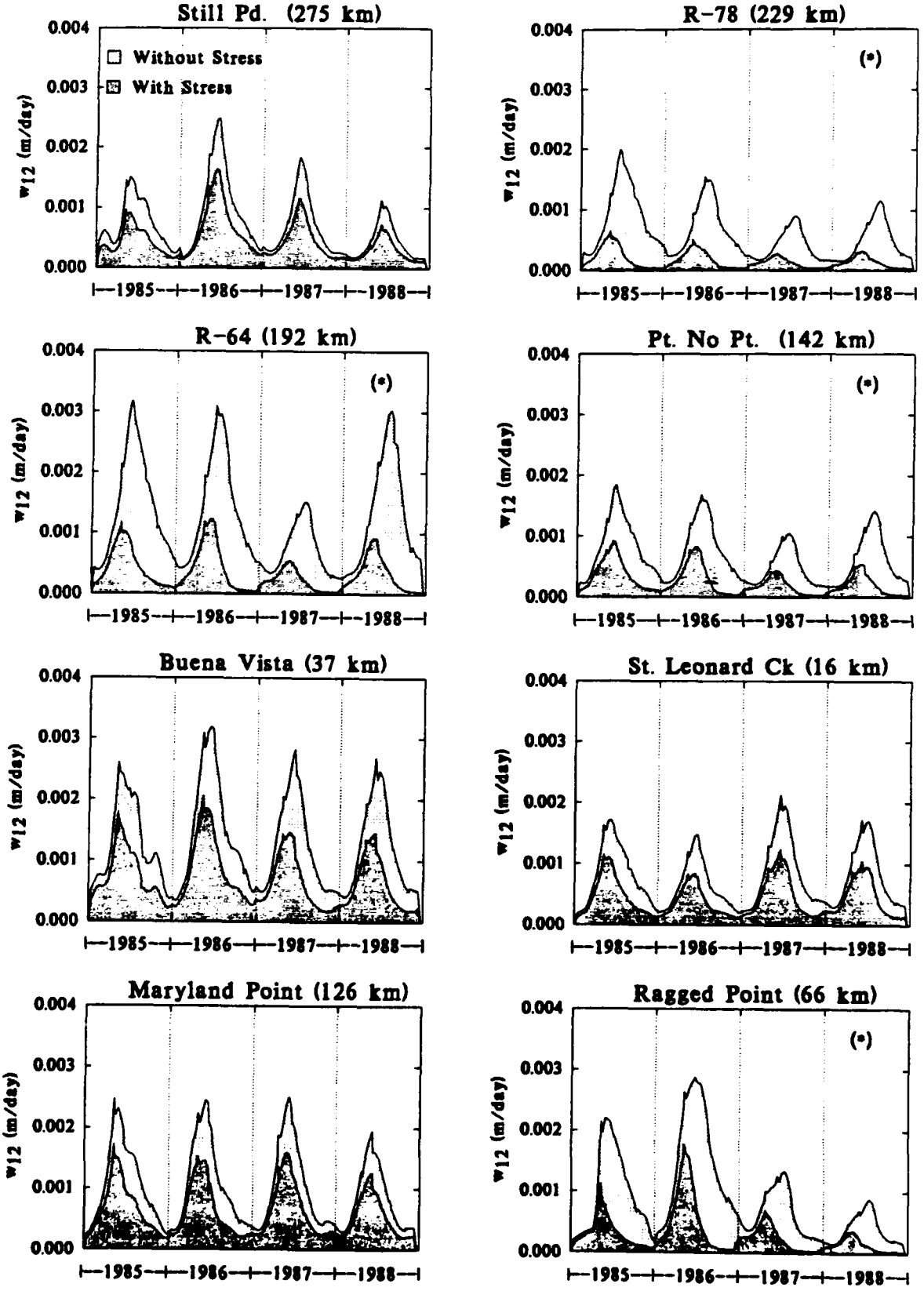

RUN104 - PLTVMIX1

Figure 10.17

Oxygen Flux Calibration

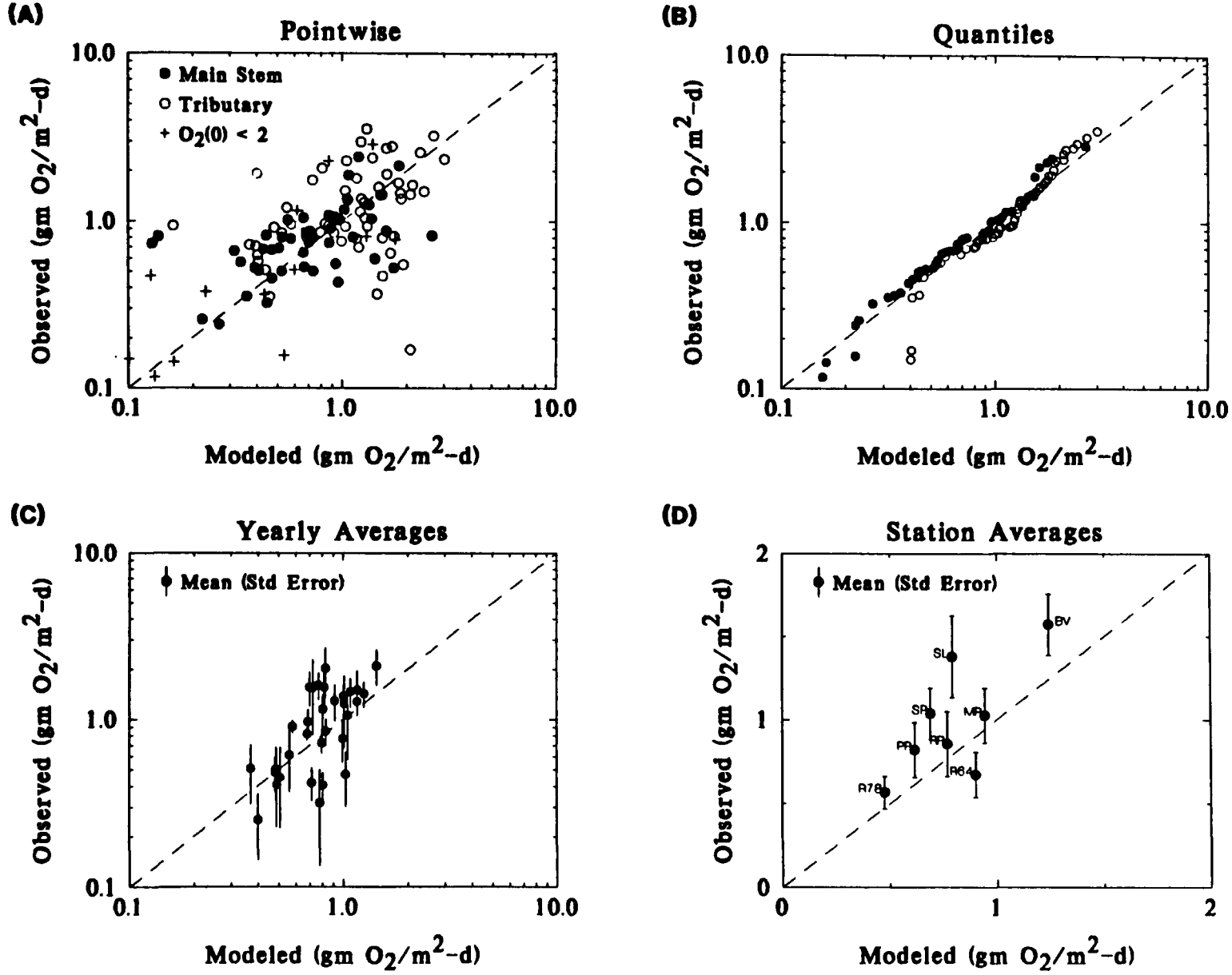

RUN104 - PLT3CMS

Figure 10.18

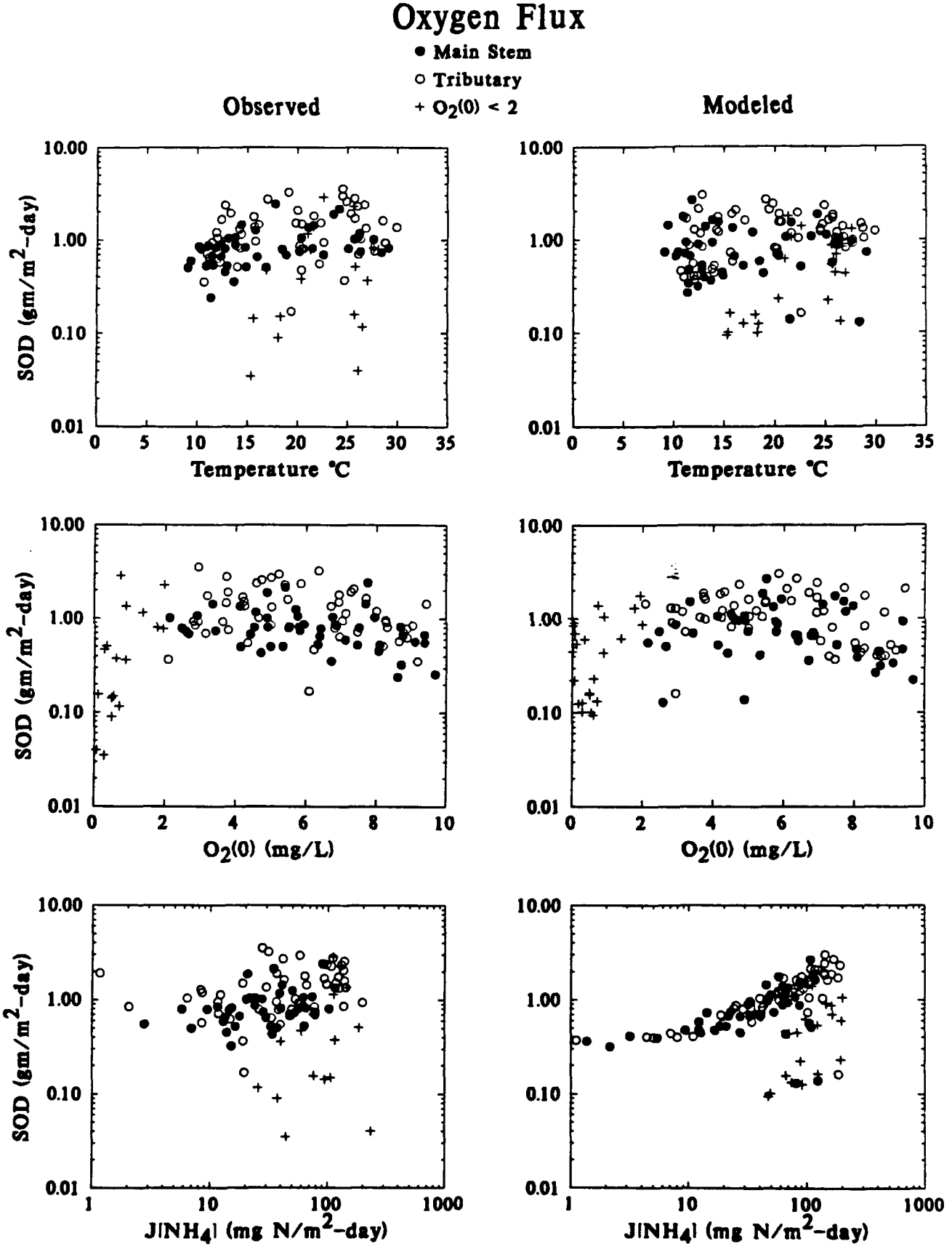

RUN104 - PLT3MOS

Figure 10.19

Flux Components

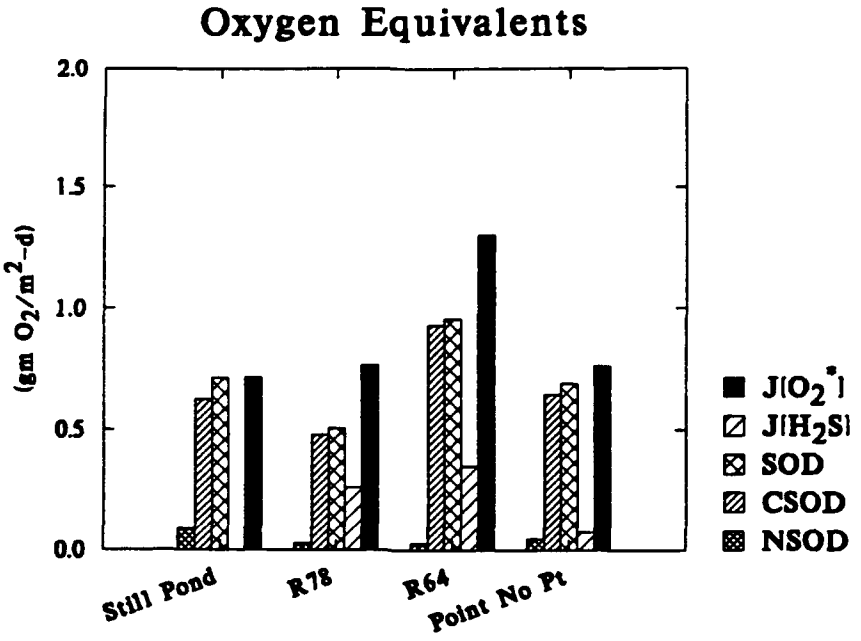

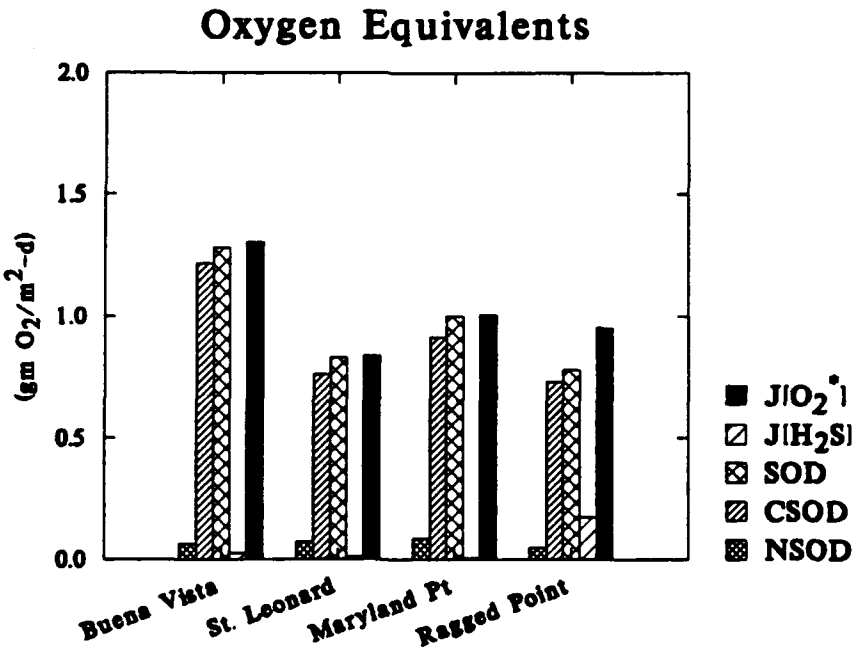

RUN104 - PLT3FR14

Figure 10.20

F. Phosphate

1. Model Parameters

Phosphate is conservative in both layers, with partitioning controlling the fraction that is dissolved and particulate. Phosphate flux is strongly affected by the overlying water oxygen concentration, $[O_2(0)]$. This mechanism is implemented by making the aerobic layer partition coefficient larger than in the anaerobic layer during oxic conditions and to remove this additional sorption as $[O_2(0)]$ approaches zero. Hence:

$$\pi_1 = \pi_2(\Delta\pi_{PO4,1}) \qquad [O_2(0)] > [O_2(0)]_{crit,PO4} \qquad (9)$$

$$\pi_1 = \pi_2(\Delta\pi_{PO4,1})^{([O_2(0)]/[O_2(0)]_{crit,PO4})} \qquad [O_2(0)] \leq [O_2(0)]_{crit,PO4} \qquad (10)$$

which smoothly reduces the aerobic layer partition coefficient to that in the anaerobic layer as $[O_2(0)]$ goes to zero. No other reactions affect the phosphate concentrations. The parameter values are:

J_{T2}	Phosphorus diagenesis, J_P, computed from eq.(VIII-6)	-	mg P/m^2-d
$\Delta\pi_{PO4,1}$	Incremental partition coefficient for phosphate in the aerobic layer	300.	L/kg
$\pi_{PO4,2}$	Partition coefficient for phosphate in the anaerobic layer	100.	L/kg
$[O_2(0)]_{crit,PO4}$	Overlying water oxygen concentration at which aerobic layer incremental partitioning starts to decrease	2.0	mg/L

2. Data Comparisons

The time series of phosphate fluxes are shown in Fig. 10.21. The dramatic effect of hypoxic and anoxic conditions is apparent. Phosphate fluxes are small during aerobic conditions. However, anoxia produces dramatic increases, approaching 50 to 100 mg P/m^2-d. This is nearly

one-half of the ammonia fluxes at that time. Since the ratio of ammonia to phosphate production by diagenesis is 7.23 gm N/gm P, the excess phosphate is being released from the phosphate stored in the sediment during the aerobic periods. This is the mechanism that produces the large anoxic fluxes. By contrast, the steady state model cannot produce fluxes that exceed the diagenetic production of phosphate.

The comparison to sediment phosphorus concentrations are shown in Fig. 10.22. The total particulate phosphorus (PP), shown in Fig. 10.22A, is made up of particulate organic (POP) and inorganic (PIP) phosphorus. Inorganic phosphorus comprises a large fraction of the total phosphorus at the upstream stations, but is less further downstream. The data for PIP (Fig. 10.22B) confirm this observation. The model captures this behavior, in particular, the decline of sediment inorganic phosphorus from Still Pond to R-78 and the rest of the main stem stations. The reason is that Still Pond is an aerobic station and the phosphate flux is quite small. As a consequence, the stored phosphorus increases relative to the rest of the main stem stations which all experience anoxic periods and high phosphate fluxes.

The calculated pore water phosphate concentrations (Fig. 10.22C) are proportional to the PIP concentrations since they are related in the model by a linear partition coefficient. A comparison of the data for PIP and pore water PO_4 indicate that this is not the case. The furthest upstream pore water concentration is lowest, whereas the PIP concentration is highest. This can be seen more directly in Fig. 10.23 which presents the seasonal distribution of solid phase, Fig. 10.23A,B, and pore water, Fig. 10.23C,D, phosphate for Sill Pond and R-64 during 1988. The partition coefficient can be chosen to represent the situation at R-64, Fig. 10.23C, but not simultaneously at Still Pond, Fig. 10.23D. This suggests that the partition coefficient is largest at the upstream station and decreases in the downstream direction. This is consistent with the iron concentrations in these sediments, which decrease in the downstream direction.

The situation is comparable to the sulfur cycle discussed above. Neither the iron - sulfur cycle nor the iron - phosphorus cycle is being modeling in detail. These results indicate that while

Phosphate Flux

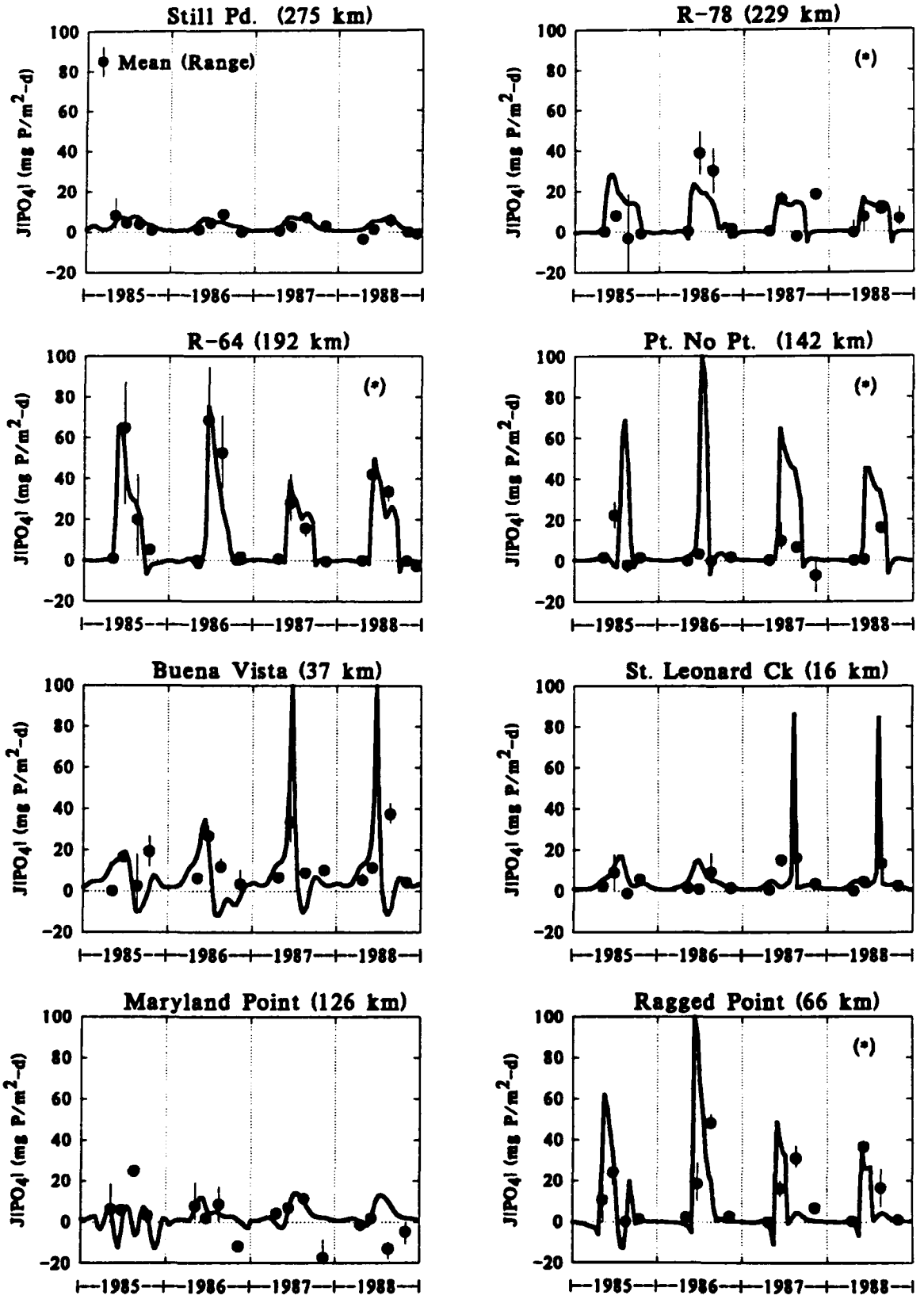

RUN104 - PLTVPO41

Figure 10.21

Sediment Composition - Phosphorus

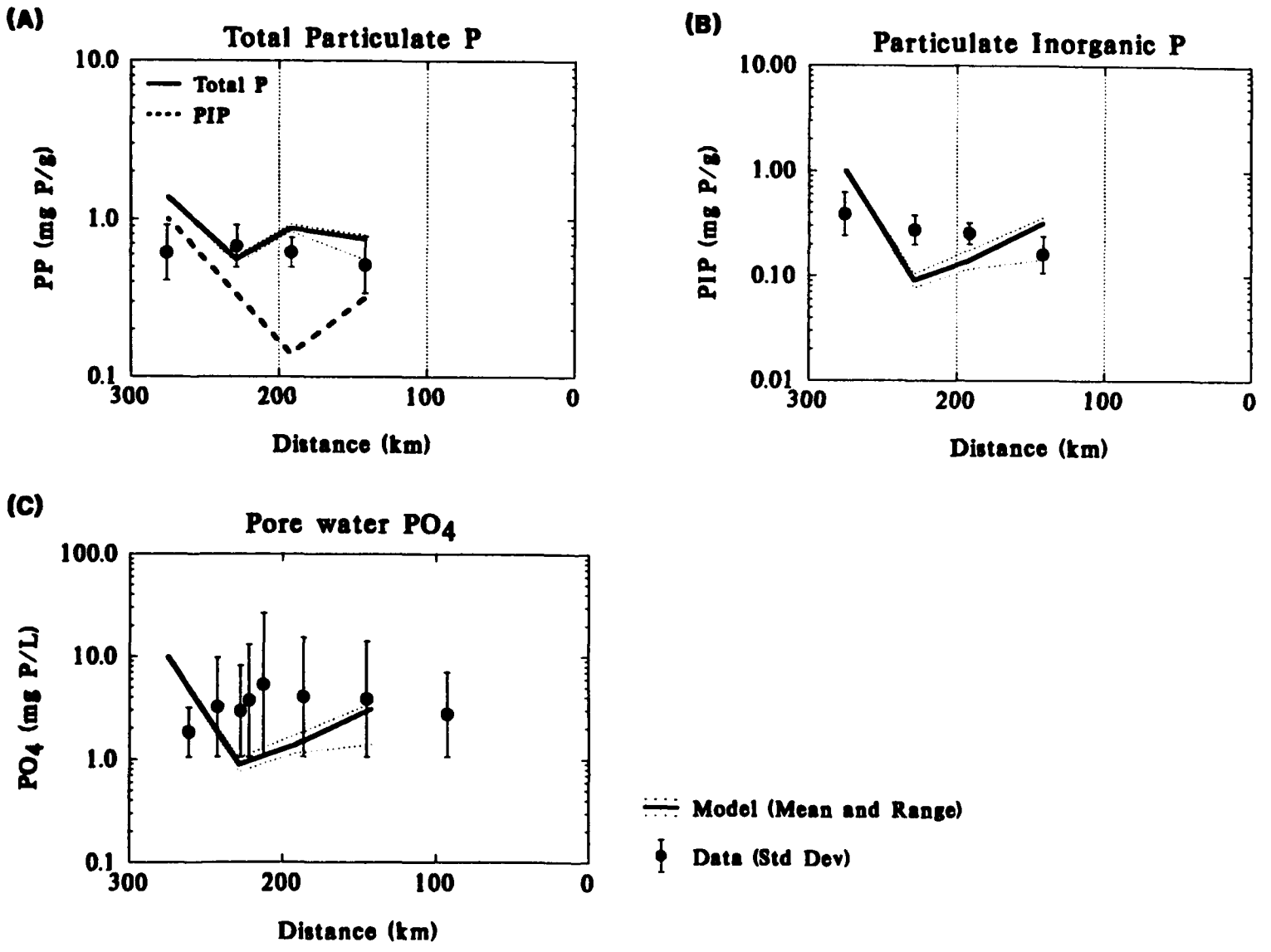

RUN104 - PLT3IWP

Figure 10.22

Seasonal Variation - Phosphate

Solid Phase

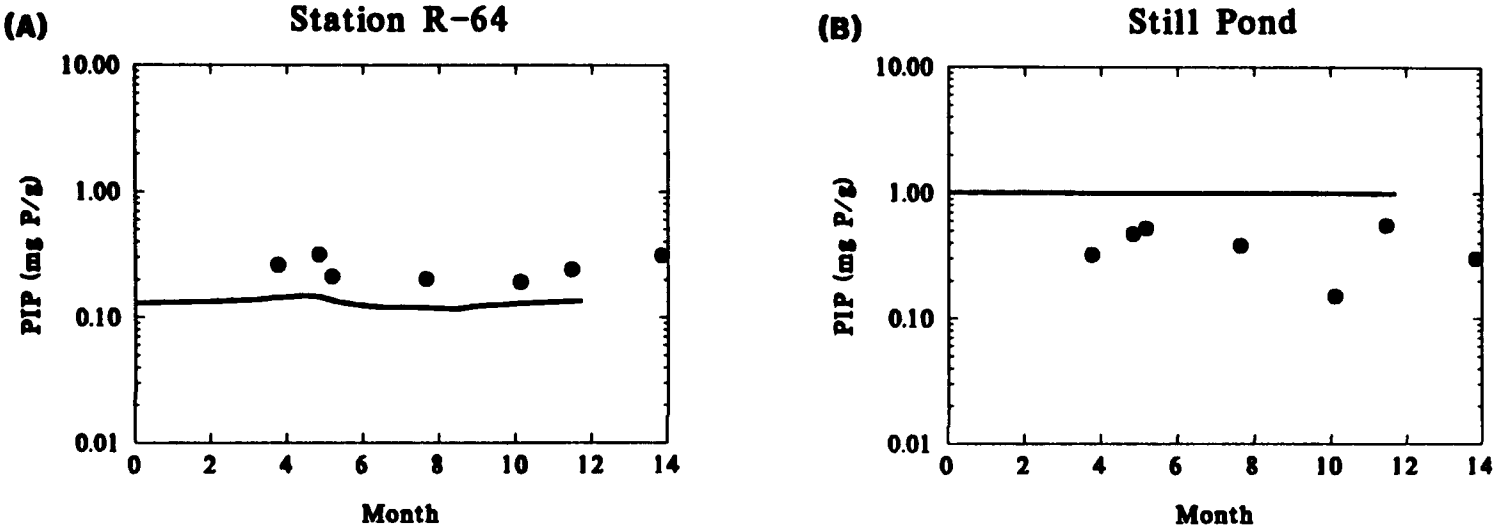

Pore Water

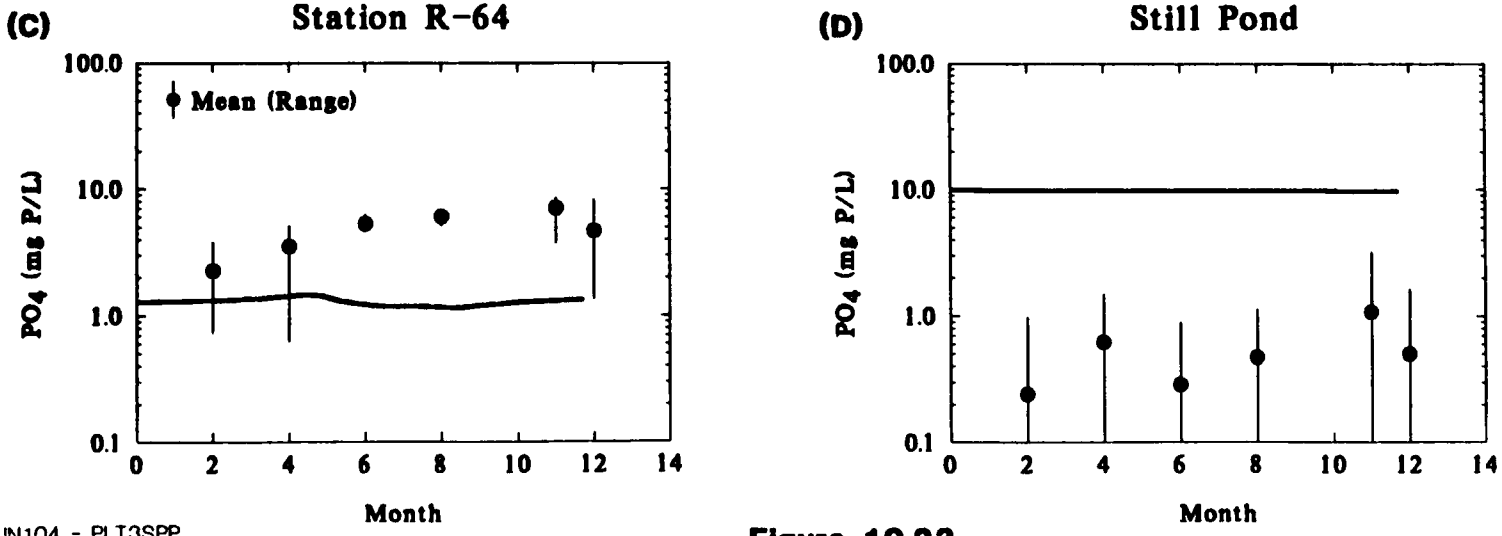

RUN104 - PLT3SPP

Figure 10.23

the use of partition coefficients with empirical oxygen dependencies can produce realistic flux models, the reproduction of the details of the pore water and solid phase composition of the sediment requires a more sophisticated chemical calculation.

Fig. 10.24 presents the pointwise, quantile, average comparisons. The scales employed are for an arcsech transformation of the data:

$$J[PO_4]^* = arcsech\left(\frac{J[PO_4]}{\beta}\right) = \ln\left(\frac{J[PO_4]}{\beta} + \sqrt{\left(\frac{J[PO_4]}{\beta}\right)^2 + 1}\right) \qquad (11)$$

This transformation is linear for values less than β and logarithmic for larger values. It also preserves the sign of the variable. The scales are constructed by applying the transformation to $J[PO_4] = 0, 1, 2, \ldots, 10, 20, \ldots$ etc., and plotting the results as tick marks. This transformation allows the simultaneous examination of positive and negative fluxes with widely varying values. For the phosphate flux data, a value of $\beta = 1$ mg P/m^2-d is chosen.

The pointwise comparison, Fig. 10.24A, is much like those seen previously, very little coherence between observed and predicted fluxes. A number of cases occur where the model predicts a negative flux and the observation is positive (top left quadrant). This occurs just after turnover when the overlying water oxygen increases. The model recreates the aerobic layer immediately, with its high partition coefficient. The resulting low aerobic layer phosphate concentration causes a flux to the sediment. A more realistic formulation would involve a model of the iron cycle. The formation of iron oxyhydroxide would take place more slowly, and the aerobic layer partition coefficient would increase more slowly.

The quantile comparison, Fig. 10.24B, shows a bias toward higher model fluxes in the main stem. However, the yearly averages, which are based on the yearly average model flux rather than the pointwise modeled fluxes, indicate a bias toward higher observed fluxes. The station averages, Fig. 10.24D, are in reasonable agreement with the observed averages, with the exception of Point

No Point. It is interesting to note that for this station, the observations straddle the predicted large anoxic fluxes, see Fig. 10.21. Therefore, the observed station average is smaller than the model yearly average.

Fig. 10.25 presents the relationship of phosphate flux to overlying water DO, the surface mass transfer coefficient, and ammonia flux. Both the model and the observations feature large (> 10 mg P/m^2-d) fluxes for low overlying water DO. No other relationship is apparent. No significant pattern is observed between phosphate flux and SOD/O_2(0). There is, however, a relationship to ammonia flux with generally increasing phosphate fluxes with the highest fluxes associated with the periods of low DO. The difficulty with the negative fluxes can also be seen. They occur at intermediate ammonia fluxes, whereas they are modeled to occur at the highest ammonia fluxes.

The flux components are displayed in Fig. 10.26A,B. The depositional flux, J_{POP}, burial of organic, $w_2 POP$, and inorganic, $w_2 PIP$, phosphorus, and the phosphate flux, $J[PO_4]$, are included. For the aerobic stations, burial of PIP is more significant than burial of POP as a sink of phosphorus. The reason is that phosphate retention in the sediments is larger for these stations since no large phosphate fluxes occur.

The relationship between the depositional source and the resulting flux during the four years of simulation is quite variable, reflecting the varying efficiency of phosphorus trapping (Fig. 10.26C). For Point No Point (PP), the flux from the sediment exceeded the flux to the sediment. This occurs at the expense of the stored phosphate. This can be seen in Fig. 10.27 which presents the time history of POP and PIP. The reason for the release of stored phosphorus is that the station had significantly longer periods of low DO in the latter years (Fig. 9.7). Since the model is equilibrated to the 1985 conditions, the state of the sediment, and in particular the stored phosphate, reflects the fluxes for that year. As the period of anoxia increased, the flux to the overlying water increased and the stored phosphorus decreased in response.

Phosphate Flux Calibration

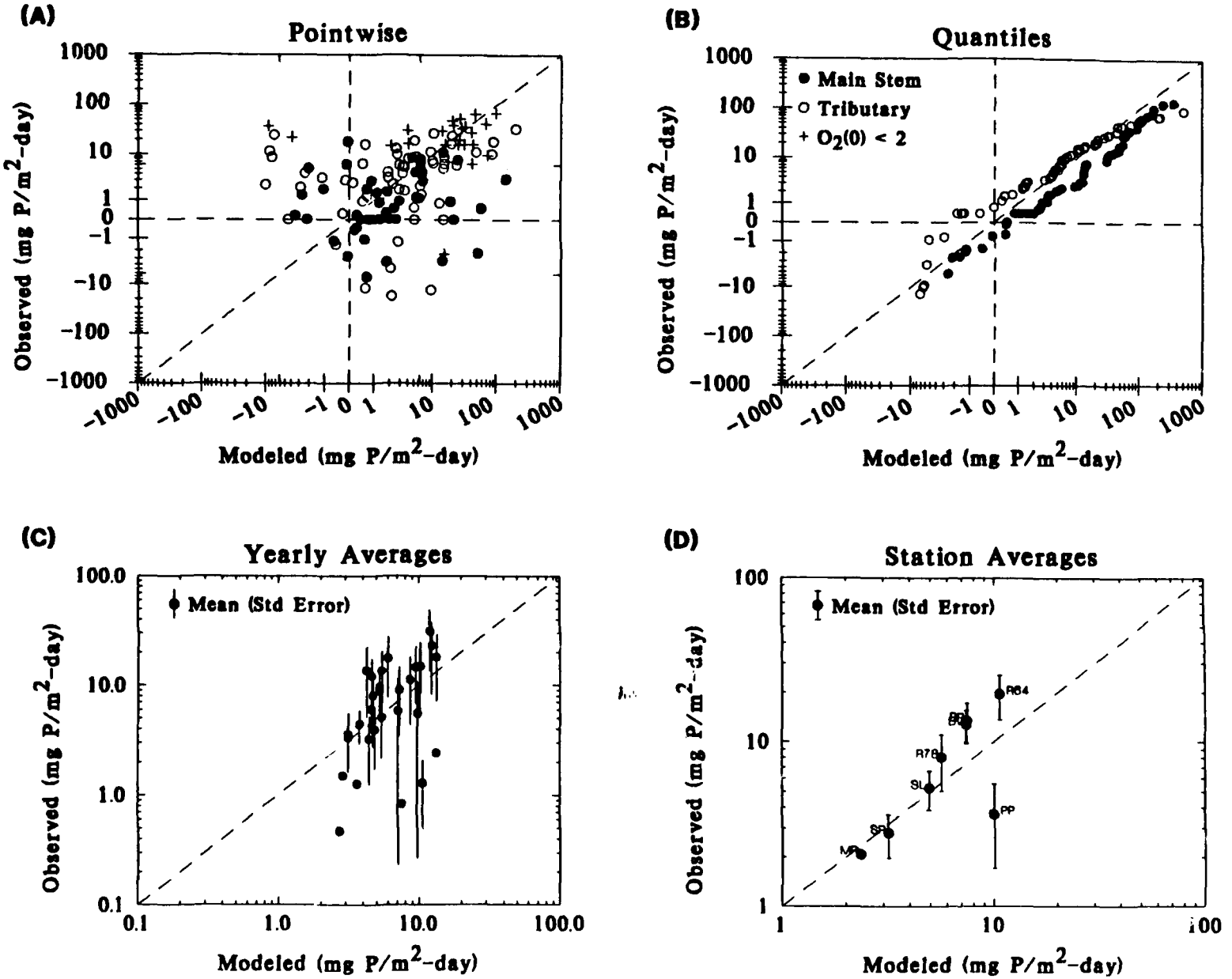

RUN104 - PLT3CMP

Figure 10.24

Phosphate Flux

● Main Stem
○ Tributary
+ $O_2(0) < 2$

Observed

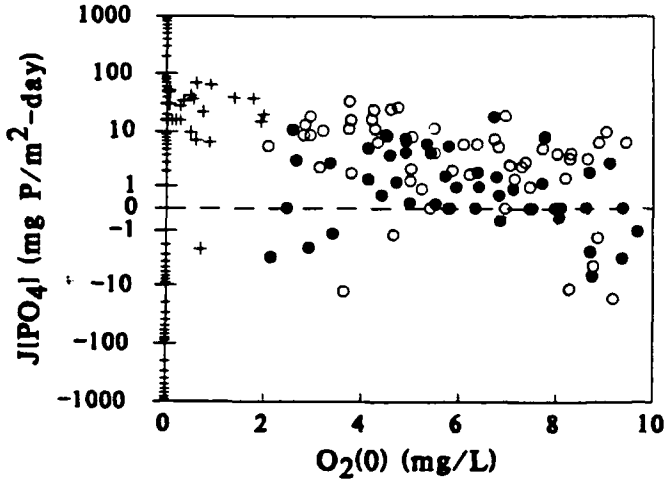

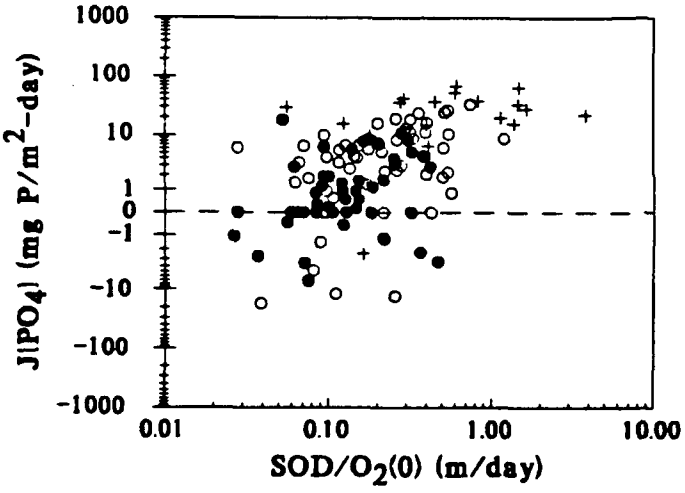

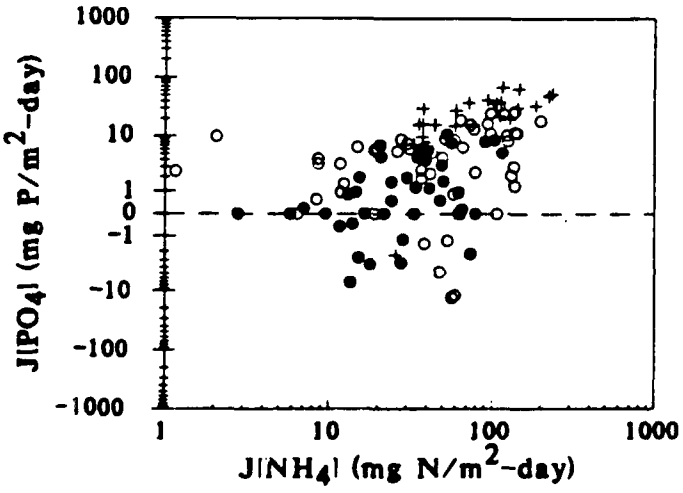

Modeled

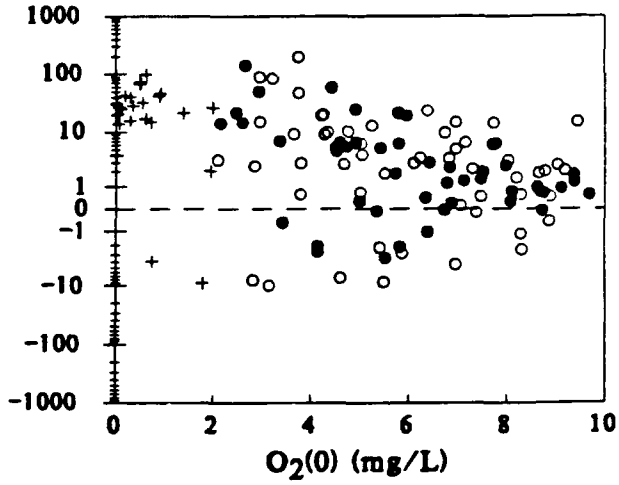

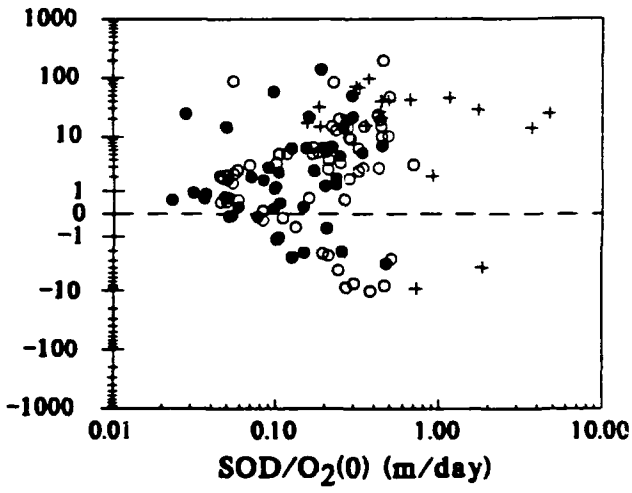

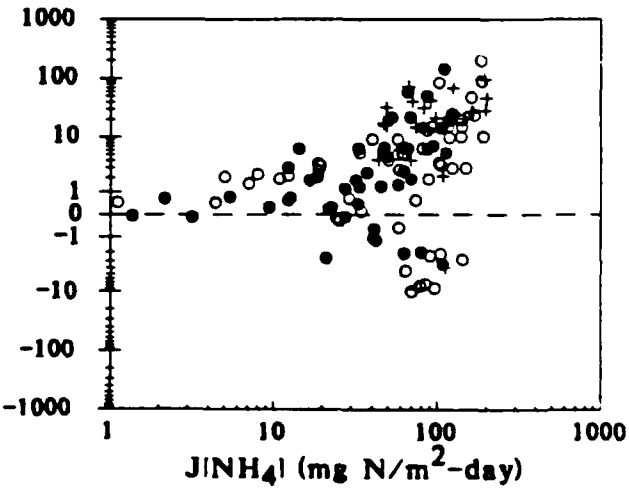

RUN104 - PLT3MOP

Figure 10.25

Flux Components

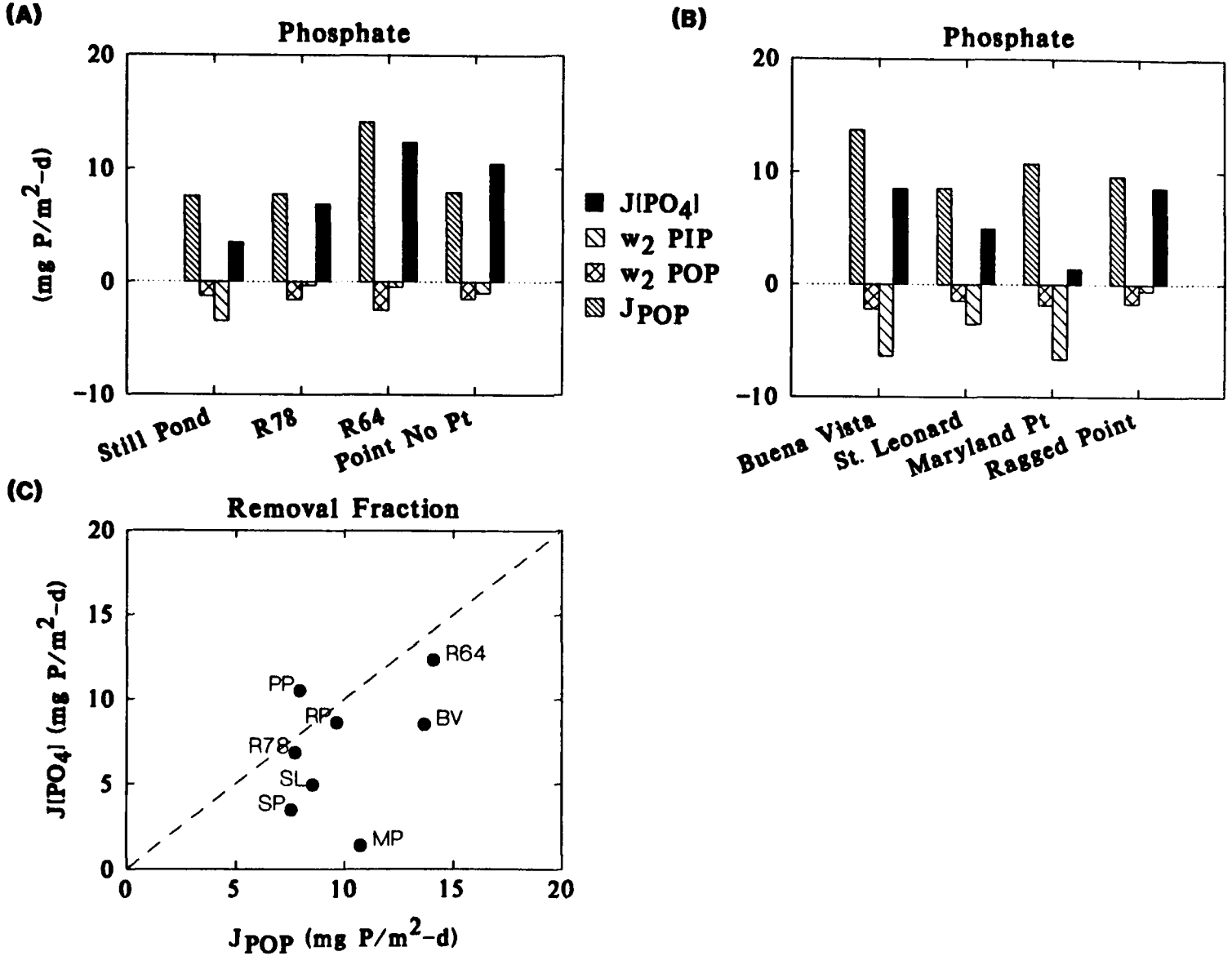

RUN104 - PLT3FR2A

Figure 10.26

Sediment Phosphorus

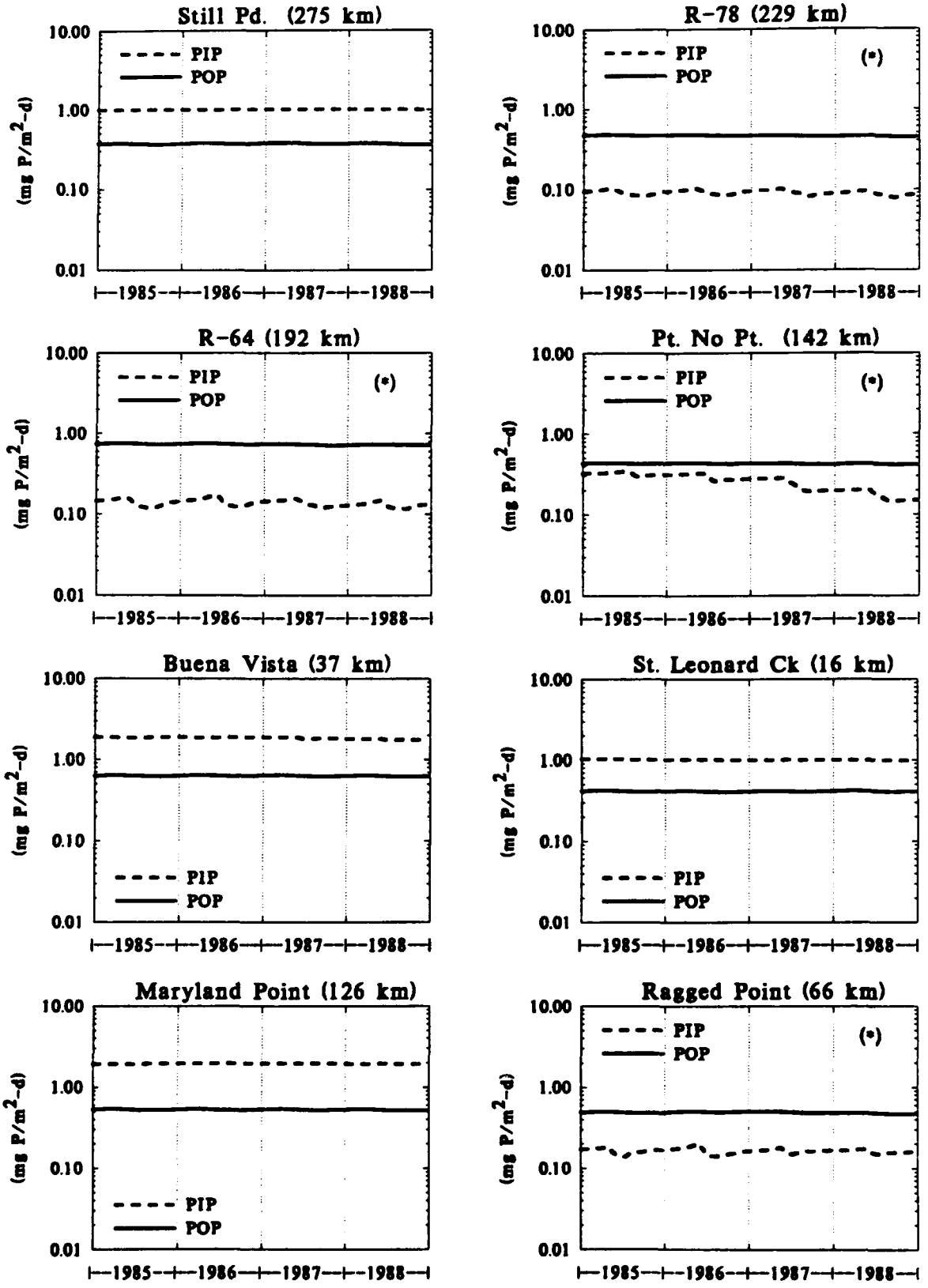

RUN104 - PLTVSPO4

Figure 10.27

This figure also highlights the difference in phosphorus composition for the aerobic and anaerobic stations. Aerobic stations have PIP concentrations that are significantly larger than POP concentration. The reverse is true for the anoxic (*) stations.

G. Silica

1. Model Parameters

The mechanism for the production of silica in sediments is different than the diagenetic formulation used for carbon, nitrogen, and phosphorus. The kinetics of dissolution are modeled using a reversible reaction which is first order in silica solubility deficit and follows a Michaelis Menton relationship in particulate silica. The kinetic source is (eq. VII-15):

$$S_{Si} = K_{Si}\theta_{Si}^{(T-20)}\frac{P_{Si}}{P_{Si}+K_{M,PSi}}([Si]_{sat}-f_{d2}[Si(2)]) \qquad (12)$$

where k_{Si} is the specific reaction rate for silica dissolution; P_{Si} is the concentration of particulate biogenic silica; $[Si]_{sat}$ is the saturation concentration of silica in the interstitial water that is in equilibrium with biogenic silica, and $f_{d2}[Si(2)]$ is the dissolved silica concentration in layer 2.

The mass balance equation for biogenic particulate silica is:

$$H_2\frac{dP_{Si}}{dt} = -S_{Si}H_2 - w_2P_{Si} + J_{PSi} + J_{DetrSi} \qquad (13)$$

where detrital silica source, J_{DetrSi}, has been added to account for silica that settles to the sediment that is not associated with the algal flux of biogenic silica.

The mass balance equation for mineralized silica can be formulated using the general mass balance equations, given in Chapter IX, as follows. The two terms in S_{Si} correspond to the source term: J_{T2}, and the layer 2 reaction velocity, κ_2, respectively.

$$J_{T2} = K_{Si}\theta_{Si}^{(T-20)}\frac{P_{Si}}{K_{M,PSi}+P_{Si}}[Si]_{sat}H_2 \qquad (14)$$

$$\kappa_2 = K_{Si}\theta_{Si}^{(T-20)}\frac{P_{Si}}{K_{M,PSi}+P_{Si}}f_{d2}[Si(2)]H_2 \qquad (15)$$

Partitioning controls the extent to which dissolved silica sorbs to solids. The same formulation as applied to phosphorus is included because it has been reported that silica can sorb to iron oxyhydroxide as discussed in Chapter VII.

$$\pi_1 = \pi_2(\Delta\pi_{Si,1}) \qquad [O_2(0)] > [O_2(0)]_{crit,Si} \qquad (16)$$

$$\pi_1 = \pi_2(\Delta\pi_{Si,1})^{([O_2(0)]/[O_2(0)]_{crit,Si})} \qquad [O_2(0)] \leq [O_2(0)]_{crit,Si} \qquad (17)$$

No other reaction is included. The parameter values are:

K_{Si}	Biogenic silica dissolution rate constant	0.50	d^{-1}
θ_{Si}	Temperature coefficient for silica oxidation	1.10	-
$[Si]_{sat}$	Saturation concentration for pore water silica	40000	mg Si/m^3
$K_{M,PSi}$	Particulate biogenic silica half saturation constant for dissolution	5.0E+07 (100.)	mg Si/m^3 (mg Si/g)
$\Delta\pi_{Si,1}$	Incremental partition coefficient for silica in the aerobic layer	10.	L/kg
$\pi_{Si,2}$	Partition coefficient for silica in the anaerobic layer	100.	L/kg
J_{PSi}	Flux of biogenic silica from the overlying water to the sediment	-	mg Si/m^2-d
J_{DetrSi}	Flux of detrital silica from the overlying water to the sediment	100.	mg Si/m^2-d

2. Data Comparisons

The time series of silica fluxes are shown in Fig. 10.28. The seasonal cycle, which is present at all the stations, arises from the temperature dependency of the dissolution reaction. The

depositional flux of particulate silica is constant in this calibration so that only temperature variation produces the seasonal variability. Silica partitioning in the aerobic sediment layer causes enhanced fluxes during periods of anoxia as can be seen in the anoxic stations (*).

Fluctuations are also caused by variations in overlying water silica concentrations as shown in Fig. 10.29, which compares the overlying water concentration, $[Si(0)]$, with the dissolved aerobic layer concentration, $f_{al}[Si(1)]$. When the overlying water concentration approaches or exceeds the aerobic layer concentration, the flux is sharply reduced, since it is proportional to the difference in concentrations. The sharp drops at Buena Vista are caused by this effect.

The sediment silica data are presented in Fig. 10.30. The longitudinal distribution of biogenic particulate silica from a survey in the fall of 1988 is compared to the model calculation at the same time, Fig. 10.30A. The observed silica is slightly greater than the model computations. The contribution of sorbed silica to the total silica concentration is small as shown.

The longitudinal distribution of pore water silica (Fig. 10.30C) indicates that computed pore water silica is lower than observations. The silica saturation concentration, $[Si]_{sat}$ = 40 mg Si/L, is shown as a dotted line. There appears to be a slight increasing trend in pore water concentration toward the mouth of the bay which is not reproduced by the model. It may be that the saturation concentration is increasing in the downstream direction. The seasonal distribution of pore water silica is shown in Fig. 10.30B,D. The model correctly computes a larger concentrations at R-64, Fig. 10.30D, relative to Still Pond, Fig. 10.30B, although the seasonal variation does not appear to be correct.

The pointwise and quantile comparisons, Fig. 10.31, are much like the previous results: a substantial amount of scatter for the pointwise comparison, Fig. 10.31A, and a slight bias of the model fluxes exceeding the observations as indicated from the quantile plots, Fig. 10.31B. The yearly average results, Fig. 10.31C, form a cluster with not much variation. The station average comparisons, Fig. 10.31D, indicate that the model result both over and underestimate the observations, but, on balance seem to reproduce the general trend.

Silica Flux

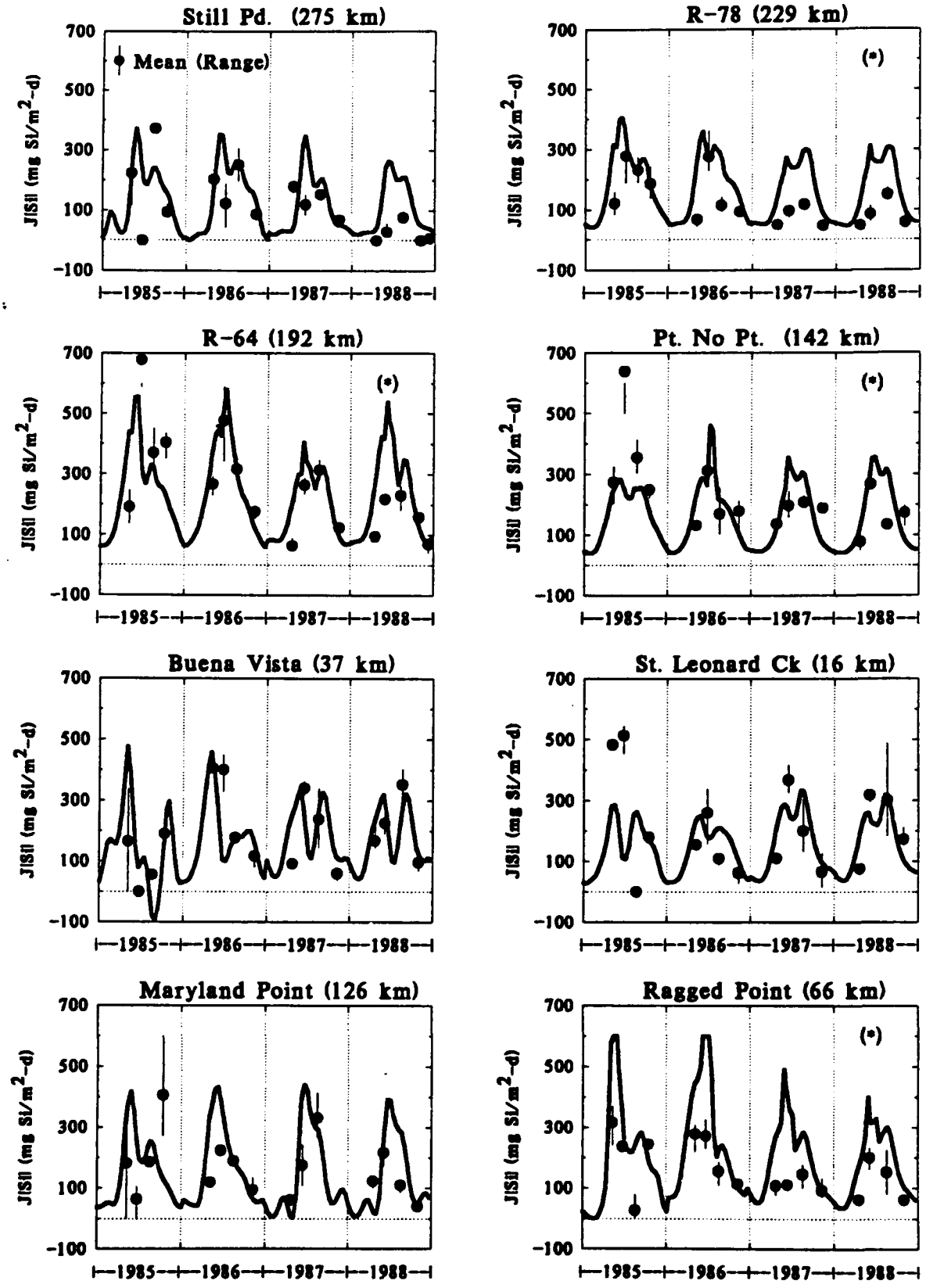

RUN104 - PLTVSI1

Figure 10.28

Silica Concentrations

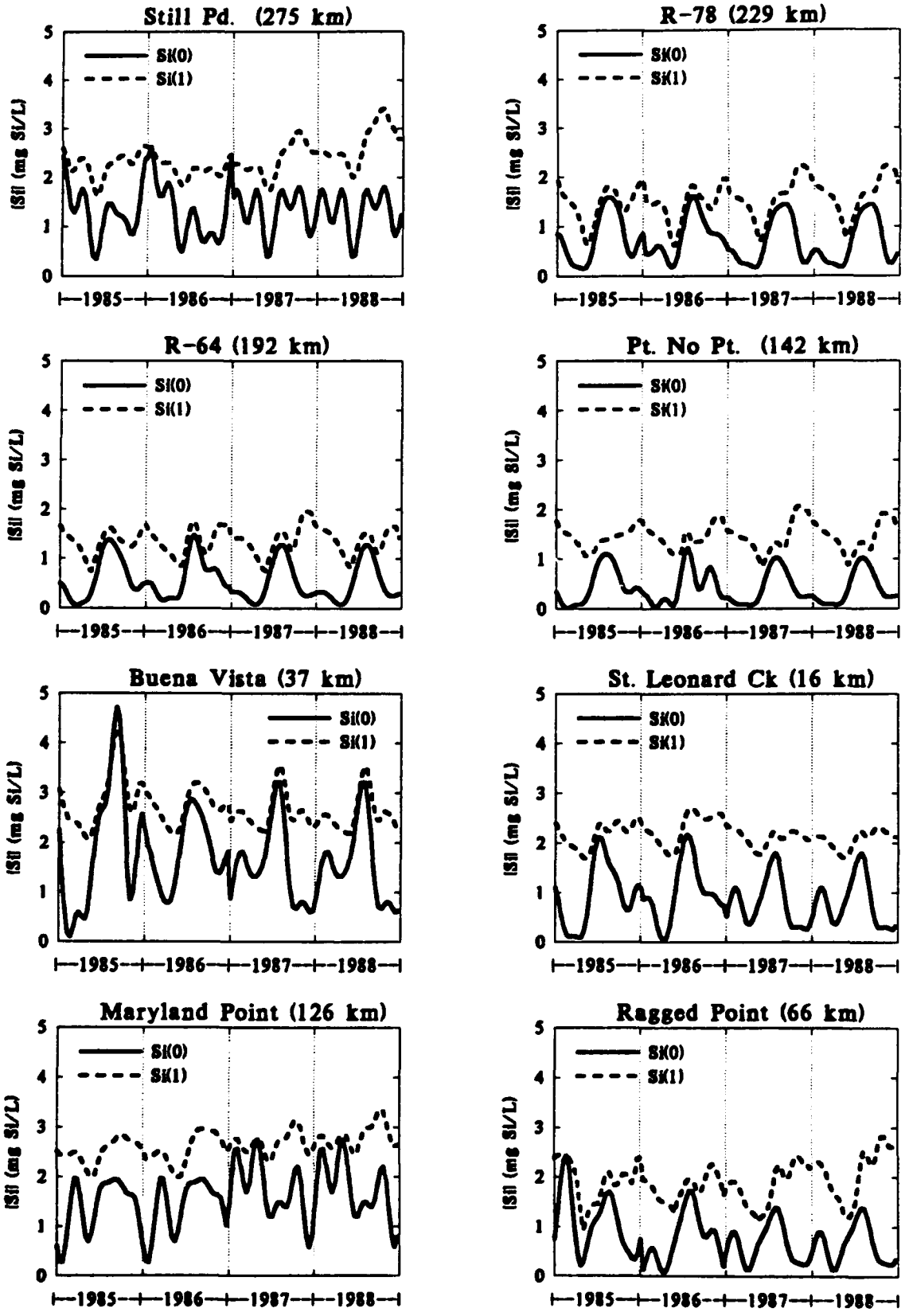

RUN104 - PLTVSID

Figure 10.29

Sediment Composition - Silica

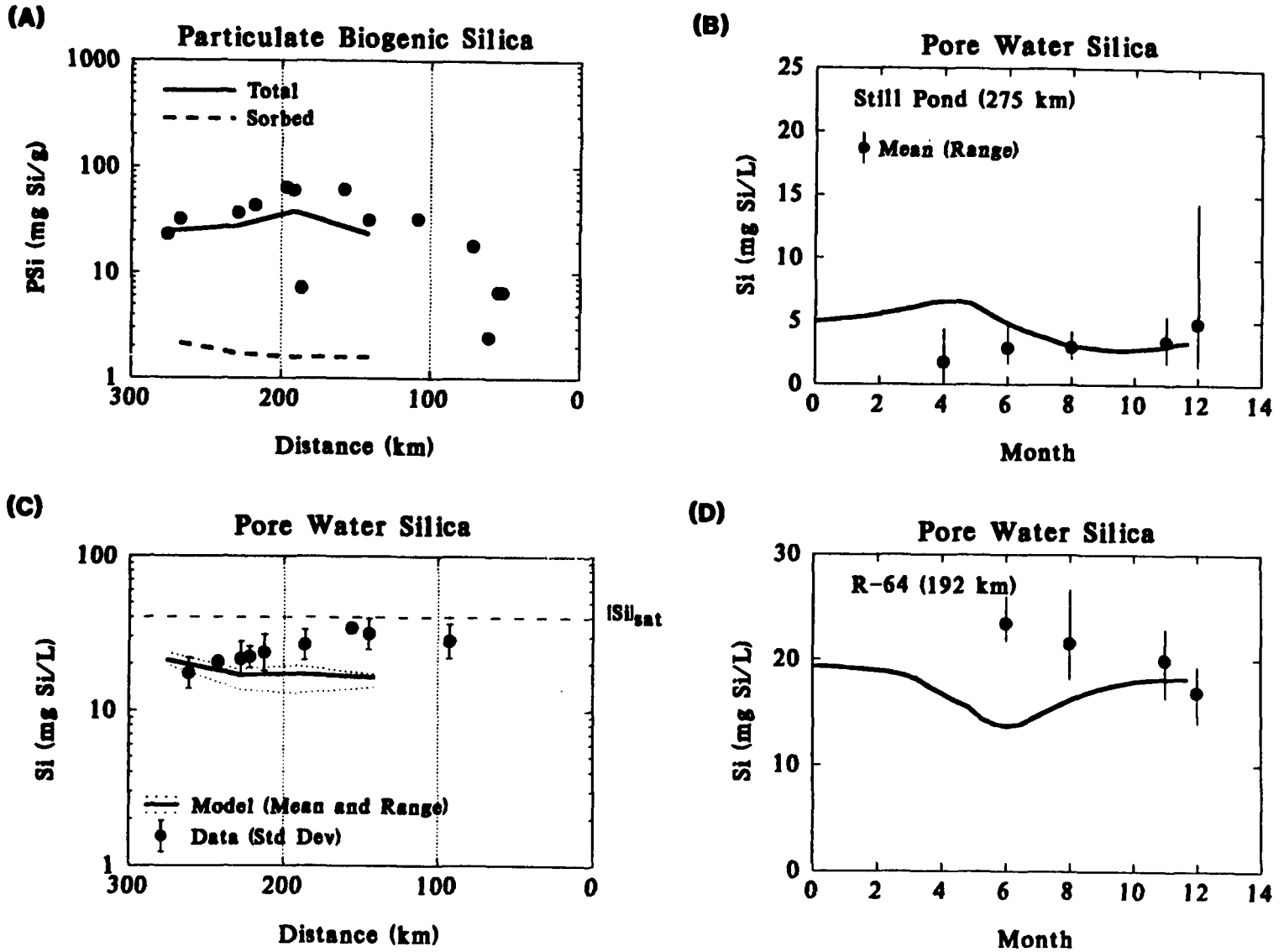

RUN104 - PLT3IPSI

Figure 10.30

Silica Flux Calibration

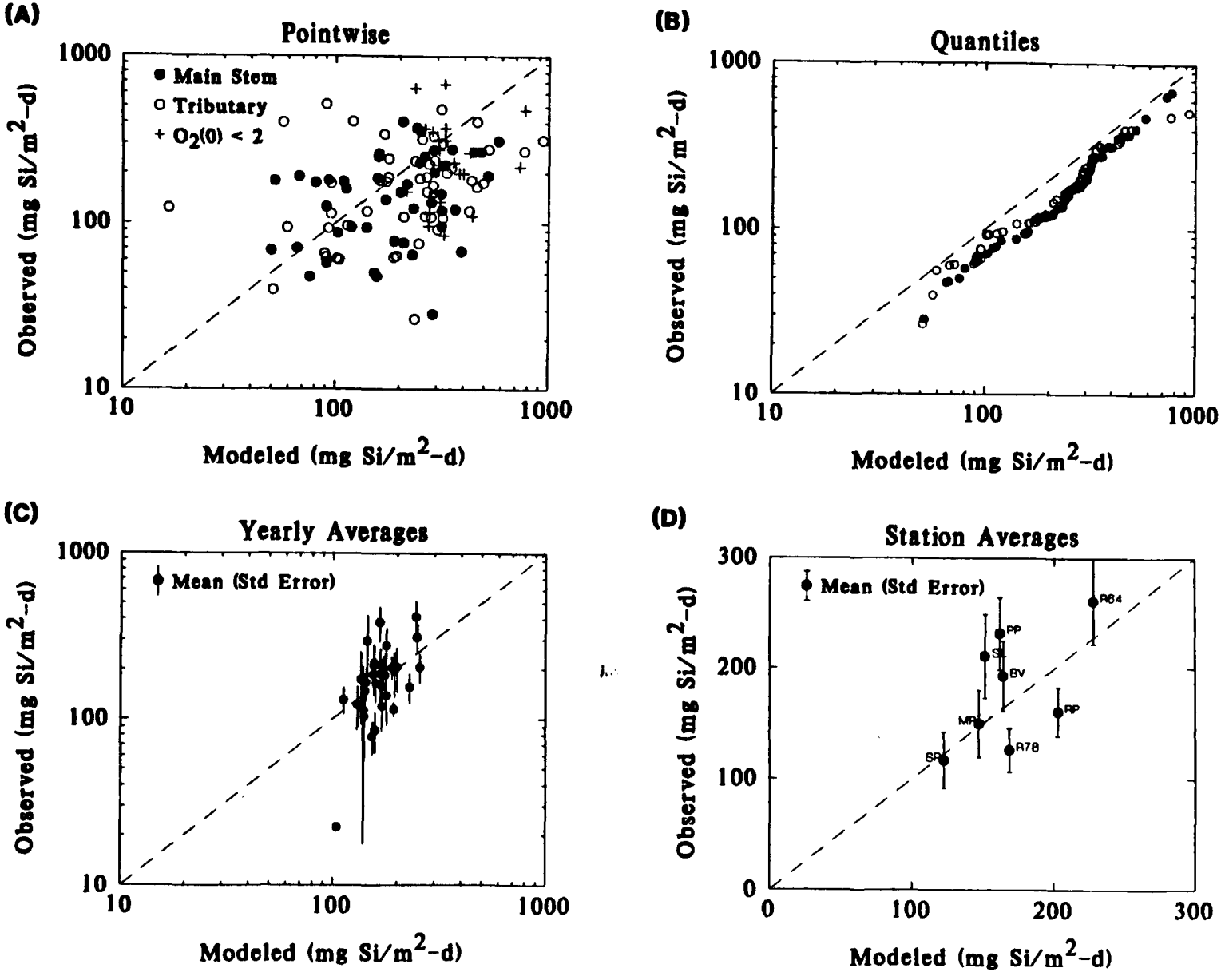

RUN104 - PLT3CMSI

Figure 10.31

The relationship of silica flux to temperature, overlying water DO, and ammonia flux are shown in Fig. 10.32. The temperature dependence in the observed fluxes, while scattered, is more pronounced than in the model results. The opposite is true for the dependency to $O_2(0)$. The data show a weak enhancement at low DO whereas the model exhibits a somewhat stronger relationship.

The silica flux is compared to the ammonia flux in the lower plots. The relationship is evident in both the data and model computations, although the model relationship is stronger due to the relationship between depositional fluxes of nitrogen and silica. The plateau in the model fluxes at ~ 80 mg Si/m^2-d is due to the additional detrital silica flux, J_{DetrSi}, which is assumed to exist at all stations, in addition to the depositional flux, J_{PSi}, which is stoichiometrically related to POM fluxes.

The flux components are shown in Fig. 10.33A,B. The components are: the sources due to biogenic, J_{PSi}, and detrital, J_{DetrSi}, silica deposition; the burial of particulate biogenic, $w_2 PSi$, and sorbed, $w_2 Si(2)$, silica; and the resulting silica flux, $J[Si]$. Burial of particulate biogenic silica is the only significant sink, since the concentration of sorbed silica is considerably smaller (Fig. 10.30). A comparison of the total silica input, $J_{TSi} = J_{PSi} + J_{DetrSi}$, to that which is recycled, $J[Si]$, is shown ing Fig. 10.30C. The removal fraction is quite variable and does not appear to be strongly related to the total silica input. This is because there is a limitation to the quantity of silica that can be recycled, which is determined by the solubility of silica. Hence, the silica fluxes are less variable than the total fluxes to the sediment.

H. Station Composite Plots

The sediment flux time series for ammonia, oxygen, phosphate, and silica are grouped by stations in Fig. 10.34-37. Since each of the fluxes are driven by the same depositional flux, modified by the appropriate stoichiometric ratios, the relationships between the various fluxes are determined by the overlying water concentrations and the kinetics.

For Still Pond, Fig. 10.34, the fluxes have a seasonal variation which are all in phase. They are not disrupted by overlying water hypoxia or anoxia. By contrast, the relationships among the fluxes at station R-64 are distinct. The ammonia and silica fluxes show a seasonal variation related to temperature. However the oxygen and phosphate fluxes are different. The oxygen flux is almost constant through the latter part of each year. The very large phosphate fluxes relative to the ammonia flux are the result of the storage of phosphorus during aerobic periods and its release during anoxia.

There is a difficulty with the calibration to the SOD data at R-64. The model cannot reconcile the observations of high ammonia, phosphate and silica fluxes that occur during the first part of each year, and the lack of variation in the oxygen flux during the same time period. The fact that the depositional fluxes of nitrogen, silica, phosphate, and carbon are all in constant stoichiometric ratio requires that the model predicts a substantial oxygen flux as the sulfide that is produced in the early part of each year is oxidized during the first half of the year. The onset of anoxia and the persistence of benthic stress suppresses the oxygen flux for the latter half of the year. This inability to account for an observed anomaly points to an area that warrants further investigation.

Stations R-78 and Point No Point, Fig. 10.35, also exhibit this difference between the seasonal variation of the ammonia and silica flux, and the oxygen flux. However, since the depositional fluxes are smaller at these stations, as indicated by the smaller ammonia fluxes, the spring increase in SOD is not as dramatic and does not contradict the observations.

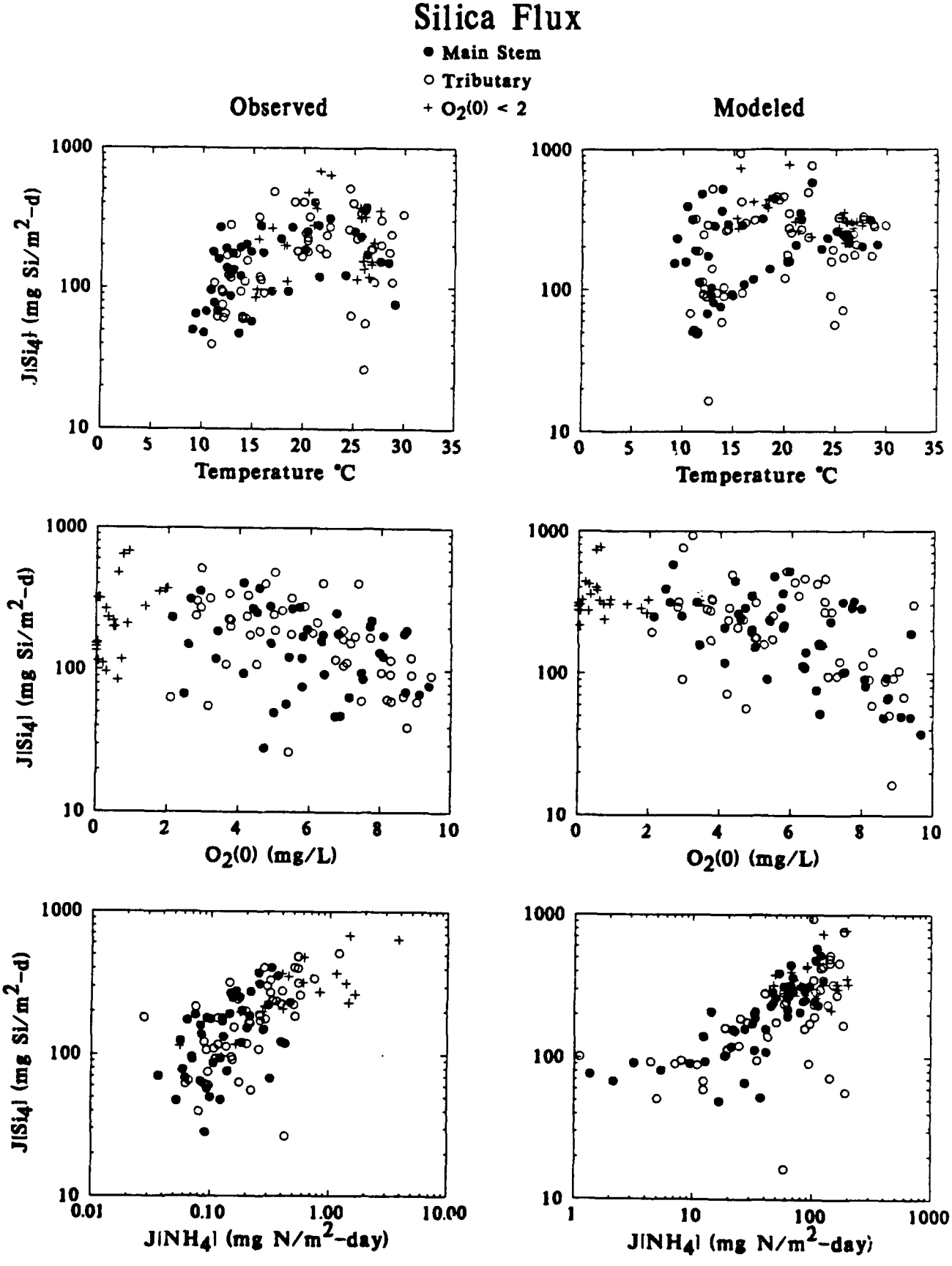

RUN104 - PLT3MOSI

Figure 10.32

Flux Components

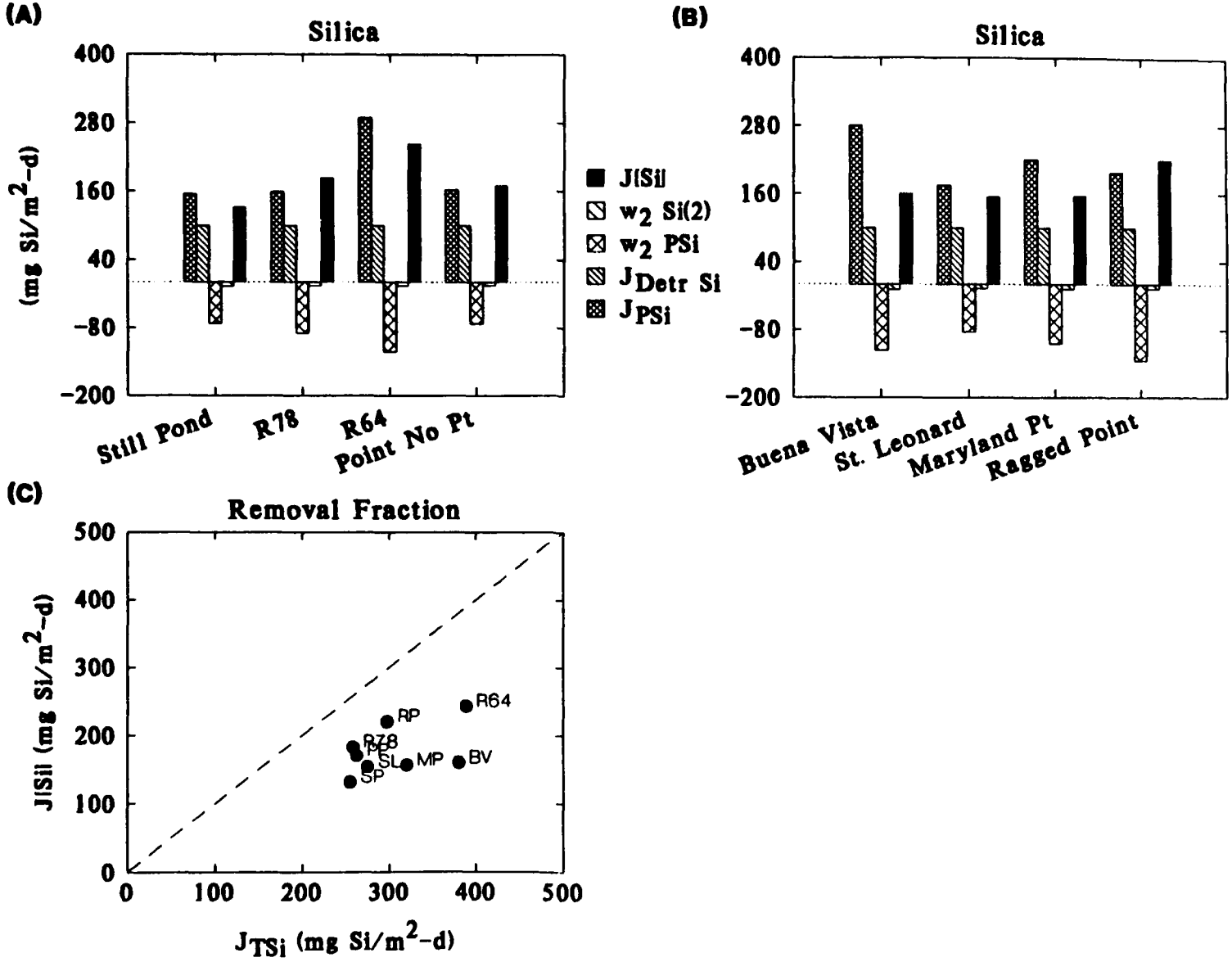

RUN104 - PLT3FR1A

Figure 10.33

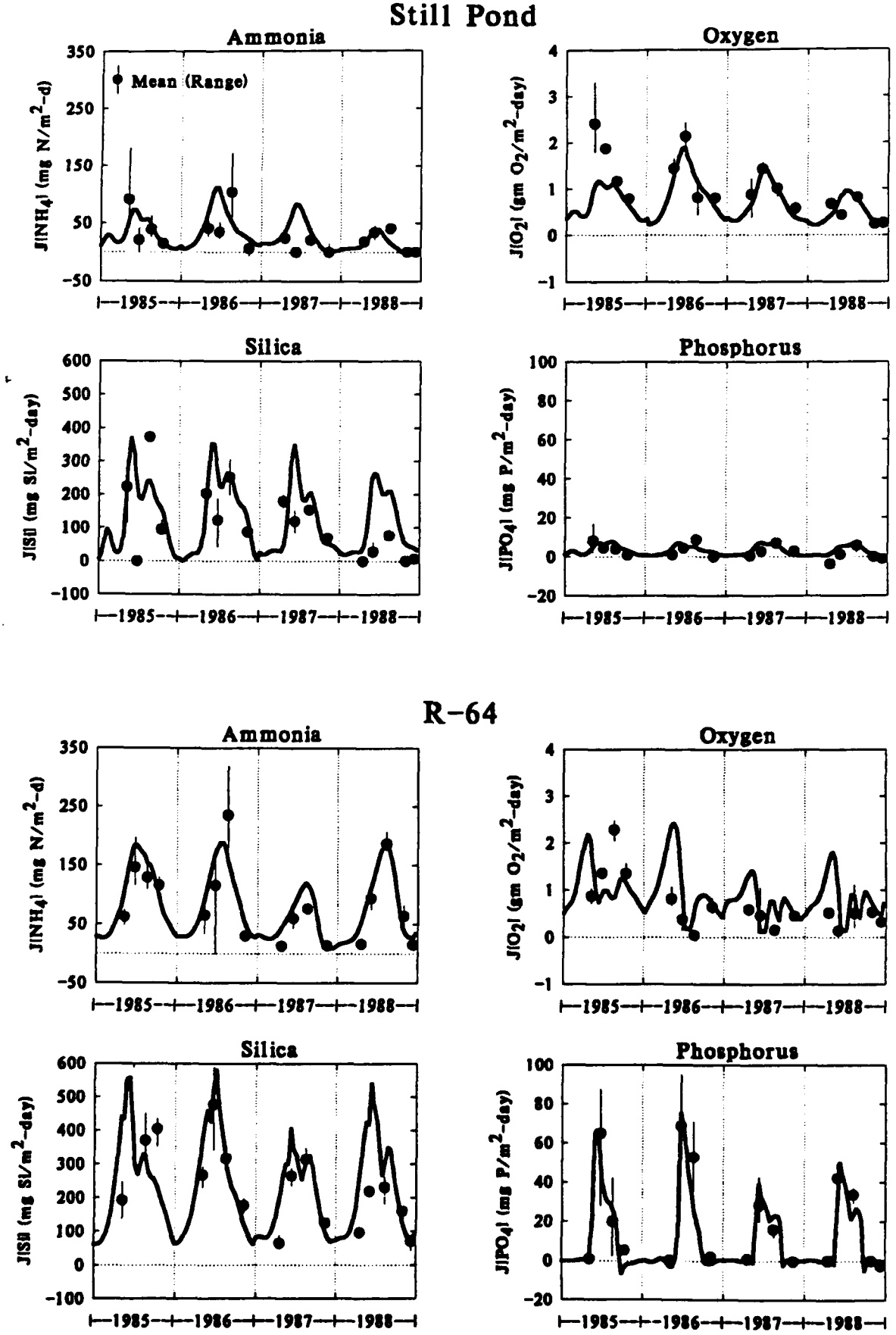

RUN104 - PLTVSTA1

Figure 10.34

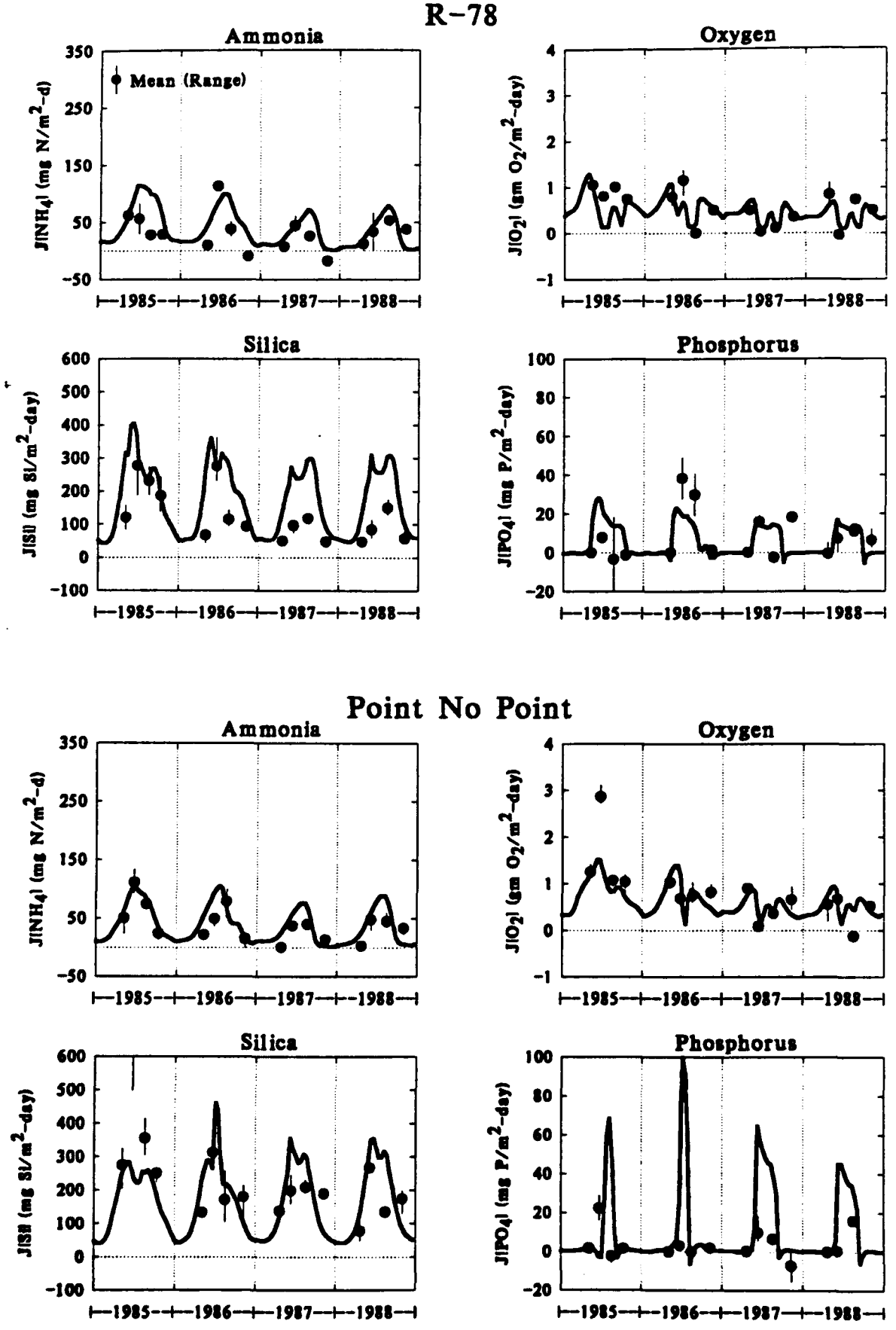

RUN104 - PLTVSTA2

Figure 10.35

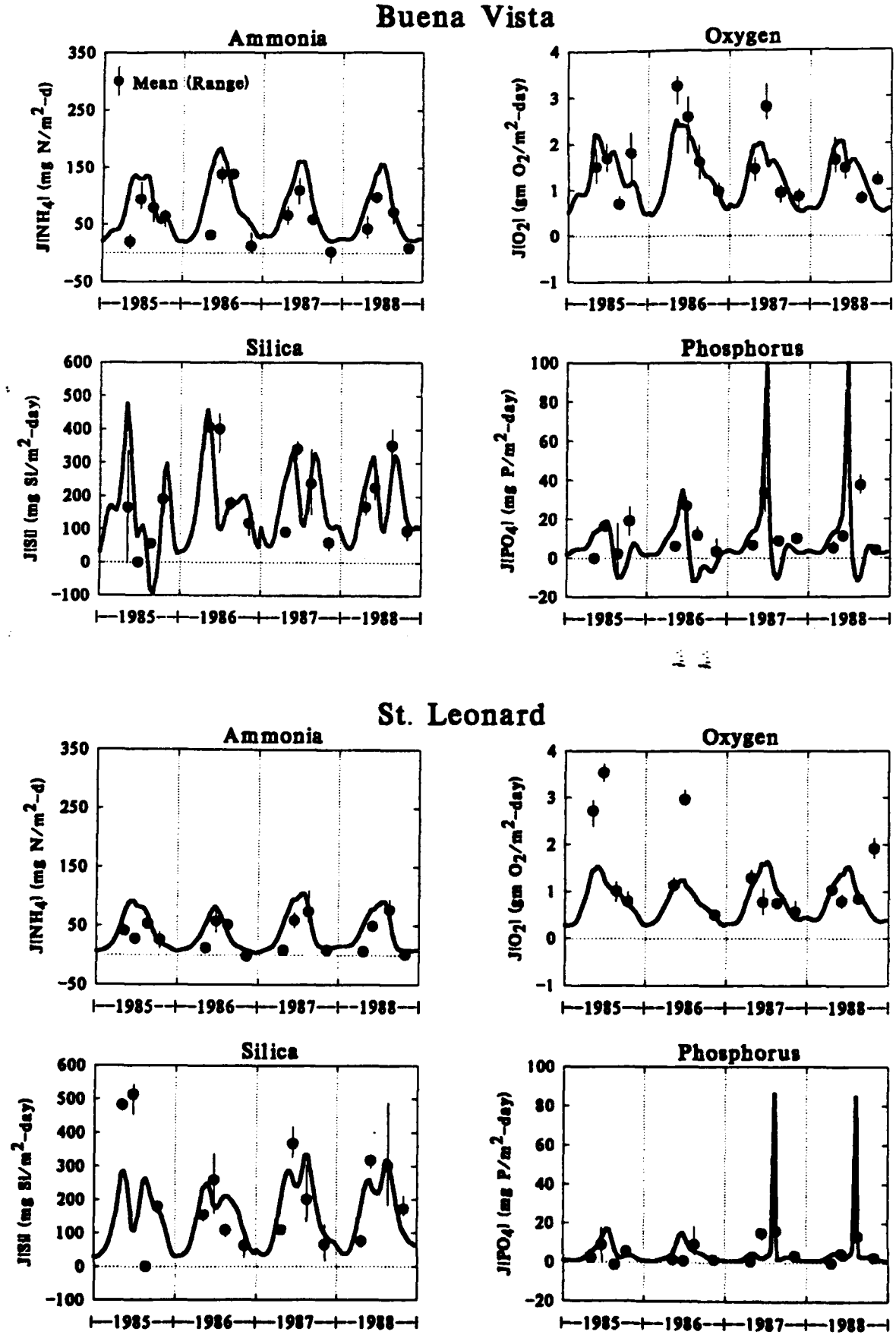

RUN104 - PLTVSTA3

Figure 10.36

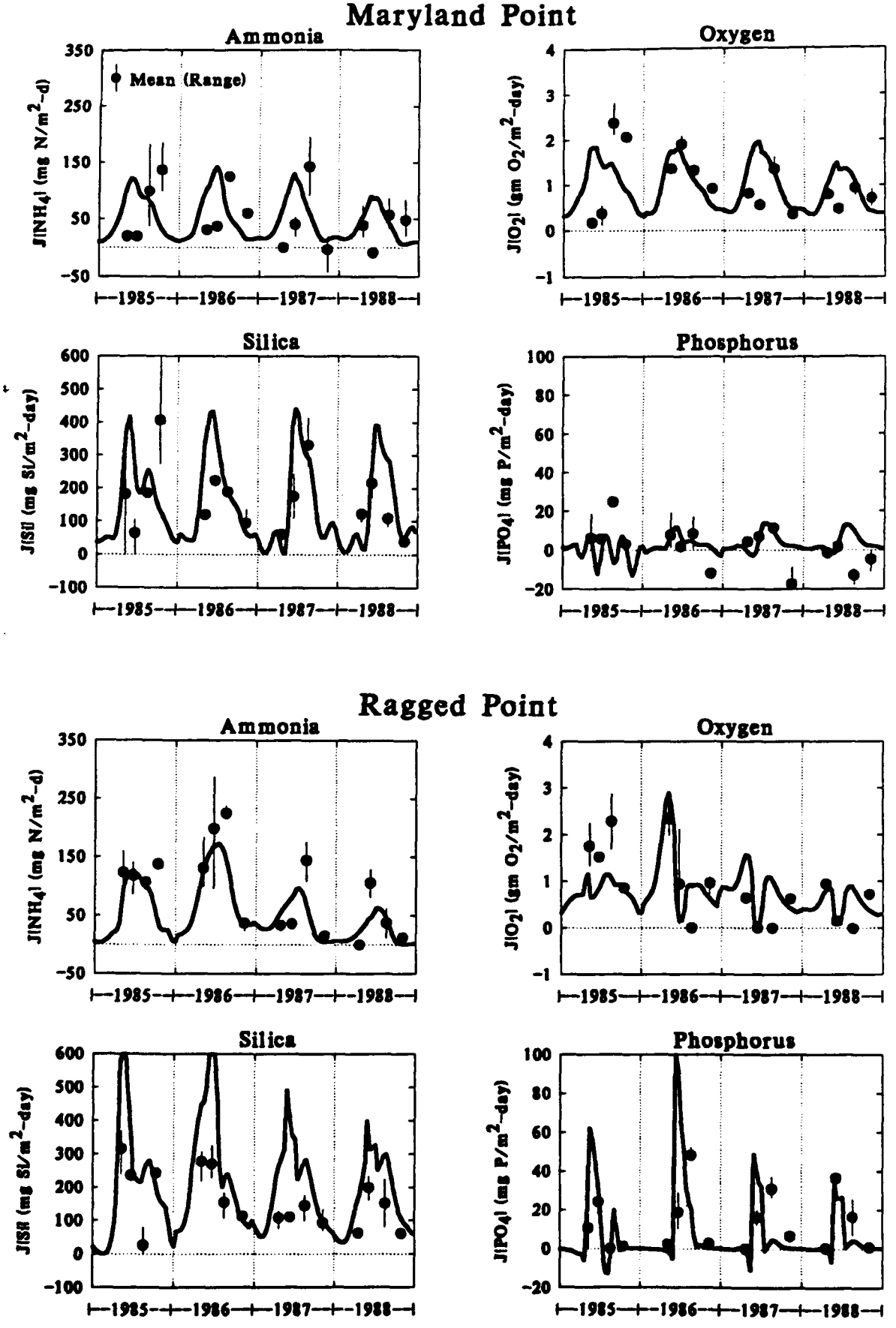

RUN104 - PLTVSTA4

Figure 10.37

The fluxes at Buena Vista and St. Leonard on the Patuxent estuary are presented in Fig. 10.36. By and large the model is a reasonable representation of the data. However, the 1985 data for St. Leonard illustrate an inconsistency which the model cannot reconcile. The large fluxes of oxygen and silica suggest a large depositional flux. However, the ammonia and phosphate fluxes suggest a smaller flux. These discrepancies cannot be reconciled within a framework that is restricted to constant stoichiometric ratios for the particulate organic matter that settles into the sediment.

For the Maryland Point and Ragged Point stations on the Potomac estuary, Fig. 10.37, the magnitude of the fluxes are in reasonable agreement with the large diagenesis flux suggested by the ammonia fluxes. The exception is the Ragged Point silica flux which is computed to be larger than the observations.

It is possible that these discrepancies are related to the assumption of a constant stoichiometric relationship between the depositional fluxes. This simplification is unavoidable if the depositional fluxes are to be estimated from ammonia diagenesis. The alternate choice - estimating the depositional fluxes independentiy using the observed fluxes to the overlying water - introduces too many degrees of freedom in the stand alone calibration thereby weakening it severely. When the sediment model is coupled to an overlying water eutrophication model, the constant stoichiometic assumption is not made. Rather the depositional fluxes result from the water column processes that produce particulate organic matter.

I. Conclusions

The stand alone calibration of the sediment flux model highlights both the strengths and weaknesses of the model. The relationships between the concentrations of solutes in the solid phase, pore water, and the sediment fluxes are rationalized within the framework of a mass balance analysis. The seasonal patterns are reproduced with reasonable fidelity for the oxic stations. The influence of anoxia on phosphate and oxygen fluxes - enhancing the former and suppressing the latter - is captured as well. The phosphate flux model employs a parameterization of the aerobic layer phosphate partitioning that depends on the overlying water DO. The suppression of the oxygen flux that persists after the anoxic period relies on the formulation of benthic stress. Although these formulations are empirical, they appear to produce reasonable simulations.

The model is not able to reproduce the pointwise distribution of the fluxes. Plots of observed versus modeled fluxes display significant scatter. This appears to be related to a lack of precise timing between computed and observed fluxes. A visual inspection of the time series plots supports this observation. By contrast, the quantile plots demonstrate that the model reproduces the overall distribution of fluxes in the main stem and the tributaries if station location and timing are not considered. The comparison of predicted and observed yearly means and station means reveals that as the degree of averaging increases, the model is usually better able to predict the observations.

This is examined quantitatively in Fig. 10.38, a plot of the square of the correlation coefficients between observed and modelled fluxes for pointwise, yearly averages, and station averages. The square of the correlation coefficient, r^2, is the fraction of the observed variance that is removed by the model predictions. If r^2 is small, very little variability is removed by the model and, therefore, it has little predictive power. If, however, r^2 approaches one, then the model is capturing all the variability. Both Pearson (Fig. 10.38A,B) - the usual correlation coefficient - and Spearman's rank correlation (Fig. 10.38C) are computed for the arithmetic and the arcsech

Correlation Coefficients

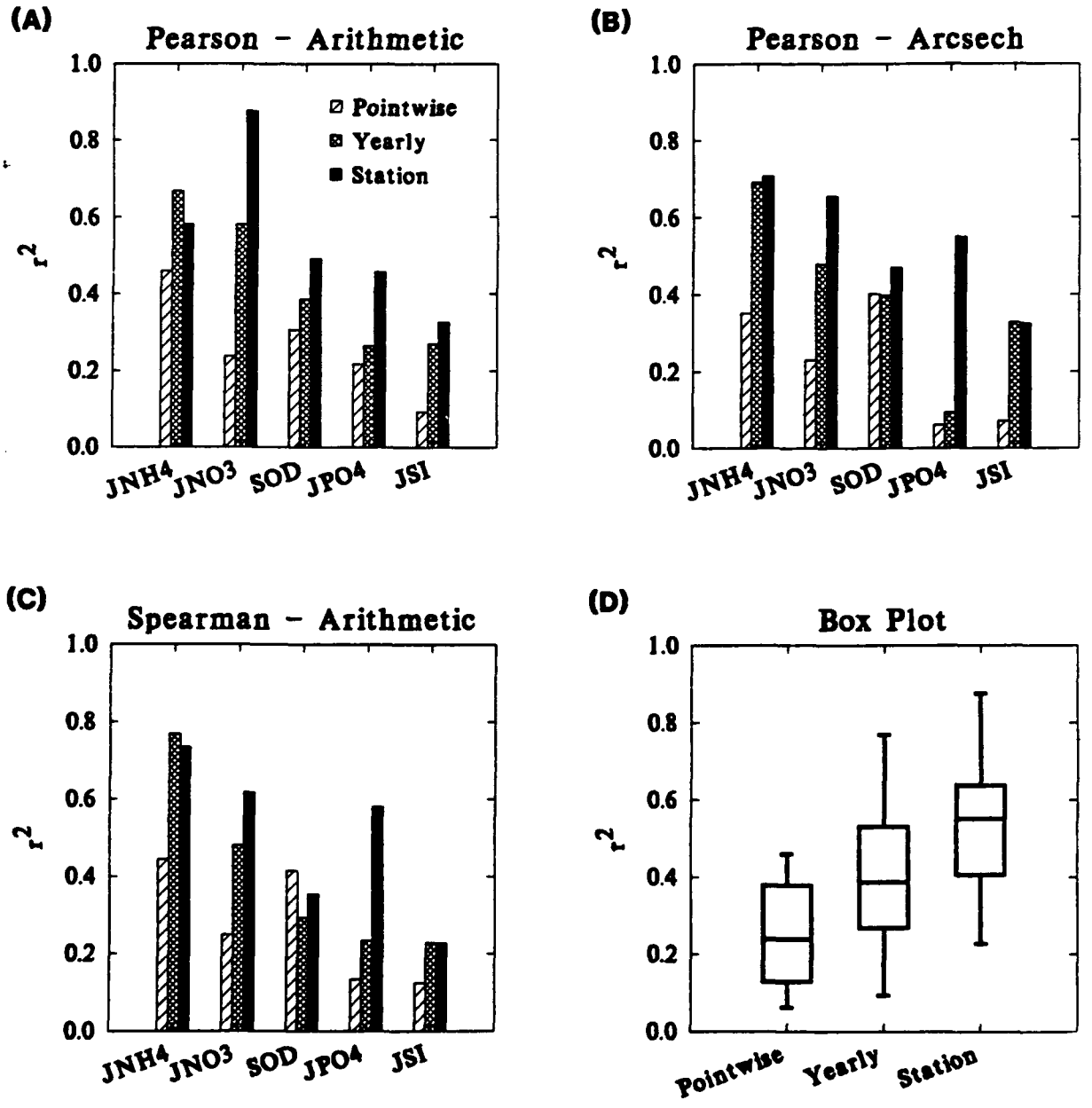

RUN104 - PLT3STT4

Figure 10.38

transformed variables. Since the Spearman's rank correlations are identical for the non-transformed and transformed data - this is because the arcsech transformation is monotonic and the rank orders are preserved - only the non-transformed results are presented.

In general, r^2 improves as the averaging increases, although sometimes the station averages decrease slightly or remain the same. Since the station averages comprise only 8 points, these correlation coefficients are quite uncertain.

The box plot, Fig. 10.38D, which combines the results of the three computational methods for r^2, summarizes the probability distributions of r^2. The median (25^{th} percentile, 75^{th} percentile) r^2 increases from 0.24 (0.13, 0.40) to 0.39 (0.27, 0.58) to 0.55 (0.35, 0.66) as the averaging interval increases.

The overall impression of the calibration is that the fine scale variations cannot be captured, but that the overall quantitative relationships between the fluxes, together with the solid phase and pore water concentrations, are successfully rationalized. The seasonal behavior and the relative variations are reproduced. Of course, the final judgement of the utility of the flux model is its performance as part of the coupled Chesapeake Bay model. Interim comparisons indicate that the modeled fluxes are in reasonable agreement with the measurements. In particular, the extensive measurements made in 1988 can be used to examine the model performance over more pronounced spatial gradients.

J. References

Boynton, W.R., Kemp, W.M., Barnes, J.M., Cowan, J.L.W., Stammerjohn, S.E., Matteson, L.L., Rohland, F.M. and Garber, J.H. (1990): Long-term characteristics and trends of benthic oxygen and Nutrient Fluxes in the Maryland portion of Chesapeake Bay. In: New Perspectives in the Chesapeake System: A research and management partnership., pp. 339-354. Editor:. Chesapeake Res. Consortium #137, Baltimore, MD.

Bricker, O.P., Matisoff, G. and Holdren Jr, G.R. (1977): Interstitial Water Chemistry of Chesapeake Bay Sediments Basic Data Report No.9. Maryland Geological Survey.

Wilkinson, L. (1990). SYSTAT: The System for Statistics. Evanston, IL, SYSTAT, Inc.

XI. TIME TO STEADY STATE

A. Introduction

Among the purposes for building a model of sediment processes - to enhance scientific understanding, to codify the known information into a coherent whole, and to establish that the formulations can indeed be used to reproduce observations - the most practical is to incorporate the model into an overall water quality model to make projections of the consequences of future actions. One question that immediately arises is: how long will it take for the sediment model to respond to changes in depositional fluxes?

The purpose of this chapter is to examine this question. The method adopted is to examine the model response - which is termed its transient response - to an abrupt change in the input depositional fluxes. The transient response of the diagenesis model is considered first, followed by an analysis of the flux models. In particular, the response of the phosphate flux model is explored using an analytical investigation. Finally, the response of the full flux model is examined using numerical simulations.

B. Diagenesis

The transient responses for particulate organic carbon, nitrogen, and phosphorus are determined by the nature of the mass balance equations. Since these are similar only the POC equations are explicitly analyzed. The conclusions apply to PON and POP as well. The mass balance equation for $G_{POC,i}$, the concentration of POC in the i^{th} diagenesis class (i = 1, 2 or 3) in the anaerobic layer is:

$$H_2 \frac{dG_{POC,i}}{dt} = -K_{POC,i} G_{POC,i} H_2 - w_2 G_{POC,i} + J_{POC,i} \qquad (1)$$

where: $K_{POC,i}$ is the first order reaction rate coefficient, w_2 is the sedimentation velocity, and $J_{POC,i}$ is the depositional flux of the i^{th} G class of POC from the overlying water to the sediment. For constant coefficients, in particular for constant temperature and depositional flux, this equation is easily solved:

$$G_{POC,i}(t) = G_{POC,i}(0)e^{\lambda t} + G_{POC,i}(\infty)(1 - e^{-\lambda t}) \tag{2}$$

where:

$$\lambda = K_{POC,i} + \frac{w_2}{H_2} \tag{3}$$

and

$$G_{POC,i}(\infty) = \frac{J_{POC,i}}{K_{POC,i}H_2 + w_2} \tag{4}$$

the final steady state concentration. The time it takes for the concentration of $G_{POC,i}(t)$ to change from the initial concentration, $G_{POC,i}(0)$, to the final concentration: $G_{POC,i}(\infty)$ is determined by the magnitude of the exponent, λ. Its inverse, τ, is called the time constant of the equation:

$$\tau = \frac{1}{\lambda} = \frac{1}{K_{POC,i} + \frac{w_2}{H_2}} \tag{5}$$

When one, two and three time constants have elapsed, the model has reached ~ 67%, ~ 86%, and ~ 95% of the new steady state value, respectively.

The time constant is related to the half life, $t_{\frac{1}{2}}$, of $G_{POC,i}$ in the sediment by the relationship:

$$t_{\frac{1}{2}} = \frac{\ln(2)}{\lambda} = 0.693\tau \qquad (6)$$

For the three G classes, the time constants and half lives are listed in Table 11.1.

Table 11.1
Time Constants, day (year) and Half Lives day (year)
(Temperature = 20 ℃)

	G_1	G_2	G_3
λ	$\sim K_{POC,1}$	$\sim K_{POC,2}$	w_2/H_2
τ	28.6 (0.078)	555. (1.52)	14,600 (40)
$t_{\frac{1}{2}}$	19.8 (0.054)	385 (1.0)	10,100 (27.7)

The magnitude of the reaction rates essentially determine the time constants for G_1 and G_2 as can be seen from eq.(5). The sedimentation velocity, w_2, and the active layer depth, H_2, determine the time constant for G_3. Since G_3 is inert, its long time constant does not affect the response time of the diagenesis flux, which is controlled by the time constants of G_1 and G_2. Thus for ammonia and nitrate the time to 95% of steady state is approximately $3\tau \approx 4.5$ years since no appreciable storage of these solutes occurs.

For the other fluxes, it is more difficult to determine the time constants because a significant amount of mass is in storage and this must be depleted in order to reach steady state. The case for phosphate is examined next.

C. Phosphate Flux

The equilibration time for the individual fluxes can be determined by an analysis of the governing equations. The method is simply to isolate λ. For phosphate, the mass balance equations for layer 1 and 2 are:

$$0 = H_1 \frac{dC_{T1}}{dt} = s(C_{d0} - f_{d1}C_{T1}) + w_{12}(f_{p2}C_{T2} - f_{p1}C_{T1}) + K_{L12}(f_{d2}C_{T2} - f_{d1}C_{T1}) - w_2 C_{T1} \quad (7)$$

$$H_2 \frac{dC_{T2}}{dt} = -w_{12}(f_{p2}C_{T2} - f_{p1}C_{T1}) - K_{L12}(f_{d2}C_{T2} - f_{d1}C_{T1}) + w_2(C_{T1} - C_{T2}) + J_P \quad (8)$$

Adding the equations yields:

$$H_2 \frac{dC_{T2}}{dt} = s(C_{d0} - f_{d1}C_{T1}) - w_2 C_{T2} + J_P \quad (9)$$

which is an equation in C_{T2} and C_{T1}. Solving the aerobic layer equation yields the relationship between the two concentrations:

$$C_{T1} = \frac{sC_{d0} + (w_{12}f_{p2} + K_{L12}f_{d2})C_{T2}}{sf_{d1} + w_{12}f_{p1} + K_{L12}f_{d1} + w_2}$$

$$= \frac{sC_{d0}}{sf_{d1} + w_{12}f_{p1} + K_{L12}f_{d1} + w_2} + \frac{w_{12}f_{p2} + K_{L12}f_{d2}}{sf_{d1} + w_{12}f_{p1} + K_{L12}f_{d1} + w_2} C_{T2}$$

$$= C_{OLW} + r_{12}C_{T2} \quad (10)$$

which is made up of two terms. The first, C_{OLW}, is due to the source of phosphate from the overlying water. The second term, which is written in terms of r_{12}, eq.(IV-9), involves C_{T2} and, therefore contributes to λ. Thus eq.(9) becomes:

$$H_2 \frac{dC_{T2}}{dt} = s(C_{d0} - f_{d1} r_{12} C_{T2}) - w_2 C_{T2} + J_P - s f_{d1} C_{OLW}) \tag{11}$$

Collecting the terms that multiply C_{T2} yields:

$$\frac{dC_{T2}}{dt} = -\lambda C_{T2} + \text{forcing fn} \tag{12}$$

so that:

$$\lambda = \frac{s f_{d1} r_{12} + w_2}{H_2} \tag{13}$$

and

$$\tau = \frac{1}{\lambda} = \frac{H_2}{s f_{d1} r_{12} + w_2} \tag{14}$$

Thus the time constant is determined by the magnitude of the loss terms in the denominator and the size of the active layer of the sediment in the numerator. The losses are via the transfer of phosphate to the overlying water, and the loss to the deep sediment by burial.

Fig. 11.1 presents an evaluation of eq.(14) using the calibrated phosphate flux model parameters for both aerobic and anaerobic overlying water. Table 11.2 lists the values used and Table 11.3 lists the rest of the necessary equations. The time constants cannot be larger than the time required for sedimentation to displace the sediment in the active layer: $\tau < H_2/w_2$ = 10 cm / 0.25 cm/yr = 40 yr.

1. Aerobic Overlying Water

For the aerobic case, particulate mixing is larger than dissolved mixing and $r_{12} \approx 1$. Thus:

$$\tau \approx \frac{H_2}{s f_{d1} + w_2} \tag{15}$$

As the surface mass transfer coefficient, s, increases, the time constant decreases (eq.15, Fig. 11.1). The reduction in the time constant as s increases occurs because the stored sediment phosphorus can be lost at an increasing rate as a flux to the overlying water.

Since the overlying water is aerobic, the dissolved fraction, f_{d1}, is small and the phosphate flux is small as well. Using the annual average for the aerobic station, s = 0.2 (m/d), yields a time constant of τ = 12.5 years.

2. Anaerobic Overlying Water

For the anaerobic case, the dissolved fraction in the aerobic layer is much larger due to the decrease in the aerobic layer partition coefficient. For this case surface mass transfer is no longer rate limiting. This can be seen from the expression for λ,eq.(13), with r_{12} explicitly included, (see eq.10):

$$\lambda = \frac{s f_{d1}\left(\frac{w_{12} f_{p2} + K_{L12} f_{d2}}{s f_{d1} + w_{12} f_{p1} + K_{L12} f_{d1} + w_2}\right) + w_2}{H_2} \tag{16}$$

For $s f_{d1}$ large relative to the particle and dissolved phase mixing coefficients, the expression simplifies to:

$$\lambda \approx \frac{w_{12} f_{p2} + K_{L12} f_{d2} + w_2}{H_2} \tag{17}$$

Time Constants - Phosphate

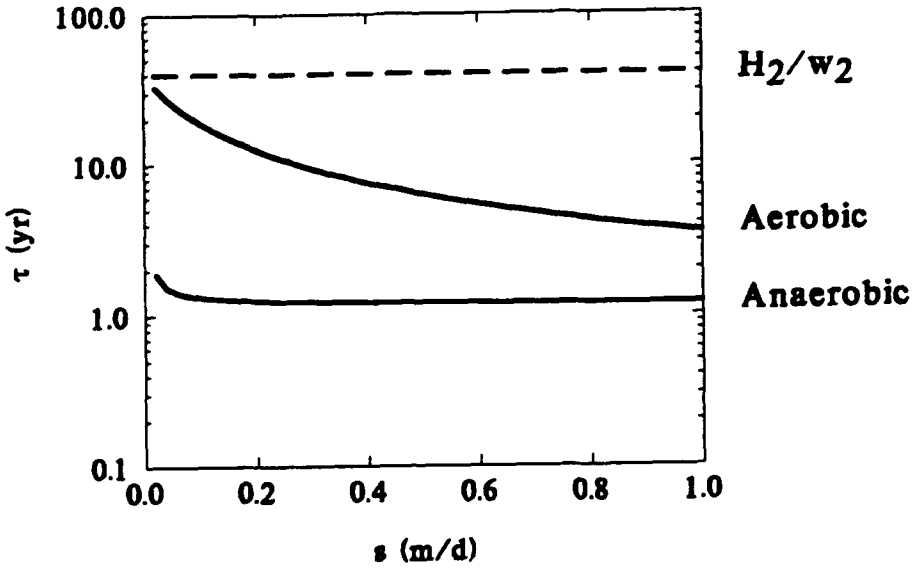

TSS2E

Figure 11.1

Thus, the rate limitation is the speed with which stored phosphate in the anaerobic layer can be transported to the aerobic layer by either particle mixing, $\omega_{12} f_{p2}$, or interstitial water diffusion, $K_{L12} f_{d2}$. Fig. 11.1 presents the results. Note that s no longer affects the time constant, which is now less than 2 years. For this calculation the minimum particle diffusion coefficient is used (Table 11.2) because bioturbation would be suppressed by the low overlying water DO. Since this time constant is much shorter than the aerobic case the response is more rapid. The actual transient responses are examined in the next section.

D. Numerical Simulations

The transient response of the full time variable model is more complex than can be captured by a simple time constant analysis. The reason is that the various components of the model interact and affect the time variable behavior. In order to analyze a specific situation, the response to an abrupt decrease of the depositional flux to 1.0% of its value is examined. A decrease to zero is not used since numerical difficulties can occur. Initially, the model is equilibrated to a constant depositional flux. All the overlying water concentrations are set to zero except oxygen. Two cases are presented: an aerobic and an anaerobic overlying water. Table 11.4 lists the parameter and input values specific to the transient response calculations.

1. Aerobic Overlying Water

The results for aerobic overlying water are shown in Fig. 11.2. Particulate organic carbon, Fig. 11.2A, decreases exponentially following the time constant analysis given above. G_1 carbon decreases rapidly whereas G_2 carbon reacts more slowly. Although not shown, particulate organic nitrogen and phosphorus react similarly. Since G_1 and G_2 nitrogen are decreasing quickly, ammonia diagenesis, J_N, also deceases as shown in Fig. 11.2B. The ammonia flux, $J[NH_4]$, decreases even more rapidly because the depth of the aerobic layer is increasing, due to the reduction in sediment oxygen demand, as shown in Fig. 11.2C. SOD is decreasing, but slightly less slowly than J_C (in units of oxygen equivalents) because the stored sulfide is also being oxidized.

The reason that SOD is slightly larger than J_C is that the oxygen consumed by nitrification is also included in the SOD. The decrease in surface mass transfer, s, as a result of the decrease in SOD is also shown.

The nitrate flux also decreases, Fig. 11.2D, but less slowly than the ammonia flux. The reason is that the initial increase in nitrification due to the increase in the depth of the aerobic zone provides additional nitrate. There is also an initial sharp decrease just after the abrupt drop in depositional flux. This is due to the initial sharp drop in surface mass transfer coefficient, Fig. 11.2C. However, the flux then increases. The reason is that the magnitude of the flux is related to the magnitude of the source of nitrate as well as the mass transfer coefficient. As shown in Fig. 11.3D, the aerobic layer nitrate concentration responds to the decrease in s by increasing in concentration, thereby increasing the flux.

This initial drop is much more apparent in the phosphate flux, Fig. 11.2E. Phosphate has a longer time constant than ammonia, nitrate, or SOD. After five years there is still a substantial phosphate flux even though phosphate diagenesis, J_P, has decreased to approximately 5% of its original value. The phosphate flux transient is projected to last for quite a long time since s has decreased, Fig. 11.2C, and the time constant for phosphate is an increasing function of s, Fig. 11.1A.

Silica, Fig. 11.2F, has the longest time constant as indicated from the results. Whereas the depositional flux of silica, J_{PSi}, drops abruptly, the silica flux remains elevated. The reason is that there is a substantial quantity of biogenic silica stored in the sediment and it provides the source for a continual supply. Additionally, the silica dissolution reaction is a function of the particulate silica concentration which is also decreasing.

The transient responses for the active layer solute concentrations are shown in Fig. 11.3. Ammonia, Fig. 11.3A, and nitrate, Fig. 11.3D, exhibit rapid declines characteristic of solutes that are not stored to a significant extent. Note the initial increase in nitrate concentration, due to the

Transient Response – Aerobic

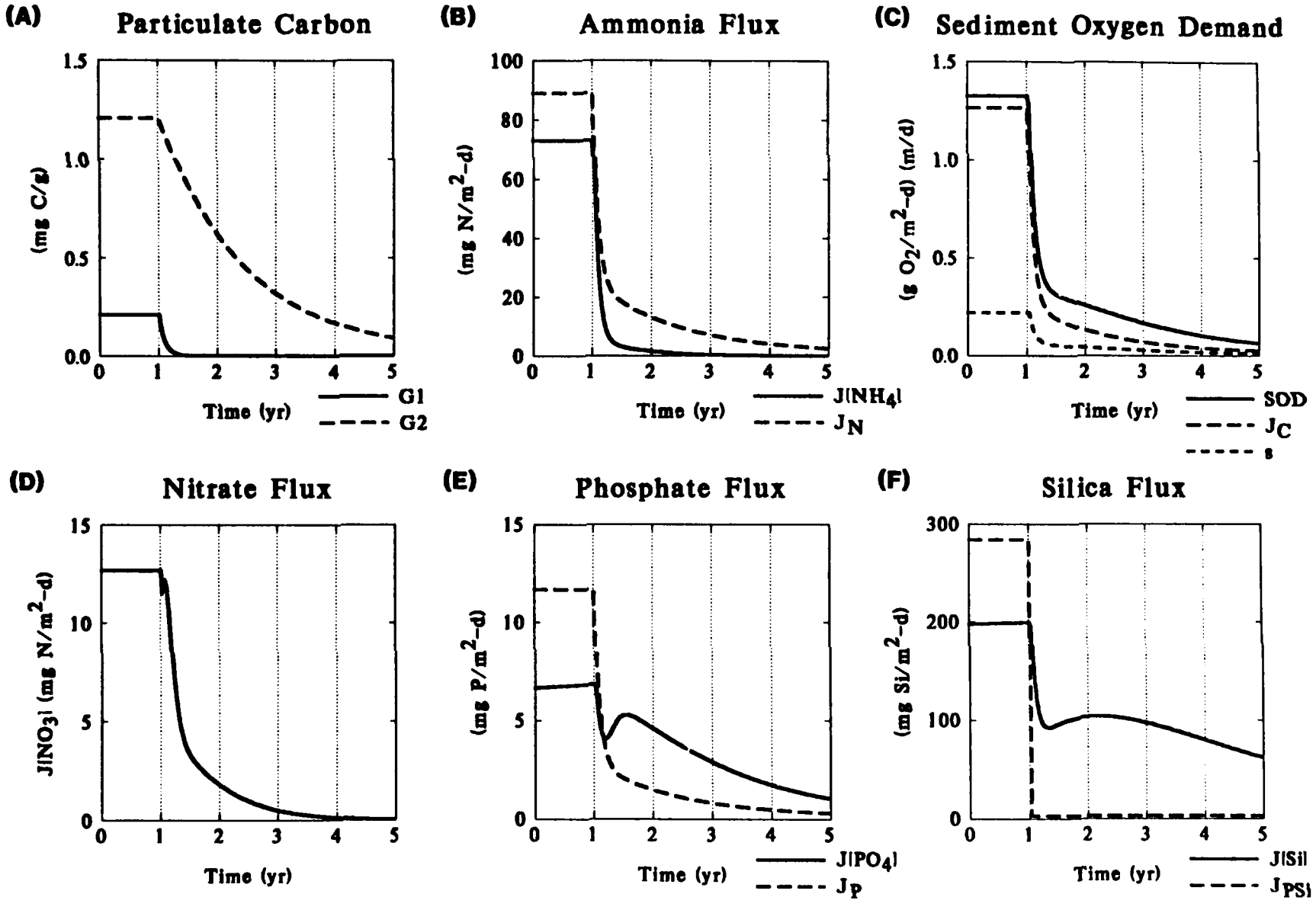

RUN98A - PLTTM1C

Figure 11.2

Transient Response - Aerobic

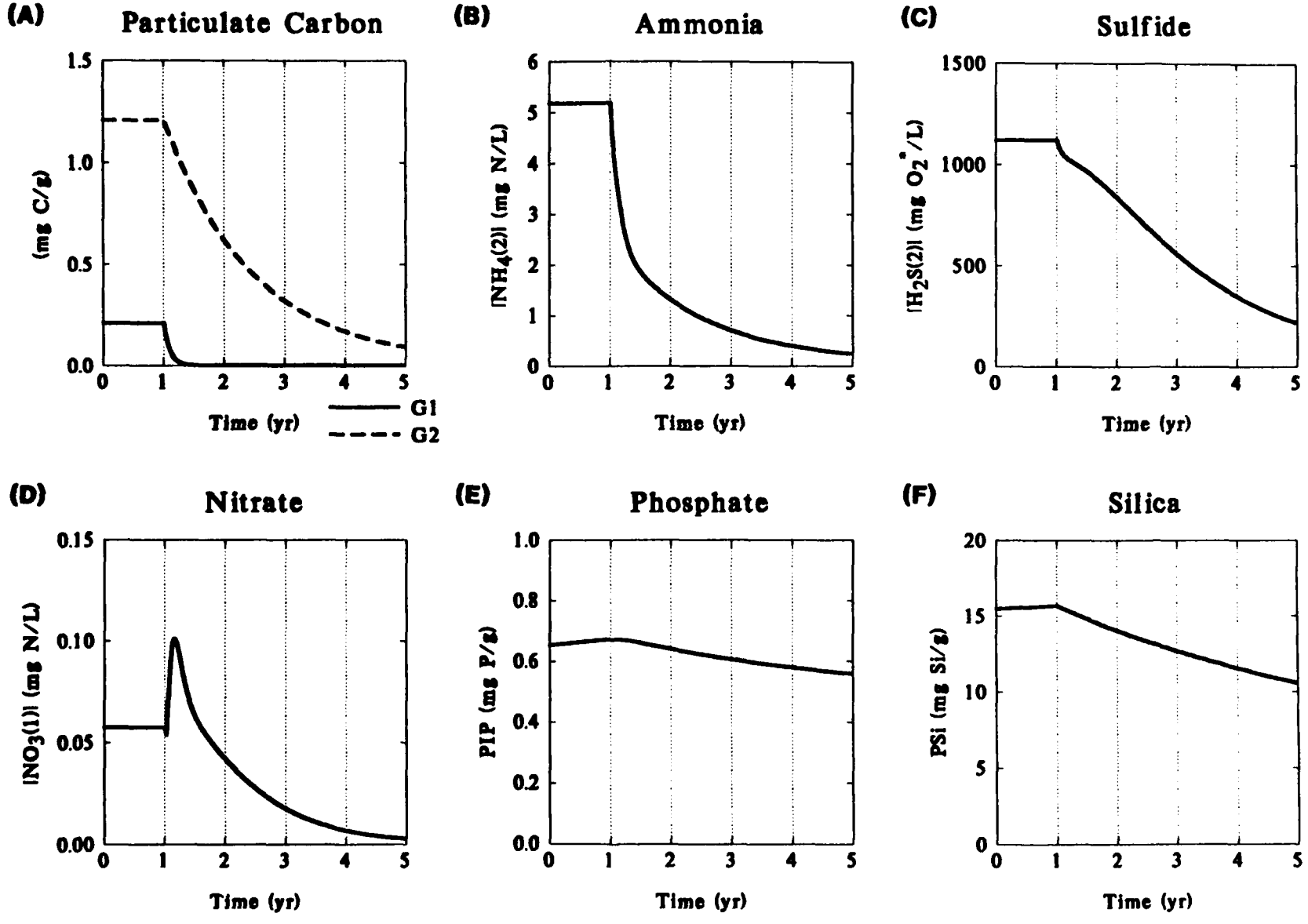

RUN98A - PLTTM1E

Figure 11.3

abrupt decrease in surface mass transfer coefficient. Sulfide, Fig. 11.3C, decreases more slowly, indicating further storage. Finally, phosphate, Fig. 11.3E, and silica, Fig. 11.3F, decrease only slightly during the first five years of the transient response.

Logarithmic plots for twenty years of simulation are shown in Fig. 11.4. Ammonia, nitrate, and SOD all reach their steady state values after ten years. However, both phosphate and silica are yet to reach their steady state values. The phosphate flux is still larger than the diagenesis flux, and both PIP and PSi are still declining after twenty years. Of course, the time constants of both phosphate and silica have as their upper bound, the time required for sedimentation to replace the sediment in the active layer. After three time constants have elapsed, $3H_2/w_2$, virtually all memory of the previous depositional flux has been removed from the system and the sediment has equilibrated to the new depositional fluxes. At this point the transient response is over.

2. Anaerobic Overlying Water

The transient response for the situation where the overlying water is anaerobic is less complex then the preceding case. The oxygen concentration is set to 0.1 mg/L rather than zero to avoid numerical problems. The results are shown in Fig. 11.5. Ammonia flux, Fig. 11.5B, is now equal to ammonia diagenesis since nitrification is limited by the low DO. It drops rapidly due to the G_1 decline and then more slowly, due to the slower G_2 decline, Fig. 11.5A. The situation for sediment oxygen demand is also more straightforward, Fig. 11.5C. Although carbon diagenesis decreases sharply, SOD, which is small to begin with due to the inhibition of sulfide oxidation by low DO, decreases slightly. The surface mass transfer coefficient, which is initially large, decreases somewhat as well. The nitrate flux, which is small to begin with, decreases further.

Phosphate flux is almost equal to phosphate diagenesis since the trapping by the aerobic layer is very small due to the reduction of phosphate sorption in response to the low overlying water DO. However, the time constant is still in excess of one year so that the transient extends beyond the first few years. Finally the silica flux exhibits almost no reduction for the first five years, indicating that the transient for silica is much longer.

Logarithmic plots for twenty years of simulation are shown in Fig. 11.6. Ammonia, nitrate, SOD, and phosphate all reach their steady state values after ten years . However, silica has yet to reach its steady state value although it is decreasing faster than the aerobic case. Again, the upper bound is set by the sedimentation rate and the depth of the active layer.

E. Conclusions

The transient response has a relatively short duration for ammonia, nitrate, and SOD. They are primarily determined by the time constant for G_2. The transient response for phosphate is of intermediate duration if the overlying water is aerobic, and is comparable to ammonia for anaerobic overlying water. For silica, the transient response is quite long, longer than the twenty years of simulated response time.

Transient Response – Aerobic

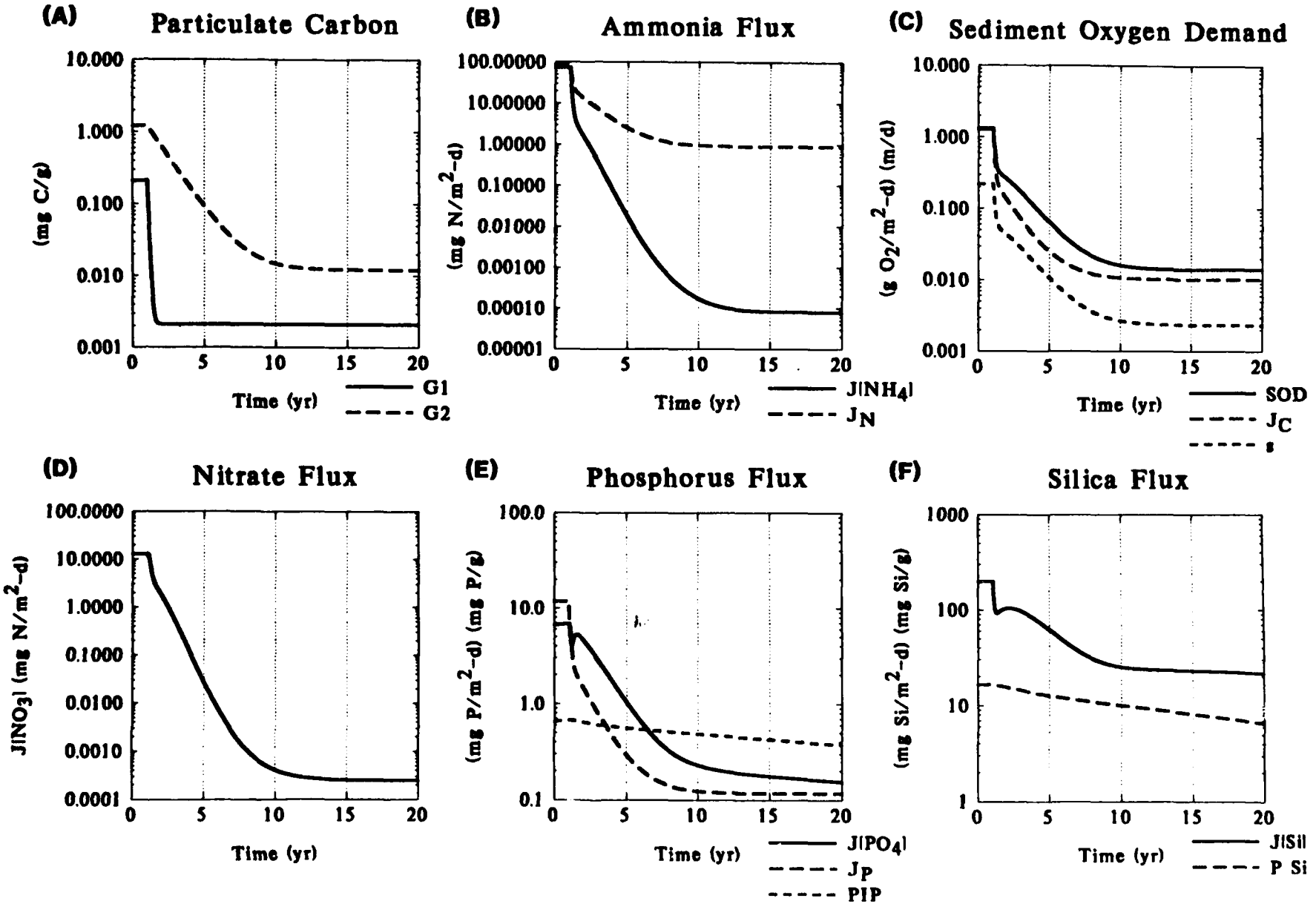

RUN98A - PLTTM1I

Figure 11.4

Transient Response – Anaerobic

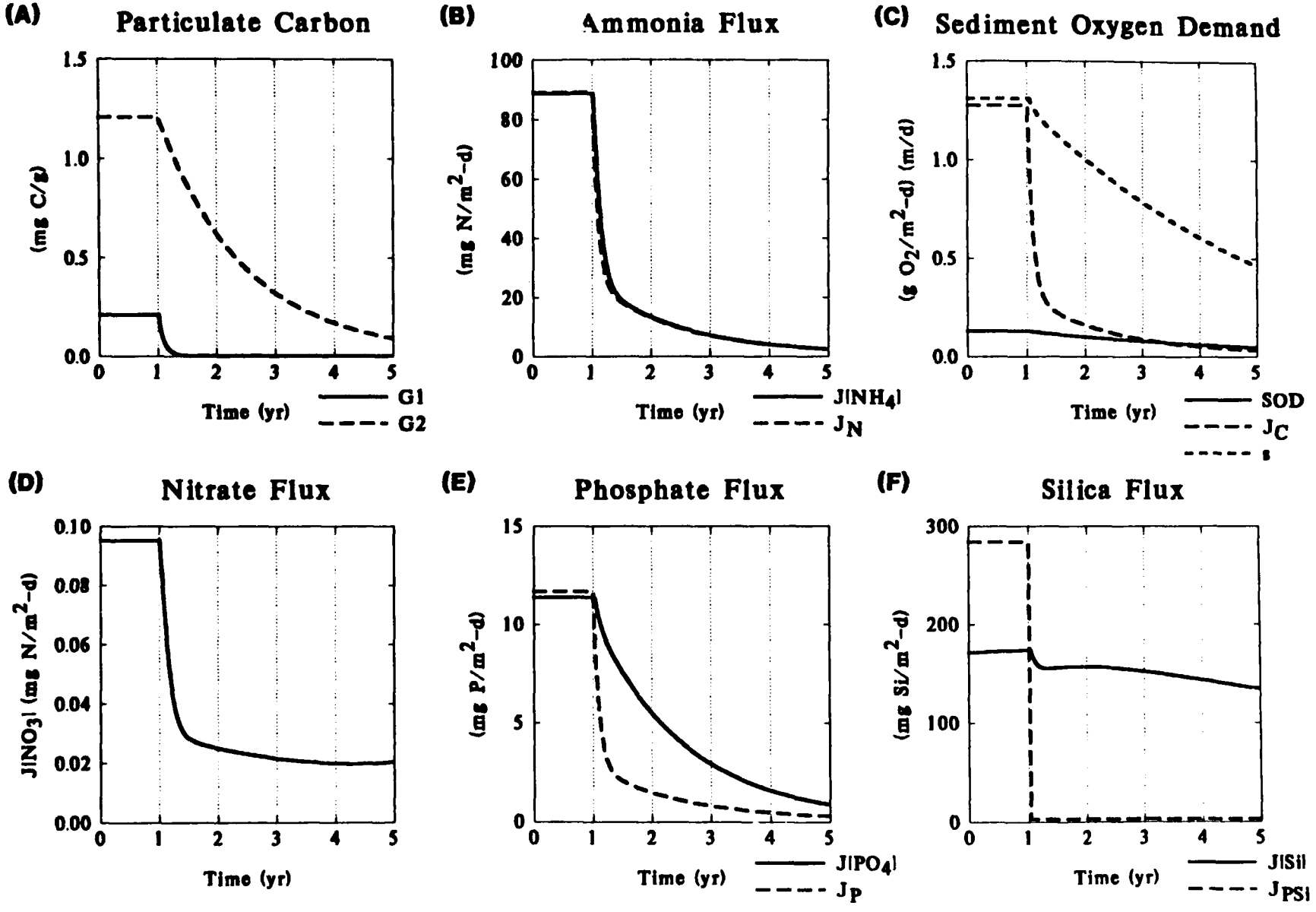

RUN98A - PLTTM1D

Figure 11.5

Transient Response – Anaerobic

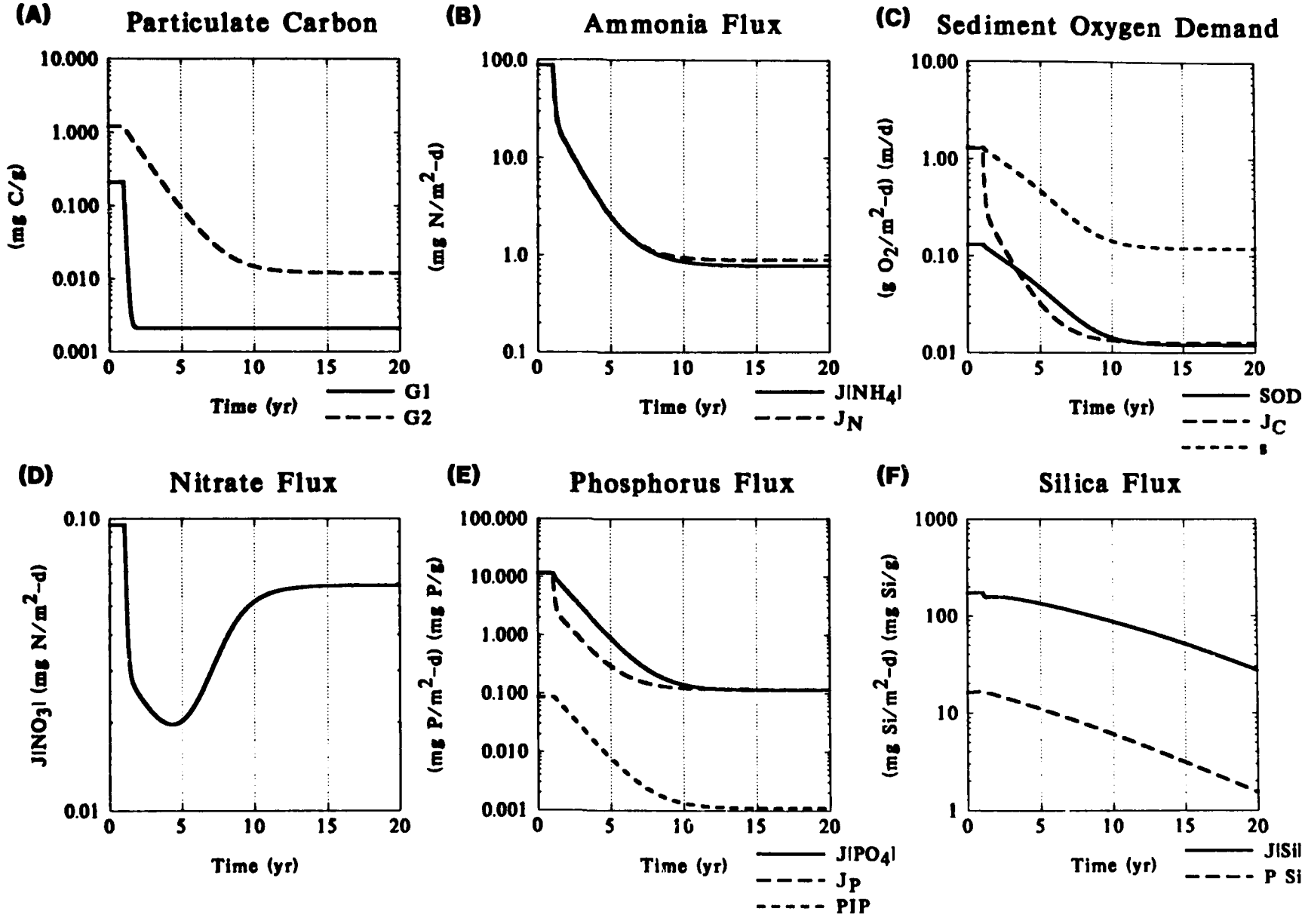

RUN98A - PLTTM1J

Figure 11.6

Table 11.2

Phosphate Flux Model Parameters

Time Constant Computation

Parameter	Aerobic	Anaerobic
$O_2(0)$	6.0 (mg/L)	0.1 (mg/L)
w_2	0.25 (cm/yr)	0.25 (cm/yr)
H_2	10 (cm)	10 (cm)
D_p	$1.2 \cdot 10^4$ (m^2/d)	$3.0 \cdot 10^6$ (m^2/d)
D_d	$1.0 \cdot 10^3$ (m^2/d)	$1.0 \cdot 10^3$ (m^2/d)
m_1	0.5 (kg/L)	0.5 (kg/L)
m_2	0.5 (kg/L)	0.5 (kg/L)
π_1	30,000 (L/kg)	133 (L/kg)
π_2	100 (L/kg)	100 (L/kg)
J_p	10 (mg P/m^2-d)	10 (mg P/m^2-d)

Table 11.3

Phosphate Flux Model Equations

$w_{12} = \frac{D_p}{H_2}$
$K_{L12} = \frac{D_d}{H_2}$
$f_{d1} = \frac{1}{1+m_1 n_1}$
$f_{p1} = 1 - f_{d1}$
$f_{d2} = \frac{1}{1+m_2 n_2}$
$f_{p2} = 1 - f_{d2}$

Table 11.4

Transient Response Parameters

Parameter	Value
J_{PON}	100 (mg N/m^2-d)
Aerobic $O_2(0)$	6.0 (mg O_2/L)
Anaerobic $O_2(0)$	0.1 (mg O_2/L)
Temperature	20.0 ℃

REPORT DOCUMENTATION PAGE

Form Approved
OMB No. 0704-0188

1. AGENCY USE ONLY *(Leave blank)*	2. REPORT DATE	3. REPORT TYPE AND DATES COVERED
	June 1993	Final report

4. TITLE AND SUBTITLE
Chesapeake Bay Sediment Flux Model

5. FUNDING NUMBERS

6. AUTHOR(S)
Dominic M. Di Toro
James J. Fitzpatrick

7. PERFORMING ORGANIZATION NAME(S) AND ADDRESS(ES)
HydroQual, Inc.
One Lethbridge Plaza
Mahwah, NJ 07430

8. PERFORMING ORGANIZATION REPORT NUMBER

9. SPONSORING/MONITORING AGENCY NAME(S) AND ADDRESS(ES)
Chesapeake Bay Program Office, U.S. Environmental Protection Agency, Annapolis, MD 21403; U.S. Army Engineer District, Baltimore, PO Box 1715, Baltimore, MD 21203-1715; U.S. Army Engineer Waterways Experiment Station, Environmental Laboratory, 3909 Halls Ferry Road, Vicksburg, MS 39180-6199

10. SPONSORING/MONITORING AGENCY REPORT NUMBER
Contract Report
EL-93-2

11. SUPPLEMENTARY NOTES
Available from National Technical Information Service, 5285 Port Royal Road, Springfield, VA 22161.

12a. DISTRIBUTION/AVAILABILITY STATEMENT
Approved for public release; distribution is unlimited.

12b. DISTRIBUTION CODE

13. ABSTRACT *(Maximum 200 words)*

Formulation and application of a predictive diagenetic sediment model are described in this report. The model considers two benthic sediment layers: a thin aerobic layer in contact with the water column and a thicker anaerobic layer. Processes represented include diagenesis, diffusion, particle mixing, and burial. Deposition of organic matter, water column concentrations, and temperature are treated as independent variables that influence sediment-water fluxes. Sediment oxygen demand and sediment-water fluxes of sulfide, ammonium, nitrate, phosphate, and silica are predicted. The model was calibrated using sediment-water flux observations collected in Chesapeake Bay 1985-1988. When independent variables were specified based on observations, the model correctly represented the time series of sediment-water fluxes observed at eight stations in the Bay and tributaries.

14. SUBJECT TERMS
Chesapeake Bay, Models, Sediments, Dissolved oxygen, Nitrogen, Eutrophication, Phosphorus

15. NUMBER OF PAGES
316

16. PRICE CODE

17. SECURITY CLASSIFICATION OF REPORT	18. SECURITY CLASSIFICATION OF THIS PAGE	19. SECURITY CLASSIFICATION OF ABSTRACT	20. LIMITATION OF ABSTRACT
UNCLASSIFIED	UNCLASSIFIED		